



TECHNICAL REPORT 3075  
September 2017

## **Mid-Latitude Mobile Wideband HF-NVIS Channel Analysis: Part 1**

Jeffery Allen  
Michael Daly  
John Meloling  
Nazia Mozaffar  
Marcos Ontiveros  
Fred Verd  
**SSC Pacific**

Demi Truong  
**Naval Research Enterprise  
Internship Program**

Approved for public release.

SSC Pacific  
San Diego, CA 92152-5001

**SSC Pacific**  
**San Diego, California 92152-5001**

---

**M. K. Yokoyama, CAPT, USN**  
**Commanding Officer**

**W. R. Bonwit**  
**Executive Director**

**ADMINISTRATIVE INFORMATION**

The work described in this report was performed for the Office of Naval Research (ONR) Code 30 by the Applied Electromagnetics Branch (Code 52250) and the Advanced Electromagnetics Technology Branch (Code 52270), Space and Naval Warfare Systems Center Pacific (SSC Pacific), San Diego, CA. Further support was provided by University of California, San Diego.

Released by  
David E. Hurdsmen, Head  
Applied Electromagnetics Branch

Under authority of  
Jodi McGee, Head  
System of Systems (SoS) and Platform  
Design Division

The citation of trade names and names of manufacturers is not to be construed as official government endorsement or approval of commercial products or services referenced in this report.

OSHKOSH® is a registered trademark of OSHKOSH Defense, LLC.  
National Instruments™ is a registered trademark of National Instruments.  
RFSpace is a registered trademark of RFSpace, Inc.  
FieldFox Spectrum Analyzer is a registered trademark of Keysight Technologies.  
MATLAB® is a registered trademark of The MathWorks, Inc.  
SpectraVue™ is a registered trademark of RFSpace, Inc.

## EXECUTIVE SUMMARY

High frequency (HF) links (2 to 30 MHz) are an alternative to the cost and tactical fragility of commercial satellite communications (SATCOM) for beyond line-of-sight (LOS) links. However, standard HF systems operating over a 3-kHz bandwidth do not provide sufficient throughput for network applications. Simply increasing bandwidth does increase throughput—provided the radios are properly designed for the time-varying wideband HF channel. The wideband HF channel is governed by the ionospheric variations caused by latitude, the night and day cycle, the direction and length of the haul, the seasons, and ionosphere disturbances. This report is the first of a series seeking a better understanding of each of these channel variations to aid in the design of wideband HF systems and the proper comparison of different HF radios and waveforms.

This report uses wideband mid-latitude HF channel soundings and three-dimensional (3-D) ray-tracing simulations to develop a statistical model of a particular nearly vertical incidence skywave (NVIS) channel. This model is expressed in a form that is programmable in a channel emulator so that different radios can be tested under controlled conditions. The 3-D ray-tracing code is validated by measurements with the intention of running the code over different times and geographic locations to generate channels that have not been measured over the air. Then, those simulated channels will be used to compute statistical models for particular geographic, temporal, and environmental conditions.

The immediate application of this particular channel is for small unit mobile ground forces with vehicle-mounted antennas. Near-term extensions support mid-latitude short-haul (200 to 1,500 km) and long-haul ship-to-ship and ship-to-shore wideband HF channels. Long-term payoffs for the warfighter will be a better HF radio design, leading to increased data rates, more stable networks, reduced power requirements, and improved low probability of detection (LPD).

# CONTENTS

<b>EXECUTIVE SUMMARY .....</b>	<b>iii</b>
<b>1 REPORT OUTLINE .....</b>	<b>1</b>
1.1 CURRENT RAY-TRACING LIMITATIONS .....	3
1.2 IONOSPHERIC PROCESSES .....	3
<b>2 MOBILE WIDEBAND HF-NVIS COMMUNICATION DESIGN .....</b>	<b>6</b>
2.1 MOBILE WIDEBAND HF-NVIS REQUIREMENTS .....	6
2.2 NARROWBAND HF-NVIS .....	7
2.3 A MOBILE WIDEBAND HF-NVIS LINK BUDGET .....	8
2.4 EVOLUTION OF WIDEBAND HF AND HF-NVIS .....	15
2.5 SUMMARY .....	22
<b>3 HF-NVIS CHANNELS AND THE IONOSPHERE .....</b>	<b>24</b>
3.1 O-MODE AND X-MODE .....	24
3.2 INDEX OF REFRACTION AND THE MAGNETIC FIELD .....	26
3.3 THE 1-HOP CHANNELS .....	28
3.4 THE 2-HOP CHANNELS .....	30
3.5 SUMMARY .....	34
<b>4 HF-NVIS CHANNEL MODELS .....</b>	<b>35</b>
4.1 GENERAL CHANNEL MODELS .....	36
4.2 PROPAGATION LOSSES IN HF AND HF-NVIS .....	40
4.3 DOPPLER SHIFT AND DOPPLER SPREAD IN HF .....	41
4.4 MID-LATITUDE HF-NVIS CHANNEL MODELS .....	43
4.5 HIGH-LATITUDE HF AND HF-NVIS MODELS .....	44
4.6 SUMMARY .....	46
<b>5 THE HF-NVIS CHANNEL SOUNDING SYSTEM .....</b>	<b>47</b>
5.1 TRANSMIT AND RECEIVE HF ANTENNAS .....	47
5.2 SOUNDING WAVEFORM .....	49
5.3 CHANNEL ESTIMATION .....	52
5.4 CALIBRATION .....	56
<b>6 SIGNAL, NOISE, AND INTERFERENCE ALONG THE MOBILE ROUTE .....</b>	<b>59</b>
6.1 SIGNAL POWER ALONG THE ROUTE .....	59
6.2 NOISE POWER ALONG THE ROUTE .....	60
6.3 INTERFERENCE ALONG THE ROUTE .....	61
<b>7 HF-NVIS CHANNEL ESTIMATES ALONG THE MOBILE ROUTE .....</b>	<b>65</b>
7.1 HF-NVIS CHANNEL AT 09:07 PST .....	67



7.2	HF-NVIS CHANNEL AT 09:41 PST .....	77
7.3	HF-NVIS CHANNEL AT 10:23 PST .....	85
7.4	HF-NVIS CHANNEL AT 13:00 PST .....	91
7.5	HF-NVIS CHANNEL AT 13:41 PST .....	98
7.6	MOBILE WIDEBAND HF-NVIS CHANNEL MODEL: NON-TID REGION.....	105
7.6.1	Delay.....	106
7.6.2	Fading.....	106
7.6.3	Doppler.....	107
7.6.4	Mode Correlation.....	108
<b>8</b>	<b>EXTENDING THE WIDEBAND HF-NVIS CHANNEL ESTIMATES .....</b>	<b>109</b>
8.1	O- AND X-MODE ARRIVAL TIMES.....	109
8.2	OVER THE WATER.....	110
8.3	NETWORKING FREQUENCIES.....	113
8.4	SUMMARY .....	114
<b>9</b>	<b>DEVELOPING THE HF-NVIS PORTFOLIO .....</b>	<b>115</b>
	<b>REFERENCES.....</b>	<b>116</b>
	<b>Appendix A CALIBRATION OF THE CHANNEL SOUNDING SYSTEM .....</b>	<b>A-1</b>
A.1	CALIBRATION FACTOR FOR RECEIVED POWER.....	A-1
A.2	EFFECT OF RECEIVE SDR INTERNAL ATTENUATION.....	A-3
	<b>Appendix B DOPPLER SHIFT MEASUREMENTS .....</b>	<b>B-1</b>
B.1	DOPPLER SHIFT DUE TO PLATFORM MOBILITY .....	B-1
B.2	DOPPLER SHIFT FROM MEASURED CHANNEL SOUNDING DATA.....	B-3
B.3	FITTING A DISTRIBUTION TO THE MEASURED DOPPLER SPREAD .....	B-4
	<b>Appendix C DOPPLER SHIFTS AND THE TIME-VARYING TRANSFER FUNCTION.....</b>	<b>C-1</b>
	<b>Appendix D 3-D IONOSPHERIC RAY TRACING USING <i>DRION</i>.....</b>	<b>D-1</b>

## Figures

1	HF-NVIS roadmap: theory, simulations, and measurements delivering channel models suitable for emulation.....	1
2	Single HF-NVIS hop .....	2
3	HF-NVIS 2-Hop .....	2
4	Ionospheric and thermospheric processes (This file is in the public domain in the United States because it was solely created by NASA) .....	3
5	Standard HF antenna pattern [19].....	7
6	Sky wave propagation showing the skip zone [19] .....	7
7	A typical upward-pointing HF-NVIS antenna pattern [19].....	8
8	HF-NVIS refracting off of the ionosphere [19] .....	8
9	Horizontal dipole [19].....	8
10	Rhombic antenna [19] .....	8

11	HMMVW with HF-NVIS loop superimposed in yellow of the same dimensions as the Harris RF-3134-AT003 antenna (photo credit: Claire Heininger, U.S. Army).....	9
12	Block diagram of the HF-NVIS link. Signal power: $p_T$ is power from the transmitting amplifier, $p_A$ is power delivered to the antenna, $p_{RAD}$ is power radiated, $p_X$ is signal power captured by receive antenna, and $p_R$ is signal power remaining after matching circuit. Gains: $G_T$ is transducer power gain of the matching circuit and $G_A$ is absolute gain of the antenna. Noise: $p_{N,RF}$ is external radio frequency (RF) noise and $p_{N,LO}$ internal receiver noise. ....	9
13	Simulated antenna pattern of a lossy vertical loop with a 59-in diameter mounted four ft above a perfect ground plane.....	10
14	Simulated gain of the lossy vertical loop above perfect ground sliced along the $y$ - $z$ plane; $G_A = 0$ dB at 5 MHz .....	10
15	Reflectance of the simulated 59-in diameter vertical loop of Figure 14; The circle marks the reflectance at 2 MHz; the end of the blue line marks the reflectance at 13 MHz.....	11
16	Matching the simulated 59-in diameter vertical loop at 5 MHz over 25 kHz using a third-order ladder .....	11
17	Sky temperatures $T_{eq}$ (K) generated by background noise sources [40, page 74].....	12
18	Urban wideband HF noise power from Equation 2.....	12
19	Power-SNR tradeoff for the 5-MHz HF-NVIS link using the 59-in diameter loop antenna operating in urban noise.....	13
20	Power-SNR tradeoffs for the 5-MHz HF-NVIS link using the 59-in diameter loop antenna operating in different noise models. The “X” is extrapolated from [85], in which the authors measure over 30-dB SNR over a 3-kHz bandwidth using a dipole antenna on transmit that translates to 21-dB SNR over a 24-kHz bandwidth. ....	14
21	Left: delay spread versus Doppler spread over long-haul wideband HF links (Reprinted with permission of the MITRE Corporation) [54]. Right: geographic location of the HF link. The lines other than the HF link are magnetic field lines.....	16
22	HF-SIMO link for over-the-air transmissions recorded in 2000; 20 kbps delivered over a 6-kHz band (figure courtesy of Annals of Geophysics) [61].....	16
23	HF-MIMO system for the over-the-air transmissions recorded in 2011; 24 kbps delivered over a 4.2-kHz band (figure courtesy of EURASIP Journal on Wireless Communications and Networking) [53] .....	17
24	Modified Giselle antenna for receive (figure courtesy of Dr. Stuart Feeney) [1].....	17
25	HF-MIMO capacity near 5.255 MHz estimated from over-the-air channel soundings recorded on 3 September 2008 [30] (figure courtesy of Radio Science).....	17
26	Vertical polarization scattering function; 10.677 MHz (figure courtesy of Dr. Kin Shing Bobby Yau) [88] .....	18
27	Dual-polarization MIMO capacity near 7 MHz estimated from over-the-air channel soundings recorded on 19 October 2012 (figure courtesy of Kuma Signals) [15].....	18
28	TX/RX crossed dipole antennas (reprinted with permission of the MITRE corporation) [66].....	19
29	OFDM and BPSK waveforms (reprinted with permission of the MITRE corporation) [66] .	19
30	Simultaneous measurement of HF-NVIS noise and interference in the early morning (figure courtesy of TrellisWare Technologies, Inc.) [24]. Vertical axis is time in seconds...	20
31	Tilting a whip to produce HF-NVIS [19].....	21
32	Compact HF-NVIS antenna [31] (figure courtesy of Hi-Q-MilitaryAntennas, Inc.).....	21
33	Mounted on an HMMWV [31] (Figure courtesy of Hi-Q-MilitaryAntennas, Inc.).....	21

34	HF-NVIS patterns produced by selected loop antennas exciting characteristic modes on a simulated EFV [71] (used with the author's permission) .....	22
35	One double horizontal loop antenna mounted on an M-ATV [33] .....	23
36	Realized gain for two horizontal loop antennas mounted on a simulated AAV over 24-kHz bandwidths as a function of frequency and ground [33].....	23
37	HF-NVIS multiple hops [20] .....	24
38	Illustration of the Earth's magnetic field .....	25
39	1-Hop O- and X-Modes .....	25
40	Top view of 1-Hops .....	25
41	Ionogram at Point Arguello on 10 February 2016 at 09:45 PST. Open source ionograms courtesy of the Global Ionospheric Radio Observatory at the University of Massachusetts, Lowell [64].....	26
42	Selected plasma frequencies (MHz) on the horizontal axis and associated heights (km) on the vertical axis. Open source ionograms courtesy of the Global Ionospheric Radio Observatory at the University of Massachusetts, Lowell [64].....	27
43	Block diagram of 1-Hop, O- and X-Mode propagation without polarization switching.....	29
44	Block diagram of 1-Hop, O- and X-Mode propagation showing polarizations switching.....	29
45	Ground reflection changing polarization .....	30
46	Block diagram of the 2-Hop O- and X-Mode channels showing ground scattering between channels .....	31
47	Horizontal reflection coefficient for sea water .....	32
48	Vertical reflection coefficient for sea water .....	32
49	Horizontal reflection coefficient for "very dry ground" .....	33
50	Vertical reflection coefficient for "very dry ground" .....	33
51	Delays caused by polarization switching and ground reflection.....	34
52	Narrowband HF-NVIS channel classification—delay spread versus Doppler spread (figure courtesy of TrellisWare Technologies, Inc. [41]) .....	35
53	Bello's channel functions.....	36
54	Scattering function estimated from 3100-km link operating at 15.5 MHz on 1 April 1992 at 07:35 UTC (reprinted with permission of the MITRE corporation) [54] .....	37
55	Plasma frequency $f_P(t, h)$ at Point Arguello; missing sample at 09:30 PST.....	41
56	Doppler shift caused by moving layer height for $f_P(t, h) = 5.82$ MHz at Point Arguello.....	42
57	Typical trough, its bounding walls, and the auroral oval (shaded) [73] (figure courtesy of Radio Science).....	45
58	HF medium-haul channels in the mid- and upper latitudes [73] .....	45
59	Block diagram of the HF-NVIS channel sounding system .....	47
60	Transmitter: 84.5-ft horizontal dipole located approximately 30 ft above the ground (yellow line) .....	48
61	Mobile HF-NVIS receiver carrying the dual-function antenna .....	48
62	Radiation pattern of dual-port loop at 5.8 MHz in the azimuthal plane .....	49
63	Radiation pattern of dual-port loop at 5.8 MHz in the elevation plane orthogonal to the plane of the loop.....	49
64	Radiation pattern of dual-port loop at 5.8 MHz in the elevation plane of the loop.....	50
65	Frame bundle.....	50
66	Simulated channel (top panel); Estimated channel (lower panel).....	54
67	Low-pass filter to generate in-band noise .....	55
68	Simulated channel (top panel); Estimated channel (lower panel).....	55
69	Received signal shaped into the frame-bundle format .....	57

70	First PN sequence of the first frame of the frame bundle .....	57
71	Comparing the real part of the measured received waveform to an ideal digital waveform. The scaling was selected to show the timing alignment .....	58
72	Extraction of the back-to-back channel to compute amplitude scaling .....	58
73	Route of the mobile HF-NVIS vehicle .....	59
74	Mobile HF-NVIS route .....	59
75	Ground range as a function of time .....	59
76	Raw whip power .....	60
77	Raw loop power .....	60
78	Raw whip noise .....	60
79	Raw loop noise .....	60
80	Average power received by the whip antenna .....	61
81	Location near Desert View Point at 09:54 PST .....	62
82	Radio tower near Desert View Point at 09:54 PST .....	62
83	Location after passing Ocotillo at 10:03 PST but prior to Coyote Wells .....	63
84	Radio tower after passing Ocotillo at 10:03 PST but prior to Coyote Wells .....	63
85	Location at 12:14 PST heading toward Ocotillo Wells .....	64
86	Cell tower enroute at 12:14 PST approaching Ocotillo Wells .....	64
87	HF-NVIS channel estimate extracted from the loop antenna over the entire experiment. The ground wave and the 3-Hop response are not labeled. ....	65
88	Receiver location along the track at 09:07 PST .....	67
89	Receiver location marked by yellow “thumbtack” at 09:07 PST .....	67
90	Channel estimate at 09:07 PST .....	68
91	Ionogram at 09:15 PST. Open source ionograms courtesy of the Global Ionospheric Radio Observatory at the University of Massachusetts, Lowell [64] .....	69
92	Estimated plasma frequency profile at 09:07 PST .....	69
93	1-Hops at 09:07 PST .....	70
94	1-Hops at 09:07 PST (top view) .....	70
95	Polarization along the 1-Hop O-Mode ray path at 09:07 PST .....	70
96	Polarization along the 1-Hop X-Mode ray path at 09:07 PST .....	70
97	Delay spread estimate at 09:07 PST .....	71
98	Scattering function estimated at 09:07 PST .....	72
99	1-Hop O-Mode amplitude and phase at 09:07 PST .....	73
100	1-Hop X-Mode amplitude and phase at 09:07 PST .....	74
101	Spectrogram at 09:07 PST .....	74
102	Spectrogram at 09:07 PST and the 1-Hop model with quadratic phase .....	75
103	“Goodness-of-fit” for the 1-Hop X-Mode amplitude at 09:07 PST .....	76
104	Fitting probability density functions to the 1-Hop X-Mode amplitude at 09:07 PST .....	76
105	Receiver location on the track at 09:41 PST .....	77
106	Receiver location marked with yellow “thumbtack” at 09:41 PST .....	77
107	Channel estimate at 09:41 PST .....	78
108	Point Arguello, CA ionogram at 09:45 PST. Open source ionograms courtesy of the Global Ionospheric Radio Observatory at the University of Massachusetts, Lowell [64] ....	79
109	Estimated plasma frequency profile at 09:41 PST .....	79
110	1-Hops at 09:41 PST .....	80
111	1-Hops at 09:41 PST (top view) .....	80
112	Polarization along the 1-Hop O-Mode ray path at 09:41 PST .....	80
113	Polarization along the 1-Hop X-Mode ray path at 09:41 PST .....	80

114	Delay spread estimate at 09:41 PST .....	81
115	Scattering function estimated at 09:41 PST .....	81
116	1-Hop O-Mode amplitude and phase at 09:41 PST .....	82
117	1-Hop X-Mode amplitude and phase at 09:41 PST .....	83
118	Spectrogram at 09:41 PST .....	84
119	Receiver location on the track at 10:23 PST .....	85
120	Channel estimate at 10:23 PST .....	85
121	Point Arguello, CA ionogram at 10:30 PST. Open source ionograms courtesy of the Global Ionospheric Radio Observatory at the University of Massachusetts, Lowell [64]....	86
122	Plasma frequency at 10:23 PST estimated from the ionograms at Point Arguello, CA, Boulder, CO, and Austin, TX.....	87
123	1-Hops at 10:23 PST .....	87
124	1-Hops at 10:23 PST (top view) .....	87
125	Polarization along the 1-Hop O-Mode ray path at 10:23 PST .....	88
126	Polarization along the 1-Hop X-Mode ray path at 10:23 PST.....	88
127	Delay spread estimate at 10:23 PST .....	88
128	1-Hop O-Mode amplitude and phase at 10:23 PST .....	89
129	1-Hop X-Mode amplitude and phase at 10:23 PST .....	89
130	“Goodness-of-fit” for the 1-Hop O-Mode amplitude at 10:23 PST .....	90
131	Fitting probability density functions to the 1-Hop O-Mode amplitude at 10:23 PST .....	90
132	Receiver location on the track at 13:00 PST .....	91
133	Receiver location at 13:00 PST marked by the yellow “thumbtack.” .....	91
134	Channel estimate from the loop antenna at 13:00 PST .....	92
135	Hybrid plasma frequency at 13:00 PST .....	93
136	Ionogram at Point Arguello, CA at 13:00 PST. Open source ionograms courtesy of the Global Ionospheric Radio Observatory at the University of Massachusetts, Lowell [64]....	93
137	Delay spread estimate at 13:00 PST .....	94
138	1-Hop O-Mode amplitude and phase at 13:00 PST .....	95
139	1-Hop X-Mode amplitude and phase at 13:00 PST .....	96
140	O-Mode Doppler spectrum estimate at 13:00 PST.....	96
141	X-Mode Doppler spectrum estimate at 13:00 PST .....	96
142	Receiver location on the track at 13:41 PST .....	98
143	Receiver location marked with yellow “thumbtack” at 13:41 PST .....	98
144	Channel estimate from the loop antenna at 13:41 PST .....	99
145	Point Arguello, CA ionogram at 13:45 PST. Open source ionograms courtesy of the Global Ionospheric Radio Observatory at the University of Massachusetts, Lowell [64]....	101
146	Hybrid plasma frequency estimate at 13:41 PST .....	101
147	Delay spread estimate at 13:41 PST .....	102
148	1-Hop O-Mode amplitude and phase at 13:41 PST .....	103
149	1-Hop X-Mode amplitude and phase at 13:41 PST .....	103
150	O-Mode Doppler spectrum estimate at 13:41 PST.....	104
151	X-Mode Doppler spectrum estimate at 13:41 PST .....	104
152	1-Hop O- and X-Mode delays.....	105
153	Joint distribution of 1-Hop delays from 09:30 to 10:30 PST .....	106
154	O-Mode delay $\tau_O$ and fitted distributions.....	106
155	Excess delay $\tau_D$ and fitted distributions .....	106
156	O-Mode envelope and scattered power .....	107
157	X-Mode envelope and scattered power.....	107

158	O-Mode Doppler.....	107
159	X-Mode Doppler.....	107
160	Estimated cross correlation between the O- and X-Modes .....	108
161	Over-the-water link between Point Loma and San Clemente Island .....	110
162	Point Arguello, CA ionogram at 15 December 2015 at 10:00 PST. Open source ionograms courtesy of the Global Ionospheric Radio Observatory at the University of Massachusetts, Lowell [64].....	111
163	1-, 2-, and 3-Hop between Point Loma and San Clemente Island, CA; 15 December 2015 at 10:00 PST .....	111
164	“Channel” between between Point Loma and San Clemente Island; 15 December 2015 at 10:00 PST .....	112
165	Relative received power over the 09:41 PST link .....	113
A-1	Block diagram of the calibration using the NI USRP transmit radio (with external power amplifiers bypassed), external attenuators, and the receive chain and receive SDR (RFSPACE® SDR-IP) .....	A-1
A-2	Channel correlation from calibration setup with a center frequency of 2 MHz.....	A-3
A-3	Channel correlation with no internal attenuation. The additional spikes are due to the received signal constantly exceeding the dynamic range of the SDR’s digitizer. ....	A-4
A-4	Channel correlation with 10-dB internal attenuation.....	A-4
A-5	Channel correlation with 20-dB internal attenuation.....	A-5
A-6	Channel correlation with 30-dB internal attenuation.....	A-5
B-1	The direction of propagation of an HF-NVIS signal between two mobile ground vehicles using NVIS antennas with velocities $v_1$ and $v_2$ .....	B-1
B-2	The root mean squared Doppler shift as a function of frequency .....	B-2
B-3	A histogram of the predicted Doppler shifts when transmitting at 2 MHz .....	B-3
B-4	A histogram of the predicted Doppler shifts when transmitting at 12 MHz .....	B-3
B-5	Doppler shifts of all correlation peaks throughout the El Centro, CA channel sounding run. Doppler shifts of the first hop O-Mode are blue dots, the part of the Doppler shift attributable to vehicle motion for the O-Mode paths are red dots, Doppler shifts of the first hop X-Mode are green dots, and the part of the Doppler shift attributable to vehicle motion for the X-Mode paths are magenta dots.....	B-4
B-6	A histogram of measured Doppler shifts of the first hop O- and X-Modes with Doppler caused by receive vehicle motion subtracted off .....	B-5
B-7	Histogram of measured O-Mode Doppler shifts with best fit Gaussian and $t$ Location-Scale distributions.....	B-5
B-8	Histogram of measured X-Mode Doppler shifts with best fit Gaussian and $t$ Location-Scale distributions.....	B-5
C-1	Time-varying filter .....	C-2

## Tables

1	Ionospheric parameters .....	4
2	Frequencies and heights characterizing the electron density profile.....	4
3	HF-NVIS channel parameters .....	4
4	Transducer power gain $G_T$ (dB) for degree 3 matching at 5 MHz of the simulated 59-in diameter vertical loop antenna. $G_T$ is the worst case gain in the bandwidth.....	11
5	Virtual heights and round-trip travel times (delay) at 5.82 MHz estimated from Figure 41 .....	26
6	Index of refraction, modes, and acute-angle polarizations .....	30

7	Mid-latitude narrowband HF-NVIS channel models; $h_k$ magnitude (abs); $\tau_k$ delay (ms); $\Delta f_k$ Doppler spread (Hz); Doppler shift is zero.....	43
8	Doppler spreading and magnetic activity [82, Table 2].....	44
9	Labeling scheme for the .WAV files .....	51
10	Parameters for the digital PN signal .....	53
11	Comparing hop times between the sounding, simulation, and the nearest ionogram (Point Arguello, CA) at 09:07 PST .....	71
12	Comparing measured and estimated Doppler shifts in Hz based on the estimated mobile speed $v = -67$ mph .....	73
13	Wideband HF-NVIS channel model; 5.82 MHz; 10 February 2016 09:07 PST .....	76
14	Comparing hop times between the sounding, simulation, and ionogram at 09:41 PST .....	78
15	Wideband HF-NVIS channel model; 5.82 MHz; 10 February 2016 09:41 PST .....	84
16	Comparing O- and X-Mode hop times between the sounding, simulation, and the nearest ionogram (Point Arguello, CA) at 10:23 PST .....	86
17	Wideband HF-NVIS channel model; 5.82 MHz; 10 February 2016 10:23 PST .....	90
18	Comparing O- and X-Mode hop times between the sounding, simulation, and the nearest ionogram (Point Arguello, CA) at 13:00 PST .....	92
19	Wideband HF-NVIS channel model; 5.82 MHz; 10 February 2016 13:00 PST .....	97
20	Comparing O- and X-Mode hop times between the sounding, simulation, and the nearest ionogram (Point Arguello, CA) at 13:41 PST .....	100
21	Wideband HF-NVIS channel model; 5.82 MHz; 10 February 2016 13:41 PST .....	104
22	Mid-Latitude mobile wideband HF-NVIS channel model using only the 1-Hop O- and X-Modes; 5.82 MHz over the non-TID region from 9:30 to 10:30 PST; interference and mode correlation are omitted from this model.....	105
23	Measured and simulated hop times as a function of frequency using the ionogram at 09:41 PST .....	109
24	Comparing simulated ray path delays to the delays estimated from the Point Arguello, CA ionogram at 15 December 2015 at 10:00 PST .....	110
25	Simulated transmitter and receiver antennas.....	112
26	Simulated propagation losses between between Point Loma and San Clemente Island; 15 December 2015 at 10:00 PST .....	113
27	Antennas on the 09:41 PST link .....	113
A-1	Pure tone power measurements and adjustment factors for each radio to go from “digital power” to incident power at the receive chain. Not included in the adjustment factors is the loss through a hybrid coupler, which was measured to be approximately 0.1 dB over the entire HF band .....	A-2
A-2	Channel correlation peak values and adjustment factors for each radio to compute incident power at the receive chain of the channel sounding waveform. Correlations are scaled by a normalization factor of 0.025133. Not included in the adjustment factors is the loss through a hybrid coupler, which was measured to be approximately 0.1 dB over the entire HF band. ....	A-3
B-1	Modeling the Doppler shift induced by the ionosphere without vehicle speed.....	B-6

# 1. REPORT OUTLINE

This report analyzes a mid-latitude wideband high frequency nearly vertical incidence skywave (HF-NVIS) channel. The immediate objective is a wideband HF-NVIS channel model suitable for software simulation and hardware emulation. The long-term objective is to produce a three-dimensional (3-D) ray-tracing code suitable for assessing HF waveforms, HF antenna designs including polarizations, automatic link establishment (ALE), and stealthy HF communications, and modeling credible HF channels in regions of tactical interest. This report is the first of a series to populate the wideband HF-NVIS channel portfolio discussed in the Executive Summary. Figure 1 shows a high-level view of this process proceeding from channel validation to statistical modeling to wideband HF channel emulation.

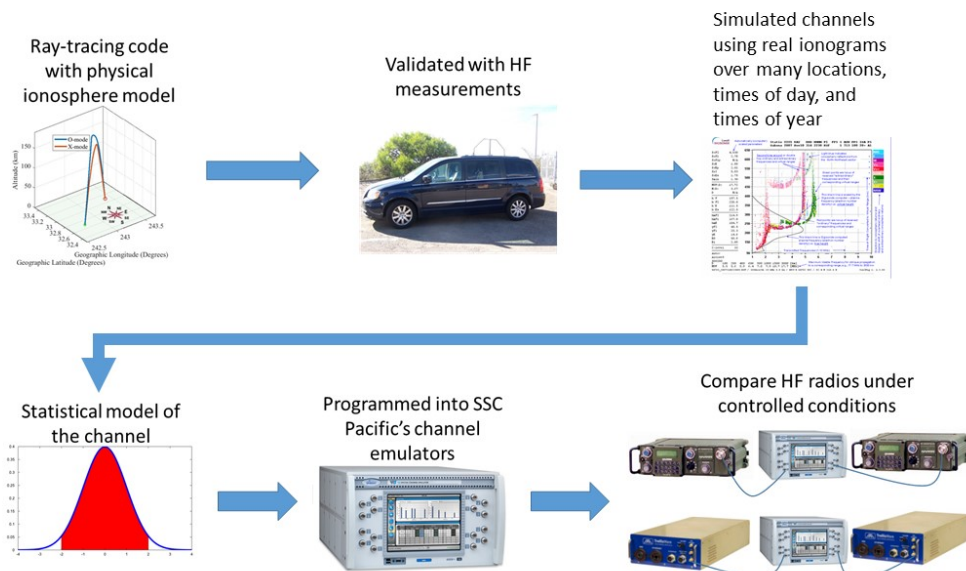


Figure 1. HF-NVIS roadmap: theory, simulations, and measurements delivering channel models suitable for emulation.

Section 2 provides a context for this roadmap and the follow-on reports. The initial Office of Naval Research (ONR) requirements for mobile HF-NVIS links—a mobile satellite communications (SATCOM) “lite”—are quantified using a basic link budget. This link budget shows that the vehicle-sized antenna is the link’s bottleneck. Accordingly, recent antenna designs are reviewed to bound the state of the art. The upshot is that further gains must come from HF-NVIS channel knowledge.

Section 3 reviews HF-NVIS channels using ray paths. Figures 2 and 3 show mid-latitude HF-NVIS ray paths linking a transmitter to its receiver. These ray paths are computed by the 3-D ray-tracing code detailed in Appendix D. These ray paths are determined by the electron density, the magnetic field, and the ions and neutral particles in a static and spherically homogeneous ionosphere determined from neighboring ionograms. The O- and X-Modes are produced by the index of refraction and the Earth’s magnetic field (O-Mode bends north; X-Mode bends south). The novelty of this section is the linking of polarization evolution along the ray path and the consequences for multiple hops. This multi-hop analysis is applied to the measured channel soundings to determine their delay structure. Once the ray paths are known, the propagation losses—spreading, mode-shedding, and absorption—may be computed under the



assumption these losses have not distorted the ray paths. Together, with the antenna coupling into these ray paths, the 3-D ray tracing permits the coherent summation of the electric field to capture Faraday fading effects, O- and X-Mode processing, dual-polarization processing, and the antenna coupling for single input multiple output (SIMO) and multiple input multiple output (MIMO) links.

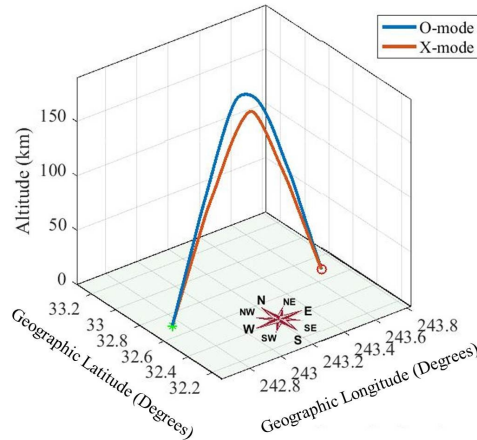


Figure 2. Single HF-NVIS hop.

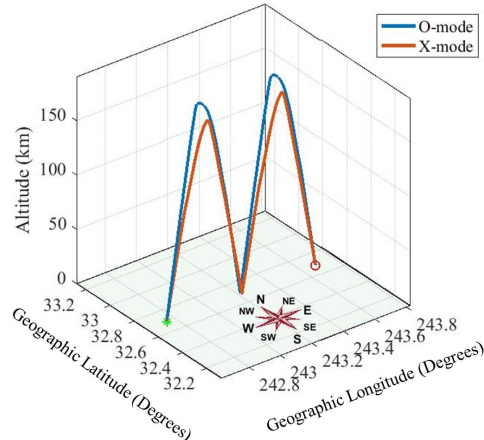


Figure 3. HF-NVIS 2-Hop.

Section 4 generalizes the discussion to an ionosphere that is time-varying and spherically inhomogeneous. In this case, the single and multiple hops of a nominal static ionosphere are subject to fast and slow fading. The section starts by reviewing time-varying channels to make explicit the scattering function, the delay spread, the Doppler spread, the Doppler shift, and the fading processes. HF-NVIS channels cluster in two classes in the Doppler-delay plane:

- Mid-latitude channels show small Doppler spread and large delay spread
- High-latitude channels show large Doppler spread and small delay spread

Section 4.4 lists the narrowband mid-latitude HF-NVIS channels suitable for programming an HF channel emulator. Section 4.5 reviews the Doppler-delay spreads for high latitudes. These surveys show relatively few wideband HF-NVIS channel models exist in a form suitable for HF channel emulators.

Sections 5, 6, and 7 pertain to the soundings and analysis of a mid-latitude channel on 10 February 2016 at 5.82 MHz over the 25-kHz band. Section 5 reviews the HF-NVIS channel sounding process: antennas, hardware, waveform, and channel estimation. Section 6 documents the signal, noise, and interference along the route. Section 7 is the channel analysis. Selected channels along the route are examined in detail using the 3-D ray-tracing code to untangle closely spaced O- and X-Modes on the first hop, identify multihops, and identify the ray paths that are not multiples of the first hop. The channel statistics suitable for a channel emulator are extracted. This section concludes by processing all the channels window to deliver an “average” wideband HF-NVIS channel ensemble suitable for a channel emulator.

Section 8 lays out selected HF system analyses made possible by this 3-D ray-tracing code:

- Augmenting HF Portfolios
- O- and X-Mode diversity gain
- Over-the-water multipath
- Multiple channels for HF Internet Protocol (HF-IP)

The close agreement between the measured and simulated HF channels in this report supports the claim that the costly, time-consuming, and non-repeatable over-the-air testing may be augmented by simulation to populate HF channel ensembles supporting HF system assessment both in simulation and emulation.

## 1.1 CURRENT RAY-TRACING LIMITATIONS

The 3-D ray-tracing code of this report includes the O- and X-Modes, multiple hops, antennas, and polarization along the ray path to coherently sum the complex-valued responses of the receive antenna to the arriving electric field. Ray-tracing codes that track power only cannot model multipath HF channel responses nor encompass the multi-antenna designs. Nevertheless, all ray-tracing codes require the electron density profile and magnetic field. Ideally, ray-tracing simulations use the time-varying electron density and magnetic fields at each spatial location along the ray path. Currently, this 3-D ray-tracing code extracts electron densities from ionograms at selected locations where the soundings are taken in time increments ranging from 5 to 30 minutes. Consequently, this electron density estimate is static and cannot model the time-varying Doppler or fading along ray paths. Similarly, the magnetic field is obtained from the Earth's magnetic field and is also a static model. Including these time-varying ionospheric processes, especially for mission planning, is a substantial challenge. Therefore, this preface closes with the illustration of the time-varying ionospheric processes.

## 1.2 IONOSPHERIC PROCESSES

Figure 4 is a superb graphic relating multiple ionospheric processes. Solar activity produces layers of varying electron densities on the sun-facing side of the ionosphere. The night-facing side of the ionosphere has a reduced density and fewer layers. In this report, the mid-latitude region is relatively stable with only one traveling ionospheric disturbance (TID) observed in these soundings; mid-latitude irregularities—the 2.5 ray paths observed in the soundings—are likely caused by sporadic E-layers. The high-latitudes show complex magnetic activity: Doppler spreads up to 16 Hz are reported in the literature [73]; HF-NVIS propagation can break down in the polar regions—the HF links propagate via the polar walls rather than overhead [73]; and Doppler effects require both time variation and the frequency variation of the electron density [36]. Nevertheless, the Hamiltonian encoded in the 3-D ray tracing supports time-varying effects.

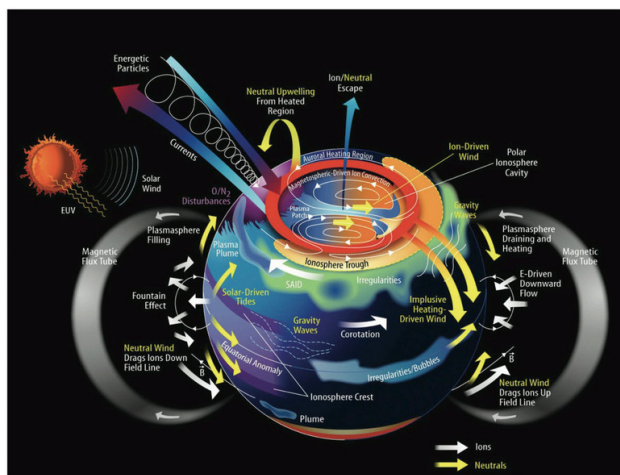


Figure 4. Ionospheric and thermospheric processes (This file is in the public domain in the United States because it was solely created by NASA).

In theory, simulation of HF system performance is possible—provided physics-based time-varying models of the ionospheric processes are available. Maslin’s observation [46, Section 8.2.3] states “predictions can only be as good as the model,” which requires the HF ensembles encompass the modeling extrema. Consequently, Section 9 details approaches to bring these time-varying models into this HF portfolio.

Tables 1, 2, and 3 define the symbols used for ionospheric parameters, the plasma frequencies and layer heights, and HF channel parameters, respectively.

Table 1. Ionospheric parameters.

$B_0$	Magnitude of the Earth’s magnetic induction field (Tesla)
$\epsilon_0$	Permittivity of free space (F/m)
$f_P$	Plasma frequency (Hz)
$f_D$	Doppler shift (Hz)
$\Delta f$	Doppler spread (Hz)
$m_e$	Electron mass (kg)
$N_e$	Electron density (number of electrons per cubic meter)
$N_n$	Neutral particle density (number of neutral particles per cubic meter)
$q_e$	Charge of an electron (C)
$T_e$	Electron temperature (K)
$\omega_P$	Plasma frequency (rad/sec)
$\omega_H$	Gyro-frequency (rad/sec)
$\omega_E$	Electron collision frequency (rad/sec)
$\omega_{E,I}$	Electron-ion collision frequency (rad/sec)
$\omega_{E,N}$	Electron-neutral collision frequency (rad/sec)

Table 2. Frequencies and heights characterizing the electron density profile.

foF2	F2 layer plasma frequency (MHz)
foF1	F1 layer plasma frequency (MHz)
foE	E layer plasma frequency (MHz)
hmF2	F2 layer $N_e$ maximum height (km)
hmF1	F1 layer $N_e$ maximum height (km)
hmE	E layer $N_e$ maximum height (km)

Table 3. HF-NVIS channel parameters.

$f_C$	Center frequency (MHz)
$f_B$	Bandwidth (kHz)
$f_D$	Doppler shift (Hz)
$\Delta f$	Doppler spread (Hz)
$\tau$	Delay (sec)

## ACRONYMS

ALE	Automatic Link Establishment
BPSK	Binary Phase-Shift Keying
CCIR	Consultative Committee on International Radio
DSTG	Defense Science and Technology Group
EFV	Expeditionary Fighting Vehicle
EM	Electromagnetic
GPS	Global Positioning System
GPSDO	GPS-disciplined Oscillator
HF	High Frequency
HF-IP	HF Internet Protocol
HMMWV	High-Mobility Multipurpose Wheeled Vehicle
IEEE	Institute of Electrical and Electronics Engineers
LCP	Left Circularly Polarized
LEP	Left Elliptical Polarized
LNA	Low-noise Amplifier
LOS	Line-of-sight
LPD	Low Probability of Detection
M-ATV	Mine-Resistant Ambush Protected All-Terrain Vehicle
MIMO	Multiple Input Multiple Output
NB	Narrowband
NVIS	Near Vertical Incidence Skywave
O-Mode	Ordinary Mode
ODE	Ordinary Differential Equation
OFDM	Orthogonal Frequency Division Multiplexing
ONR	Office of Naval Research
PA	Power Amplifier
PMFS	Phase Modulation Fading Simulator
PN	Pseudorandom noise
PST	Pacific Standard Time
QMFS	Quadrature Modulation Fading Simulator
RCP	Right Circularly Polarized
REP	Right Elliptical Polarized
RIFF	Resource Interchange File Format
RF	Radio Frequency
SATCOM	Satellite Communications
SBIR	Small Business Innovation Research
SDR	Software-defined Radio
SIMO	Single Input Multiple Output
SISO	Single Input Single Output
SNR	Signal-to-Noise Ratio
SPAWAR	Space and Naval Warfare Center
TID	Traveling Ionospheric Disturbance
USRP	Universal Software Radio Peripheral
VOACAP	Voice of America Coverage Analysis Program
VSWR	Voltage Standing Wave Ratio
WB	Wideband
X-Mode	Extraordinary Mode

## 2. MOBILE WIDEBAND HF-NVIS COMMUNICATION DESIGN

Sklar observes that radio design intertwines *requirements* and the *channel* [72]:

The design of any digital communication systems begins with a description of the channel (receiver power, available bandwidth, noise statistics, ... ) and a definition of the system requirements (data rate and error performance).

This report adapts Sklar's system-level view for HF-NVIS operating on a mobile platform. Section 2.1 sets out the mobile wideband HF-NVIS requirements. Section 2.2 reviews HF-NVIS propagation and the antenna patterns necessary to send and receive on the HF-NVIS links. Section 2.3 analyzes the tradeoffs to operate HF-NVIS from a ground vehicle. Section 2.4 reviews progress in wideband HF relevant to mobile wideband HF-NVIS. The vehicle-sized antennas are the bottleneck of these HF-NVIS systems. Therefore, understanding the HF-NVIS channel is necessary to optimize the link from these power- and bandwidth-limited platforms.

### 2.1 MOBILE WIDEBAND HF-NVIS REQUIREMENTS

ONR observed communication shortfalls in expeditionary and irregular warfare [49]:

- SATCOM is easy to jam
- Mountainous terrain blocks line-of-sight (LOS) communications
- An HF skip zone exists that causes certain distances to be unreachable by HF waves when using certain antenna types

One solution exploits the nearly vertical skywaves of HF-NVIS to lift data “up and over” terrain, cover the HF skip zone, and offer a SATCOM “lite” link. Therefore, ONR's *Improved HF Communications* Small Business Innovation Research (SBIR) sought a link suitable for Small Unit Communications Platforms using the following requirements:

- Power: ground vehicles (150 Watts); manpack (20 Watts)
- Throughput: 100 kbps
- Range: 0 to 100 miles
- Frequency: 2 to 12 MHz
- Bandwidth: 3 to 24 kHz

Implicit in “mobile” is the requirement that the wideband HF-NVIS antenna fits on an operational vehicle and does not interfere with mission requirements. Section 2.4 illustrates current and proposed vehicle-mounted HF-NVIS antennas. Conventional HF bandwidth is 3 kHz. Wider bands typically step in multiples of 3-kHz up to 24-kHz (MIL-STD-188-110C Appendix D [26]). This report uses the 24-kHz bandwidth.

## 2.2 NARROWBAND HF-NVIS

The *NVIS Army Field Manual 24-18* provides an excellent summary of conventional HF shortfalls [20]:

Sky waves, generated by standard antennas (for example, doublets) which efficiently launch the sky wave, will not return to earth at a range of less than 161 kilometers (100 mi). This can leave a skip zone of at least 80 to 113 kilometers (50 to 70 mi) where HF communications will not function. This means that units such as long-range patrols, armored cavalry deployed as advance or covering forces, air defense early warning teams, and many division-corps, division-brigade, division-DISCOM and division-DIVARTY stations are in the skip zone and thus unreachable by HF radio even though HF is a primary means of communication to these units.

Figure 5 shows a standard HF antenna pattern that launches most of the HF energy at approximately 20° elevation angle. Figure 6 illustrates the skip zones produced by standard HF antennas.

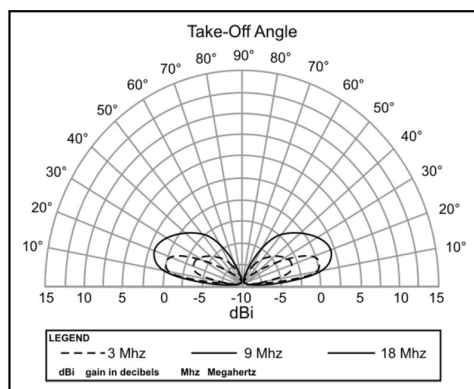


Figure C-1. 32-foot vertical whip, vertical antenna pattern

Figure 5. Standard HF antenna pattern [19].

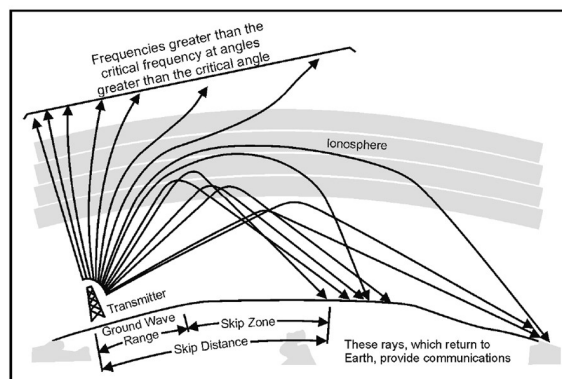


Figure B-6. Sky wave transmission paths

Figure 6. Sky wave propagation showing the skip zone [19].

The *Army Field Manual 24-18* describes how HF-NVIS propagation overcomes the skip zone [20]:

Energy radiated in a near-vertical incidence direction is not reflected down to a pinpoint on the Earth's surface. If it is radiated on too high a frequency, the energy penetrates the ionosphere and continues on out into space. Energy radiated on a low enough frequency is reflected back to earth at all angles (including the zenith), resulting in the energy striking the earth in an omnidirectional pattern without dead spots (that is, without a skip zone). Such a mode is called a near-vertical incidence sky wave (NVIS).

Figure 7 shows an antenna pattern radiating most of its power in the upward direction. Figure 8 illustrates the nearly vertical skywaves refracting off the ionosphere and illuminating the terrain from zero to 100 km. Horizontal dipoles, rhombic antennas, V antennas, and loops are common geometries for HF-NVIS antennas. Figures 9 and 10 illustrate that these standard HF-NVIS antenna scale with wavelength (e.g., the horizontal dipole is 98 ft long at 5 MHz). Thus, the challenge for mobile WBHF is to design a vehicle-sized antenna.

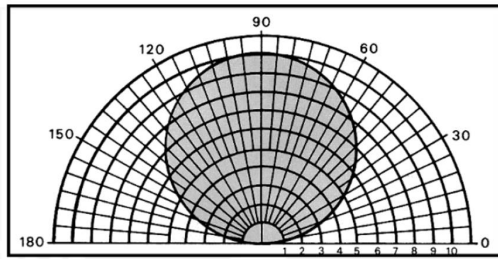


Figure M-4. Typical elevation plane pattern.

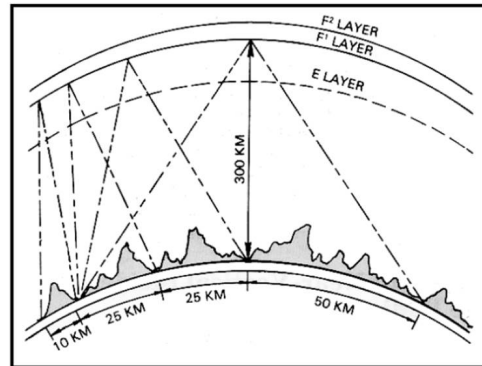


Figure M-1. Near-vertical incidence sky-wave propagation concept.

Figure 7. A typical upward-pointing HF-NVIS antenna pattern [19].

Figure 8. HF-NVIS refracting off of the ionosphere [19].

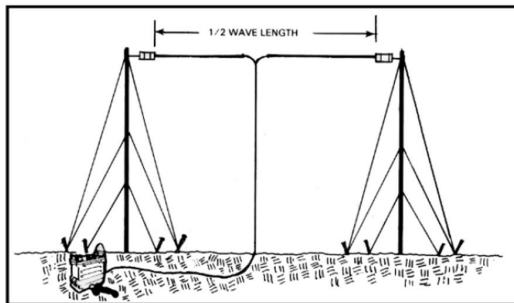


Figure 3-12. Center-fed Hertz antenna with two upright supports.

Figure 9. Horizontal dipole [19].

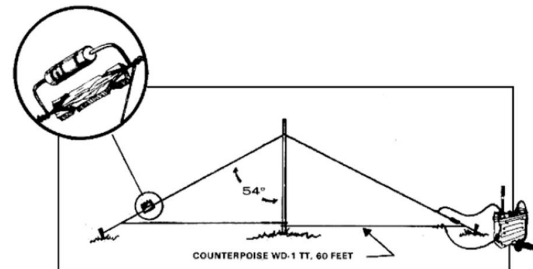


Figure 3-36. Vertical half-rhombic antenna.

Figure 10. Rhombic antenna [19].

## 2.3 A MOBILE WIDEBAND HF-NVIS LINK BUDGET

This section steps through a basic link budget to quantify the antenna bottleneck of the mobile HF-NVIS link. The antenna dominates the link. Consequently, only a simplified HF-NVIS link budget is necessary [77]. All antennas scale to wavelength. The wavelengths in HF range from 10 to 100 m as frequency sweeps down from 30 to 3 MHz. The vertical whip cut to a quarter wavelength sizes from 2.5 to 25 m (e.g., the 32-foot vertical whip in Figure 5 operates at 7.7 MHz, assuming a quarter wavelength). HF-NVIS operates in 2 to 12 MHz as pointed by the *NVIS Army Field Manual 24-18* [20]:

The main difference between this short-range NVIS mode and the standard long-range sky-wave HF mode is the lower frequency required to avoid penetrating the ionosphere and the angle of incident signal upon the ionosphere. To attain an NVIS effect, the energy must be radiated strong enough at angles greater than about 75 or 80 degrees from the horizontal on a frequency that the ionosphere will reflect at that location and time.

Antennas do not necessarily have to be exactly a quarter or half wavelength to operate, but antennas smaller than this standard (electrically-small antennas) suffer from decreased gain and bandwidth. Therefore, the long wavelengths required for HF-NVIS make antenna size problematic for



vehicle-mounted antennas. Figure 11 shows a 59-in diameter loop antenna superimposed where it would be mounted on a High-Mobility Multipurpose Wheeled Vehicle (HMMWV). This loop is the exemplar illustrating trade-offs required for mobile HF-NVIS operations. An idealization of this loop, idealized matching circuits, and standard noise models constitute the HF-NVIS link model analyzed in this section.



Figure 11. HMMWV with HF-NVIS loop superimposed in yellow of the same dimensions as the Harris RF-3134-AT003 antenna (photo credit: Claire Heininger, U.S. Army).

Figure 12 is a high-level block diagram of the HF-NVIS link. For this discussion, the HF-NVIS channel is modeled as a lossy channel with identical antenna and matching circuits at the transmitter and receiver.

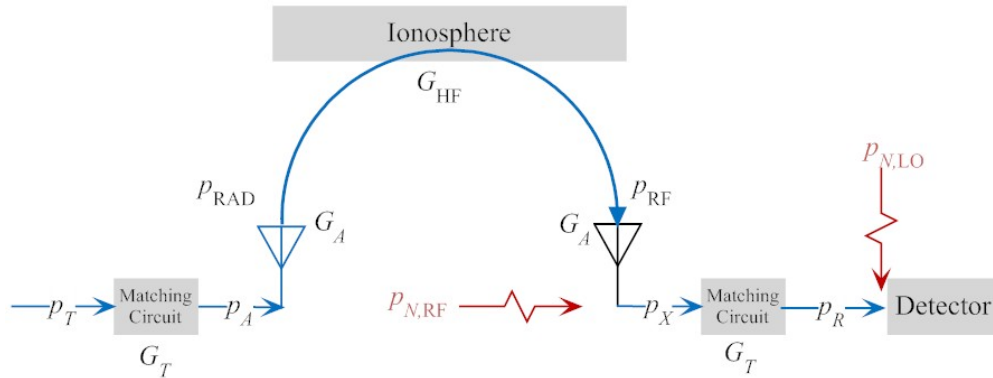


Figure 12. Block diagram of the HF-NVIS link. Signal power:  $p_T$  is power from the transmitting amplifier,  $p_A$  is power delivered to the antenna,  $p_{RAD}$  is power radiated,  $p_X$  is signal power captured by receive antenna, and  $p_R$  is signal power remaining after matching circuit. Gains:  $G_T$  is transducer power gain of the matching circuit and  $G_A$  is absolute gain of the antenna. Noise:  $p_{N,RF}$  is external radio frequency (RF) noise and  $p_{N,LO}$  internal receiver noise.



The HF-NVIS link must have a sufficiently large signal-to-noise ratio (SNR). The SNR is measured at the input to the receiver's detector is

$$\text{SNR} = \frac{p_R}{p_{N,LO} + G_T G_{APN,RF}}.$$

The local noise  $p_{N,LO}$  is assumed to be negligible compared to the received noise power  $G_T G_{APN,RF}$ . Consequently, the SNR admits the approximation

$$\text{SNR} \approx \frac{p_R}{G_T G_A p_{N,RF}} = \frac{G_T G_A p_{RF}}{G_T G_A p_{N,RF}} = \frac{p_{RF}}{p_{N,RF}} = \frac{G_{HF} G_T G_A p_T}{p_{N,RF}}. \quad (1)$$

The antenna gain, matching circuits, and the noise levels are reviewed to determine WBHF-NVIS trade-offs.

**Antenna Gain:** The trade-off discussion must start with a particular antenna. Figure 13 shows a simulated loop antenna and its gain pattern at 12 MHz over a perfect ground plane. There is no vehicle in this simulation. Thus, the antenna's nulls precisely align along the  $x$ -axis. Figure 14 compares gain patterns across the HF band. Referring to Figure 12, the antenna gain  $G_A$  is the ratio of the radiated power  $p_{RAD}$  to the power available  $p_A$  to the antenna:

$$G_A = \frac{p_{RAD}}{p_A}.$$

Figure 14 shows that antenna gain rapidly falls off as frequency decreases.

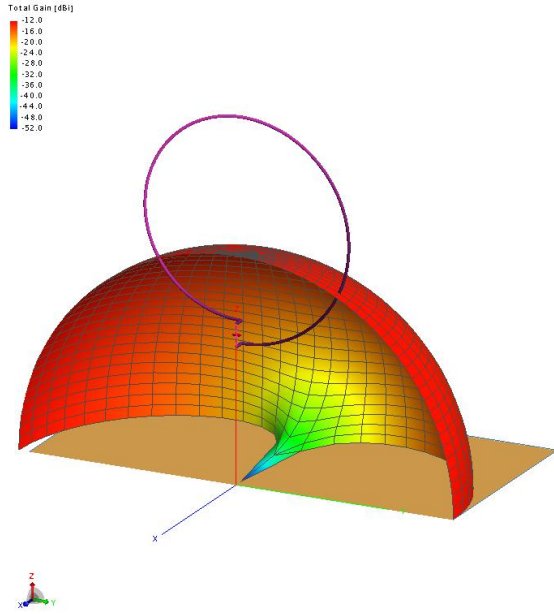


Figure 13. Simulated antenna pattern of a lossy vertical loop with a 59-in diameter mounted four ft above a perfect ground plane.

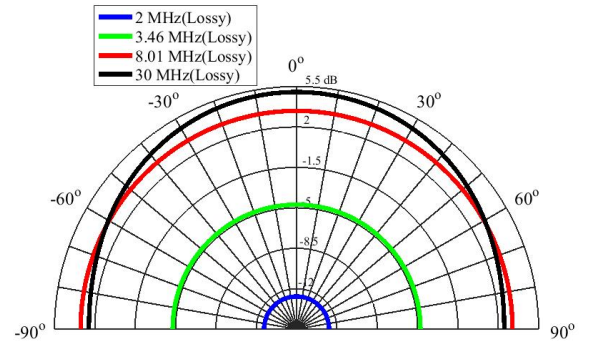


Figure 14. Simulated gain of the lossy vertical loop above perfect ground sliced along the  $y$ - $z$  plane;  $G_A = 0$  dB at 5 MHz.

Figure 15 plots the simulated reflectance obtained from the simulated vertical loop antenna. The Smith chart shows this antenna behaves as a “one-coil” inductor: The loop’s reflectance starts as an inductor at 2 MHz and follows the induction circle counter-clockwise around the Smith chart to the open circuit with increasing frequency. An electrically small antenna requires a matching circuit. Increasing the bandwidth severely challenges the matching circuit. Figure 16 reports the matching at 5 MHz over the 25-kHz band over all possible three-stage LC ladders. The circuit decreases the maximum voltage standing wave ratio (VSWR) over the 25-kHz band from 5,177 down to 22.4. Equivalently, this lossless matching sets the matched transducer power gain  $G_T = -7.9$  dB.

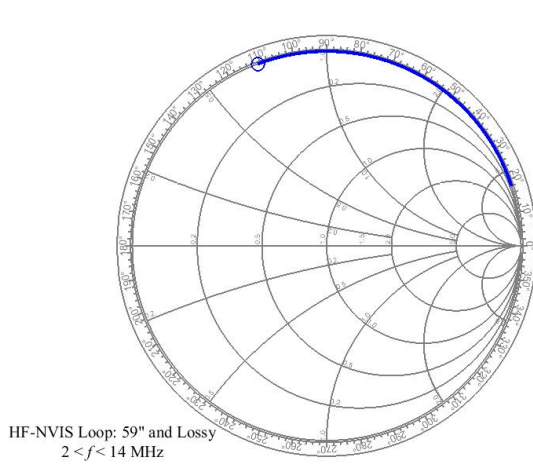


Figure 15. Reflectance of the simulated 59-in diameter vertical loop of Figure 14; The circle marks the reflectance at 2 MHz; the end of the blue line marks the reflectance at 13 MHz.

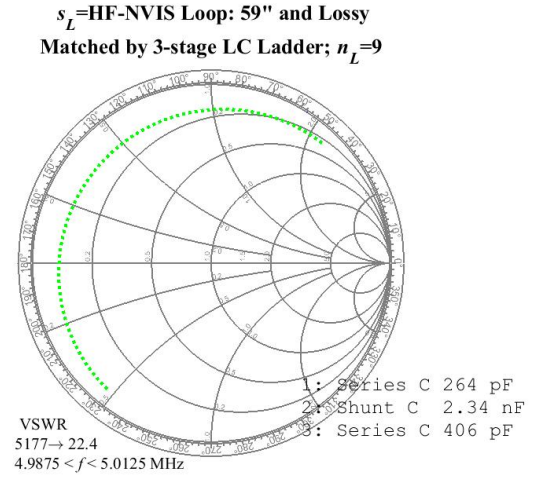


Figure 16. Matching the simulated 59-in diameter vertical loop at 5 MHz over 25 kHz using a third-order ladder.

Table 4 puts this single matching circuit in context. The table reports on this matching for 12-, 25-, and 50-kHz bandwidths. The line labeled “Ladder” lists the transducer power gain over all possible LC ladders containing at most three inductors or capacitors. The line labeled “State-space” is the best possible match over all lossless two-ports that contain at most three reactive elements [67]. Because the state-space matching class contains the LC ladders, the state-space gain exceeds the ladder gain. Looking at the table from top to bottom, the state-space matching shows there exist two-port topologies that deliver at least 2 dB more gain over the LC ladders. Looking at the table from right to left, doubling the bandwidth costs 3 dB regardless of the matching topology. Because the state-space matching class contains the LC ladders, the state-space gain exceeds the ladder gain. Looking at the table from top to bottom, the state-space matching shows there exist two-port topologies delivering at least 2 dB more gain over the LC ladders. Looking at the table from right to left, doubling the bandwidth costs 3 dB regardless of the matching topology. The forthcoming link budget for the 25-kHz bandwidth uses the general matching  $G_T = -5.4$  dB.

Table 4. Transducer power gain  $G_T$  (dB) for degree 3 matching at 5 MHz of the simulated 59-in diameter vertical loop antenna.  $G_T$  is the worst case gain in the bandwidth.

Matching	12 kHz	25 kHz	50 kHz
Ladder	−5.1	−7.9	−10.7
State-space	−2.8	−5.4	−8.3

**RF Noise:** The external RF noise is modeled as zero-mean, complex-valued Gaussian with flat spectrum across the frequency band. As such, only the variance or, equivalently, in-band noise power  $p_{N,\text{RF}}$ , is required to model this Gaussian noise. This noise power is modeled as [40, page 76]

$$p_{N,\text{RF}} = \kappa_B T_{\text{eq}} f_B, \quad (2)$$

where Boltzmann's constant is  $\kappa_B = 1.38 \times 10^{-23} \text{ (W} \cdot \text{K}^{-1} \cdot \text{Hz}^{-1})$ ,  $T_{\text{eq}}$  is the effective operating temperature (K), and  $f_B$  is the bandwidth (Hz). Figure 17 plots  $T_{\text{eq}}$  as a function of frequency for selected RF noise scenarios. The “Urban Man-Made Noise” sets the noise level for these WBHF-NVIS links. Figure 18 plots the urban noise power modeled by Equation (2) for three frequency bands.

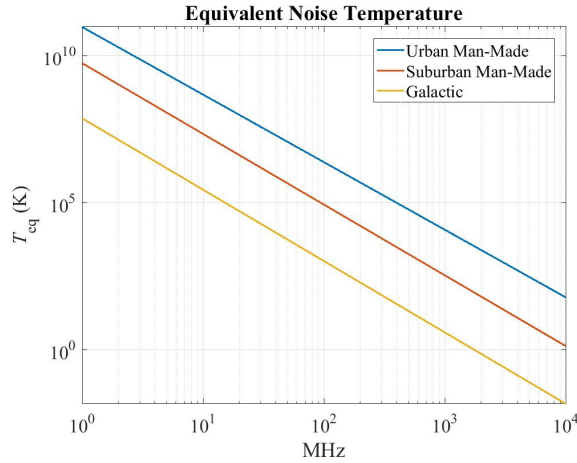


Figure 17. Sky temperatures  $T_{\text{eq}}$  (K) generated by background noise sources [40, page 74].

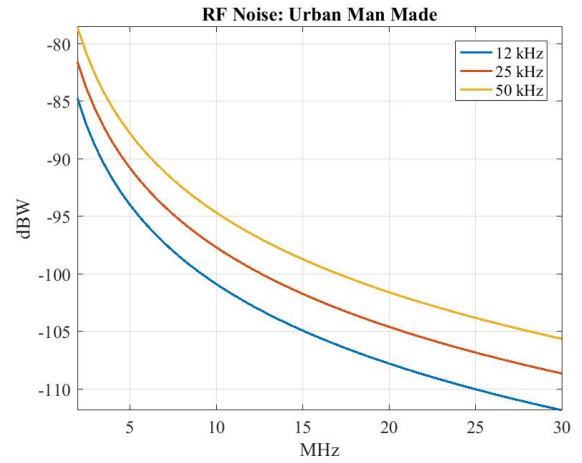


Figure 18. Urban wideband HF noise power from Equation (2).

**HF Gain:** This report bounds the gain along an HF ray path as the product of the spreading, absorption, and mode-shedding gains:

$$G_{\text{HF}} = G_{\text{SPREAD}} \times G_{\text{ABSORB}} \times G_{\text{SHED}}. \quad (3)$$

The spreading or free-space gain sets a convenient upper bound on the HF gain [87, Eq. 3.23]:

$$G_{\text{HF}} \leq G_{\text{SPREAD}} = \left( \frac{\lambda}{4\pi s} \right)^2, \quad (4)$$

where  $s$  is the length of the ray path. A single ray path with a 500-km length has a spreading gain of approximately  $G_{\text{SPREAD}} \approx -100 \text{ dB}$  at 5 MHz. Equation 4 assumes standard spherical spreading approximating the more realistic astigmatic spreading caused by refraction through the ionosphere [55]. Absorption and mode-shedding gains are discussed in later sections. Only this standard spreading bounds the link budget.

**HF-NVIS Link:** Transmit power  $p_T$  and SNR tradeoffs are governed by Equation (1):

$$\text{SNR} \leq G_T + G_A + G_{\text{HF}} + p_T - p_{N,\text{RF}} \quad [\text{dB}]. \quad (5)$$

Equation (5) directs attention to those parts of the HF-NVIS link that can improve these Power-SNR tradeoffs. The transmit power  $p_T$ , the RF noise  $p_{N,\text{RF}}$ , and the HF link gain  $G_{\text{HF}}$  are fixed by the platform and the operating environment. Examples 1 and 2 assess the HF-NVIS link budget using bandwidth and noise.

**Example 1 (HF-NVIS and Bandwidth)** Figure 19 shows Power-SNR curves at 5 MHz for three bandwidths. The link budget is set by Figure 12 using the 59-in diameter vertical loop antenna to transmit. Figure 14 sets the antenna gain as  $G_A = 0$  dB at 5 MHz. Table 4 sets the transducer power gains  $G_T$  for each bandwidth assuming best possible state-space matching limited to three reactive elements. Figure 18 sets the urban noise  $p_{N,\text{RF}}$  for each bandwidth. The HF gain is bounded as  $G_{\text{HF}} = -100$  dB. If the transmitter is limited to  $p_t = 100$  Watts, the 50-kHz bandwidth is not feasible. The 25-kHz bandwidth forces the link to operate with an SNR less than 5 dB. Only the 12-kHz bandwidth delivers an SNR exceeding 10 dB.

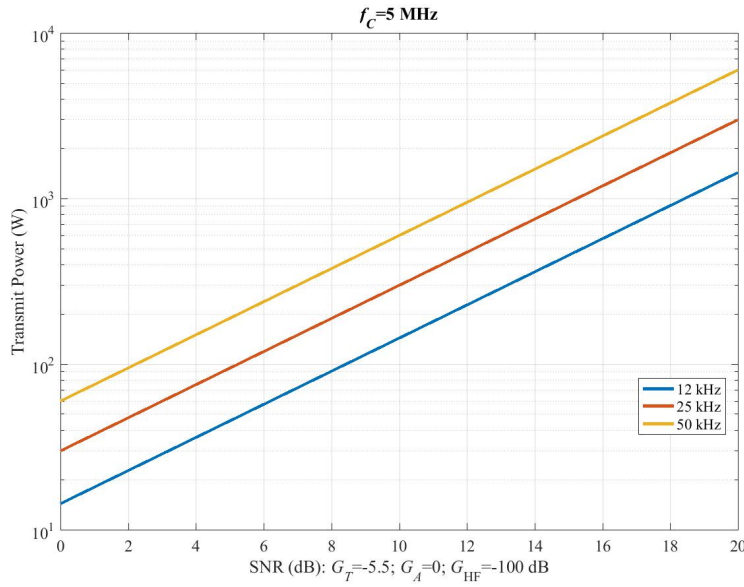


Figure 19. Power-SNR tradeoff for the 5-MHz HF-NVIS link using the 59-in diameter loop antenna operating in urban noise.

**Example 2 (HF-NVIS Link and Noise)** Figure 20 shows power-SNR curves at 5 MHz for three noise scenarios. As in Example 1, the link budget is set by Figure 12 using the 59-in diameter vertical loop antenna to transmit. Figure 14 sets the antenna gain as  $G_A = 0$  dB at 5 MHz. Table 4 sets the transducer power gains  $G_T = -5.5$  dB for the 24-kHz bandwidth assuming best possible state-space matching limited to three reactive elements (24-kHz is used for comparison). The HF gain is bounded as  $G_{HF} = -100$  dB. Figure 18 sets the noise powers  $p_{N,RF}$  for the 24-kHz band. At transmit power  $p_T = 100$  Watts, the urban noise limits the SNR to 5 dB. However, suburban noise has an SNR exceeding 15 dB.

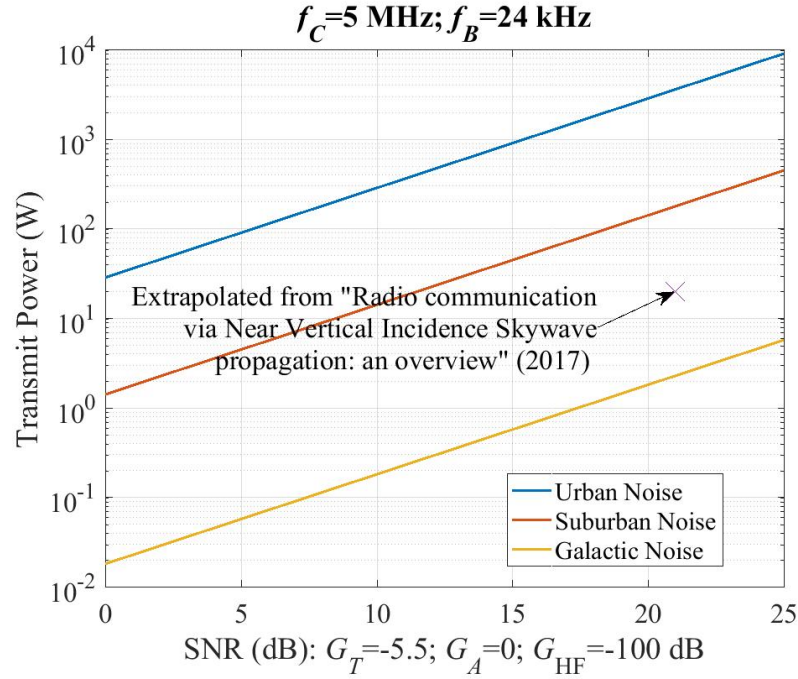


Figure 20. Power-SNR tradeoffs for the 5-MHz HF-NVIS link using the 59-in diameter loop antenna operating in different noise models. The “X” is extrapolated from [85], in which the authors measure over 30-dB SNR over a 3-kHz bandwidth using a dipole antenna on transmit that translates to 21-dB SNR over a 24-kHz bandwidth.

Examples 1 and 2 show that the HF-NVIS antenna is the fundamental design parameter for this power-only equation. Recent antenna designs boosting antenna and matching gain are reviewed in Section 2.4. Equation (5) models power only—signal processing gain obtained by exploiting the HF-NVIS channel is not included in the end-to-end throughput. For example, Section 3 discusses the multiple hops common to most HF channels, regardless of whether the channel is narrowband or wideband. Receiver processing exploiting these multiple hops inserts the associated diversity gain in Equation (5). Likewise, wideband HF channels typically allow the O- and X-Mode paths to be distinguished. Receiver processing exploiting these different modes also inserts this diversity gain in Equation (5).

The HF channels also supports propagation over polarization modes. If the transmitter is dual-polarization and the receiver is dual-polarization, then  $2 \times 2$  MIMO gains are possible. The payoff from this approach is considerable. Essentially, there can be up to two channels rather than a single channel. Thus, the 12-kHz channel’s matching can be exploited to deliver bit rates commensurate with a 24-kHz bandwidth. However, antenna size on a vehicle limits this  $2 \times 2$  MIMO gain. Therefore, Section 2.4 reviews progress in wideband HF communications emphasizing mobile communications to guide the analysis of the experimental measurements.

## 2.4 EVOLUTION OF WIDEBAND HF AND HF-NVIS

This section reviews selected highlights in wideband HF communications emphasizing wideband HF measurements, insights for wideband channel communications, and concludes with a review of mobile HF-NVIS systems. The wideband HF literature goes back at least five decades and the progress by MITRE nicely brackets the topic. In 1983, Perry made explicit the payoff for wideband HF [60]:

Wideband HF will offer an alternative to satellite and tropospheric-scatter communications. It will permit the use of low-data-rate spread spectrum signaling, with the attendant virtues of anti-jam protection and covertness.

This paper cites the wideband HF measurements made in the 1960s over 2,000-km paths [7] and develops over-the-air equalizers operating across 1-MHz bandwidths.

In 1986, Saluous and Shearman sought to [65] “determine the widest bandwidth that can be used for HF ionospheric propagation without channel equalization.” Their HF-NVIS measurements were collected over a 234-km link in the United Kingdom using frequency sweeps up to 5 MHz. These measurements show coherent bandwidth is limited by the following effects:

- Polarization interference between the two magnetoionic waves produces deep fades, and
- Phase nonlinearity with frequency increases the duration of the pulse response and thereby limits the rate of digital transmission

In 1989, Wagner-Goldstein-Meyers-Bello measured HF channels using 1-MHz bandwidths in the mid- and high-latitudes over short- and long-haul paths and obtained the following fundamental insight regarding wideband HF channel communications [81]:

For a simple specular channel, rapid fading occurs as a consequence of signals from more than one mode having different Doppler shifts and being received simultaneously. The ability to isolate and to respond exclusively to a single specular return offers the opportunity of eliminating rapid fading for non-disturbed channels.

In 1990, Katal summarized performances for the standard ground-mounted HF-NVIS antennas [39]. The horizontal quad loop antenna (quarter wavelength per side; quarter wavelength above ground) has the greatest gain at high take-off angles. Katal also examined the long-wire antennas and reports that the actual radiation pattern differs from the theoretical calculation because of ohmic loss. In 1992, Nissen and Bello measured HF channels at several frequencies using 1-MHz bands over a 3100-km link between Greenland and Massachusetts [54], shown in Figure 21. Although the channels linked the high latitudes to the mid-latitudes, the joint distribution of the measured delay spread and Doppler spread matches other measurements of high-latitude channels (See Section 4.5).

Starting in the early 2000s, several countries began assessing HF-MIMO. All systems employ large antennas (relative to a ground vehicle) and static ground-based arrays.

**China:** In 2004, Xu, Zhang, Yang, and Wang simulated HF-MIMO over the Consultative Committee on International Radio (CCIR) poor channel (2-ms delay; 1 Hz Doppler spread) showing that a  $2 \times 2$  MIMO system delivered better performance over a comparable single input single output (SISO) system [86]. In 2005, Zhang, Yang, Luo, and Xu again simulated HF-MIMO over the CCIR poor channel to report that the simulated  $2 \times 2$  MIMO system yields 4–15-dB diversity gain over a comparable SISO system [91].



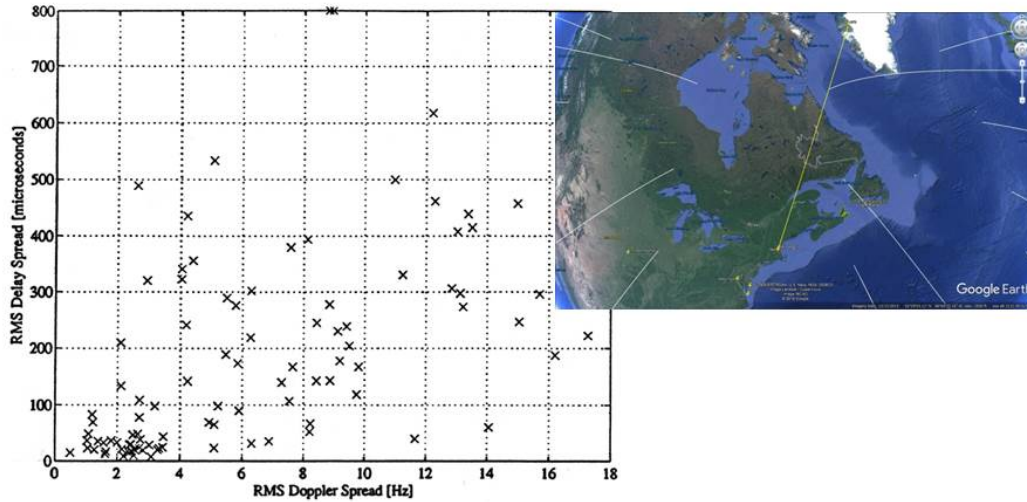


Figure 21. Left: delay spread versus Doppler spread over long-haul wideband HF links (Reprinted with permission of the MITRE Corporation) [54]. Right: geographic location of the HF link. The lines other than the HF link are magnetic field lines.

**France:** In 2004, Perrine, Erhel, Lemur, Bertel, and Bourdillon reported on one of the first over-the-air wideband HF SIMO experiments over a 300-km link in France between Poitiers and Monterfil conducted at the end of year in 2000 [61]. Figure 22 is a schematic of the system using a single transmit antenna and multiple co-located antennas—four loops and four dipoles—to exploit polarization diversity.

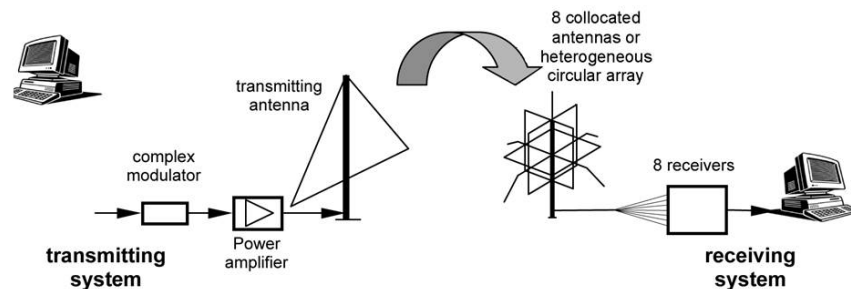


Figure 22. HF-SIMO link for over-the-air transmissions recorded in 2000; 20 kbps delivered over a 6-kHz band (figure courtesy of Annals of Geophysics) [61].

In 2009, Ndao and associates began an HF-MIMO effort starting with simulations leading to over-the-air experiments over a 280-km link between Monterfil and Lucay in April of 2011 [51, 52]. Figure 23 is a schematic of the HF-MIMO system. Their 2013 paper summarizes these efforts [53]:

The simulation of the global system, including a realistic model of the ionospheric channel, indicates a significant capacity gain if compared to a SISO system. An experimental validation, involving a 280-km long radio link, confirms this prediction and underlines the possibility to reach a data rate of 24.09 kbps within a 4.2-kHz wide bandwidth with a good quality of service. This performance significantly exceeds values encountered in current standards.

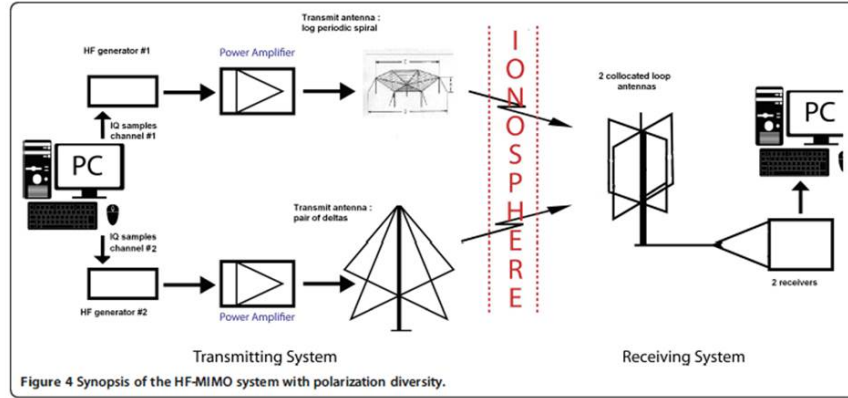


Figure 23. HF-MIMO system for the over-the-air transmissions recorded in 2011; 24 kbps delivered over a 4.2-kHz band (figure courtesy of EURASIP Journal on Wireless Communications and Networking) [53].

**United Kingdom:** In 2006, Strangeways estimated HF-MIMO channel capacities [74], [75]. From September 2007 to September 2008, the University of Leicester and Durham University conducted HF-MIMO channel soundings over the 255-km path between these two sites [1], [29], [30], [22]. Both the transmitter site and the receiver site were populated with heterogeneous antennas spread over tens of meters. A typical transmit antenna was a 7-m vertical whip. Figure 24 shows a Giselle-type antenna [45] used for receive. Although the Giselle-type antennas can be sized for vehicles, realizing multiple HF transmitters from a mobile platform is problematic because of the coupling between the antennas. Figure 25 presents an upper bound of the capacity of these HF-MIMO channels estimated from the channel soundings and idealized assumptions. Although the SISO-to-MIMO capacity gains are small at low SNR, the reduction in SNR even at low capacity is significant. At 5 bps/Hz, a  $4 \times 4$  MIMO system needs an SNR of 6 dB in comparison to the 15 dB required by SISO. This SNR reduction of 9 dB corresponds to a transmitter power reduction by a factor of 8. Problematic for mobile HF-MIMO are the array sizes and the size of the individual elements of the array.



Figure 24. Modified Giselle antenna for receive (figure courtesy of Dr. Stuart Feeney) [1].

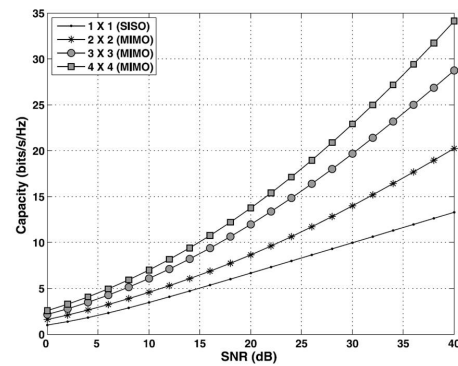


Figure 25. HF-MIMO capacity near 5.255 MHz estimated from over-the-air channel soundings recorded on 3 September 2008 [30] (figure courtesy of Radio Science).



**Australia:** The University of Adelaide and the Defense Science and Technology Group (DSTG) have a long history of HF research, with an emphasis on over-the-horizon HF radar. In 2003, Brine, Lim, Massie, and Marwood produced idealized HF-MIMO channel capacity estimates based on HF soundings from Darwin to Adelaide [10]. In 2005, Yau conducted dual-polarization channel soundings over a 1,200-km path from Alice Springs to Lake Bennet in Australia. Figure 26 shows a channel’s scattering function for vertical polarization at 10.677 MHz estimated from a 46-kHz band [88]. The channel shows three modes spread in delay by 2 ms and Doppler spreading from  $-0.5$  to  $0.8$  Hz.

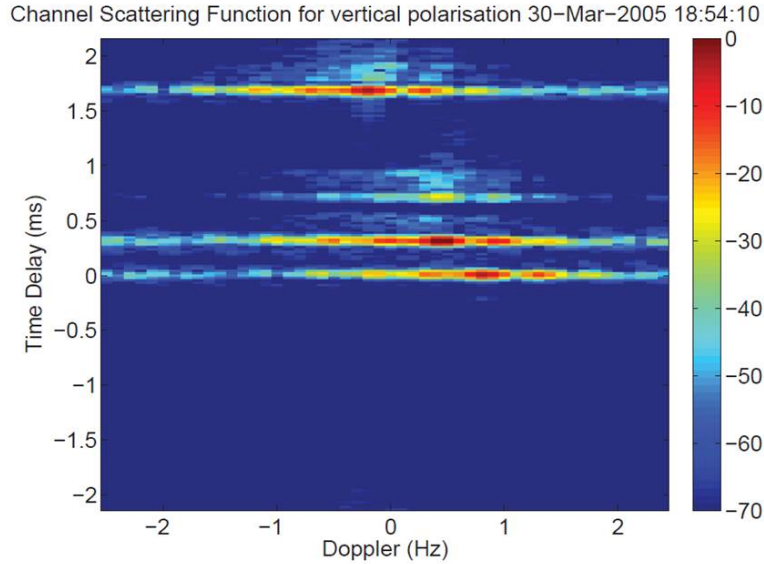


Figure 26. Vertical polarization scattering function; 10.677 MHz (figure courtesy of Dr. Kin Shing Bobby Yau) [88].

**United States:** In October 2012, Kuma Signals, LLC conducted dual-polarization HF-NVIS channel soundings over a 19.7-km link in Austin, TX at 7.08806 MHz [15]. Both the transmitter and receiver used two co-located, orthogonal, horizontal dipoles cut to 85 ft in length. Figure 27 compares the the ergodic capacity between the SISO and the  $2 \times 2$  MIMO using the channel matrix estimated from the soundings. Kuma Signals used these channel estimates to propose a MIMO waveform, backwards compatible MIL-STD-188-110C Appendix D, promising “... a 116% improvement in overall throughput and a 15-dB SNR improvement for the highest-rate modes ... [16]”

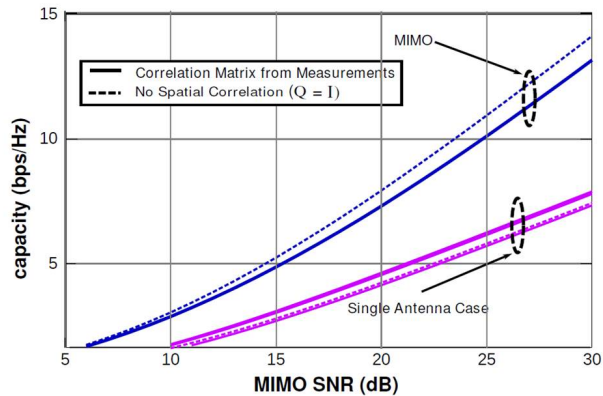


Figure 27. Dual-polarization MIMO capacity near 7 MHz estimated from over-the-air channel soundings recorded on 19 October 2012 (figure courtesy of Kuma Signals) [15].

In December 2013, MITRE conducted wideband dual-polarization HF-MIMO experiments over a 50-km link from Bedford, MA, to Worcester, MA, at 5-MHz using a 49-kHz bandwidth. Figure 28 shows the crossed dipole antennas used at both the transmitter and receiver. The system used approximately 5 W per channel to deliver 94 kbps using binary phase-shift keying (BPSK) and 9 kbps with sparse orthogonal frequency division multiplexing (OFDM). Figure 29 shows the bit error rate as a function of SNR for OFDM (upper plot) and BPSK (lower plot).

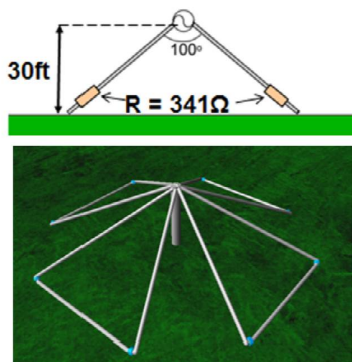


Figure 28. TX/RX crossed dipole antennas (reprinted with permission of the MITRE corporation) [66].

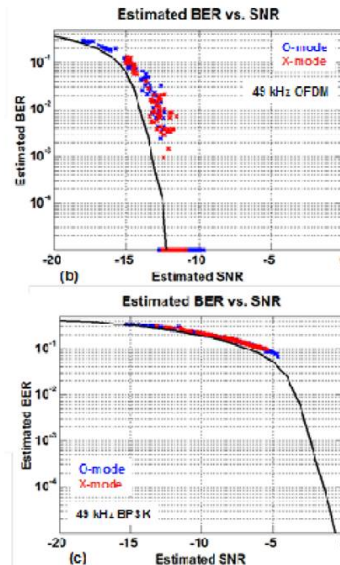


Figure 29. OFDM and BPSK waveforms (reprinted with permission of the MITRE corporation) [66].

In 2014, TrellisWare Technologies, Inc. conducted soundings over 19 days across 200 HF-NVIS channels using 24-kHz bandwidths sweeping from 2 to 12 MHz. The transmitter was located in Rancho Bernardo, CA. Two synchronized HF-NVIS receivers were located in Encinitas, CA (ground range  $\approx 12$  mi) and Los Angeles, CA (ground range  $\approx 120$  mi). Synchronization permits direct comparison of noise, interference, and channel states. Figure 30 compares the noise and interference between the two HF-NVIS channels at 4:30 am (Pacific Standard Time) PST.

Both sites show common interference near 6 MHz, 7.5 MHz, 9.75 MHz, and 11.75 MHz. The Los Angeles receiver measured wideband impulsive noise (horizontal lines), likely caused by lightning, and larger low frequency noise. In contrast, the Encinitas receiver shows a higher noise floor above 11 MHz. These measurements support Bark's observation [5]:

The HF radio channel is one of the most difficult channels for two main reasons: the frequency-selective fading caused by ionospheric multipath propagation, and the severe interference from other users . . . in many cases, the performance of the HF systems is limited rather by interference than by bad propagation conditions . . .

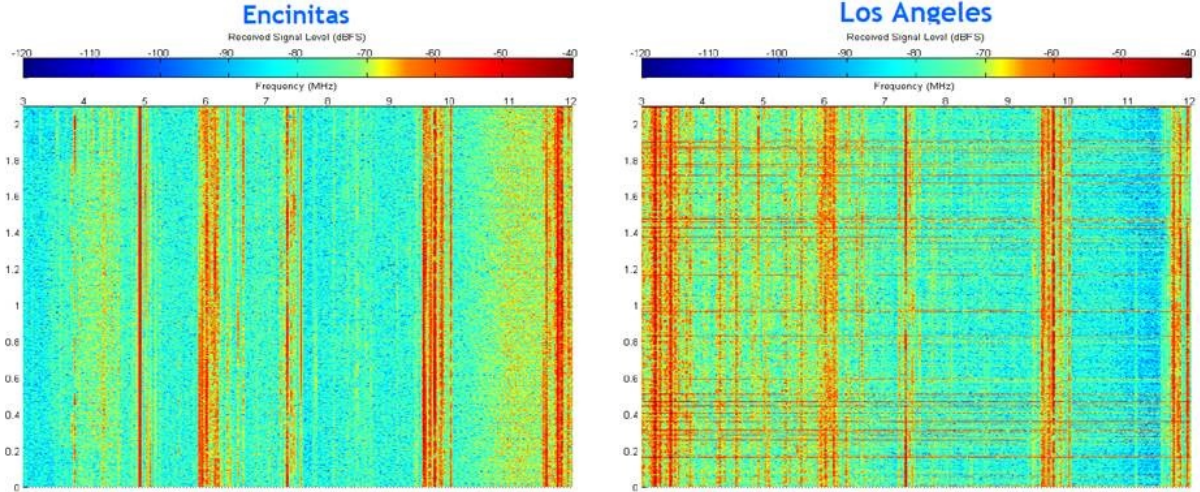


Figure 30. Simultaneous measurement of HF-NVIS noise and interference in the early morning (figure courtesy of TrellisWare Technologies, Inc.) [24]. Vertical axis is time in seconds.

Consequently, any HF-NVIS system must adapt to the location-specific noise and interference. Analysis of the nine terabytes of channel soundings showed that the standard *narrowband models* do not capture the *wideband channel features* [79]:

traditional doubly-spread HF channel models are . . . ill-suited to describe complex NVIS propagation phenomena. In particular, it is observed that the NVIS channel is often non-stationary over a few minutes; with taps rapidly shifting in delay, exhibiting abrupt changes in phase characteristics, and periodic variations in magnitude.

The limitation of this observation is that the measurements are mid-latitude. High-latitude HF channels are known to be more complex. Some of the narrowband phenomena are reviewed in Section 4.5.

**Assessment for mobile HF-MIMO:** MIMO only makes sense when there are multiple paths. The HF-NVIS channels typically admit at least two paths—the O- and X-Modes. Therefore, dual-polarization MIMO is possible provided the transmitter and receiver are equipped with antennas that match these modes. Section 3 shows that the O- and X-Mode are left and right elliptically polarized. Therefore, equipping the transmitter and receiver with two orthogonal antennas is one realization of this particular  $2 \times 2$  MIMO. This setup also avoids the fading caused by these modes canceling in a single antenna. However, broadcasting from multiple HF antennas on a ground vehicle is challenging—the cross coupling between antennas essentially voids the MIMO gain. Therefore, a SIMO architecture is currently the most feasible candidate for mobile HF-NVIS. An excellent analysis of the antenna selection for non-mobile HF-SIMO is found in the 2015 paper by Erhel, Lemur, Oger, and Masson [21].

**Mobile HF-NVIS:** The antenna is the bottleneck for any mobile HF-NVIS communication system. Filipović's observations are particularly insightful [33]:

Any vehicular mounted antenna will have a quality factor far below the fundamental upper limit for its electrical size. This is because for the [platform] to remain mobile and functional, an antenna cannot fill the entire space of the ... platform.

One approach to the mobile HF-NVIS antenna simply adapts an existing antenna to the vehicle. Figure 31 shows the canonical *tilted whip antenna*. Any proposed HF-NVIS antenna system must deliver greater performance than this existing antenna system.

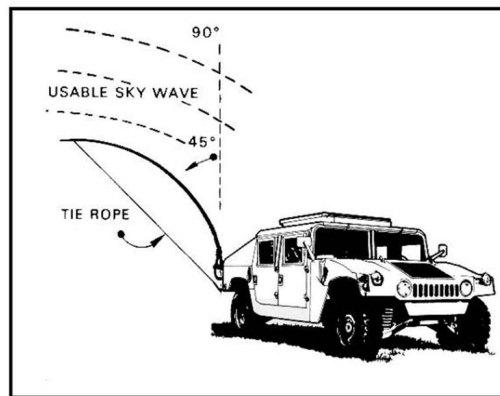


Figure M-9. Tying the whip antenna down.

Figure 31. Tilting a whip to produce HF-NVIS [19].

Several research teams provided designs using the platform itself to boost antenna performance. In 2002, Austin and Lui analyzed tilted whips and loops on a simulated generic vehicle to find that a capacitive-loaded loop is the preferable configuration [4]. In 2010, Deng and associates proposed spiral antennas [18]. Figures 32 and 33 show a recent HF/HF-NVIS antenna developed for ground-mobile applications that uses inductive tuning.



Figure 32. Compact HF-NVIS antenna [31] (figure courtesy of Hi-Q-MilitaryAntennas, Inc.).



Figure 33. Mounted on an HMMWV [31] (Figure courtesy of Hi-Q-MilitaryAntennas, Inc.).



In 2016, Shih and Behdad applied characteristic modes to design mobile HF-NVIS antennas using the platform as part of the antenna system [71]. Figure 34 shows the simulated HF-NVIS patterns generated by low-profile loop antennas mounted on a simplified model of an Expeditionary Fighting Vehicle (EFV). The vehicle is excited by low-profile loop antennas mounted lengthwise in the rear. The number of antennas increases viewing the figure from left to right. The gain patterns are plotted over each antenna configuration and show the NVIS directionality. The current flows on the EFV are excited by the antenna configurations. These simultaneous visualization of the current flows and associated patterns guide the placement of antennas.

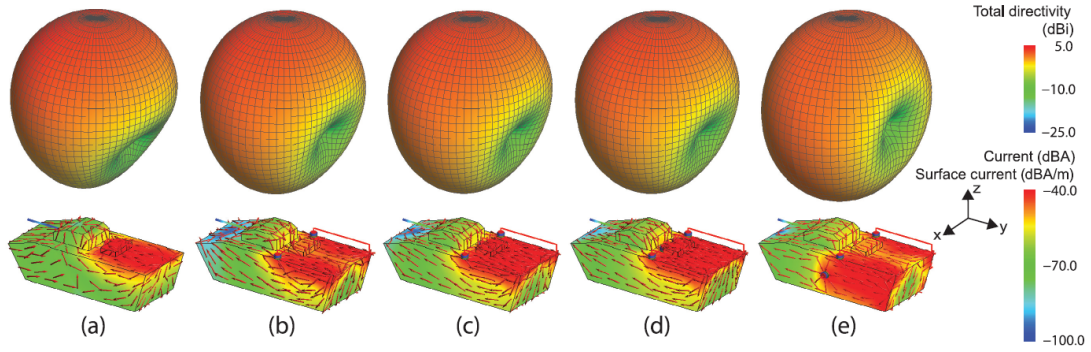


Figure 34. HF-NVIS patterns produced by selected loop antennas exciting characteristic modes on a simulated EFV [71] (used with the author's permission).

In 2016, a substantial study of vehicle-mounted, wideband HF-NVIS was completed by Filipović's team at the University of Colorado [33]. Several types of antennas (e.g., half-loop, inverted-L, and top-loaded monopole) were analyzed on several vehicle types. Figure 35 shows one double horizontal loop antenna mounted on an Oshkosh Defense® mine-resistant ambush protected all-terrain vehicle (M-ATV). This study encompassed the realized gain—matching and upward radiation—as affected by realistic vehicles operating over various ground planes.

Figure 36 shows the effect of the ground on these vehicle-mounted antennas. The resulting realized gain  $G_R$  encompasses the transducer power gain  $G_T$  of matching circuit and the antenna gain  $G_A$  in the upward direction:

$$G_R = G_T + G_A \quad [\text{dB}].$$

Figure 36 shows that ground conditions degrade performance upwards of 5 dB. Therefore, any credible link budget for a mobile HF-NVIS system must also include the operational ground.

## 2.5 SUMMARY

This in-depth assessment of mobile HF-NVIS shows that the antenna is the bottleneck of this HF link. MIMO promises some boost in throughput, but size limitations preclude multiple transmitters operating from a vehicle platform. Consequently, only SIMO systems may deliver useful performance. Specifically, the SIMO diversity gain could reduce bandwidth requirements. Reduced bandwidth enables better matching and lower power. Regardless of the MIMO flavor, all these diversity schemes require knowledge of the HF-NVIS channel and the O- and X-Modes. Accordingly, the next section undertakes a review of the HF-NVIS channel emphasizing SIMO usage via the O- and X-Modes.



Figure 35. One double horizontal loop antenna mounted on an M-ATV [33].

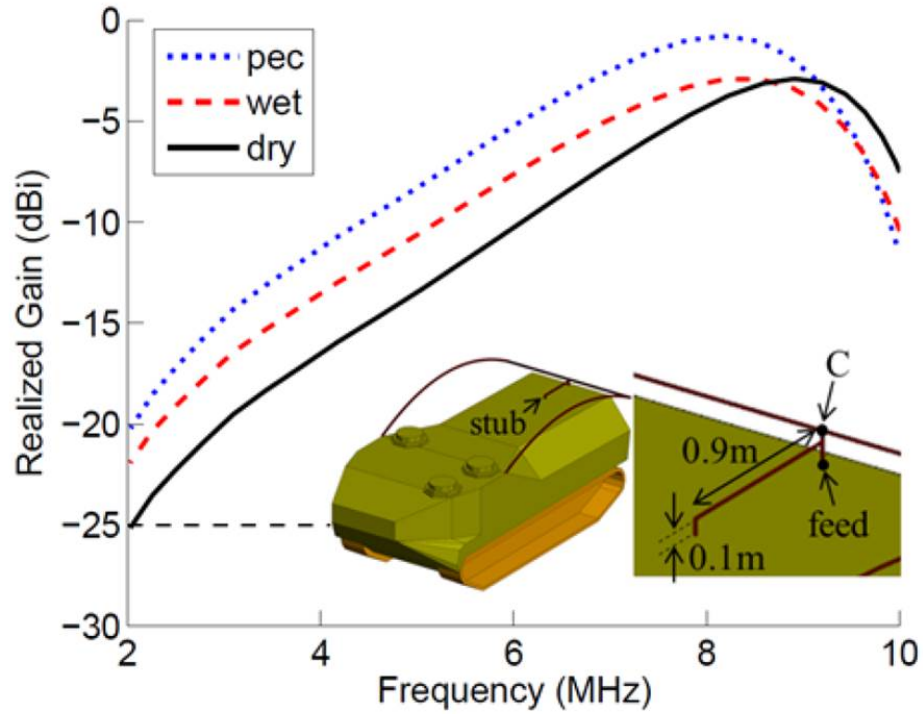


Figure 36. Realized gain for two horizontal loop antennas mounted on a simulated AAV over 24-kHz bandwidths as a function of frequency and ground [33].

### 3. HF-NVIS CHANNELS AND THE IONOSPHERE

The HF-NVIS channels are governed by the ionosphere. Figure 37 is a schematic showing some of the multiple hops that the HF-NVIS rays may take when traveling from the transmitter to receiver.

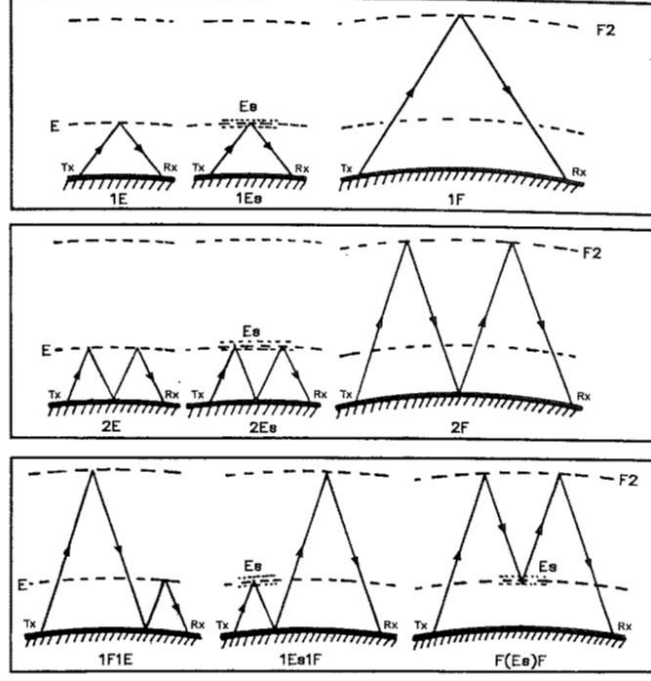


Figure 37. HF-NVIS multiple hops [20].

Each hop induces a delay, attenuation, fading, and frequency shift in the transmitted signal  $s_T(t)$ . For example, if the channel exhibits the rightmost hops in Figure 37, the received signal  $s_R(t)$  should have the structure

$$s_R(t) = a_F(t)s_T(t - \tau_F) + a_{2F}(t)s_T(t - \tau_{2F}) + a_{F(Es)F}(t)s_T(t - \tau_{F(Es)F}), \quad (6)$$

where the 1-Hop has delay  $\tau_F$ , the 2-Hop has delay  $\tau_{2F}$ , and the third hop has delay  $\tau_{F(Es)F}$ . The amplitudes  $a_F(t)$  are time-varying and exhibit more attenuation and fading as the hop number increases. The measured channels show 1-, 2-, 2.5-, 3- and 4-Hops. Therefore, the HF-NVIS channel appears to be completely determined by this model. However, Equation (6) implicitly assumes that the antennas are already folded into the channel and that polarization is absent. More to the point, the ordinary mode (O-Mode) and the extraordinary mode (X-Mode) are absent from this model. This section reviews the O- and X-Modes, their presence in the ionograms, and concludes with a general model encompassing these modes and the antennas in the HF-NVIS link.

#### 3.1 O-MODE AND X-MODE

A high-level description of the O- and X-Modes is found in Gillies [27]:

“... when a wave propagates through an ionized medium with an external magnetic field, two different indices of refraction exist. These two indices correspond to two modes of propagation. The ordinary mode (O-Mode) and the extraordinary mode (X-Mode) are affected differently by the external magnetic field (B-field).”

Figure 38 illustrates the Earth's magnetic field. The magnetic field runs approximately north-south in the mid-latitudes. Waves traveling north-to-south are less affected by the magnetic field than waves traveling east-to-west. Figures 39 and 40 show simulated ray paths for HF-NVIS waves traveling west-to-east. The magnetic field pushes the O-Mode to the north and the X-Mode to the south. The O-Mode also travels higher but arrives sooner because of the differing index of refraction along each of the paths.

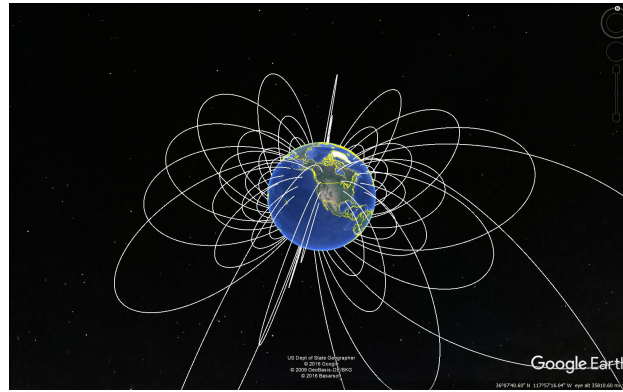


Figure 38. Illustration of the Earth's magnetic field.

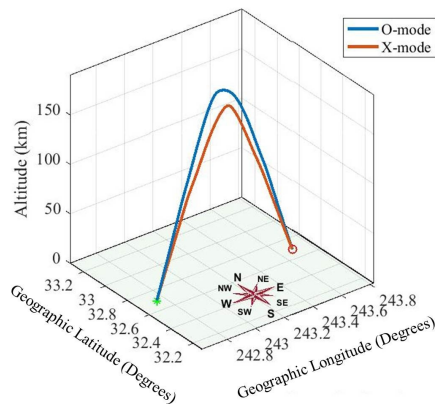


Figure 39. 1-Hop O- and X-Modes.

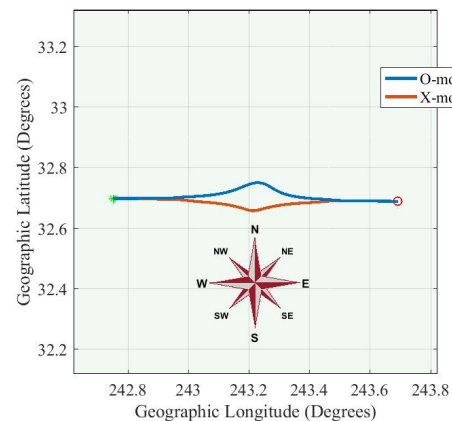


Figure 40. Top view of 1-Hops.

Travel times for both HF-NVIS rays can be approximated from the associated ionograms [47, page 51]:

“An ionogram is a plot of the apparent length of the propagation path as a function of frequency.”

Figure 41 is an annotated ionogram showing the virtual heights where the upward traveling waves are reflected back to Earth. This ionogram was recorded at Point Arguello, CA, on 10 February 2016 at 09:45 PST. At each frequency, the sounding first refracts off the ionosphere and travels back to the station producing the first “1-Hop” layer. This sounding then reflects off the ground, travels upward a second time to refract off the ionosphere, and then travels back to the station to produce the “2-Hop” layer. The difference in the refractive index for the O- and X-Modes becomes more apparent with each hop and increasing frequency.



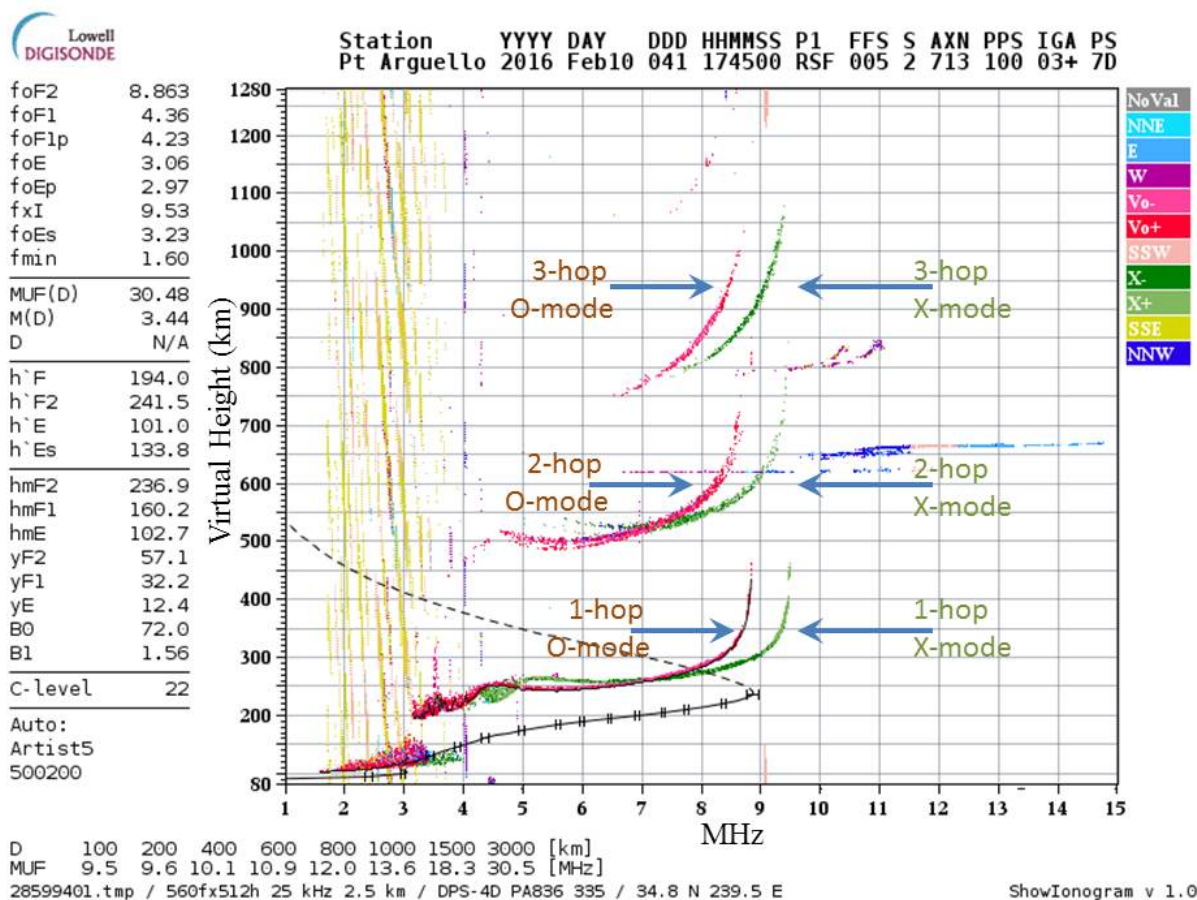


Figure 41. Ionogram at Point Arguello on 10 February 2016 at 09:45 PST. Open source ionograms courtesy of the Global Ionospheric Radio Observatory at the University of Massachusetts, Lowell [64].

Table 5 lists the heights for the 1-Hop modes and their associated round-trip travel times by dividing the virtual round-trip distance by the speed of light. The “virtual” heights are determined by multiplying the actual time-of-flight and the speed of light. This “virtual” height model assumes the waves travel at the speed of light—not the actual physics where the speed of propagation is determined by the index of refraction causing the upward traveling wave to slow and then reverse as it refracts back to Earth. These delays show that the simple model of Equation (6) must be extended to encompass the O- and X-Modes.

Table 5. Virtual heights and round-trip travel times (delay) at 5.82 MHz estimated from Figure 41.

1-Hop	height (km)	delay (ms)
O-Mode	240	1.60
X-Mode	260	1.73

### 3.2 INDEX OF REFRACTION AND THE MAGNETIC FIELD

The O- and X-Modes are determined by the electron density and the magnetic field of the Earth. Figure 42 is an ionogram recorded at Austin, TX, on 10 February 2016 at 12:10 PST that displays the plasma frequency (black line) as a function of height.

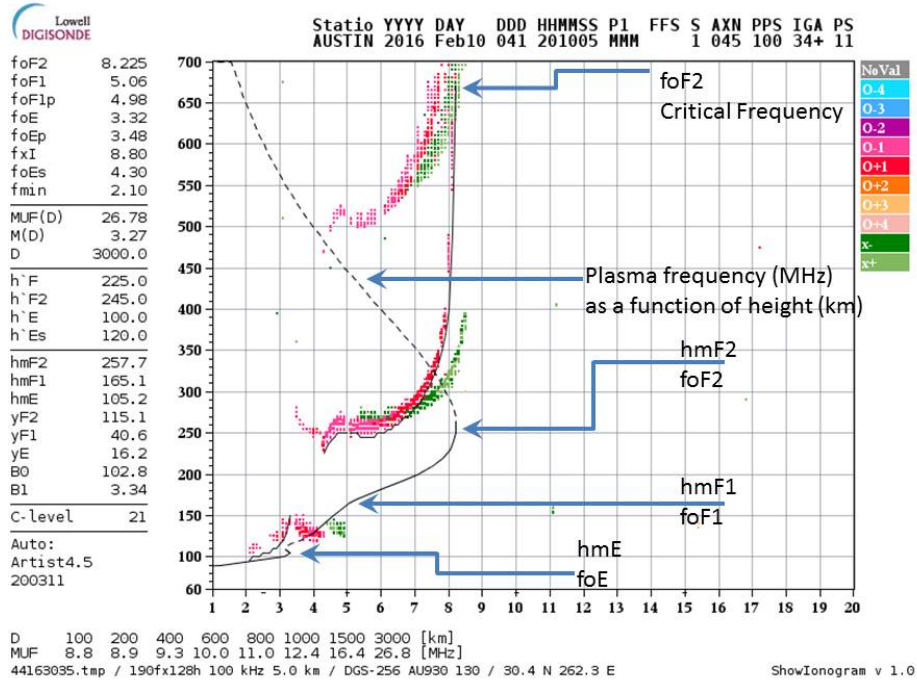


Figure 42. Selected plasma frequencies (MHz) on the horizontal axis and associated heights (km) on the vertical axis. Open source ionograms courtesy of the Global Ionospheric Radio Observatory at the University of Massachusetts, Lowell [64].

The plasma frequency  $f_P$  links to the electron density  $N_e$  as [58, Eq. 6.42]:

$$N_e(h) := f_P(h)^2 \frac{4\pi^2 e_0 m_e}{q_e^2} [N \cdot m^{-3}], \quad (7)$$

where  $N_e$  is the number of electrons per cubic meter,  $f_P$  is measured in Hertz, and the remaining constants are

$e_0$	$8.85418782 \cdot 10^{-12}$	Permittivity of free space (F/m)
$m_e$	$9.10938291 \cdot 10^{-31}$	Electron mass (kg)
$q_e$	$-1.60217657 \cdot 10^{-19}$	Charge of an electron (C)

The electron density  $N_e$  and the Earth's magnetic field determine the *phase refractive indices*  $n_{\pm}$  governing the O- and X-Mode propagation through the ionosphere [69, Eq. 5], [17, Eq. 3.8]:

$$n_{\pm}^2 := 1 - \frac{X}{1 - jZ - \frac{Y_T^2}{2(1-X-jZ)} \pm \sqrt{Y_L^2 + \frac{Y_T^4}{4(1-X-jZ)^2}}}, \quad (8)$$

where the magnetoionic frequencies  $X$ ,  $Y$ , and  $Z$  are described in Equations (9), (10), and (11).

**Plasma Frequency:** The electron density determines the normalized *plasma frequency squared* [89, Eq. 4.1.5]:

$$X = \frac{\omega_P^2}{\omega^2}; \quad \omega_P = 2\pi f_P, \omega = 2\pi f \quad (9)$$

where the normalization is made with respect to the operating HF frequency  $f$ .

**Gyro Frequencies:** The Earth's magnetic field causes the electrons to rotate around the magnetic lines of force. The evolution of the polarization along the ray path is governed by this rotation or *gyro-frequency* [89, Eq. 4.4.3]

$$\omega_H = \frac{q_e}{m_e} B_0 \quad [\text{rad} \cdot \text{sec}^{-1}],$$

where  $B_0$  is the magnitude of the Earth's magnetic induction field vector  $\mathbf{B}_0$  and determines the normalized gyro-frequency [89, Eq. 4.4.3]

$$Y = \frac{\omega_H}{\omega}. \quad (10)$$

The direction of the Earth's magnetic field with respect to the ray path appears in the refractive index via the longitudinal and transverse components of the normalized gyro-frequency [89, Eq. 4.5.8]

$$\begin{bmatrix} Y_L \\ Y_T \end{bmatrix} = Y \begin{bmatrix} \cos(\theta_H) \\ \sin(\theta_H) \end{bmatrix} = \frac{q_e}{\omega m_e} \mathbf{B}_0,$$

where  $\theta_H$  is the angle between the magnetic field and the wave vector.

**Electron Collision Frequency:** The collisions of the electrons with ions and neutral molecules determines the local absorption along the ray path and the subsequent total absorption. Absorption appears in the index of refraction  $n$  via the normalized *electron collision frequency*  $\omega_E$ :

$$Z = \frac{\omega_E}{\omega} \quad (11)$$

The electron collision frequency is the sum of electron-ion collision frequency  $\omega_{E,I}$  and the electron-neutral collision frequency  $\omega_{E,N}$  [90]:

$$\begin{aligned} \omega_{E,I} &= 10^{-6} \times N_e \times T_e^{-3/2} \left\{ 59 + 4.18 \log \left( \frac{T_e}{N_e} \right) \right\} \quad [\text{rad} \cdot \text{sec}^{-1}], \\ \omega_{E,N} &= 5.4 \cdot 10^{-16} \times N_n \times T_e^{1/2} \quad [\text{rad} \cdot \text{sec}^{-1}], \end{aligned}$$

where  $T_e$  is the electron temperature and  $N_n$  is the neutral particle density. .

**Channel Modeling:** The electron density profile and the Earth's magnetic field govern the O- and X-Modes via the phase refractive index  $n_{\pm}$ . Extracting the time-of-flight and propagation losses along these modes is the basic channel modeling. The complications are that the antennas must couple into these modes and that the polarization evolves along these ray paths. The next two sections examine these effects for 1-Hop and 2-Hop channels.

### 3.3 THE 1-HOP CHANNELS

Figure 37 shows only 1-Hop channels whereas the O- and X-Mode propagation produce two distinct channels. As remarked in the introduction to this section, “channels” implies that the transmitter antenna launches an electromagnetic (EM) wave into each mode and the receiver antenna intercepts the EM wave from each mode. Vatberg and Lundborg offer an excellent description of this O- and X-Mode propagation [80]:

When the wave first enters the ionosphere, it will split into two wave modes, ordinary (O) and extraordinary (X). If the polarization of the incident wave matches one of the modes exactly, all the power will go into that wave and the other mode will be suppressed, but generally, both modes will be generated, and these will propagate independently.

Figure 43 illustrates the simplest propagation along the modes, the mode “shedding” [27], and the interaction of both antennas at the transmitter and receiver with these modes. The left and right elliptical polarizations are oriented in the right-handed coordinate system with propagation into the page marked by the “ $\otimes$ ” [58, Figure 6.3]. The descriptor “simplest” means the polarization orientation does not change along the modes. However, Booker’s 1934 paper derived that orientation of the polarization can change along the modes [9].

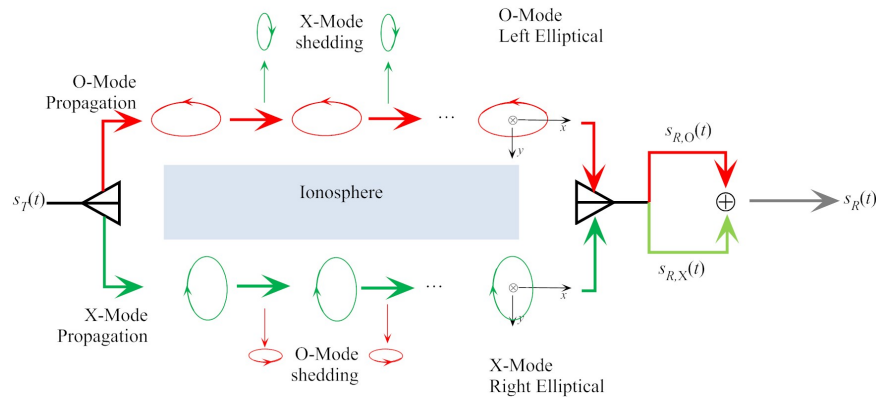


Figure 43. Block diagram of 1-Hop, O- and X-Mode propagation without polarization switching.

Figure 44 illustrates one possibility where the polarization along both modes swings through the linear polarization and reverses. Indeed, Booker’s 1934 paper shows polarization switching right-left-right on one path and left-right-left on the other path.

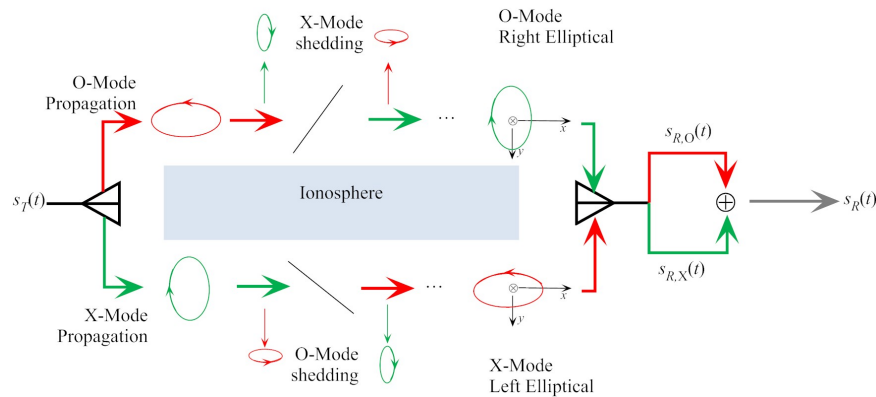


Figure 44. Block diagram of 1-Hop, O- and X-Mode propagation showing polarizations switching.

Appleton established the nomenclature of the O- and X-Modes and their polarizations [3]:

The polarizations of the magnetic forces in the two waves are similar ellipses the major axes of which are at right angles. For a direction of propagation making an acute angle with the positive direction of the magnetic field, the polarization of the ordinary wave is left-handed and that of the extraordinary wave right-handed.

Table 6 links the  $\pm$  sign in the refractive index of Equation (8) the O- and X-Modes, and their polarizations under Appleton’s acute angle constraint. The right- and left-elliptical polarizations determined by the O- and X-Modes are necessary to calculate the voltage response at the receive antenna generated by the down-coming waves. Likewise, the polarization of the transmit antenna that launches the up-going wave determines how the electric field will “split when the wave enters the ionosphere.” Thus, interaction of the transmit and receive antennas with the O- and X-Modes are critical to the end-to-end HF-NVIS channel model. Consequently, Equation (6) should generalize as a coherent sum of the O- and X-channels [80], [70]:

$$s_R(t) = s_{R,O}(t) + s_{R,X}(t).$$

The “O” and “X” label the O-Mode or X-Mode channels measured at the receiver. In terms of the experimental measurements, the O-Mode channel is the LEP component of the received electric field—provided the polarization has not switched on this 1-Hop channel. Likewise, the X-Mode channel is the REP component of the received electric field—provided the polarization has not switched on this 1-Hop channel. Consequently, if the HF-NVIS channel is modeled as the 1-Hop of Figure 43, the O- and X-Mode responses at the receiver are modeled as

$$s_{R,O}(t) = a_{F,O}(t)s_T(t - \tau_{F,O}),$$

$$s_{R,X}(t) = a_{F,X}(t)s_T(t - \tau_{F,X}).$$

The “F” refers to the F-layer refraction and the “O” and “X” label the O-Mode or X-Mode propagation. The channel fading coefficients  $a_{F,O}(t)$  and  $a_{F,X}(t)$  encompass the transmit and receive antennas feeding into the O- and X-Mode channels.

### 3.4 THE 2-HOP CHANNELS

Including multiple hops requires that the channel model include ground reflections. Ground reflections typically change the polarization on the multiple hops. Figure 45 is adapted from the cover of Balanis’ book [6]. The figure shows an incident left circular polarized (LCP) planewave reflecting as a right circular polarized (RCP) planewave.

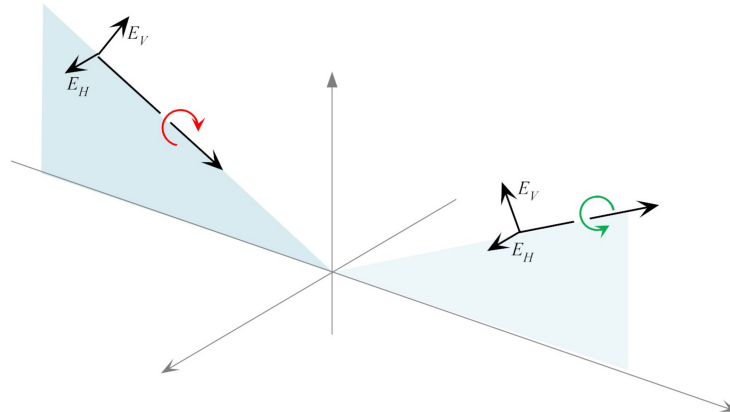


Figure 45. Ground reflection changing polarization.

Table 6. Index of refraction, modes, and acute-angle polarizations.

$n_{\pm}$	Mode	Polarization
+	O-Mode	Left Elliptical (LEP)
–	X-Mode	Right Elliptical (REP)

Figure 46 is a block diagram showing the propagation for two hops. The figure shows that the reflection from the ground bounce causes a mixing of the polarizations.

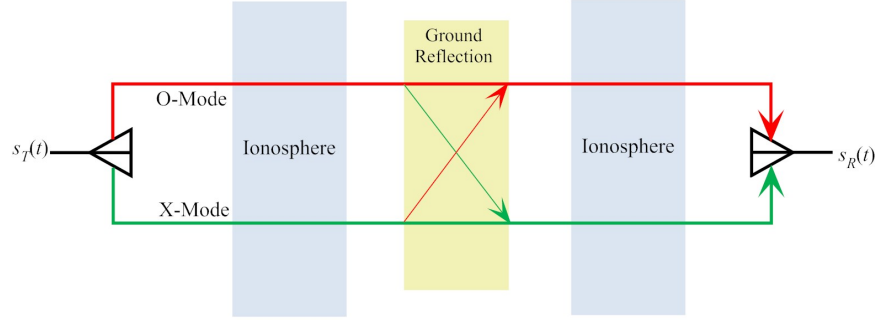


Figure 46. Block diagram of the 2-Hop O- and X-Mode channels showing ground scattering between channels.

In the extreme case where the O- and X-Modes are circular, the plane-wave components of the incident electric field

$$\begin{bmatrix} E_{LCP}^i \\ E_{RCP}^i \end{bmatrix} = \begin{bmatrix} E_O^i \\ E_X^i \end{bmatrix}$$

and the reflected electric field

$$\begin{bmatrix} E_{LCP}^r \\ E_{RCP}^r \end{bmatrix} = \begin{bmatrix} E_O^r \\ E_X^r \end{bmatrix}$$

link across the ground reflection as

$$\begin{bmatrix} E_{LCP}^r \\ E_{RCP}^r \end{bmatrix} = \begin{bmatrix} \rho_{LL} & \rho_{LR} \\ \rho_{RL} & \rho_{RR} \end{bmatrix} \begin{bmatrix} E_{LCP}^i \\ E_{RCP}^i \end{bmatrix}.$$

The conversion between circular and rectangular field components is [50, Eq. 6.119]

$$\begin{bmatrix} E_{LCP} \\ E_{RCP} \end{bmatrix} = \frac{1}{2} \begin{bmatrix} 1 & -j \\ 1 & +j \end{bmatrix} \begin{bmatrix} E_H \\ E_V \end{bmatrix}.$$

If the ground scattering matrix in rectangular coordinates is

$$\begin{bmatrix} E_H^r \\ E_V^r \end{bmatrix} = \begin{bmatrix} \rho_H & 0 \\ 0 & \rho_V \end{bmatrix} \begin{bmatrix} E_H^i \\ E_V^i \end{bmatrix},$$

where  $E_H^r$  and  $E_V^r$  are the horizontal and vertical components of the reflected field,  $E_H^i$  and  $E_V^i$  are the horizontal and vertical components of the incident fields, and  $\rho_H$  and  $\rho_V$  are available from measurements, the ground scattering matrix in circular coordinates is

$$\begin{bmatrix} \rho_{LL} & \rho_{LR} \\ \rho_{RL} & \rho_{RR} \end{bmatrix} = \frac{\rho_H}{2} \begin{bmatrix} 1 & 1 \\ 1 & 1 \end{bmatrix} + \frac{\rho_V}{2} \begin{bmatrix} 1 & -1 \\ -1 & 1 \end{bmatrix}.$$

The following examples show two extremes of the ground scattering matrix. The first example shows that sea water almost completely “flips” the mode with little loss. The second example shows that dry ground still flips the modes but also absorbs power.

**Example 3 (Scattering from Sea Water Surface)** Figures 47 and 48 show the horizontal and vertical reflection coefficients for sea water as a function of the grazing angle or elevation from horizon. The plots show for near vertical incident angles (grazing angle near  $90^\circ$ ),  $\rho_H \approx -1$  and  $\rho_V \approx 1$ . Consequently, the circular scattering matrix for sea water

$$\begin{bmatrix} \rho_{LL} & \rho_{LR} \\ \rho_{RL} & \rho_{RR} \end{bmatrix} \approx -\frac{1}{2} \begin{bmatrix} 1 & 1 \\ 1 & 1 \end{bmatrix} + \frac{1}{2} \begin{bmatrix} 1 & -1 \\ -1 & 1 \end{bmatrix} = \begin{bmatrix} 0 & -1 \\ -1 & 0 \end{bmatrix}$$

reflects the incident LCP as RCP and conversely. Thus, 2-Hop channels reflecting off sea water support only the O-to-X and X-to-O channels, unless the modes flip in the ionosphere as described in Section 3.3.

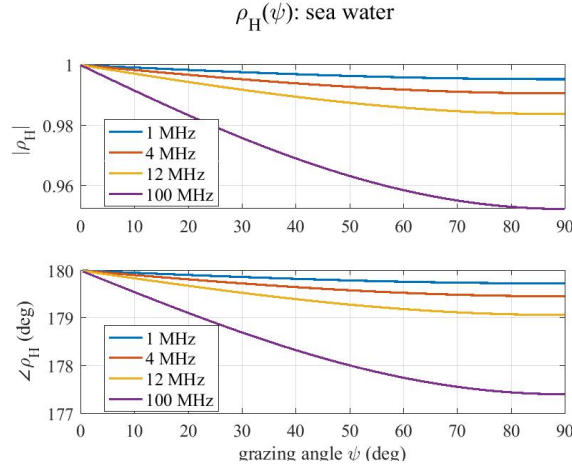


Figure 47. Horizontal reflection coefficient for sea water.

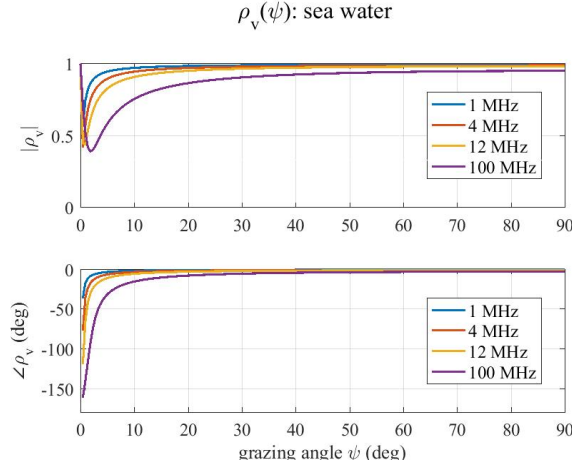


Figure 48. Vertical reflection coefficient for sea water.



**Example 4 (Scattering from very dry ground)** Figures 49 and 50 show the horizontal and vertical reflection coefficients for “very dry ground” as a function of the grazing angle or elevation from horizon. The plots show for near vertical incident angles (grazing angle near  $90^\circ$ ),  $\rho_H \approx -1/2$  and  $\rho_V \approx 1/2$ . Consequently, the circular scattering matrix for very dry ground

$$\begin{bmatrix} \rho_{LL} & \rho_{LR} \\ \rho_{RL} & \rho_{RR} \end{bmatrix} \approx -\frac{1}{4} \begin{bmatrix} 1 & 1 \\ 1 & 1 \end{bmatrix} + \frac{1}{4} \begin{bmatrix} 1 & -1 \\ -1 & 1 \end{bmatrix} = \frac{1}{2} \begin{bmatrix} 0 & -1 \\ -1 & 0 \end{bmatrix}$$

reflects most of the attenuated incident LCP as RCP and conversely. Thus, 2-Hop channels reflecting off very dry ground support only the O-to-X and X-to-O channels, unless the modes flip in the ionosphere as described in Section 3.3.

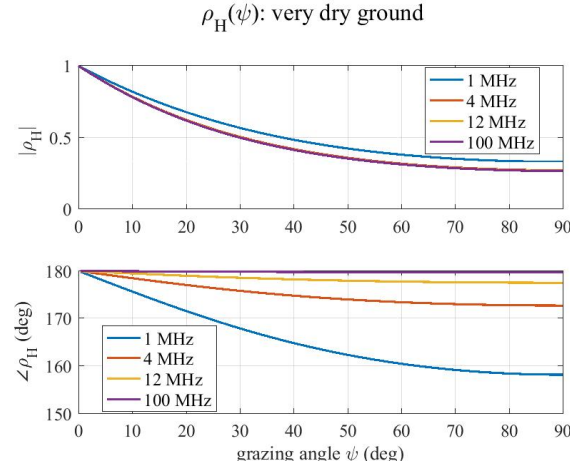


Figure 49. Horizontal reflection coefficient for “very dry ground.”

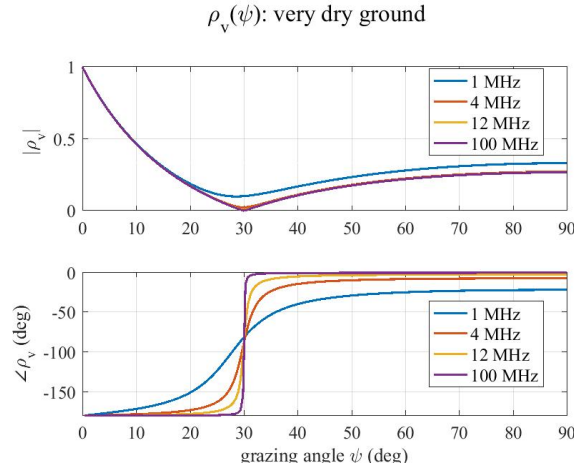


Figure 50. Vertical reflection coefficient for “very dry ground.”



Figure 51 tabulates the delays modeled by the 2-Hop channels. At launch, the first hop enters the ionosphere either left or right circular polarization. Upon exiting the ionosphere from either the O-Mode or X-Mode first hop, the polarization may be reversed. The ground reflection strongly reverses this polarization. The polarization mismatch further filters the reflected wave to match the mode for the second hop. To model the 2-Hop time delays, all that matters is tracking the modes that the rays use to travel through the ionosphere.

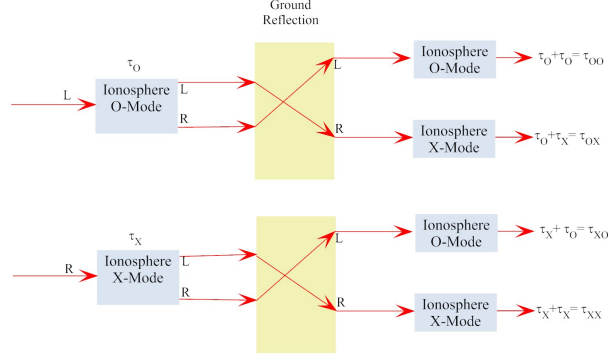


Figure 51. Delays caused by polarization switching and ground reflection.

If the HF-NVIS channel is modeled as the 1-Hop of Figure 43 and the 2-Hop of Figure 46, the the received O- and X-Mode responses are modeled as

$$s_{R,O}(t) \approx a_{F,O}(t)s_T(t - \tau_{F,O}) + a_{F,OX}(t)s_T(t - \tau_{F,OX}) + a_{F,OO}(t)s_T(t - \tau_{F,OO}),$$

$$s_{R,X}(t) \approx a_{F,X}(t)s_T(t - \tau_{F,X}) + a_{F,XO}(t)s_T(t - \tau_{F,XO}) + a_{F,XX}(t)s_T(t - \tau_{F,XX}),$$

using the convention of Figure 51.

### 3.5 SUMMARY

This report finds that the polarization reverses during the hops. Consequently, O- and X-Mode responses encompassing both 1-Hop and 2-Hop—specific to this polarization switching—are approximated as follows:

$$s_{R,O}(t) \approx a_{F,O}(t)s_T(t - \tau_{F,O}) + a_{F,OO}(t)s_T(t - \tau_{F,OO}),$$

$$s_{R,X}(t) \approx a_{F,X}(t)s_T(t - \tau_{F,X}) + a_{F,XX}(t)s_T(t - \tau_{F,XX}).$$

These responses are generally sufficient to model the measured HF-NVIS channels, although ground waves and weak 3-Hop modes are also observed.

## 4. HF-NVIS CHANNEL MODELS

This section reviews two approaches for modeling the HF-NVIS channel functions. The first approach uses specific channel models simulating transmissions for waveform assessments. These models specify channel delays and Doppler shifts that spread the transmitted signal in time and frequency. If  $s_T(t)$  denotes the transmitted signal, the received signal  $s_R(t)$  is modeled as

$$s_R(t) = \sum_{k=1}^K a_k e^{+j2\pi f_k t} s_T(t - \tau_k),$$

where the delays  $\tau_k$ 's, Doppler shifts  $f_k$ 's, and amplitudes  $a_k$ 's are specified as either a few deterministic values or as statistical ensembles modeling more complex multipath propagation. The second approach is based on the statistics of the delay  $\{\tau_k\}$  and Doppler  $\{f_k\}$  ensembles. Figure 52 shows how these HF-NVIS ensembles *jointly* layout in the *delay Doppler* plane. Measured HF-NVIS channels determine two distinct clusters. The mid-latitude channels spread delays up to 8 ms while limited to 1-Hz spreads in frequency. The high-latitude channels spread Doppler up to 16 Hz while limited to 3 ms in delay spreads.

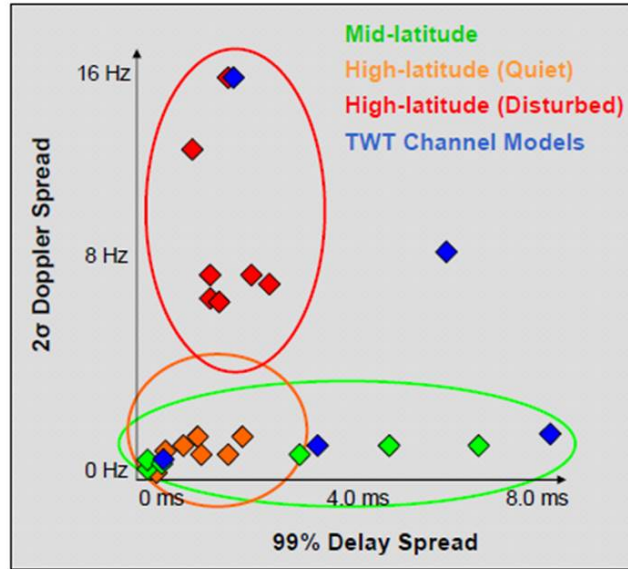


Figure 3-1: Survey of reported HF-NVIS channel measurements

Figure 52. Narrowband HF-NVIS channel classification—delay spread versus Doppler spread (figure courtesy of TrellisWare Technologies, Inc. [41]).

This section surveys selected narrowband HF-NVIS channels using the delay Doppler spreads of Figure 52. Section 4.1 reviews time-varying channels necessary to describe the delay spread, the Doppler spread, and the scattering function. Channel simulation and emulation requires models of the fading on the ray paths, the associated delays and Doppler. Section 4.2 reviews propagation losses along the ray paths, their connection to the magneto-ionic frequencies, and the ionogram. Section 4.3 reviews the Doppler shifts and spreads and points out the fine sampling of the electron density required for modeling Doppler. Section 4.4 tabulates selected narrowband mid-latitude HF-NVIS channels and the associated channel parameters for HF channel emulation. Section 4.5 describes selected narrowband high-latitude HF-NVIS channels. One payoff of this report is extending Figure 52 with the wideband mid-latitude measurements. Section 4.6 remarks on the gaps in the measured HF-NVIS channels and the HF-NVIS channel models.

#### 4.1 GENERAL CHANNEL MODELS

The fundamentals of time-varying channels were laid out by Bello [8] and Kailath [38] in the early 1960s. Mathematically, a time-varying channel  $h(t, \tau)$  maps the transmitted signal  $s_T(t)$  to the received signal  $s_R(t)$  as [8, Eq. 8]

$$s_R(t) = \int_{-\infty}^{\infty} h(t, \tau) s_T(t - \tau) d\tau. \quad (12)$$

This *delay-spread* function  $h(t, \tau)$  models the channel as a collection of impulse responses indexed by time. Typically,  $t$  is the “slow time” and the delay  $\tau$  is the “fast” time. The delay-spread function  $h(t, \tau)$  is part of Bello’s time-varying channel framework illustrated in Figure 53.

Taking the Fourier transform in delay produces the *Time-variant Transfer function* [8, Eq. 18]:

$$T(t, \nu) := \int_{-\infty}^{\infty} e^{-j2\pi\nu\tau} h(t, \tau) d\tau$$

that models the channel as a collection of transfer functions indexed by time [8, Eq. 19]. Taking the Fourier transform in time produces the *Delay Doppler* function [8, Eq. 18]:

$$U(f, \tau) := \int_{-\infty}^{\infty} e^{+j2\pi ft} h(t, \tau) dt.$$

The covariance of the delay Doppler function—the scattering function—has emerged as a workhorse for stochastic channels. The delay Doppler function has covariance

$$R_{UU}(f, \tau; f', \tau') = E[U(f, \tau) \overline{U(f', \tau')}].$$

Under the *wide-sense stationary, uncorrelated scattering* assumptions,

$$R_{UU}(f, \tau; f', \tau') = P(f, \tau) \delta(\tau - \tau') \delta(f - f'), \quad (13)$$

where  $P(\tau, f)$  is called the *scattering function*. The practical value of the scattering function is succinctly described [81]:

Channel characteristics such as the extent of dispersive and multipath delay spread and the extent of Doppler shift and spread are concisely represented by the channel scattering function. The character of the return, specular or diffuse, and its multimodal or multipath composition are also usually evident from an examination of the channel scattering function.

Figure 54 shows an estimate of the scattering function for a long-haul wideband HF channel from Greenland to Massachusetts (See Figure 21). This channel has multiple modes spread in between 100 to 200  $\mu$ s in delay and spread between 5 to 10 Hz in Doppler.

Theoretical channel models show that the scattering function measures the *joint* distribution delay and Doppler. Two common time-varying channel models are the quadrature modulation fading simulator (QMFS) and the phase modulation fading simulator (PMFS).

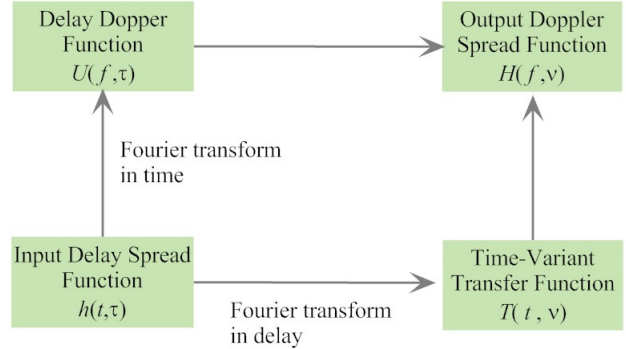


Figure 53. Bello’s channel functions.

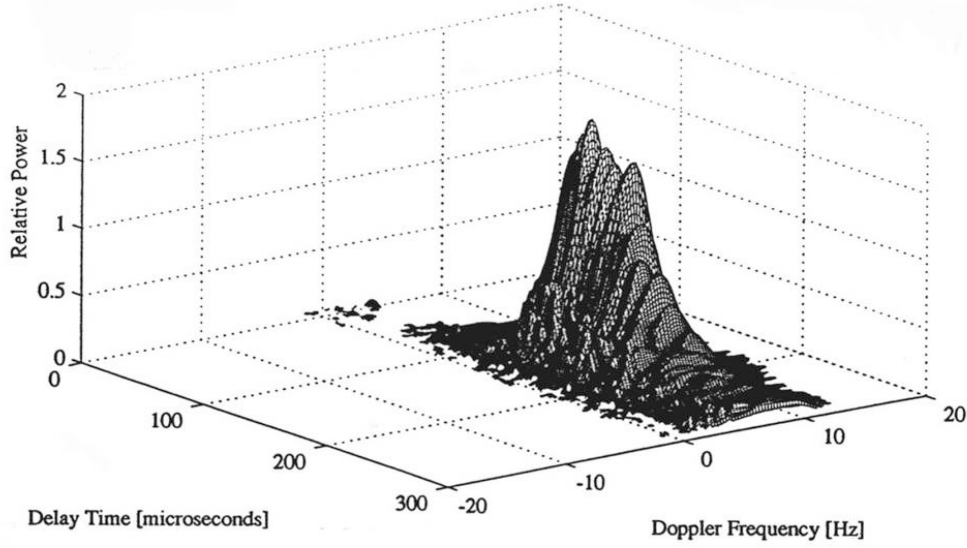


Figure 54. Scattering function estimated from 3100-km link operating at 15.5 MHz on 1 April 1992 at 07:35 UTC (reprinted with permission of the MITRE Corporation) [54].

**Example 5 (QMFS)** [56], [12], [63, pages 697–703]: *The QMFS is the stochastic channel model*

$$h(t, \tau) = \sum_{k=1}^K a_k(t) \delta(\tau - \tau_k),$$

where the  $\{a_k(t)\}$ 's are complex-valued, jointly wide-sense stationary (JWSS), uncorrelated Gaussian random processes with mean and spectral shape determined by the propagation environment.

*Remarks:*

1. The QMFS maps the transmitted signal  $s_T(t)$  to the received signal  $s_R(t)$  as faded and delayed copies of  $s_T(t)$

$$s_R(t) = \int_{-\infty}^{\infty} h(t, \tau) s_T(t - \tau) d\tau = \sum_{k=1}^K a_k(t) s_T(t - \tau_k).$$

2. Physically, this model “leads to a physical picture of the channel as a continuum of non-moving scintillating scatterers” [8].
3. More general models admit time-varying delays  $\tau_n(t)$ .
4. Most RF channel emulators model an RF channel via QMFS where each path is parameterized by delay and fading.

**Example 6 (PMFS)** [32]: *The PMFS is the stochastic channel model*

$$h(t, \tau) = \frac{1}{\sqrt{K}} \sum_{n=1}^K a_n e^{j2\pi f_n t} \delta(\tau - \tau_n). \quad (14)$$

*This model is governed by the following assumptions:*

- *PMFS-1: The  $(a_k, f_k, \tau_k)$ 's are independent and identically-distributed.*
- *PMFS-2: The  $a_k$ 's have zero mean.*
- *PMFS-3: The  $a_k$ 's are independent from the  $f_k$ 's and the  $\tau_k$ 's.*

*Remarks:*

1. The PMFS maps the transmitted signal  $s_T(t)$  to the received signal  $s_R(t)$  as shifted and delayed copies of  $s_T(t)$  :

$$s_R(t) = \int_{-\infty}^{\infty} h(t, \tau) s_T(t - \tau) d\tau = \frac{1}{\sqrt{K}} \sum_{k=1}^K a_k e^{+j2\pi f_k t} s_T(t - \tau_k).$$

2. PMFS-1 makes explicit that there exists a density  $p_{a,f,\tau}(a, f, \tau)$ . PMFS-2 “uncorrelates” each path. PMFS-3 separates the density  $p_a(a)$  of the  $a_k$ 's from the Doppler and delay:

$$p_{a,f,\tau}(a, f, \tau) = p_a(a) p_{f,\tau}(f, \tau).$$

3. The Delay-Doppler function  $U(f, \tau)$  takes the elegant form showing how the signal “spreads” in time and frequency:

$$U(f, \tau) = \frac{1}{\sqrt{K}} \sum_{k=1}^K a_k \delta(f - f_k) \delta(\tau - \tau_k).$$

4. Assumptions PMFS-1, PMFS-2, and PMFS-3 force  $E[U(f, \tau)] = 0$  and covariance:

$$\begin{aligned} R_{UU}(f, \tau; f', \tau') &= E[U(f, \tau) \overline{U(f', \tau')}] \\ &= \frac{1}{K} \sum_{k=1}^K \sum_{k'=1}^K E[a_k \bar{a}_{k'}] E[\delta(f - f_k) \delta(\tau - \tau_k) \delta(f' - f_{k'}) \delta(\tau' - \tau_{k'})] \\ &= \frac{1}{K} \sum_{n=1}^K \sigma_a^2 \delta(f' - f) \delta(\tau' - \tau) p_{f,\tau}(f, \tau) \\ &= \sigma_a^2 p_{f,\tau}(f, \tau) \delta(f - f') \delta(\tau - \tau'). \end{aligned} \tag{15}$$

Thus, the PMFS gives a straight-forward derivation that the scattering function is proportional to the probability distribution of the Doppler and delays. The marginal distributions determine the delay and Doppler spreads of Figure 52.

**Doppler Spread:** The Doppler spread has probability density

$$p_f(f) = \int_0^{\infty} p_{\tau,f}(\tau, f) d\tau.$$

Typically, the mean is the Doppler shift

$$f_D := \int_{-\infty}^{\infty} f p_f(f) df$$

and the variance

$$\sigma_f^2 := \int_{-\infty}^{\infty} (f - f_D)^2 p_f(f) df$$

determines the Doppler spread or frequency spread [34]

$$\Delta f = 2 \times \sigma_f$$

that is the “ $2 \times \sigma$ ” label in the Doppler-spread axis of Figure 52.

**Delay Spread:** The delay spread has probability density

$$p_\tau(\tau) = \int_{-\infty}^{\infty} p_{\tau,f}(\tau, f) df.$$

The cumulative distribution

$$F_\tau(\tau) = \int_0^\tau p_\tau(u) du$$

determines the “99%” used in the delay-spread axis of Figure 52. The following examples specialize these general channel models to the HF-NVIS channels.

**Example 7 (WBHF-NVIS 1-Hop)** *The wideband HF-NVIS channel model based on the O- and X-Modes from Section 3 has the form*

$$h(t, \tau) = h_O(t, \tau) + h_X(t, \tau)$$

where the delay-spread functions for the O- and X-Modes are

$$\begin{aligned} h_O(t, \tau) &= a_{F,O}(t) \delta(\tau - \tau_{F,O}) \\ h_X(t, \tau) &= a_{F,X}(t) \delta(\tau - \tau_{F,X}). \end{aligned}$$

This 1-Hop model describes most of the HF-NVIS channels measured for this report. There are 2-Hop and 3-Hop observed in the measured HF-NVIS channels. However, the dry ground absorbs 3 to 7 dB of the power on reflection. Consequently, 2-Hop amplitudes are typically 10 to 20 dB below the first hop. In addition, the O- and X-Modes appear to switch polarizations (See Figure 51). Therefore, these 1- and 2-Hop channels are modeled as follows.

**Example 8 (WBHF-NVIS 2-Hop Channels With Polarization-Switching)** *The wideband HF-NVIS channel model based on the O- and X-Modes from Section 3.4 has the form*

$$h(t, \tau) = h_O(t, \tau) + h_X(t, \tau) \tag{16}$$

where the delay-spread functions for the O- and X-Modes are

$$\begin{aligned} h_O(t, \tau) &= a_{F,O}(t) \delta(\tau - \tau_{F,O}) + a_{F,OO}(t) \delta(\tau - \tau_{F,OO}) \\ h_X(t, \tau) &= a_{F,X}(t) \delta(\tau - \tau_{F,X}) + a_{F,XX}(t) \delta(\tau - \tau_{F,XX}), \end{aligned}$$

assuming the polarizations switch in the ionosphere on both modes.

The bulk of the HF-NVIS channel literature is narrowband. The standard 3-kHz bandwidth limits path resolution to 0.33 ms. The forthcoming HF-NVIS measurements and simulations report the O- and X-Modes on a given hop are separated by at most 0.15 ms. Consequently, narrowband HF-NVIS channels must lump both modes into a single path. This narrowband fading differs from the wideband fading because the O- and X-Mode interference causes deep fades when the receiver cannot separate the two modes. That is, the narrowband receiver may lose information in the deep fades whereas a wideband system would not.

**Example 9 (NBHF-NVIS)** *The narrowband HF-NVIS channel model has the form*

$$h(t, \tau) = a_1(t)\delta(\tau - \tau_1) + a_2(t)\delta(\tau - \tau_2) + a_3(t)\delta(\tau - \tau_3), \quad (17)$$

where the fading processes  $a_k(t)$  encompass the antennas at both the transmitter and receiver and lumps the O- and X-Modes into a single path.

The fading processes for HF-NVIS channels are typically parameterized by their mean amplitude, the delays, the fading model or Doppler spread, and the Doppler shift.

#### 4.2 PROPAGATION LOSSES IN HF AND HF-NVIS

Discounting the transmit and receive antennas coupling into the O- and X-Mode ray paths and the loss caused by ground reflections on multiple hops, there are at least three propagation effects that reduce the transmitted power along every ray path [46, page 25], [47, Section 6.8]:

- Spherical Spreading
- Mode Shedding
- Absorption

Equation (3), repeated here for convenience, models these effects as

$$G_{\text{HF}} = G_{\text{SPREAD}} \times G_{\text{ABSORB}} \times G_{\text{SHED}}.$$

Spreading is approximated by the standard free-space loss caused by spherical propagation [47, Section 6.8]:

$$G_{\text{SPREAD}} = \left( \frac{\lambda}{4\pi s} \right)^2,$$

where  $s$  is the length of the ray path and typically ranges from  $-90$  to  $-110$  dB for HF-NVIS. The length of the ray path is a relatively stable computation. Therefore, the spreading loss is considered a stable computation.

Mode shedding caused by the polarization evolving along each ray path and is in Sections 3.3 and 3.4. The 3-D ray trace code estimates mode shedding to range from  $-3$  to  $-2$  dB for this simulation. This polarization is governed by the Earth's magnetic field—relatively stable and well-known—so tracking polarization along the ray path is considered a stable computation. Thus, mode-shedding estimate is considered a stable computation.

Absorption is the loss caused by the electron collisions with the heavy neutral molecules and with the ions in the ionosphere [25]. Absorption appears in the refractive index  $n$  via the normalized electron-collision frequency  $Z$  (Equation 11). Although absorption is reported to range from  $-20$  to  $0$  dB for HF propagation in general [47, Section 4.8], absorption modeling shortfalls are significant and absorption research is on-going [59]. If the refractive index  $n$  has real and imaginary parts  $n = \mu + j\chi$  the attenuation along the path is modeled as [11, Eq. 14.35]

$$G_{\text{ABSORB}} = \exp \left( -kc_0 \int \frac{\chi}{\mu} dt \right),$$

where  $k$  is the wave number and the integral over time  $t$  is along the ray path. Implicit in this integral is that the index of refraction takes on four values—the Booker quartic—that requires knowing the upward and downward directions of propagation. The Hamiltonians used in the 3-D ray tracing avoid the Booker quartic but have “computational difficulties” [36]. Consequently, semi-empirical absorption models are still under development [59], [69]. Therefore, the 3-D ray-tracing code will estimate the absorption from measurements by modeling the other losses and compare to the absorption computed by the Hamiltonians.

### 4.3 DOPPLER SHIFT AND DOPPLER SPREAD IN HF

Doppler spread and Doppler shift are caused by the time-varying ionosphere, vehicle motion, and the variation of the ionosphere with respect to frequency. The access to ionograms limit Doppler modeling and comparison with measurements. Therefore, this section reviews the Doppler mechanisms to put the Doppler measurements in context. In 1994, Malachias measured both the *Doppler spread* and *Doppler shift* in HF signals and describes two sources of Doppler shift caused by the ionosphere [44]:

If the layer descends, ... the virtual height descends a proportional amount and the group path ... from transmitter to receiver becomes shorter. The Doppler shift is thus proportional to the path length change. Analogous to this situation, is when the electron density beneath the layer increases, lowering the reflection height, with a similar decrease in the group path. With respect to the propagating wave, the two actions are indistinguishable, and a Doppler shift likewise occurs for a change in electron density of the layer.

This description makes explicit the Doppler caused by the changing geometry and changes in the electron density. Recall that electron density is proportional to the square of the plasma frequency (Equation 7). Figure 55 plots the plasma frequency  $f_P(h, t)$  as a function of height and time. The layer height  $h(f_C, t)$  is determined by  $f_C = f_P(h(f_C, t), t)$  during the time of the channel sounding. The 15-minute sampling of the ionograms causes the discrete appearance. Roughly speaking, the layer height decreases during the interval 08:00 to 11:00 PST remains relatively constant to 14:00, and then begins to increase. There is an exceptional event at 11:00 PST.

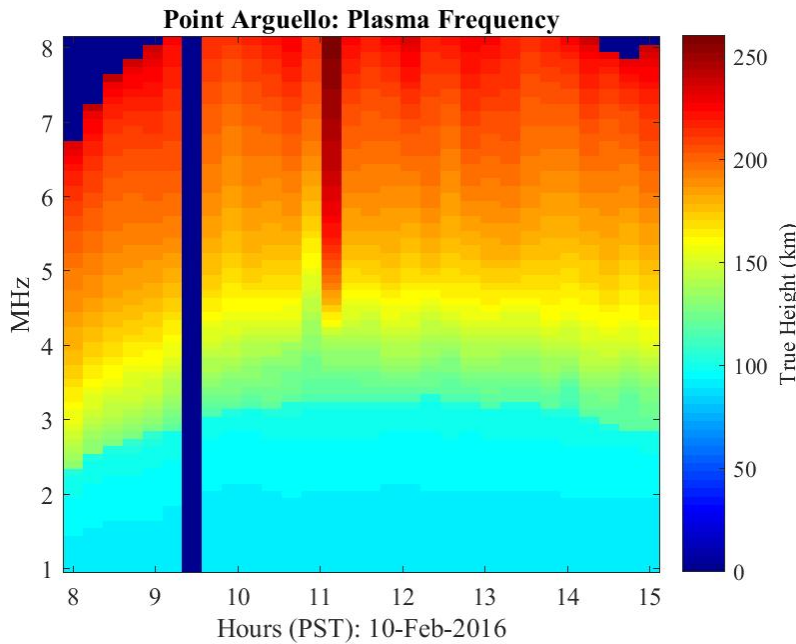


Figure 55. Plasma frequency  $f_P(t, h)$  at Point Arguello; missing sample at 09:30 PST.



Figure 56 shows one estimate of the Doppler shift caused by the layer-movement only. The associated Doppler shift is

$$f_D(f_C, t) = \frac{1}{\lambda_C} \frac{\partial h}{\partial t}(f_C, t); \quad \lambda_C = \frac{c_0}{f_C},$$

where this differential is approximated by computing the numerical derivative of a spline fit to the height. Consequently, the 15-minute sampling implies that this Doppler estimate is only a rough estimate of the Doppler shift.

This estimate omits the change in the electron density as a function of time and frequency. Indeed, the infinitesimal Doppler shift along the ray path given in Equation D-1 requires both  $\partial N_e / \partial t$  and  $\partial N_e / \partial \omega$ . Therefore, time-varying changes in the electron density will not be modeled in this report—only the measured Doppler shift will be reported.

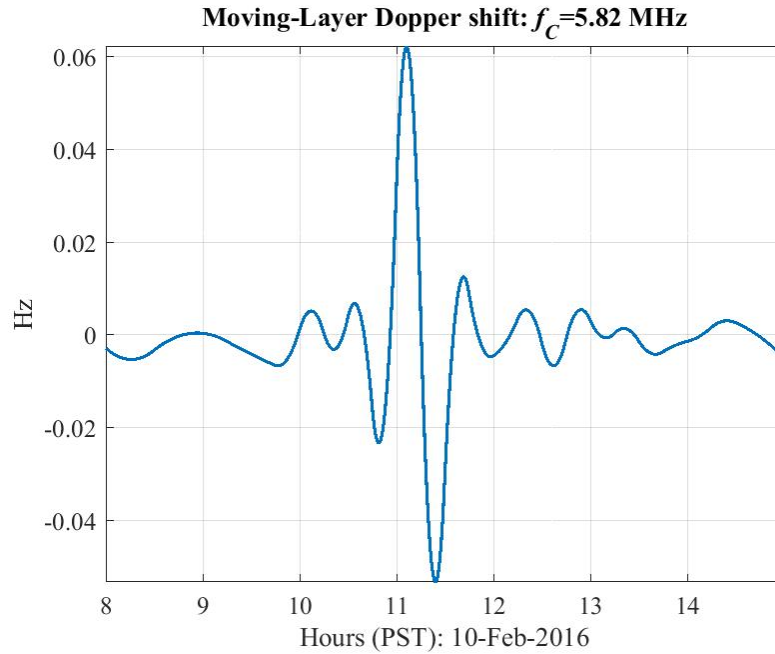


Figure 56. Doppler shift caused by moving layer height for  $f_P(t, h) = 5.82$  MHz at Point Arguello.

Doppler spread is an ensemble of the Doppler shifts. Referring to Equation (14), with a single delay, such as the O- and X-Mode ray path observed in the over-the-air measurements, the delay-spread function takes the form

$$h(t, \tau) = a_0 \delta(t - \tau_0) \exp(\phi(t))$$

where the instantaneous phase  $\phi(t)$  is the integral of the instantaneous frequency  $\{f_i(t)\}$ :

$$\phi(t) = \phi_0 + 2\pi \int_0^t f_i(u) du.$$

If the instantaneous frequency is narrowband, the Doppler shift is

$$f_D = E[f_i(t)]$$

and the power spectrum of the phase modulation

$$\Phi(t) := \exp(\phi(t))$$

is proportional to the probability of the Doppler arising in Equation (15)

$$P_{\Phi\Phi}(f) \propto p_f(f)$$

by Woodward's Theorem [57]. Consequently, an estimate of the delay spread  $\Delta f$  is obtained by fitting the Gaussian distribution to a sampling of the instantaneous frequency.

#### 4.4 MID-LATITUDE HF-NVIS CHANNEL MODELS

Table 7 lists the current narrowband HF-NVIS channel models. The model is a narrowband model of Example 9 Equation (17) is repeated here for convenience:

$$h(t, \tau) = a_1(t)\delta(\tau - \tau_1) + a_2(t)\delta(\tau - \tau_2) + a_3(t)\delta(\tau - \tau_3).$$

The “Disturbed” model comes from the ITU-R F.1487 [34], where only the delay difference of 7 ms is reported. For consistency, the first path is assigned a delay of  $\tau_1 = 1.7$  ms [2]. This delay then sets the delay of the second path as  $\tau_2 = 8.7$  ms.

Table 7. Mid-latitude narrowband HF-NVIS channel models;  $h_k$  magnitude (abs);  $\tau_k$  delay (ms);  $\Delta f_k$  Doppler spread (Hz); Doppler shift is zero.

Descriptor	$h_1$	$\tau_1$	$\Delta f_1$	$h_2$	$\tau_2$	$\Delta f_2$	$h_3$	$\tau_3$	$\Delta f_3$	Reference
Good	0.4	1.7	0.2							[2]
Medium	0.4	1.7	0.5	0.2	4.6	0.5				[2]
Poor	0.4	1.7	1.0	0.2	4.6	1.0	0.15	8.3	1.0	[2]
Disturbed	1.0	1.7	1.0	1.0	8.7	1.0				[34]

This report assumes the simple fading on the taps [76, Section 1.2.2]:

$$a_k(t) = e^{+j2\pi f_{D,k}t} \{s_k + g_k(t)\},$$

where  $\{g_k(t)\}$  is a zero-mean, complex-valued, circular, Gaussian stochastic process with variance  $2\sigma_k^2$ . The gain of the tap is the sum of the specular and diffuse “power”

$$h_k^2 := E[|a_k(t)|^2] = |s_k|^2 + 2\sigma_k^2.$$

The ratio of the specular to the diffused power sets the  $K$ -factor:

$$K = \frac{|s_k|^2}{2\sigma_k^2}.$$

The Doppler spread  $\Delta f_k$  is determined by the power spectra of the fading processes. A Gaussian power spectrum is a standard assumption for mid-latitude medium-haul HF [34, Eq. 2]:

$$P_k(f) := \frac{1}{\sigma_{f,k}\sqrt{2\pi}} \exp\left(-\frac{f^2}{2\sigma_{f,k}^2}\right).$$

The multimode power spectrum is not needed because the wide bandwidth separates modes [34]. This particular spectrum sets Doppler spread as [34, page 3]:

$$\Delta f_k := 2\sigma_{f,k}.$$

This report extracts these channel parameters from the HF-NVIS channel soundings and compares with the 3-D ray-tracing code.

## 4.5 HIGH-LATITUDE HF AND HF-NVIS MODELS

There is long-term interest in high-latitude HF channels and an emerging interest in the high-latitude HF-NVIS channels. This section reviews selected high-latitude HF channel phenomena to complete the discussion of delay spread versus Doppler spread (Figure 52) supporting future channel modeling efforts. At the system level, Figure 52 reports high-latitude channels have relatively small delay spread but larger Doppler spreads compared to the mid-latitude channels. The larger Doppler spreads are typically attributed to magnetic activity [82].

Table 8. Doppler spreading and magnetic activity [82, Table 2].

Magnetic condition	Time	Doppler spread (Hz)	Delay spread (ms)
Quiet	Day	0.09	0.080
Perturbed	Day	6.2	0.812
Post-perturbation	Day	0.6	0.545
Quiet	Night	1.6	0.583
Disturbed	Night	7.6	1.159
Disturbed	Night	12.6	0.571

At the physical level, Feinblum and Horan offer the following insights on the high-latitude ionosphere [23]:

The most striking feature of the mid-to-high-latitude ionosphere is probably the highly localized region of very low electron densities at the F2 peak which is observed at night at geographic latitudes from about 35° N to about 70°N . . . referred to as the “main trough” . . . the “mid-latitude trough,” the “high-latitude trough,” or the “Ottawa trough.”

Figure 57 shows typical poleward and equatorward walls that delineate the trough. Although the trough is a night-time feature during the winter months, the trough changes the nature of the HF-NVIS propagation from vertical reflections off the ionosphere to wall reflections [73]:

The reduction in electron density means that the signal radiated by HF radio communication systems operating under the trough may no longer be ionospherically reflected along the great circle path. However, the signal can still be reflected from gradients in the poleward and equatorward walls of the trough or scattered from irregularities embedded in the trough or in the auroral region which lies just poleward of the trough.

Figure 57 also shows two mid-latitude HF links marked in blue. These links are within the trough. There is a high-latitude channel above 63° North marked in red. Figure 58 reports the delay and Doppler spreads measured over both these medium-haul HF links (4.64–18.38 MHz). The mid-latitude channels spread to 4.5 ms in delay while the high-latitude channels spread to 14 Hz in Doppler. Thus, the medium-haul HF soundings show the same Delay-Doppler structure as the HF-NVIS channels—the mid-latitude channels spread in delay while the high-latitude channels spread in Doppler.

The final observation on these high-latitude channels occurs near the auroral oval (shaded region) [73].

Within the polar cap ionosphere, features of particular note are convecting patches and sun-aligned arcs of enhanced electron density that can lead to signals arriving in directions displaced from the great circle path by up to 100°.

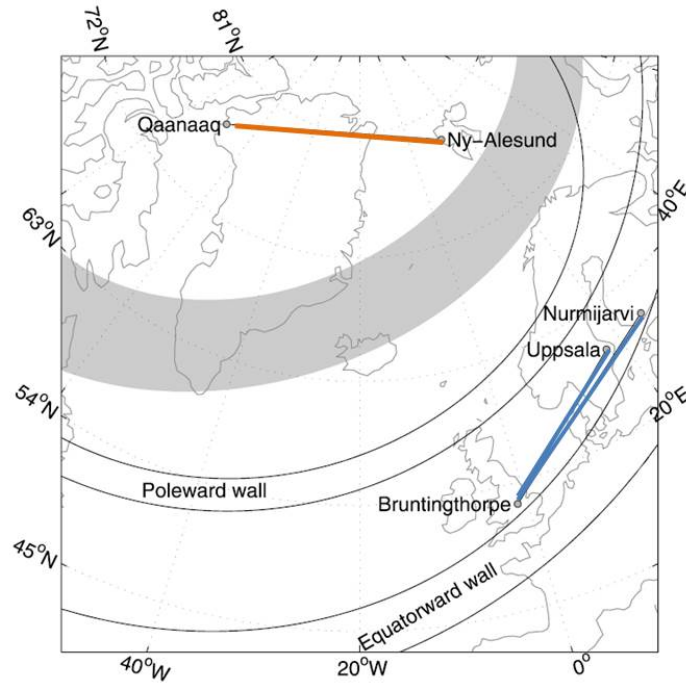


Figure 57. Typical trough, its bounding walls, and the auroral oval (shaded) [73] (figure courtesy of Radio Science).

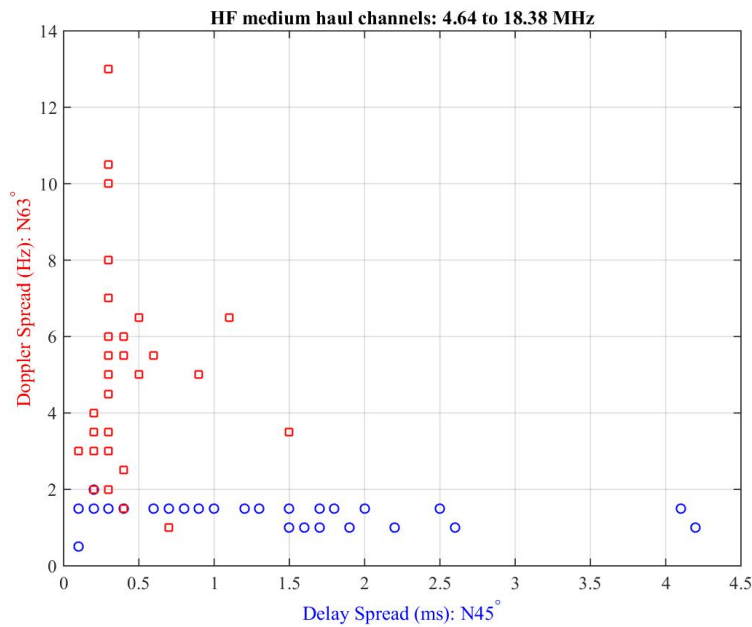


Figure 58. HF medium-haul channels in the mid- and upper latitudes [73].

Consequently, HF radio systems operating in the high-latitudes must adapt waveforms, frequencies, and antenna patterns to account for the large Doppler spreads and non-vertical paths.

## 4.6 SUMMARY

This section reviewed two approaches for modeling the HF-NVIS channel functions:

- Realizations of channel parameters for HF channel emulation
- The delay Doppler spreads describing classes of HF channels

The superb wideband HF measurements of Wager and Goldstein taken in 1995 are an excellent example of the latter [82]. Figure 58 shows that the medium-haul HF channels cluster in the mid-latitude or high-latitude behaviors of Figure 52. If these measurements are still extant, a re-analysis to extract ray path statistics would deliver channel parameters for the wideband HF medium-haul in the high latitudes—without the substantial cost of high-latitude field measurements. There still remains the need for high-latitude HF-NVIS measurements to clarify antenna performance, measure ray path delays and Doppler shifts as affected by the magnetic field, estimate polarization-switching along the ray paths, and compare absorption models to the measurements.

Table 7 shows the limited HF-NVIS channel models available for HF-NVIS channel emulation. Although these limited narrowband HF-NVIS channel soundings have been boosted by the wideband HF-NVIS soundings of TrellisWare [79], publication of that massive database is pending as of this report.

The wideband soundings described in this report and the follow-on reports serve three purposes. The first and immediate goal is to provide wideband HF-NVIS channel models for both channel simulation and emulation. Second and more lasting, is that these measurements validate the 3-D ray-tracing code. Consequently, credible mid-latitude HF-NVIS channels may be simulated without costly field tests. Third, and contributing to the understanding of the HF wireless channel, the 3-D ray-tracing code explicitly models the antenna's coupling into the electric field. Consequently, the coherent interaction of multiple antennas and time-varying polarizations—necessary for the SIMO, MIMO, and dual-polarization configurations—is correctly modeled and linked to the polarization evaluation on the O- and X-Modes. As such, this 3-D ray-tracing code is better suited for HF wireless engineering than the power-tracking codes.

## 5. THE HF-NVIS CHANNEL SOUNDING SYSTEM

Figure 59 is a block diagram of the HF-NVIS channel sounding system. The transmitter is an 85-ft horizontal dipole antenna located at the Model Range of Space and Naval Warfare Systems Center Pacific (SSC Pacific). This stationary transmitter broadcasts a pseudorandom noise (PN) sequence for wideband channel sounding. The receiver is carried in a mobile van equipped with a two-port antenna. The receiver carried in the mobile van phases the ports so that the sounding sequence is simultaneously received on a vertical whip that has the standard HF antenna pattern similar to Figure 5 and a vertical loop that has an HF-NVIS pattern similar to Figure 7. Consequently, this system design allows simultaneous side-by-side comparisons between a standard HF system and an HF-NVIS system in the same over-the-air experiment. The following sections detail key components of this system. Section 5.1 documents the HF antennas and their measured patterns. Section 5.2 describes the sounding waveform and the archiving scheme of the channel soundings. Section 5.3 reviews the channel estimation scheme and synthetic examples showing the effect of additive noise. Section 5.4 makes explicit the relative calibration used in this report.

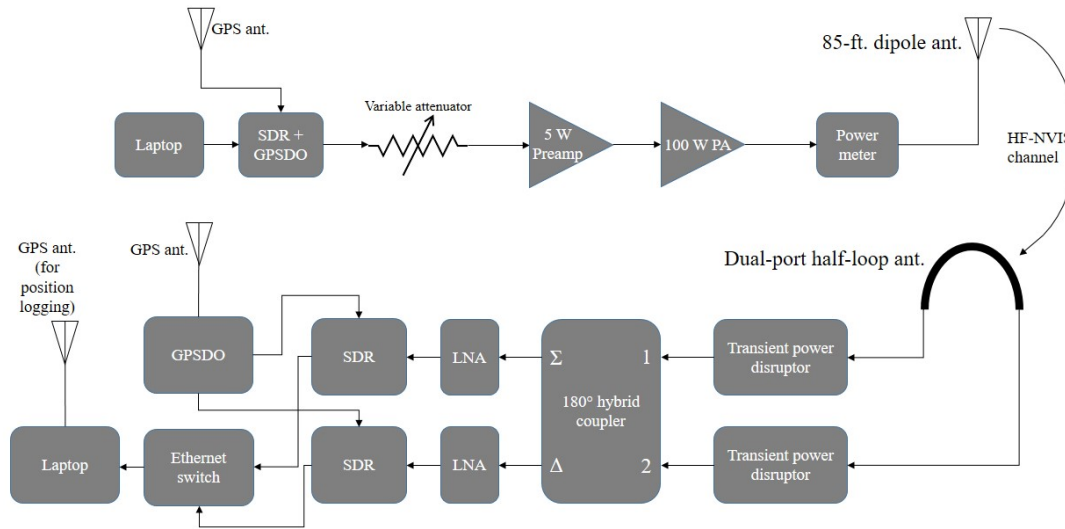


Figure 59. Block diagram of the HF-NVIS channel sounding system.

### 5.1 TRANSMIT AND RECEIVE HF ANTENNAS

The transmit antenna is a horizontal half-wave wire dipole approximately 84.5 ft long. It is hung about 30 ft in the air between two wooden masts. The antenna's braided wire arms are connected to a Unadilla® W2DU HF 1:1 balun. Also connected to the balun is about 50 ft of coaxial cable that goes through a hole in the ground to the transmitter in an underground tunnel. The balun has a ferrite sleeve that chokes the current on the cable shield. The ground plane beneath the antenna and masts is a metal mesh that approximates a perfect ground for HF frequencies. The dipole and ground plane occupy the open space above a circular outdoor pattern range shown in Figure 60.

Figure 61 shows the receiving half-loop mounted on the top of the mobile receiver. This half-loop is based on the design in [83] and adapted for the HF band in [13] and [14]. The loop is connected to a metal ground plane slightly smaller than the minivan roof. This ground plane is secured to a luggage rack and not electrically connected to the van body.



Figure 60. Transmitter: 84.5-ft horizontal dipole located approximately 30 ft above the ground (yellow line).



Figure 61. Mobile HF-NVIS receiver carrying the dual-function antenna.

The half-loop is electrically small for the HF band and on a small ground plane, and is inefficient at receiving radiation. However, because the external HF environment is much noisier compared to higher frequencies due to the favorable propagation of interference over long distances, the receive system is external noise limited. This means that the internal noise in the receive chain is insignificant compared to the external noise received by the loop. Making the loop larger would increase the received signal strength but also the received noise, and therefore would not significantly improve the SNR. The ends of the loops float about an inch over the ground plane. These ends are connected to coaxial cables with 4:1 Guanella unun transformers [28]. The coaxial cables from each port then connect to the two input ports of a 180° hybrid coupler. The sum port adds both ports of the loop and generates a dipole radiation pattern. The difference port adds both loop ports out of phase and generates a loop radiation pattern.

The hemispherical radiation pattern of the half-loop on its ground plane was measured at the outdoor pattern range (Model Range). Figures 62, 63, and 64 show the directivities in three cut planes measured at 5.8 MHz. Figure 62 shows the approximate azimuth cut plane around the antenna. This is only



approximate because the probe dipole antenna was  $5^\circ$  above the horizon, which was as low to the horizon as the dipole could get without touching the ground plane. The dominant polarization is  $E_\theta$ .

In Figure 62, the dipole (whip) mode of operation produces the expected omni-directional  $E_\theta$  radiation pattern in azimuth. The loop mode  $E_\theta$  pattern has two nulls at loop broadside as expected. In Figure 63, half of the elevation cut plane that is broadside to the loop is shown. The dominant polarizations for both antenna modes is  $E_\theta$ . The whip mode has a null at zenith and a maximum at the horizon. The loop mode has a null at the horizon and a maximum at zenith. In Figure 64, the whip mode again has a maximum at the horizon and a null at zenith in the dominant  $E_\theta$  polarization. The loop mode has a high  $E_\theta$  level both at the zenith and close to the horizon because the cut plane is in the plane of the loop. At the horizon, the pattern still goes to zero because the antenna is directly above a ground plane. Overall, the measured half-loop pattern has the main characteristics of an ideal half-loop above a ground plane.

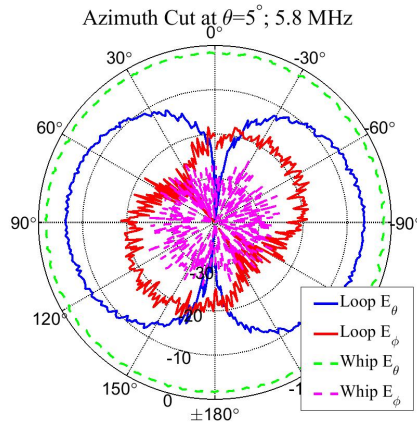


Figure 62. Radiation pattern of dual-port loop at 5.8 MHz in the azimuthal plane.

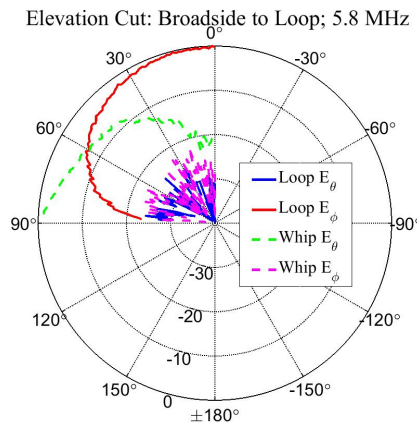


Figure 63. Radiation pattern of dual-port loop at 5.8 MHz in the elevation plane orthogonal to the plane of the loop.

## 5.2 SOUNDING WAVEFORM

Figure 65 shows the channel-sounding waveforms organized into a frame bundle. Each frame bundle consists of 58 1-second frames. Each frame consists of 22 PN bursts followed by dead time. Recording



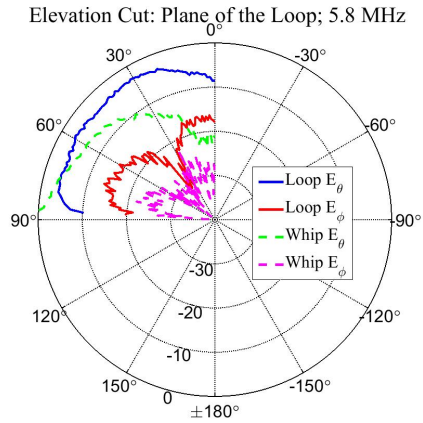


Figure 64. Radiation pattern of dual-port loop at 5.8 MHz in the elevation plane of the loop.

a frame bundle starts on each minute. The final 2 seconds of each minute are reserved for saving of the recordings of each software-defined radio to disk.

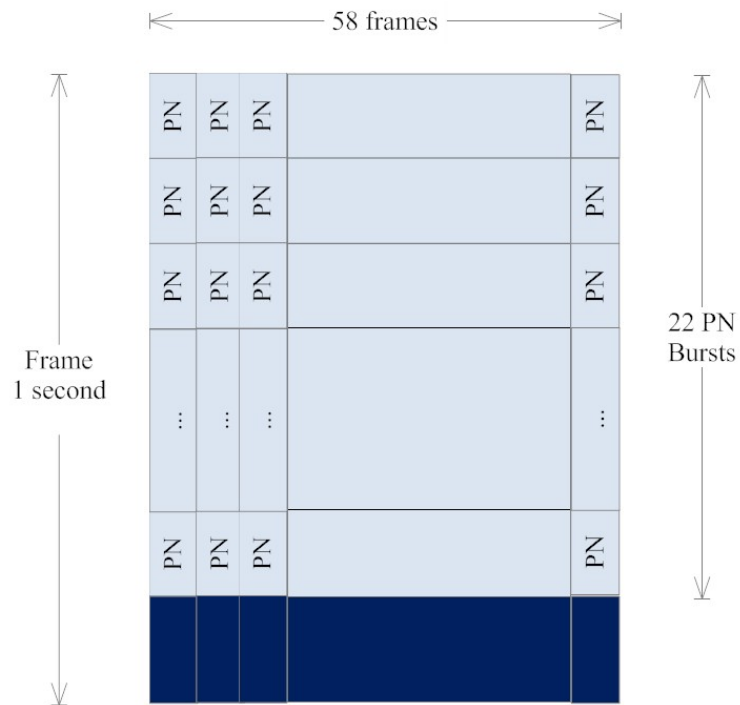


Figure 65. Frame bundle.

Each PN burst  $s_{\text{PN}}(t)$  is a waveform obtained from the BPSK sequence with a square-root raised cosine pulse shaping:

$$s_{\text{PN}}(t) = \sum_{n=1}^{N_P} b_n s_{\sqrt{\text{RC}}}(t - nT_{\text{sym}}), \quad (18)$$

where  $N_P$  is the length of the PN10 sequence:  $N_P = 1023$ , the  $b_n$ 's are the PN10 symbols:  $b_n = \pm 1$ , and  $s_{\sqrt{\text{RC}}}(t)$  denotes the square-root raised cosine pulse with symbol period  $T_{\text{sym}}$ . For the channel sounding shown in Figure 65, the symbol rate is  $R_{\text{sym}} = 25$  kbps so that symbol duration is

$$T_{\text{sym}} = R_{\text{sym}}^{-1} = 40 \text{ } [\mu\text{s}].$$

Each frame  $s_F(t)$  consists of  $N_B = 22$  PN bursts

$$s_F(t) = \sum_{n_b=1}^{N_B} s_{\text{PN}}(t - n_b T_B),$$

where each burst has duration

$$T_B = N_P T_{\text{sym}} = 40.092 \text{ } [\text{ms}].$$

The  $N_B = 22$  PN bursts produce a transmission “on” time of duration

$$T_B = N_B T_T = 900.240 \text{ } [\text{ms}].$$

The remainder of the 1-second frame consists is the dead time lasting

$$T_D = 99.760 \text{ } [\text{ms}].$$

Each frame bundle is recorded in a .WAV file corresponding to the whip or NVIS antenna and stamped with the date and UTC stamp. On 10 February 2016, 370 files were recorded from the whip and another 370 files were recorded from the loop as the van (Figure 61) traveled from Point Loma, San Diego, CA, to El Centro, CA, and back (Figures 73 and 74) starting at 8:30 a.m. PST and ending at 3:08 p.m. PST. Table 9 shows the labeling and interpretation for two sample files.

Table 9. Labeling scheme for the .WAV files.

File	Antenna	Date	PST
NVIS_20160210_162800.wav	Loop	10-Feb-2016	8:28 a.m.
GND_20160210_230800.wav	Whip	10-Feb-2016	3:08 p.m.

Conversion from UTC time to local PST, on this date, requires that 8 hours be subtracted from the UTC hours:

$$\begin{aligned} 162800 &\mapsto (16 - 8):28:00 = 08:28 \text{ PST} \\ 230800 &\mapsto (23 - 8):08:00 = 15:08 \text{ PST} \end{aligned}$$

### 5.3 CHANNEL ESTIMATION

The HF-NVIS channel is sounded by the PN bursts in the frame bundle of Figure 65. The HF-NVIS channel is estimated by standard correlation that assumes the channel is stationary over all the PN bursts in a frame as a sum  $K$  delays where  $K$  is unknown

$$h(t) = \sum_{k=1}^K h_k \delta(t - \tau_k).$$

The received signal  $s_R(t)$  is modeled as noise-corrupted multipath,

$$s_R(t) = h * s_{PN}(t) + g(t) = \int_{-\infty}^{\infty} h(t') s_{PN}(t - t') dt' + g(t),$$

where  $\{g(t)\}$  is the zero-mean noise. Correlation processing simply filters the received signal against the “extraction” signal  $s_X(t)$  designed to register a strong *unit peak* with each PN sequence. A noisy version of a stationary channel is then extracted as follows:

$$\begin{aligned} s_X * s_R(t) &= h * s_X * s_T(t) + s_X * g(t) \\ &= \sum_{k=1}^K h_k (s_X * s_T)(t - \tau_k) + s_X * g(t) \\ &\approx \sum_{k=1}^K h_k \delta(t - \tau_k) + s_X * g(t). \end{aligned}$$

The extraction signal is scaled to register a unit response for the channel. Consequently, the noise level in the channel estimate is suppressed by the magnitude of this filter. The next example computes the suppression for white noise.

**Example 10 (White Noise)** *Although zero-mean continuous-time white noise exists only as a generalized random process with covariance [57, Eq. 9-40]*

$$R_{gg}(\tau) = \sigma_g^2 \delta(\tau)$$

*this limiting case provides insight into the filtered noise:*

$$\begin{aligned} E[|s_X * g(t)|^2] &= \int_{-\infty}^{\infty} dt_1 \int_{-\infty}^{\infty} dt_2 \overline{s_X(t_1)} s_X(t_2) R_{gg}(t_2 - t_1) \\ &= \sigma_g^2 \int_{-\infty}^{\infty} dt_1 \int_{-\infty}^{\infty} dt_2 \overline{s_X(t_1)} s_X(t_2) \delta(t_2 - t_1) \\ &= \sigma_g^2 \int_{-\infty}^{\infty} |s_X(t)|^2 dt. \end{aligned}$$

Channel estimation is performed in the digital domain. The extraction signal is the time-reversed copy of the digital PN signal extended by a few extra symbols. The time-limited square-root raised cosine function as the square-root raised cosine function observed over  $N_{\text{sym}}$  symbols centered at  $t = 0$  is defined as:

$$s_{\sqrt{\text{RC}}}(N_{\text{sym}}; t) = s_{\sqrt{\text{RC}}}(t) \times 1_{[-T_D/2, T_D/2]}(t); \quad T_D = N_{\text{sym}} T_{\text{sym}}.$$

The time-limited PN signal as the time-limited version of Equation (18) is defined as:

$$s_{\text{PN}}(N_{\text{sym}}; t) = \sum_{n=1}^{N_P} b_n s_{\sqrt{\text{RC}}}(N_{\text{sym}}; t - nT_{\text{sym}}). \quad (19)$$

The digital, time-limited square-root raised cosine function by sample using  $N_{\text{sps}}$  samples per symbol is defined as:

$$s_{\text{PN}}(N_{\text{sym}}, N_{\text{sps}}; t_k) = s_{\text{PN}}(N_{\text{sym}}; t_k); \quad t_k = \frac{k}{f_s}, f_s = R_{\text{sym}} N_{\text{sps}}.$$

The extraction signal is

$$s_X(t_k) := \frac{s_{\text{PN}}(N_{\text{sym}}, N_{\text{sps}}; t_k)}{\|s_{\text{PN}}(N_{\text{sym}}, N_{\text{sps}})\|_2^2}.$$

Table 10 lists the parameters for the extraction signal specific for this channel sounding and sets  $\|s_{\text{PN}}(N_{\text{sym}}, N_{\text{sps}})\|_2^2 = 31 \text{ dB}$ .

Table 10. Parameters for the digital PN signal.

Variable	Value	Description
$f_s$	100	Digital sampling rate (kHz)
$\beta$	0.35	roll-off factor
$N_{\text{sym}}$	11	Number of symbols
$N_{\text{sps}}$	4	Number of samples per symbol
$R_{\text{sym}}$	25	Symbol rate (kHz)

**Example 11 (Simulated Channel)** Figure 66 reports on the performance of this channel estimation scheme using the PN signal parameterized by Table 10. The upper panel shows a simulated channel  $h(t)$  with taps spread over 10 ms. The received signal  $s_R(t)$  is the time-limited PN signal  $s_{\text{PN}}(t)$  of Equation (19) filtered through this channel and corrupted by white Gaussian noise:

$$s_R(t) = h * s_{\text{PN}}(t) + g(t).$$

The specified SNR sets the variance of the noise reported as the “wideband input noise”:

$$\text{SNR} = \frac{\|h * s_{\text{PN}}\|_2^2}{\sigma_g^2}.$$

The lower panel reports on the channel estimate:

$$h_{\text{EST}}(t) = s_X * s_R(t) + s_X * g(t) = h(t) + s_X * g(t).$$

The peaks of the channel register while the output noise level is reduced by approximately 31 dB.

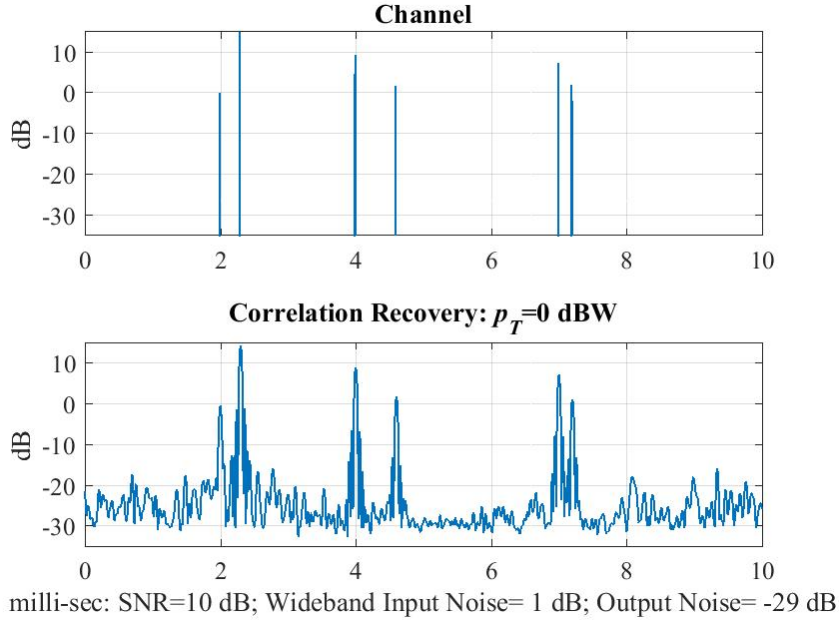


Figure 66. Simulated channel (top panel); Estimated channel (lower panel).

Example 11 uses a bandwidth of 25 kHz that is oversampled by a factor of four:  $f_s = 100$  kHz. The digital noise in this example has flat spectrum spread over the entire 100-kHz band. The next example assesses channel recovery when the in-band noise is confined to the 25-kHz band.

**Example 12 (In-Band Noise)** Figure 67 shows the low-pass filter that determines the in-band noise spectrum. Figure 68 shows the performance of this channel estimation scheme against a realization of this in-band noise. The upper panel shows a simulated channel  $h(t)$  with taps spread over 10 ms. The received signal is the  $s_{PN}(t)$  of Equation (19) filtered through this channel and corrupted by the filtered Gaussian noise:

$$s_R(t) = h * s_{PN}(t) + g(t).$$

The specified SNR sets the variance of the noise reported as the “In-Band Input Noise”:

$$\text{SNR} = \frac{\|h * s_{PN}\|_2^2}{\sigma_g^2}.$$

The lower panel of Figure 68 reports on the channel estimate:

$$h_{\text{EST}}(t) = s_X * s_R(t) + s_X * g(t) = h(t) + s_X * g(t).$$

The peaks of the channel still register, the output noise is reduced by approximately 25 dB, and the noise floor is smoother.

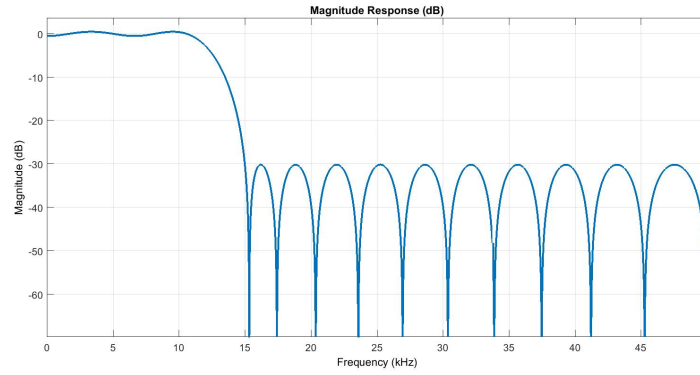


Figure 67. Low-pass filter to generate in-band noise.

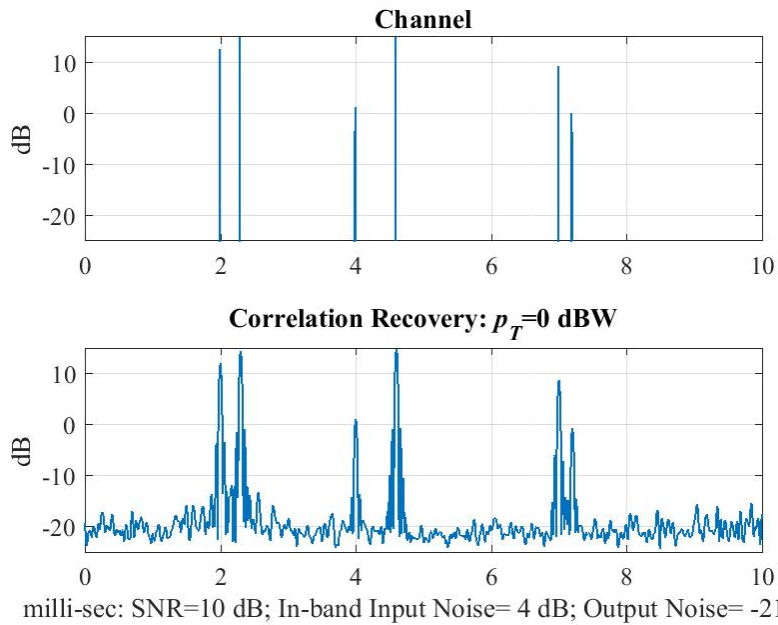


Figure 68. Simulated channel (top panel); Estimated channel (lower panel).

## 5.4 CALIBRATION

The preceding section reported on channel estimation in an ideal digital simulation using the implicit assumptions:

- Perfect waveform synthesis
- Perfect synchronization between transmitter and receiver
- No delay between transmitter and receiver
- Perfect amplitude control
- Zero system noise

In contrast, all real-world channel sounding systems do not generate ideal waveforms, suffer from jitter in synchronization, and exhibit end-to-end delays caused by processing. The end-to-end amplitude can only be known by measurement. Therefore, timing and gain calibrations are necessary to compensate these effects.

On 2 March 2016, the transmitter and receiver shown in Figure 59 were connected with cables for back-to-back testing. This section reports on the testing and determines the necessary timing and amplitude compensation—assuming linear operation of the amplifiers and demodulators—so that the frame-bundle processing reports no delay and unit amplitude for this back-to-back channel. Therefore, applying this calibration to the over-the-air measurements should only register the HF channels, the transmitter’s power, and the antenna effects.

Figure 69 shows the received signal reshaped into the format of the ideal frame-bundle of Figure 65. The crisp edges and straight lines demonstrates that the channel sounding system is maintaining tight synchronization

Figure 70 records the first PN sequence of the first frame of the frame bundle. This waveform shows that the transmitter is producing high-quality analog waveforms and digitizing the waveform in the receiver.

Figure 71 is a close-up view comparing the real part of this measured waveform to its ideal digital waveform delayed to compensate for the system delays. The scaling was selected to show that the received wave aligns with the ideal waveform. That is, any processing done in the receiver can assume the received waveform is well-modeled by its associated ideal waveform.

Figure 72 correlates the real-world received waveform  $s_R(t)$  against the idealized extraction signal  $s_X(t)$  using the compensating system delays. The single peak shows that the system delays have been compensated. The peak value of 0.025136 is amplitude scaling necessary to produce the unit height. A slightly improved value is the “ $g_{\text{cal}} = -15.9976$ ” (dB) reported on the forthcoming channel estimation plots.



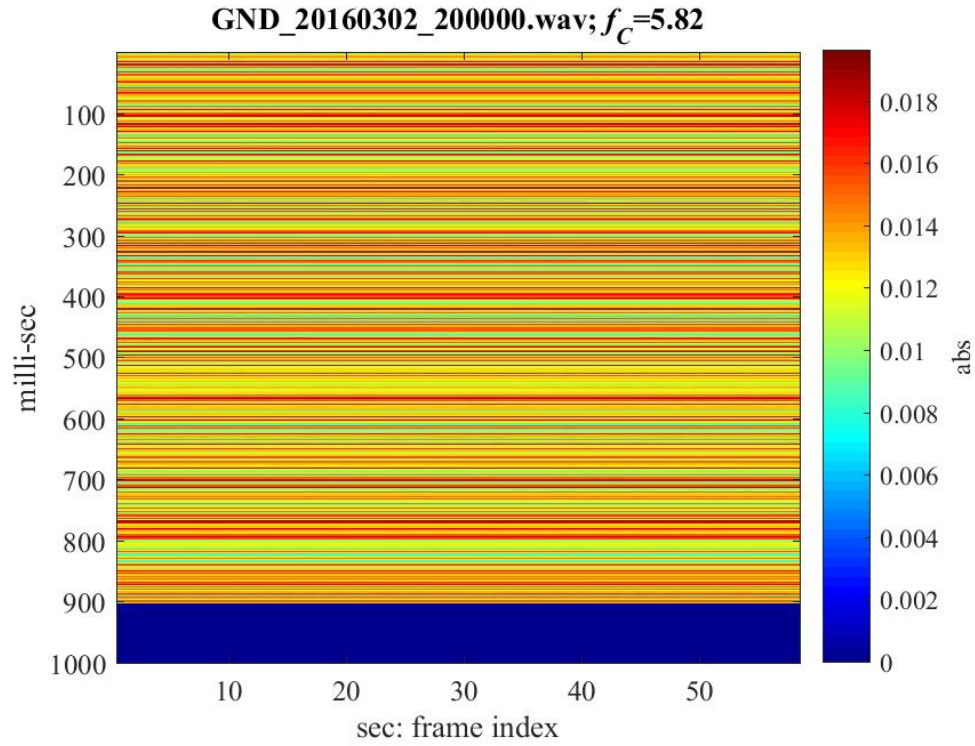


Figure 69. Received signal shaped into the frame-bundle format.

GND\_20160302\_200000.wav: First PN10 Sequence

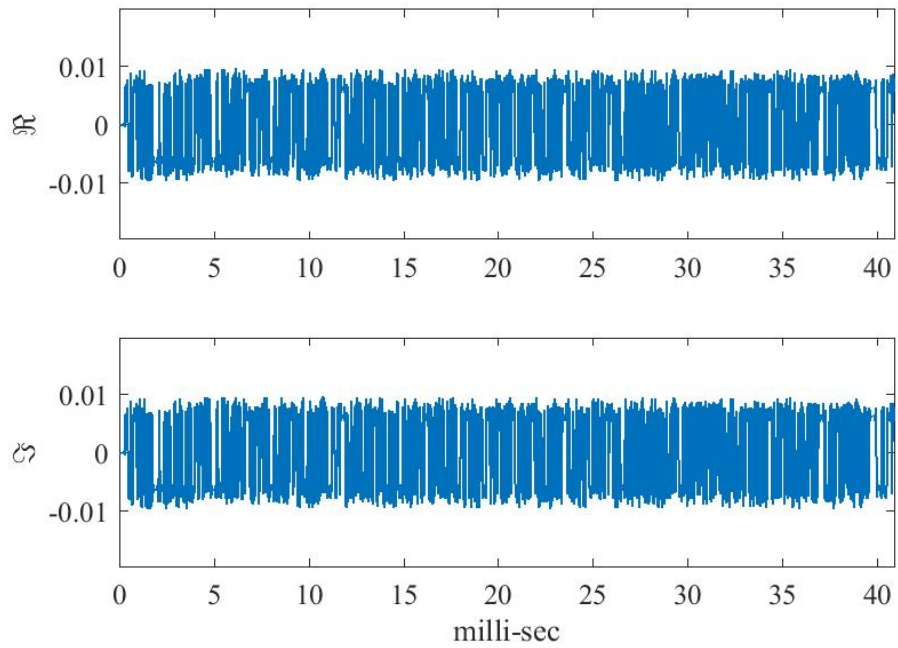


Figure 70. First PN sequence of the first frame of the frame bundle.

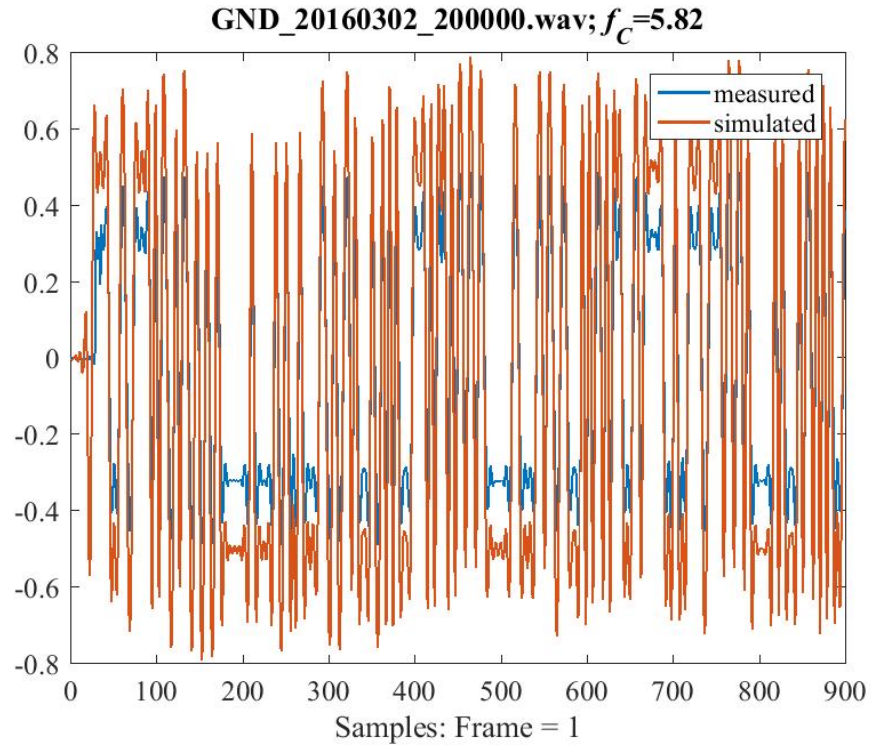


Figure 71. Comparing the real part of the measured received waveform to an ideal digital waveform. The scaling was selected to show the timing alignment.

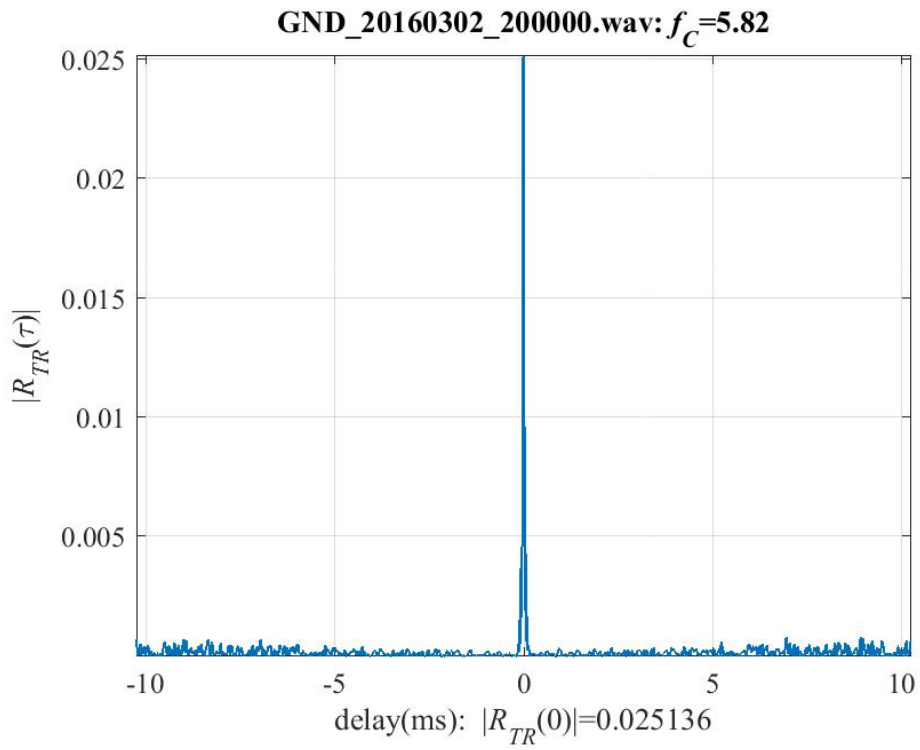


Figure 72. Extraction of the back-to-back channel to compute amplitude scaling.

## 6. SIGNAL, NOISE, AND INTERFERENCE ALONG THE MOBILE ROUTE

Figure 73 shows the route of the mobile HF-NVIS receiver on 10 February 2016 marked in red. The starting point is Point Loma, CA, at 8:30 a.m. PST. The outbound route traveled on Interstate 8 East arriving near El Centro, CA, at 10:30 a.m. PST. The return loop traveled north to the Salton Sea, crossed Anza-Borrego Desert Park, and returned through the Cuyamaca Mountains. Figure 74 isolates the route for clarity. Figure 75 reports the ground range as a function of the time along the route.



Figure 73. Route of the mobile HF-NVIS vehicle.

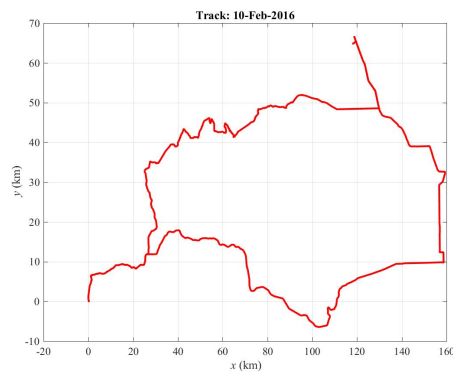


Figure 74. Mobile HF-NVIS route.

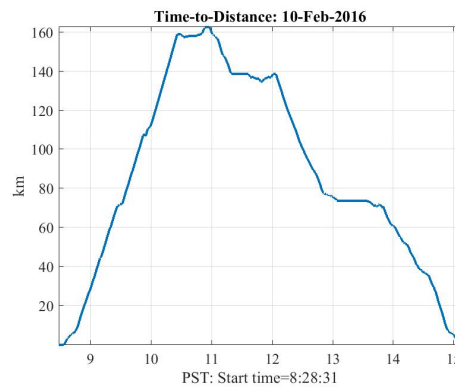


Figure 75. Ground range as a function of time.

### 6.1 SIGNAL POWER ALONG THE ROUTE

The transmit power delivered to the horizontal dipole was approximately 90 Watts at 5.82 MHz over a 25-kHz band. The transmit signal consists of a repeating sequence of frame bundles as shown in Figure 65. Each frame bundle starts at the beginning of each minute and lasts 58 seconds. These frame bundles are simultaneously received through the whip and loop antennas enabling side-by-side comparisons between the standard HF and the HF-NVIS channels.

Figures 76 and 77 compare the “raw” power received by the whip and loop antennas. The quotes around “raw” mean that the power is computed by averaging the entire received digital signal recorded in each frame bundle. All 58 frames are included in this average, including the dead time at the end of each frame. The dB reported is computed directly from the digital audio signal in the .WAV files—no conversion to dBW is applied. Comparing the plots shows that the noise floor of the loop antenna is approximately 25 dB lower than the whip, excepting the interference “spikes” and the broad region between 10:00 and 11:00 PST. This comparison opens the conjecture that the up-ward pointing loop rejects much of the HF noise arriving from the side that is swamping the whip.

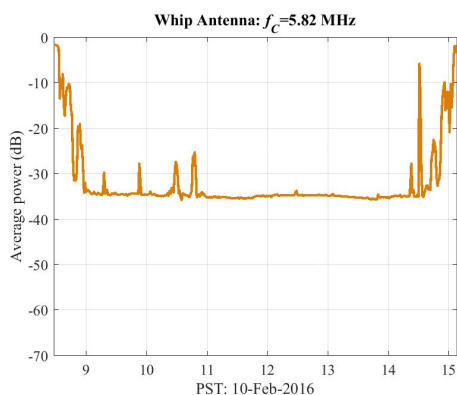


Figure 76. Raw whip power.

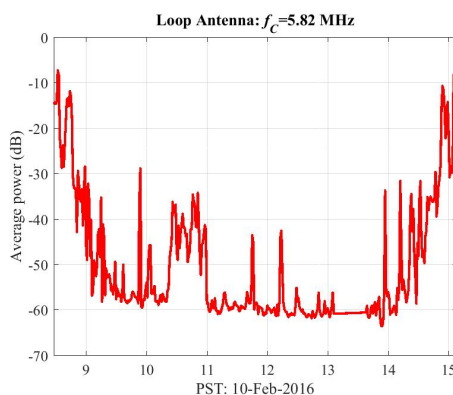


Figure 77. Raw loop power.

## 6.2 NOISE POWER ALONG THE ROUTE

Figure 78 and 79 support the conjecture that the HF-NVIS loop antenna is rejecting the local HF noise by comparing the “noise only” portion at the end of each frame. The dB reported is computed directly from the digital audio signal in the .WAV files—no conversion to dBW is applied. Comparison of these plots show that the loop noise is still 25 dB lower than the whip noise, excepting the interference “spikes” and the broad region between 10:00 and 11:00 PST. Comparison with the preceding raw power plots also shows that the signal received by the whip is essentially lost once the ground wave is blocked—there is negligible shift in power levels between the “on” time in the frame bundle in comparison to the dead time.

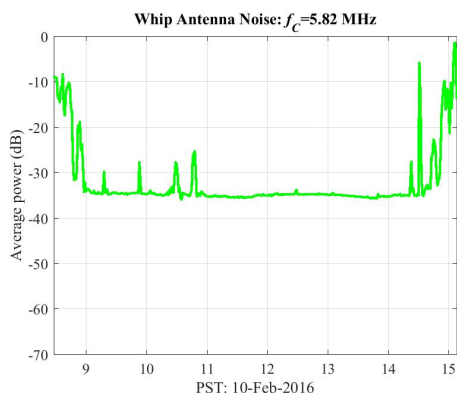


Figure 78. Raw whip noise.

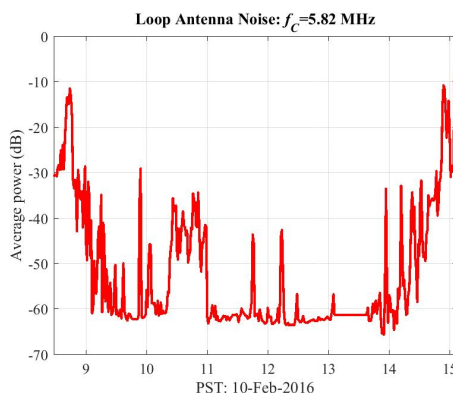


Figure 79. Raw loop noise.

A complicating factor between the difference in unwanted received power between whip and loop antennas is the presence of interfering signals. The next section examines possible sources of these interfering signals: cell towers are associated with the “spikes” and the city of El Centro, CA lines up with

the broad swath between 10:00 and 11:00 PST. One solution for mitigating cell tower effects is to move the receiver a few hundred feet. However, the swath of urban interference is persistent as the vehicle travels through El Centro, CA. This RF interference opens a design objective for placing an HF-NVIS antenna on a platform: these platform-mounted antennas should adapt to their platform by maximizing a null at the horizon over all azimuth angles.

### 6.3 INTERFERENCE ALONG THE ROUTE

Figure 80 reports on possible sources of the spikes observed in the HF-NVIS channel. The assumption is that the loop antenna has an upward pointing pattern. Therefore, overhead sources such as high-voltage power lines passing over the freeway and cell towers immediately adjacent to the freeway couple into this antenna.

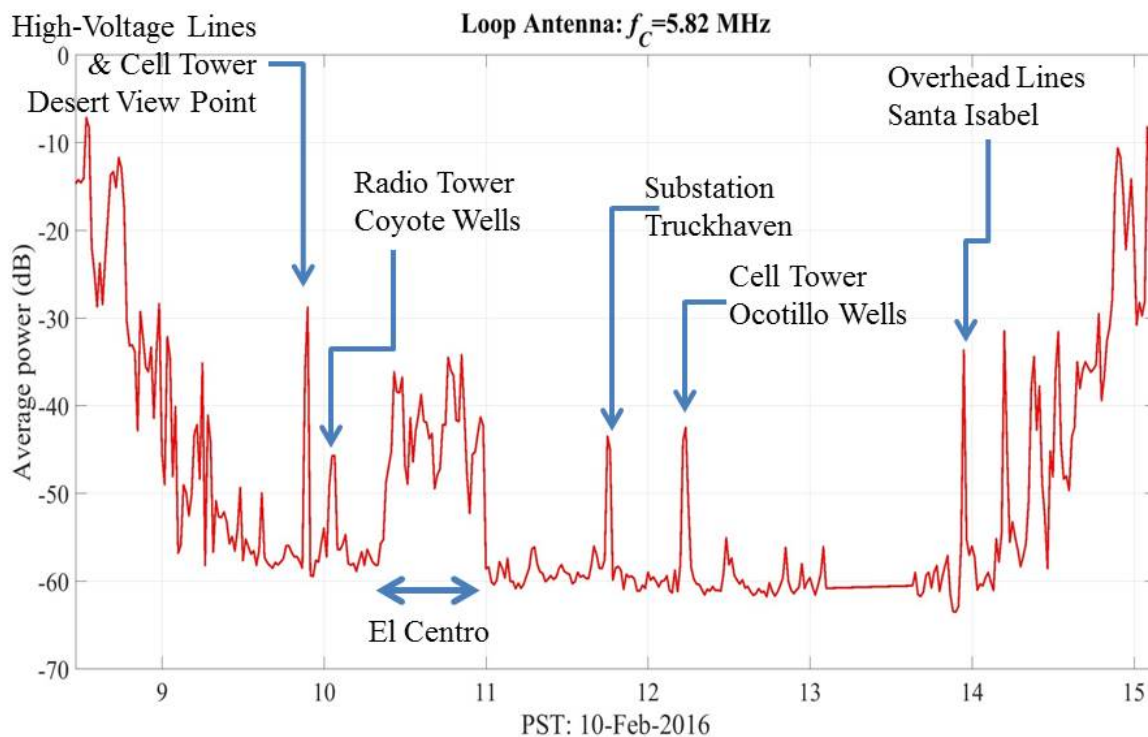


Figure 80. Average power received by the whip antenna.

5

Identifying the source of all spikes is problematic. For example, Figures 81 and 82 locate a cell tower near Desert View point and high-voltage lines parallel to the highway. However, two of these cell towers are in relatively isolated areas. Figures 83 and 84 locate an isolated radio tower at 10:03 PST. Figures 85 and 86 locate isolated radio tower at 12:14 PST. The isolation of these towers makes associating the spikes with these sources more plausible than the cell tower near high-voltage lines.



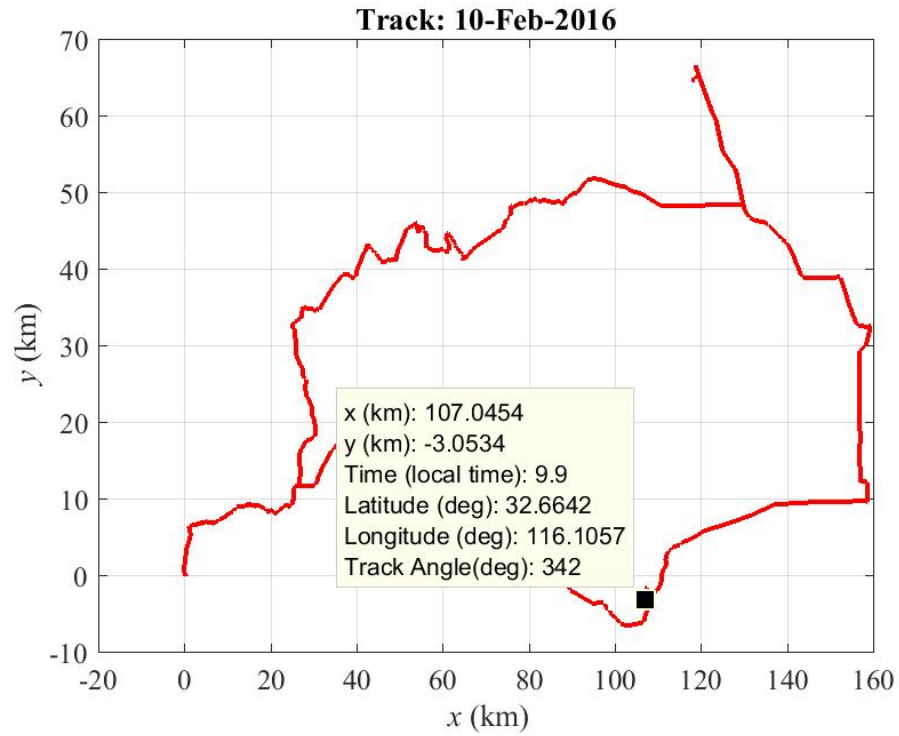


Figure 81. Location near Desert View Point at 09:54 PST.



Figure 82. Radio tower near Desert View Point at 09:54 PST.

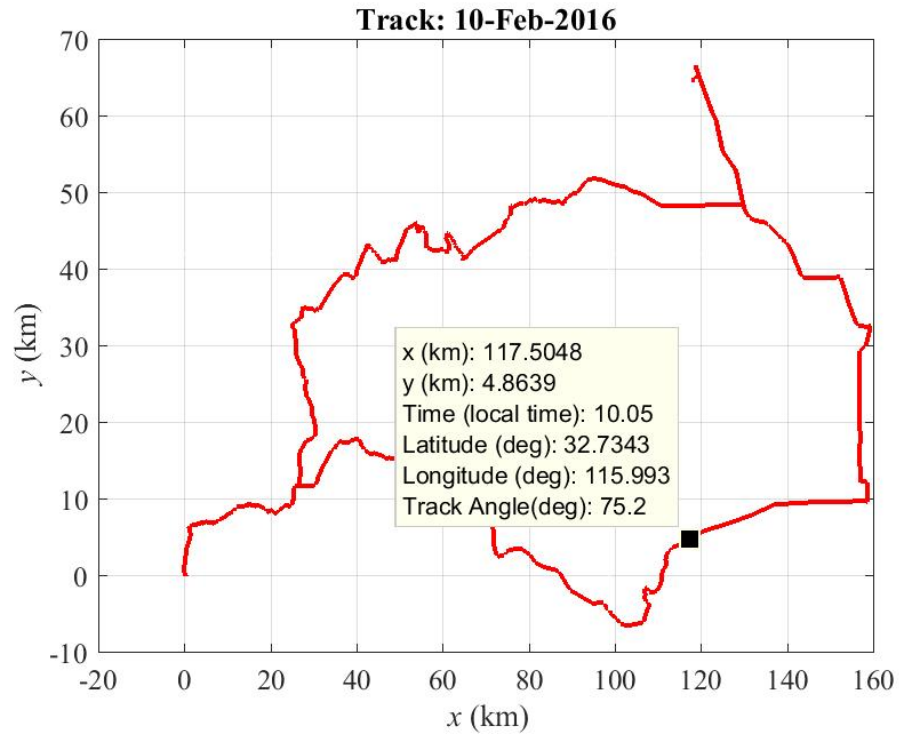


Figure 83. Location after passing Ocotillo at 10:03 PST but prior to Coyote Wells.



Figure 84. Radio tower after passing Ocotillo at 10:03 PST but prior to Coyote Wells.

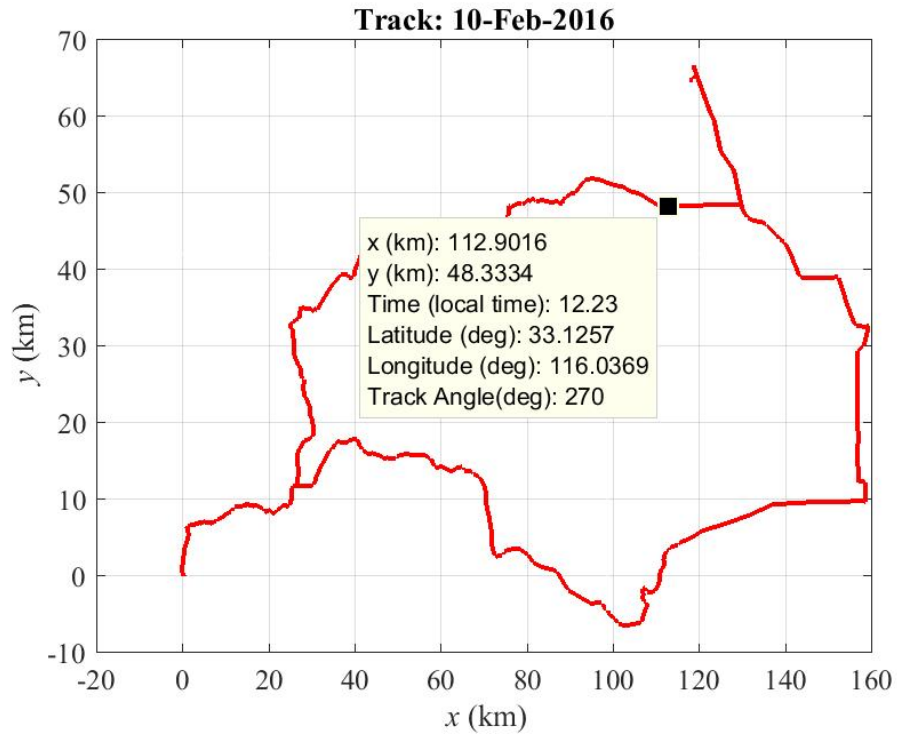


Figure 85. Location at 12:14 PST heading toward Ocotillo Wells.



Figure 86. Cell tower enroute at 12:14 PST approaching Ocotillo Wells.



## 7. HF-NVIS CHANNEL ESTIMATES ALONG THE MOBILE ROUTE

Figure 87 displays all the HF-NVIS channel soundings by plotting the magnitude of the delay-spread function  $h(t, \tau)$  described in Section 4.1. Each vertical slice at time  $t$  is an estimate of the impulse response of the channel with delay  $\tau$  measured in milliseconds. The vertical striations are the interference sources reported in Section 6.3. The strong responses at the beginning and end of the day are caused by the mobile vehicle departing and arriving back at the transmitter's site. The dB scale was selected to display the HF-NVIS channels for most of the day.

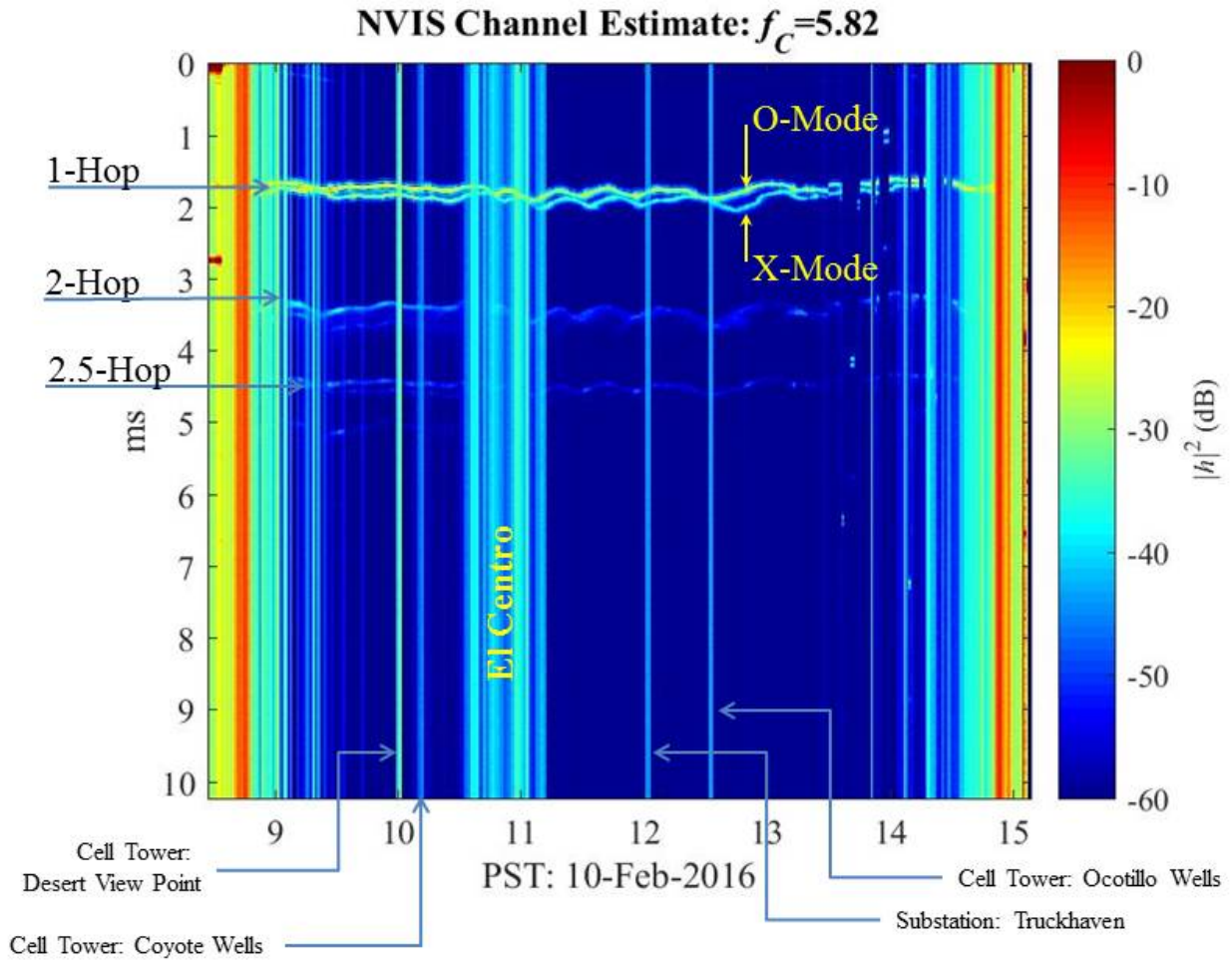


Figure 87. HF-NVIS channel estimate extracted from the loop antenna over the entire experiment. The ground wave and the 3-Hop response are not labeled.

On this day and at this frequency, this mobile wideband HF-NVIS channel is well-modeled by Equation (16) and repeated here for convenience:

$$h(t, \tau) = h_o(t, \tau) + h_x(t, \tau),$$

where the channel functions for the O- and X-Modes admit the approximations

$$\begin{aligned} h_O(t, \tau) &\approx a_{F,O}(t)\delta(\tau - \tau_{F,O}) + a_{F,OX}(t)\delta(\tau - \tau_{F,OX}) \\ h_X(t, \tau) &\approx a_{F,X}(t)\delta(\tau - \tau_{F,X}) + a_{F,XO}(t)\delta(\tau - \tau_{F,XO}). \end{aligned}$$

The ground wave, the 2.5-Hop, and the 3-Hop channels are not included in this model. The 2.5-Hop is tentatively identified similar to the “FesF” ray paths of Figure 37 produced by the sporadic E-layer (See [17, Figure 6.27(f)]). From the perspective of HF radio testing, this 2-Hop model captures the dominant 1-Hop ray paths and models self-interference with the 2-Hop ray paths. However, the 1-Hop approximation is still a credible model for HF radio testing because most of the 2-Hop ray paths arrive with 10 dB or more attenuation relative to the 1-Hops:

$$h(t, \tau) = a_{F,O}(t)\delta(\tau - \tau_{F,O}) + a_{F,X}(t)\delta(\tau - \tau_{F,X}). \quad (20)$$

Figure 87 shows that both the 1-Hop ray paths dominate across most of the day. The O-Mode arrives first with typically greater power. The arrival of the modes is slightly bowed in the middle of the plot corresponding to the distance of the mobile from the transmitters. The arrival time of both modes also modulated starting an 11:00 PST and lasting to 13:00 PST. The current conjecture is that this modulation is a TID in the f2 layer.

This section examines the channel at selected times along the route. Each channel assessed against the ionogram and the synthetic channel model predicted by the 3-D ray-tracing code. The fading processes, the delay spread, the Doppler shifts, and the Doppler spreads are discussed relative to each channel. This section concludes by gathering the preceding observations to model the 1-Hop model of Equation (20) in a form suitable to program a channel emulator.

## 7.1 HF-NVIS CHANNEL AT 09:07 PST

Figure 88 locates the mobile receiver approximately 40 km north-east of the transmitter as it enters the foothills of the Cuyamaca Mountains near Flynn Springs, CA. This is shown on the map in Figure 89. There appears to be little interference from cell towers or other sites along the route. The vehicle is pointed at  $83.5^\circ$  and traveling 60–80 mph.

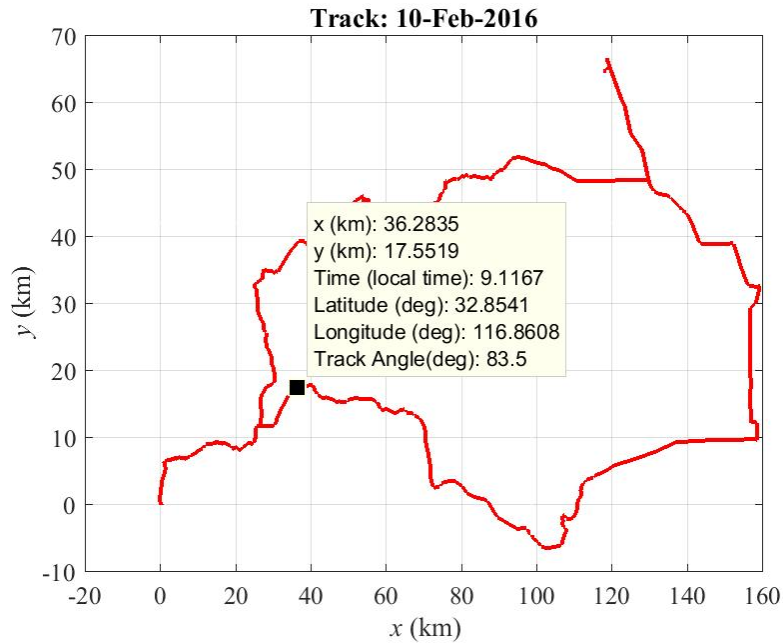


Figure 88. Receiver location along the track at 09:07 PST.

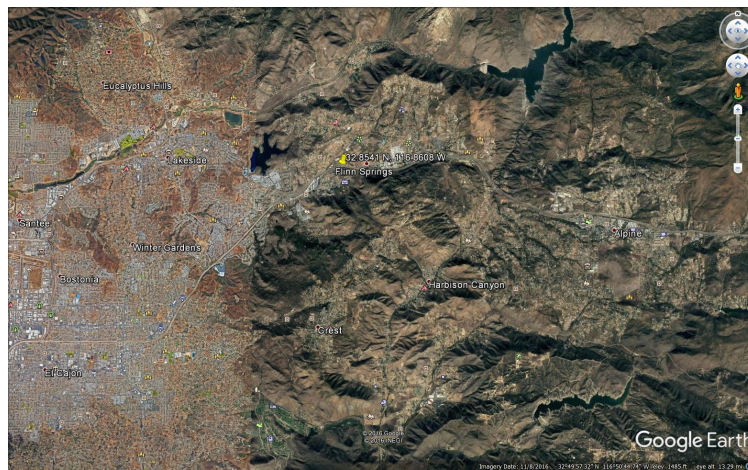


Figure 89. Receiver location marked by yellow “thumbtack” at 09:07 PST.

Figure 90 shows the magnitude of estimated channel averaged over the sounding. The channel contains multiple ray paths: the ground wave, the 1-Hop, 2-Hop, 2.5-Hop, 3-Hop, and 4-Hop. Each hop, excepting the ground wave, contains the O- and X-Mode ray paths.

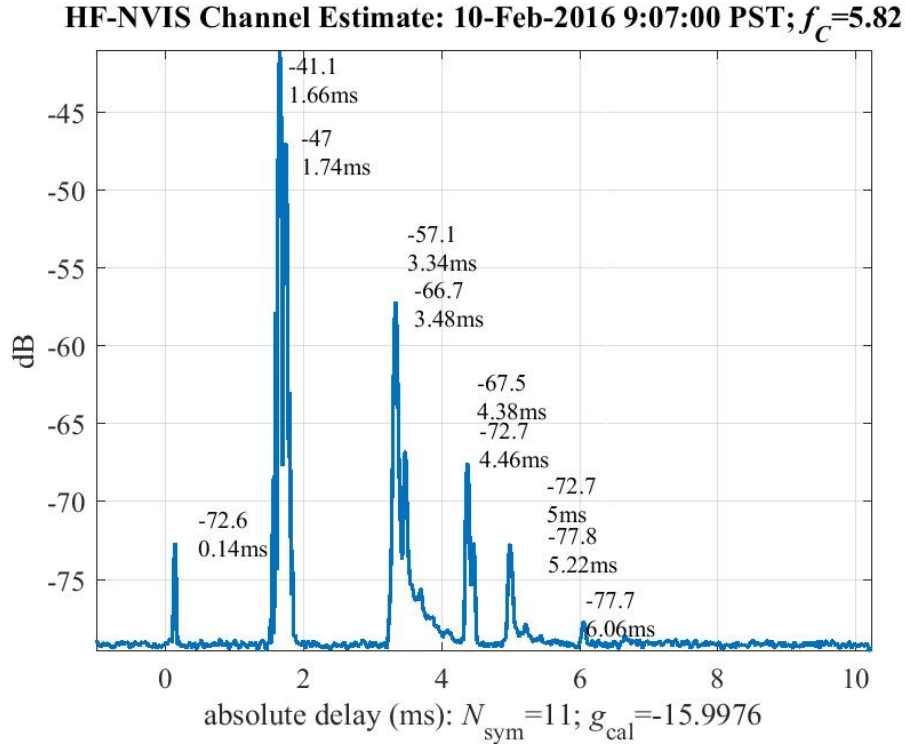


Figure 90. Channel estimate at 09:07 PST.

The distance between the transmitter and receiver is approximately

$$d_G \approx 40.1223 \text{ [km]}$$

and sets the delay in the ground wave as

$$t_G = \frac{d_G}{c_0} \approx 0.1337 \text{ [ms]}.$$

The accuracy of this ground wave delay is one verification that the system delays are correctly calibrated in Section 5.4. The discussion now focuses on these measured hop times and the hop times computed by the 3-D ray-tracing code.

Figure 91 shows the nearest ionogram measured at Point Arguello, CA, at 09:15 PST. The ionogram shows four vertical bounces where the O-Mode arrives before the X-Mode. The black curve on this ionogram is the estimated plasma frequency that determines the electron density; see Equation (7). The ray-tracing code uses the hybrid ionogram obtained by spatially averaging the ionograms at Point Arguello, CA, Boulder, CO, and Austin, TX. Figure 92 shows this hybrid plasma frequency profile used in the 3-D ray-tracing code.

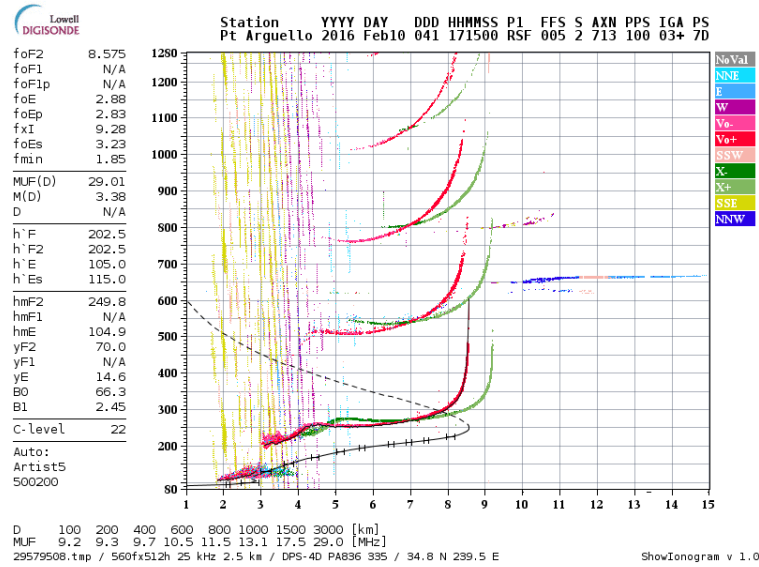


Figure 91. Ionogram at 09:15 PST. Open source ionograms courtesy of the Global Ionospheric Radio Observatory at the University of Massachusetts, Lowell [64].

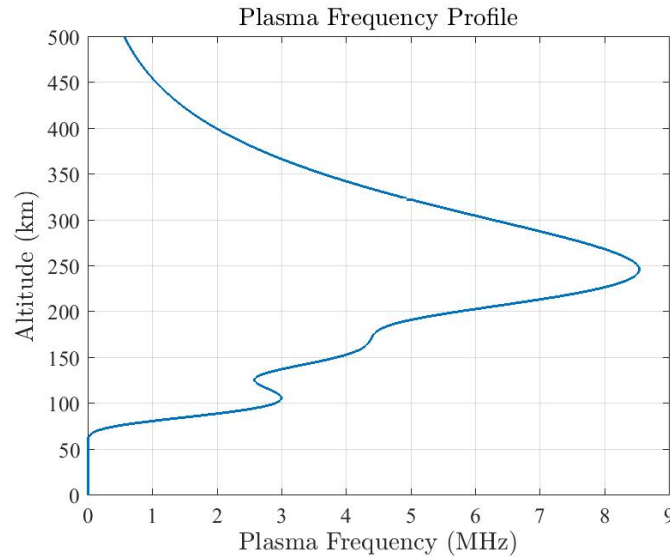


Figure 92. Estimated plasma frequency profile at 09:07 PST.

Figures 93 and 94 show the 1-Hop O- and X-Modes traveling northeast from the transmitter to the mobile receiver. The Earth's magnetic field bends the O-Mode north and the X-Mode south. Figures 95 and 96 show the polarization along these paths. The O-Mode path starts with LCP and ends with RCP

passing through vertical polarization. The X-Mode path starts with RCP and ends with LCP passing through horizontal polarization. This polarization switching and the ground reflection determine that the 2-Hop ray paths having the OO- and XX-Mode structure discussed in Example 8.

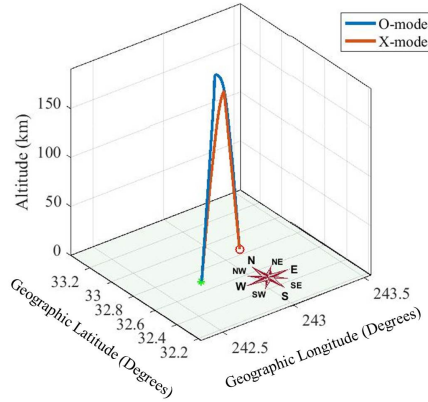


Figure 93. 1-Hops at 09:07 PST.

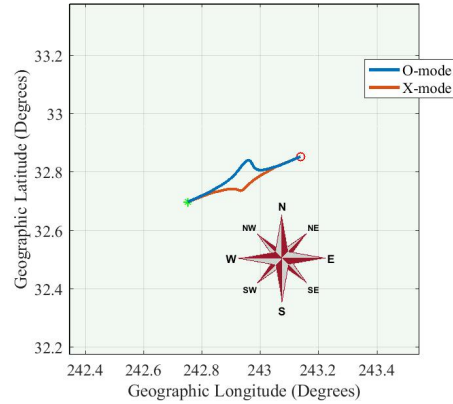


Figure 94. 1-Hops at 09:07 PST (top view).

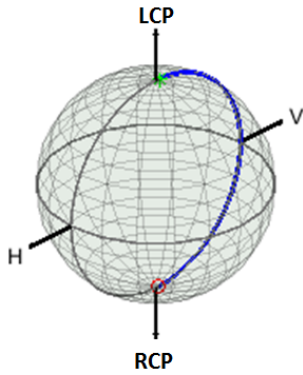


Figure 95. Polarization along the 1-Hop O-Mode ray path at 09:07 PST.

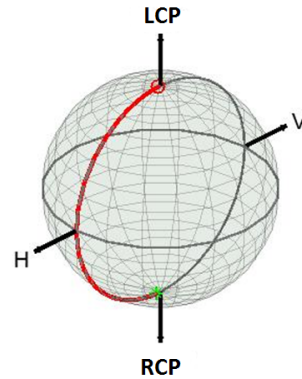


Figure 96. Polarization along the 1-Hop X-Mode ray path at 09:07 PST.

Table 11 compares the hop times between this sounding, the ray paths computed by the 3-D ray-tracing code, and estimates obtained from the ionogram. The table reports that the hop times produced by the ray-tracing code have a consistent positive bias of 0.1 ms. The bottom layer of the plasma frequency profile is critical for computing accurate ray paths—raising the layer causes hop times to increase because of the longer path in the ionosphere. Comparison between the measured and simulated plasma profile shows the simulated profile starts at a slightly lower altitude. Although tweaking the ionogram layers can force the simulated hop times to line up with the measured hop times, this “fitting the model” after the experiment is not an approach that supports HF mission planning. Rather, improved ionogram modeling boosts performance of *any* ray-tracing codes.



Table 11. Comparing hop times between the sounding, simulation, and the nearest ionogram (Point Arguello, CA) at 09:07 PST.

09:07 PST	Measured	Simulation	Ionogram
1-Hop O-Mode	1.66 ms	1.71 ms	1.67 ms
1-Hop X-Mode	1.74 ms	1.86 ms	1.85 ms
2-Hop O-Mode	3.34 ms	3.42 ms	3.34 ms
2-Hop X-Mode	3.48 ms	3.70 ms	3.36 ms
2.5-Hop O-Mode (?)	4.38 ms	—	—
2.5-Hop X-Mode (?)	4.46 ms	—	—
3-Hop O-Mode	5.00 ms	5.12 ms	5.07 ms
3-Hop X-Mode	5.22 ms	5.54 ms	—
4-Hop O-Mode	6.06 ms	6.84 ms	6.80 ms

This section closes with an analysis of the Doppler shifts, the Doppler spreading, and the fading. Figure 97 shows an estimate of the delay-spread function  $h(t, \tau)$  of Equation (12) where “ $t$ ” is determined by the timing of the PN sequences. Averaging the magnitude of this delay-spread function produces the estimated HF-NVIS channel estimate of Figure 90.

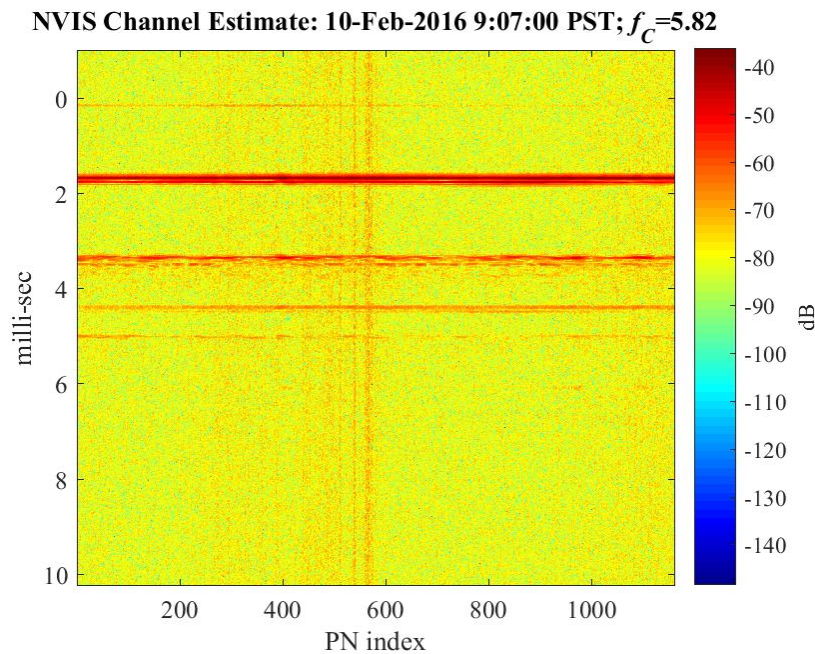


Figure 97. Delay spread estimate at 09:07 PST.

The closely spaced O- and X-Mode channels show slow modulations with the noise floor switching to lower level midway through the sounding. The ground wave is just visible at 0.14 ms. The 1-Hop ray paths are the strongest just before 2 ms. The 2-Hop at 3.4 ms show the strongest modulation. The 3-Hop are at 5 ms while the unidentified 2.5-Hop are between the 2- and 3-Hop.

Figure 98 shows an estimate of the scattering function described in Equation (13). This estimate is computed by taking the discrete Fourier transform of the delay-spread function  $h(t, \tau)$  over the time variable  $t$  where uniform time samples are obtained by resampling over the PN bursts to handle the “dead” time shown in Figure 65. The expectation operator in Equation (13) is approximated by Wiener filtering. This estimate of the scattering function shows the delay and Doppler of the 1-, 2-, 2.5-, 3-, and 4-Hop. This estimate even registers the ground wave and shows the ground wave with Doppler shift  $f_{D,GRND} = -0.5833$  Hz producing a credible vehicle speed of [87, Eq. 4.9]

$$v = \lambda_C f_{D,GRND} = -67 \text{ [mph]},$$

where the minus sign has the vehicle moving away from the transmitter.

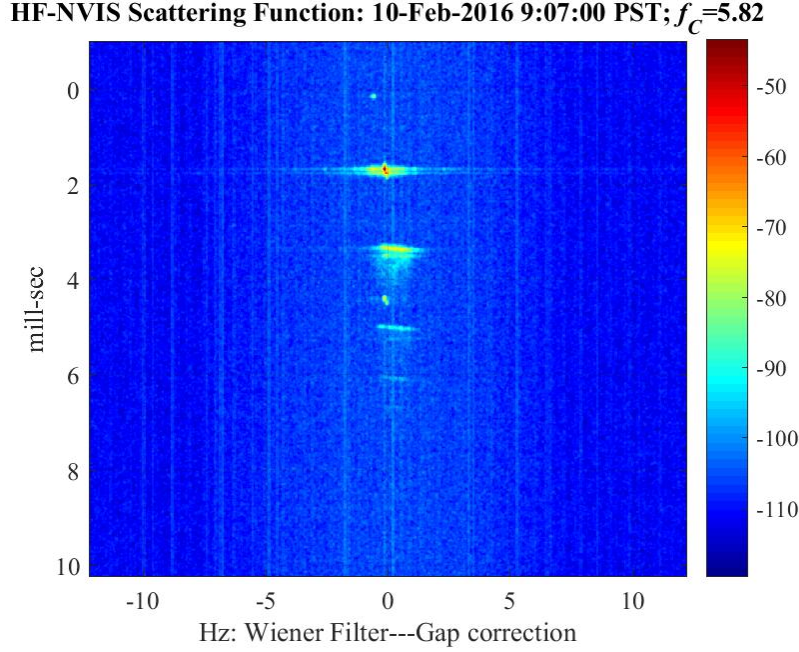


Figure 98. Scattering function estimated at 09:07 PST.

The limitation of the scattering function estimate is that the relatively small Doppler shifts and Doppler spreads are not well-resolved. Therefore, examination of the individual ray paths is necessary to extract more reliable Doppler and fading estimates.

Figure 99 displays the amplitude and phase of the 1-Hop O-Mode channel obtained from the delay-spread function at the O-Mode delay:

$$h_O(t) = |h_O(t)| \angle h_O(t) = h(t, \tau_O).$$

The amplitude in the upper panel shows slow and fast fading. The Rayleigh fading  $f_{N,O} \approx 0.159$  Hz measured around the median line is a one-parameter compromise to this non-stationary fading. However, the lower panel shows the unwrapped phase and an excellent fit of the quadratic phase model

$$\angle h_O(t) \approx \phi_O(t) := \phi_0 + \phi_1 t + \phi_2 t^2. \quad (21)$$

The linear term estimates the Doppler shift reported on this plot:

$$f_O = \frac{1}{2\pi} \left. \frac{d\phi_O}{dt}(t) \right|_{t=0}.$$



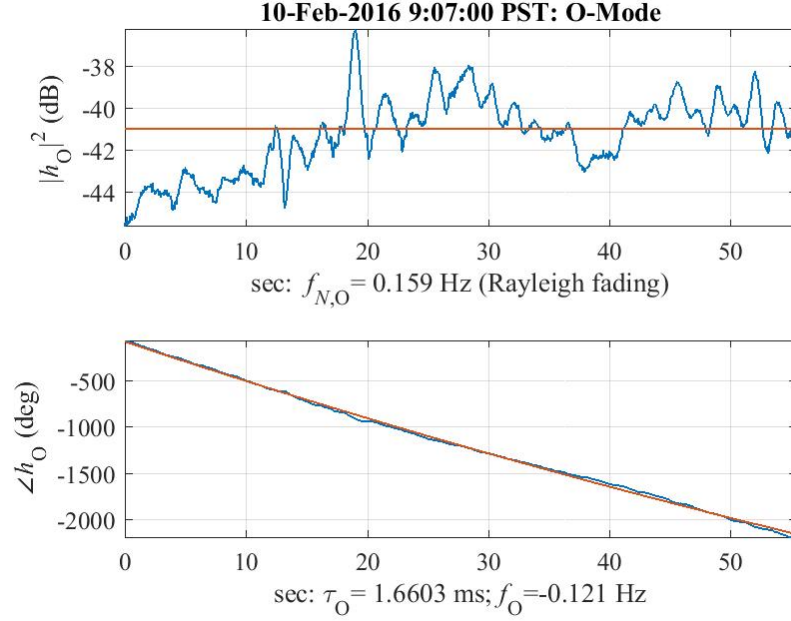


Figure 99. 1-Hop O-Mode amplitude and phase at 09:07 PST.

Figure 100 reports the same computations for the 1-Hop X-Mode channel's amplitude and phase:

$$h_X(t) = |h_X(t)|\angle h_X(t) = h(t, \tau_X).$$

The amplitude in the upper panel shows fast and slow fading with a relatively stationary region between 10 and 30 seconds. The Rayleigh fading  $f_{N,O} \approx 0.33$  Hz is a forced “fit” to this envelope as measured by the median line. The lower panel shows the phase and the excellent fit of a quadratic phase model:

$$\angle h_X(t) \approx \phi_X(t) := \phi_0 + \phi_1 t + \phi_2 t^2 \quad (22)$$

The Doppler shift reported on this panel is determined from the linear term:

$$f_X = \frac{1}{2\pi} \left. \frac{d\phi_X(t)}{dt} \right|_{t=0}.$$

Table 12 compares the Doppler shifts extracted from the O- and X-Mode over-the-air measurements with estimates obtained from the vehicle speed extracted from the scattering function and simulated elevation angles computed by the 3-D ray-tracing code. At best, the comparison shows that all the Doppler shifts are small.

Table 12. Comparing measured and estimated Doppler shifts in Hz based on the estimated mobile speed  $v = -67$  mph.

09:07 PST	Measured Doppler shift	Estimated Doppler shift	Simulated elevation
1-Hop O-Mode	-0.12 Hz	-0.10 Hz	85.7670°
1-Hop X-Mode	-0.04 Hz	-0.11 Hz	85.0298°

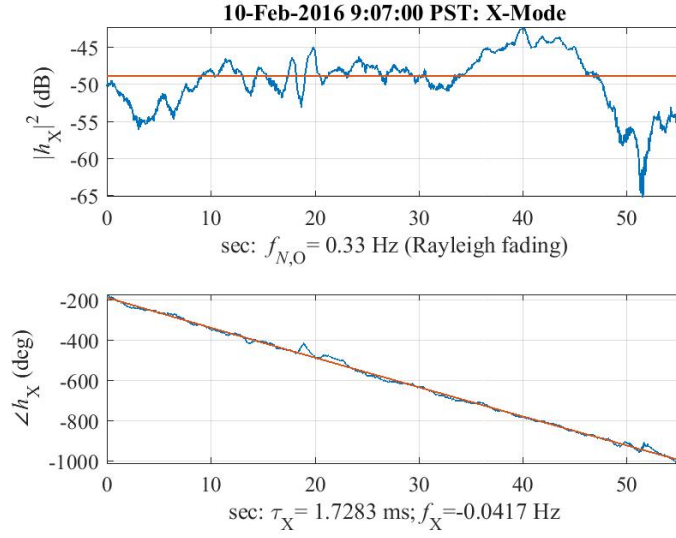


Figure 100. 1-Hop X-Mode amplitude and phase at 09:07 PST.

Doppler structure is revealed by the time-varying transfer function repeated here for convenience:

$$T(t, f) := \int_{-\infty}^{\infty} e^{-j2\pi f\tau} h(t, \tau) d\tau.$$

Figure 101 shows the magnitude of the time-varying transfer function for this channel. The channel's frequency response as a function of time is a “spectrogram.”

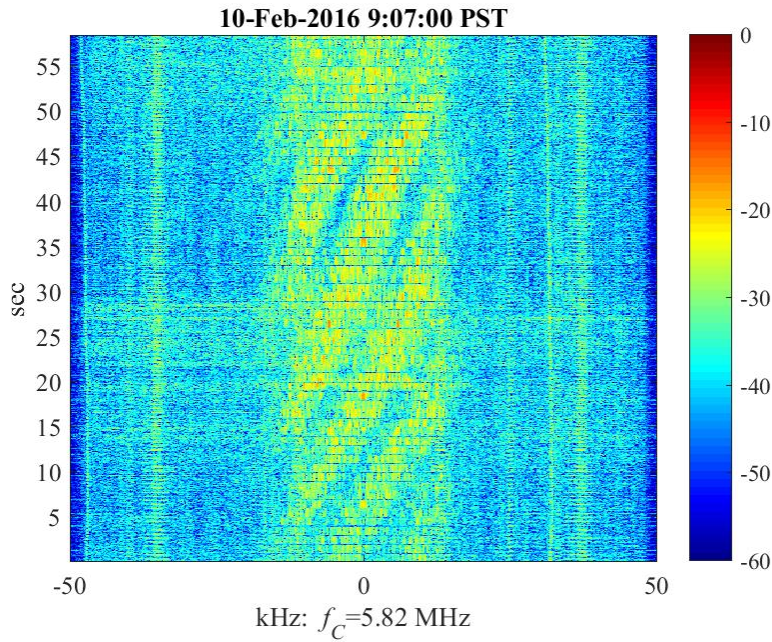


Figure 101. Spectrogram at 09:07 PST.

Nulls caused by different Doppler shifts on the 1-Hop O- and X-Modes appear to wrap over the 25-kHz band. Appendix C shows how the 1-Hop linear phase model

$$h(t, \tau) = h_O e^{+j2\pi f_O t} \delta(t - \tau_O) + h_X e^{+j2\pi f_X t} \delta(t - \tau_X)$$

produces the time-varying transfer function

$$T(t, f) = h_O e^{+j2\pi f_O t} e^{-j2\pi f \tau_O} + h_X e^{+j2\pi f_X t} e^{-j2\pi f \tau_X}$$

with constant phase along straight lines in the time-frequency plane. However, the wrapping in Figure 101 is better modeled by the quadratic phase model of Equations (21) and (22). The corresponding time-varying transfer function

$$T(t, f) = h_O e^{+j\phi_O(t)} e^{-j2\pi f \tau_O} + h_X e^{+j\phi_X(t)} e^{-j2\pi f \tau_X}$$

has constant phase along quadratic curves in the time-frequency plane. Figure 102 overlays the lines of constant quadratic phase on the spectrogram.

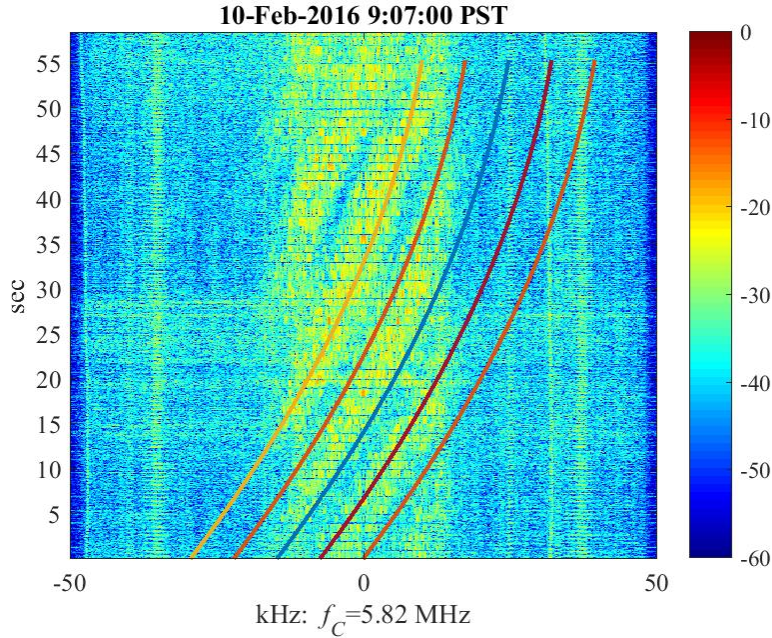


Figure 102. Spectrogram at 09:07 PST and the 1-Hop model with quadratic phase.

This relatively good fit of the quadratic phase model argues that the 1-Hop delay-spread function should have the form

$$h(t, \tau) = h_O e^{+j\phi_O(t)} \delta(t - \tau_O) + h_X e^{+j\phi_X(t)} \delta(t - \tau_X).$$

Most channel emulators handle the linear phase term as a Doppler shift. The significance of this quadratic phase model for channel emulation is an open question.

Turning to the problem of identifying the fading processes, the best approach is based on the ray path physics. Rician fading is claimed to be a plausible fading model on the ray paths [17, Section 7.7.6]. However, fading identification is confounded by fast and slow fading [87, Section 4.10.2]. Figure 100 shows the X-Mode fading is relatively stationary over the first 30 seconds. Figure 99 shows the O-Mode fading has both fast and slow fading. Fading identification is restricted to the X-Mode over the first 30 seconds.

Figure 103 shows the “goodness-of-fit” ranking estimated over this window. Although Rician fading has a significance level over 80% for this particular estimate, these “goodness-of-fit” tests are extremely sensitive to the correlation between samples. This particular plot was produced using every 10th sample. Figure 104 fits selected distributions to the sample histogram of the X-Mode fading restricted to the first 30 seconds. Although no distribution shows a compelling fit, the physical basis for the Rician fading makes it a natural candidate for the fading process.

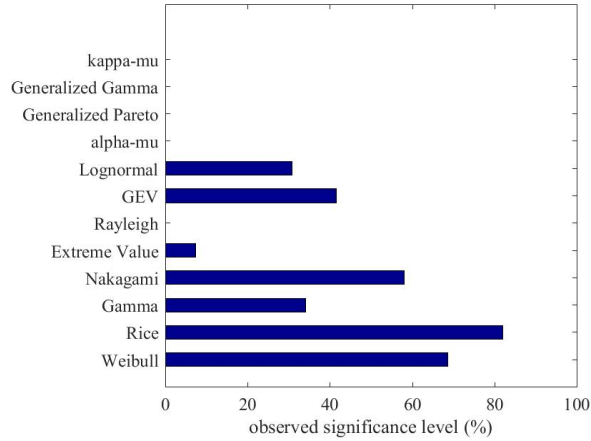


Figure 103. “Goodness-of-fit” for the 1-Hop X-Mode amplitude at 09:07 PST.

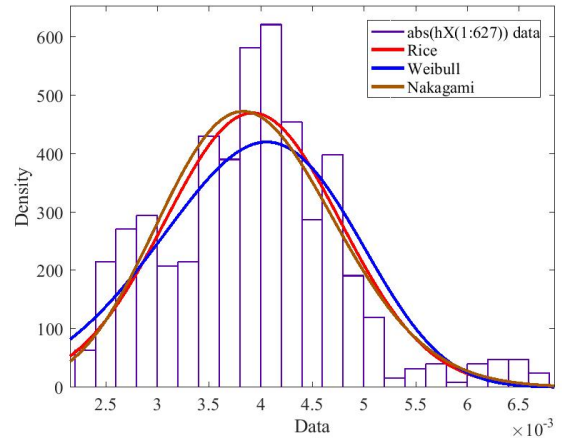


Figure 104. Fitting probability density functions to the 1-Hop X-Mode amplitude at 09:07 PST.

Table 13 encapsulates this channel in a form suitable for a channel emulator as discussed in Section 4.4. The model employs only the 1-Hop O- and X-Modes. The total path loss is scaled to the 1-Hop O-Mode and encompasses both the transmit and receive antenna, including the latter’s orientation and velocity on the mobile.

Table 13. Wideband HF-NVIS channel model; 5.82 MHz; 10 February 2016 09:07 PST.

09:07 PST	Path delay	Total path loss	Doppler shift	Fade rate	Rician $K$ factor
1-Hop O-Mode	1.66 ms	0 dB	−0.12 Hz	0.16 Hz	8.7 dB
1-Hop X-Mode	1.83 ms	−5.9 dB	−0.04 Hz	0.33 Hz	10.0 dB



## 7.2 HF-NVIS CHANNEL AT 09:41 PST

Figure 105 locates the mobile receiver approximately 90 km due east of the transmitter. Figure 106 shows the mobile receiver traveling through the rolling foothills near Boulevard, CA. There appears to be little interference from cell towers or other sites along the route. The vehicle is pointed at  $116.3^\circ$  and traveling 60–80 mph.

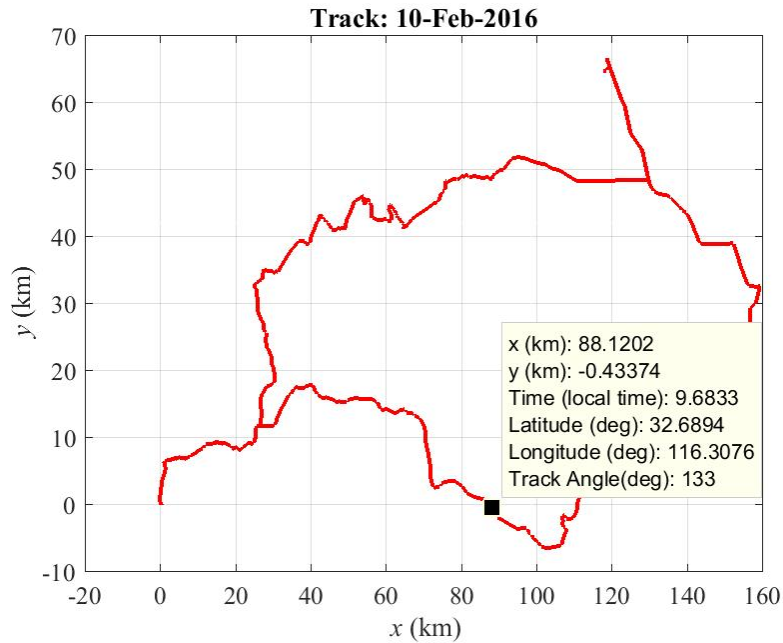


Figure 105. Receiver location on the track at 09:41 PST.

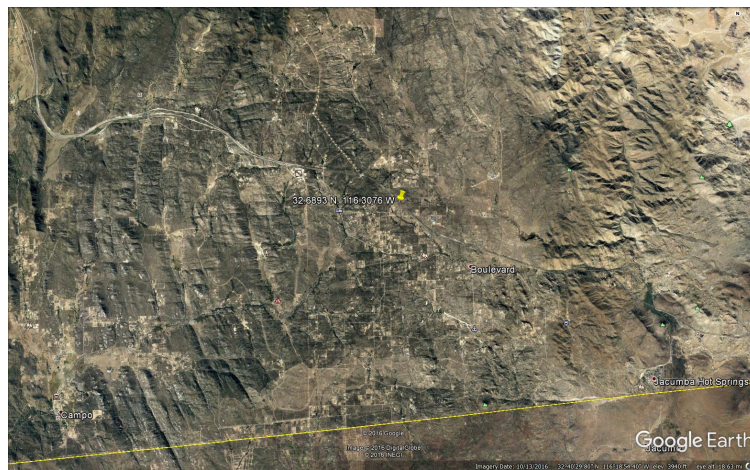


Figure 106. Receiver location marked with yellow "thumbtack" at 09:41 PST.

Figure 107 shows the estimated channel contains multiple ray paths. Table 14 compares the hop times between this sounding, the ray paths computed by the 3-D ray-tracing code, and estimates obtained from the nearest ionogram.

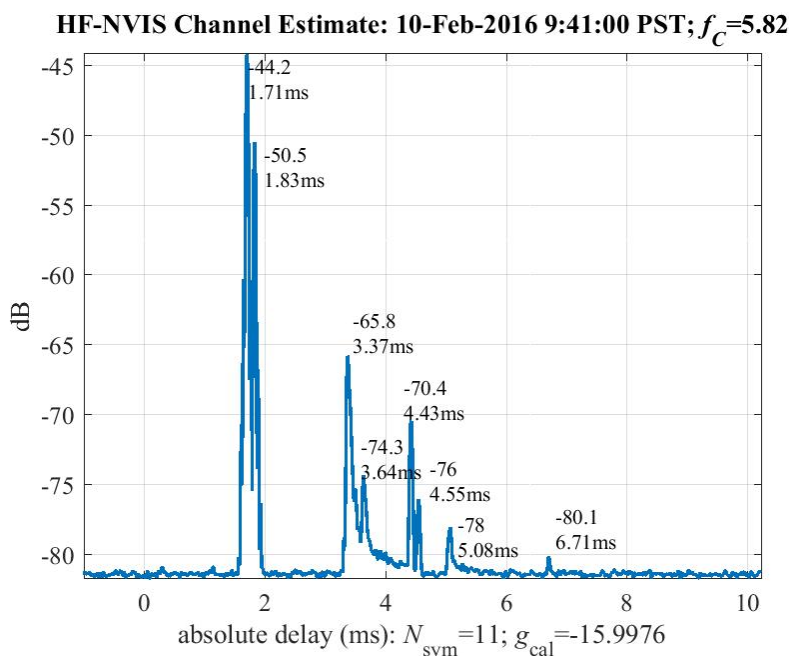


Figure 107. Channel estimate at 09:41 PST.

Table 14. Comparing hop times between the sounding, simulation, and ionogram at 09:41 PST.

09:41 PST	Measured	Simulation	Ionogram
1-Hop O-Mode	1.71 ms	1.69 ms	1.60 ms
1-Hop X-Mode	1.83 ms	1.85 ms	1.73 ms
2-Hop O-Mode	3.37 ms	3.34 ms	3.23 ms
2-Hop X-Mode	3.64 ms	3.65 ms	3.33 ms
2.5-Hop O-Mode (?)	4.43 ms	—	—
2.5-Hop X-Mode (?)	4.55 ms	—	—
3-Hop O-Mode	5.08 ms	5.00 ms	—
3-Hop X-Mode	—	—	—
4-Hop O-Mode	6.71 ms	6.66 ms	—

Figure 108 is the nearest ionogram. This ionogram shows the 1-Hop and 2-Hop paths arrive with the O-Mode followed by the X-Mode.

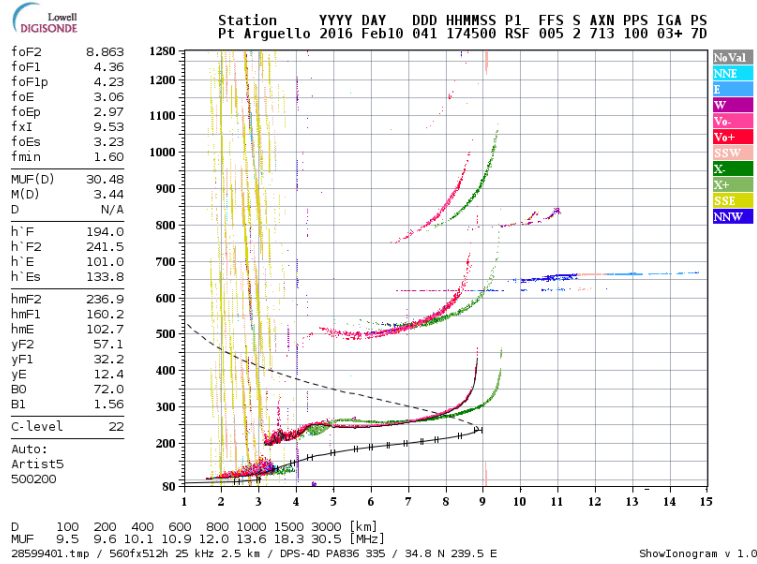


Figure 108. Point Arguello, CA ionogram at 09:45 PST. Open source ionograms courtesy of the Global Ionospheric Radio Observatory at the University of Massachusetts, Lowell [64].

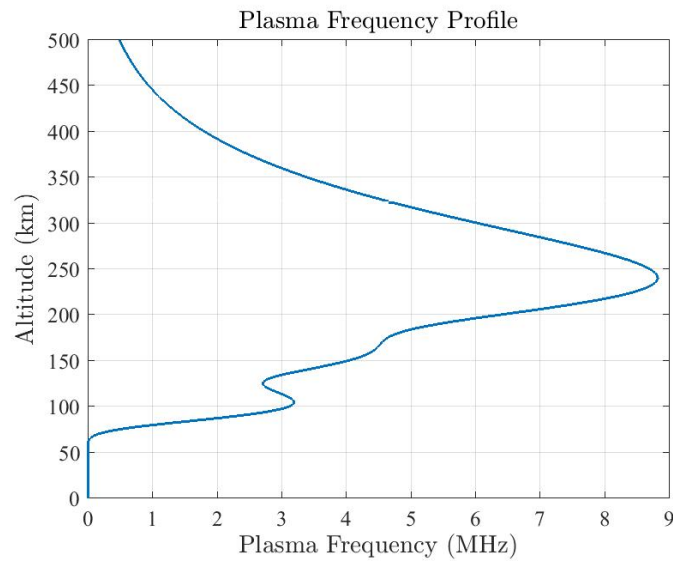


Figure 109. Estimated plasma frequency profile at 09:41 PST.

The ray-tracing code uses the hybrid ionogram obtained by spatially averaging the ionograms at Point Arguello, CA, Boulder, CO, and Austin, TX. Figure 109 shows the plasma frequency  $f_P(h)$  obtained from this hybrid ionogram. Figure 110 and 111 shows the simulated 1-Hop ray paths with the O-Mode bending north and the X-Mode bending south. Figures 112 and 113 show that the polarization switches on both ray paths.

This polarization switching and the reflection determine that the 2-Hop ray paths will be OO- and XX-Modes discussed in Example 8. Table 14 reports that the ray-tracing code produces very accurate hop times using these 1-, 2-, 3-, and 4-Hop models.

Figures 110 and 111 display the O- and X-Mode 1-Hops traveling from the transmitter to the mobile receiver due east. This orientation reveals the maximum bending caused by the Earth's magnetic field. Figures 112 and 113 show the polarization along these paths. The O-Mode path starts with LCP and ends with RCP passing through vertical polarization. The X-Mode path starts with RCP and ends with LCP passing through horizontal polarization. This polarization switching and the ground reflection determine that the 2-Hop ray paths reported in Table 14 are the OO- and XX-Modes discussed in Example 8.

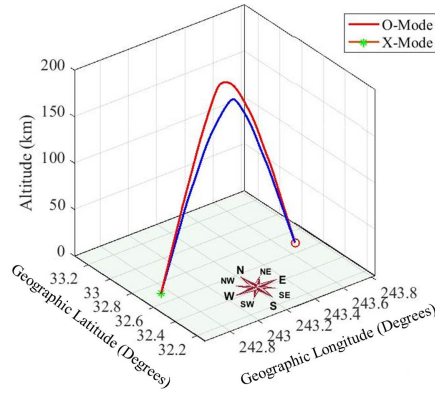


Figure 110. 1-Hops at 09:41 PST.

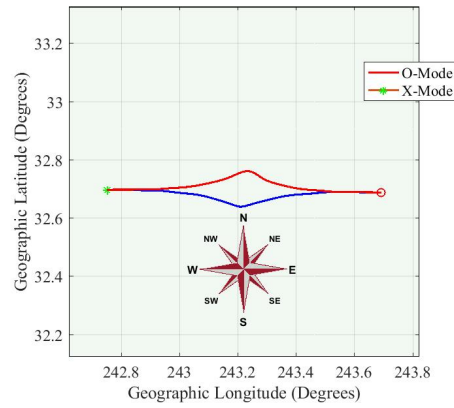


Figure 111. 1-Hops at 09:41 PST (top view).

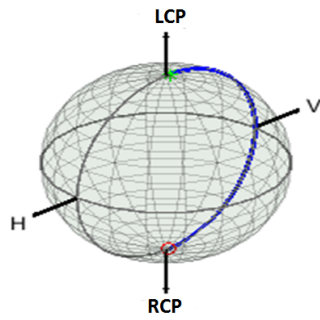


Figure 112. Polarization along the 1-Hop O-Mode ray path at 09:41 PST.

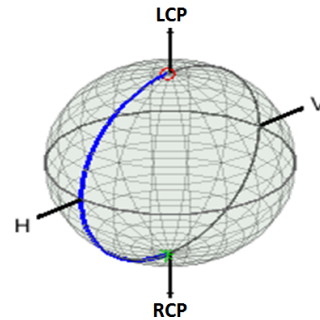


Figure 113. Polarization along the 1-Hop X-Mode ray path at 09:41 PST.



Figure 114 estimates the delay-spread function  $h(t, \tau)$  where “ $t$ ” is determined by the timing of the PN sequences. The closely spaced O- and X-Mode channels show slow modulations against a relatively flat noise floor. The 1-Hop ray paths are the strongest just before 2 ms. The 2-Hop at 3.4 ms show the strongest modulation. The 3-Hop are at 5 ms while the unidentified 2.5-Hop are between the 2- and 3-Hops.

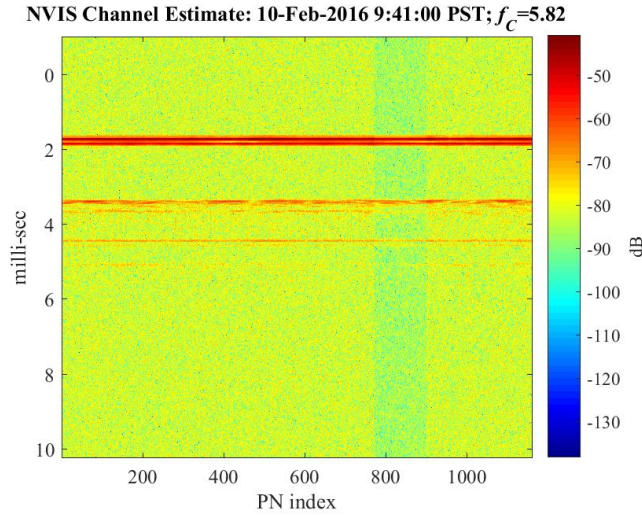


Figure 114. Delay spread estimate at 09:41 PST.

Figure 115 estimates the scattering function for this channel. This estimate is computed by taking the discrete Fourier transform of the delay-spread function  $h(t, \tau)$  over the time variable  $t$  without resampling over the PN bursts to handle the “dead” time shown in Figure 65. The expectation operator in Equation (13) is approximated by Wiener filtering. This estimate of the scattering function shows the delay and Doppler of the 1-, 2-, 2.5-, 3-, and 4-Hop. This estimate shows the increasing delays between the O- and X-Modes as the hops increase and the slight Doppler differences between the hops.

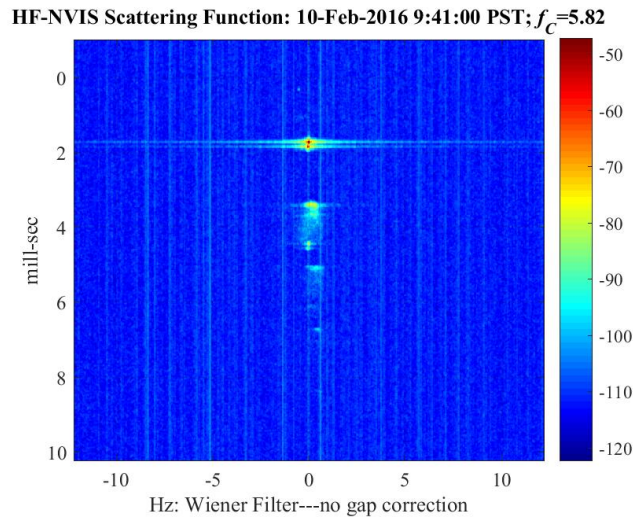


Figure 115. Scattering function estimated at 09:41 PST.

The limitation of the scattering function estimate is that the relatively small Doppler shifts and Doppler spreads are not well-resolved. Therefore, examination of the individual ray paths is necessary to extract more reliable Doppler and fading estimates.

Figure 116 displays the amplitude and phase of the 1-Hop O-Mode channel obtained from the delay-spread function at the O-Mode delay

$$h_O(t) = |h_O(t)|\angle h_O(t) = h(t, \tau_O).$$

The amplitude in the upper panel appears to show multiple fading processes. However, the mean level is -44 dB while the variation is only  $\pm 3$  dB. That is, the fading is approximately Rician. Consequently, the Rayleigh fading estimate  $f_{N,O} \approx 0.477$  Hz measured around the median line is a reasonable fit of a one-parameter model to this nearly Rician fading. The lower panel shows the phase and a quadratic fit

$$\angle h_O(t) \approx \phi_O(t) := \phi_0 + \phi_1 t + \phi_2 t^2$$

where the linear term estimates the Doppler shift as

$$f_O = \frac{1}{2\pi} \left. \frac{d\phi_O}{dt}(t) \right|_{t=0} \approx -0.247 \text{ [Hz]}.$$

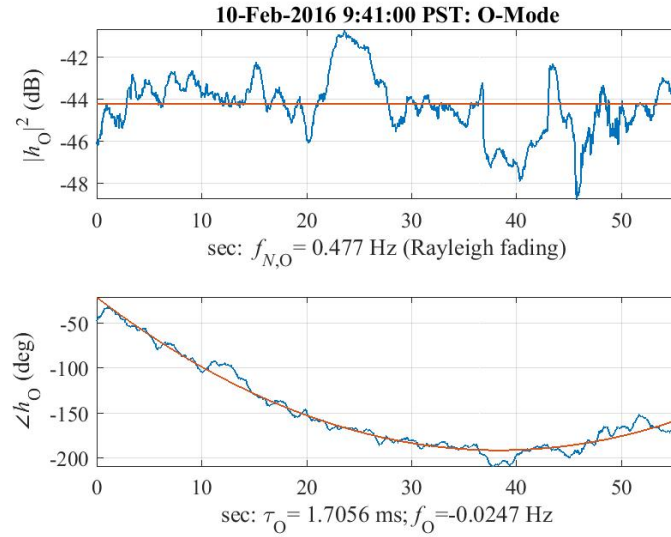


Figure 116. 1-Hop O-Mode amplitude and phase at 09:41 PST.

Figure 117 reports the same computations for the 1-Hop X-Mode channel. The amplitude in the upper panel shows relatively stationary fast fading so that the Rayleigh fading  $f_{N,X} \approx 0.416$  Hz is a reasonable estimate from this measurement.

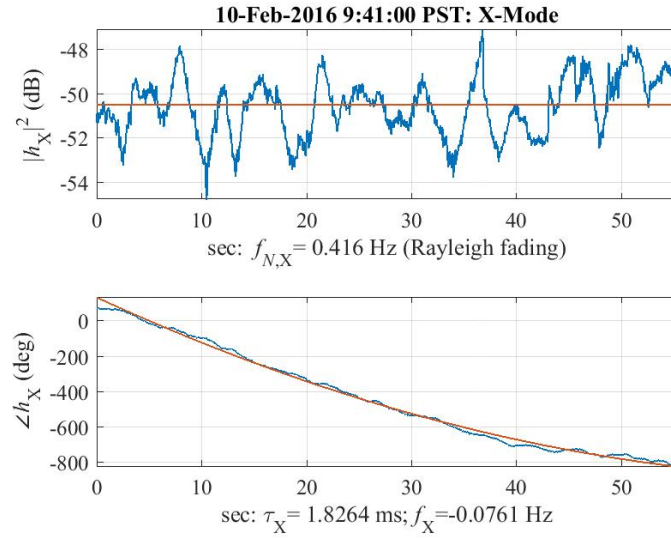


Figure 117. 1-Hop X-Mode amplitude and phase at 09:41 PST.

Figure 118 shows the spectrogram for this channel sounding and the quadratic phase lines. This spectrogram is the magnitude of the time-varying transfer function. Similar to the spectrogram at 09:07 PST, the estimated Doppler extracted from the O- and X-Modes provides an excellent fit to the nulls wrapping over the 25-kHz band. Consequently, these Doppler estimates, albeit small, are reported in the fading description. Table 15 encapsulates this channel in a form suitable for a channel emulator. The model employs only the 1-Hop O- and X-Modes. The total path loss is scaled to the 1-Hop O-Mode and encompasses both the transmit and receive antennas, including the latter's orientation and velocity on the mobile receiver.

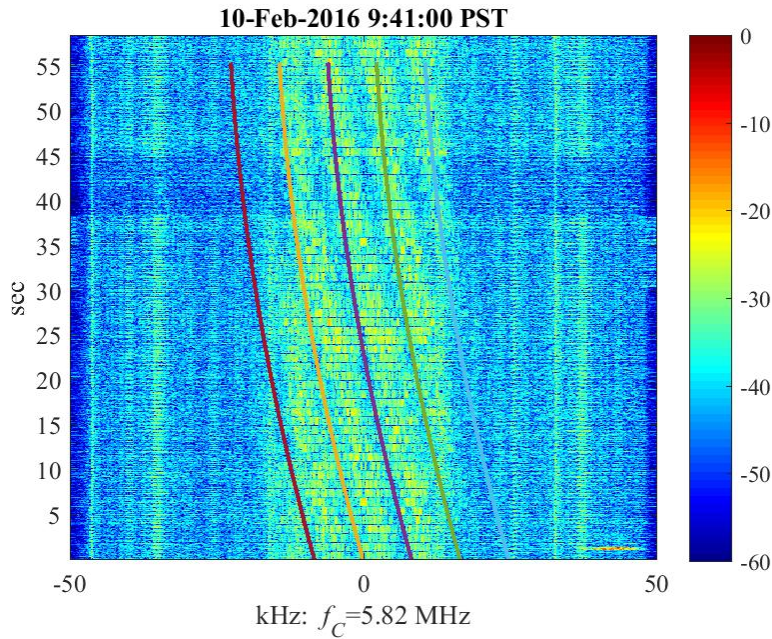


Figure 118. Spectrogram at 09:41 PST.

Table 15 encapsulates this channel in a form suitable for channel emulator. The model employs only the 1-Hop O- and X-Modes. The total path loss is scaled to the 1-Hop O-Mode and encompasses both the transmit and receive antenna, including the latter's orientation and velocity on the mobile.

Table 15. Wideband HF-NVIS channel model; 5.82 MHz; 10 February 2016 09:41 PST.

09:41 PST	Path delay	Total path loss	Doppler shift	Fade rate	Rician $K$ factor
1-Hop O-Mode	1.71 ms	0 dB	-0.02 Hz	0.48 Hz	12.6 dB
1-Hop X-Mode	1.83 ms	-6.3 dB	-0.08 Hz	0.41 Hz	13.4 dB

### 7.3 HF-NVIS CHANNEL AT 10:23 PST

Figure 119 locates the mobile at the southeastern part of the loop almost 160 km from the transmitter. The terrain is flat desert. There is no interference from cell towers or El Centro, CA. The vehicle is pointed at  $89.4^\circ$  or almost due east and traveling between 60 to 80 mph. Therefore, the maximum Doppler shift is 0.7 Hz. Figure 120 shows the estimated channel consists of two strong ray paths followed by some smaller ray paths. Figure 121 is the nearest ionogram showing the ray paths at 5.82 MHz arrive in O-Mode followed by X-Mode order. Table 16 compares the hop times between this sounding, the ray paths computed by the 3-D ray-tracing code, and estimates obtained from the ionogram. The ray-tracing code predicts O-Mode ray paths also arrive before their associated X-Mode ray paths. The ray-tracing code uses a hybrid ionogram obtained by spatially averaging the ionograms at Point Arguello, CA, Boulder, CO, and Austin, TX. The ray-tracing code produces accurate hop times for the O-Mode hops but overestimates the X-Mode hops time by appropriately 0.2 ms. The table also lists two paths observed between the 2-Hop and 3-Hop. These are tentatively identified “FESF” ray paths of Figure 37 that might be produced by a sporadic E-layer [17, Figure 6.27(f)].

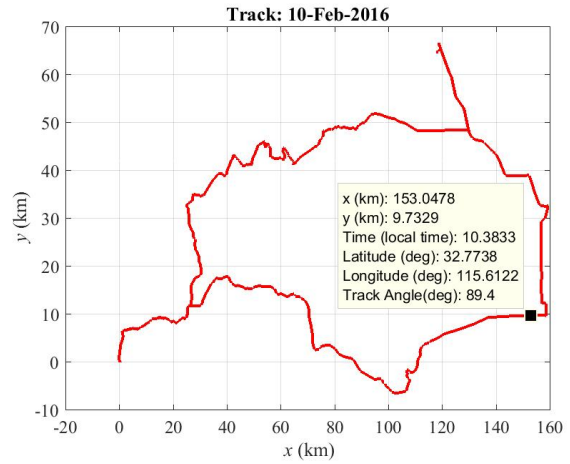


Figure 119. Receiver location on the track at 10:23 PST.

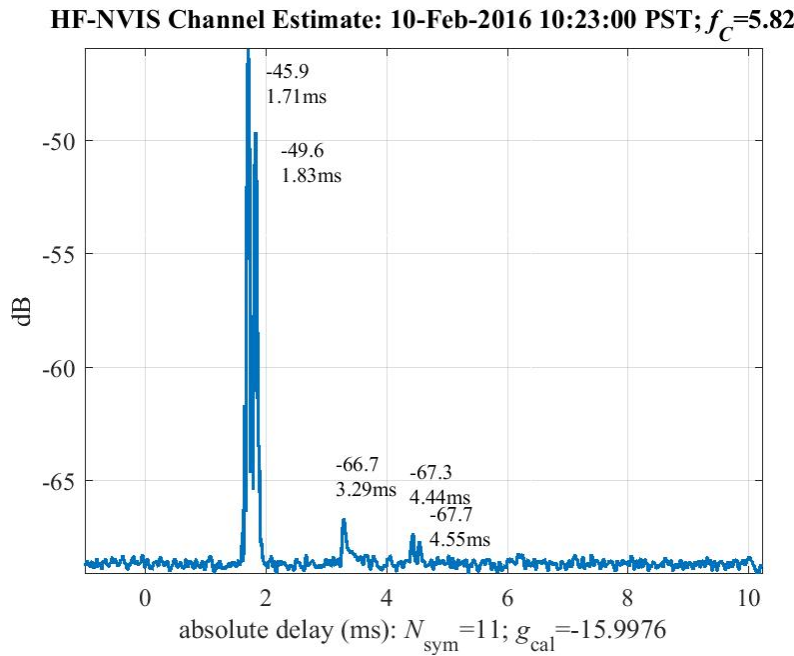


Figure 120. Channel estimate at 10:23 PST.

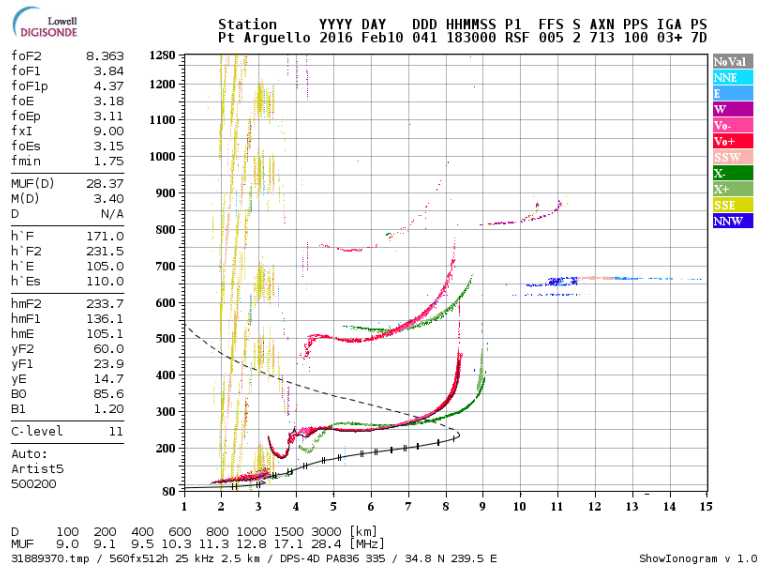


Figure 121. Point Arguello, CA ionogram at 10:30 PST. Open source ionograms courtesy of the Global Ionospheric Radio Observatory at the University of Massachusetts, Lowell [64].

Table 16. Comparing O- and X-Mode hop times between the sounding, simulation, and the nearest ionogram (Point Arguello, CA) at 10:23 PST.

10:23 PST	Measured	Simulation	Ionogram
1-Hop O-Mode	1.71 ms	1.73 ms	1.67 ms
1-Hop X-Mode	1.83 ms	1.91 ms	1.80 ms
2-Hop O-Mode	3.29 ms	3.33 ms	3.27 ms
2-Hop X-Mode	—	3.67 ms	3.53 ms
2.5-Hop O-Mode (?)	4.44 ms	—	4.30 ms
2.5-Hop X-Mode (?)	4.55 ms	—	4.60 ms
3-Hop O-Mode	—	4.96 ms	4.93 ms
3-Hop X-Mode	—	5.47 ms	—



Figure 122 shows the plasma frequency  $f_P(h)$  estimated by spatially averaging the nearest three ionograms. This estimated plasma frequency determines the electron density profile  $N_e(h)$  and the associated index of refraction used by the 3-D ray-tracing code to compute the ray paths. Comparison of this hybrid plasma frequency with the plasma frequency at Figure 121 shows that the gross shapes are similar. However, the profile's lower edge is critical for any ray-tracing coding. Comparison shows that the hybrid plasma frequency may start too low and introduce a bias for longer times in the ionosphere.

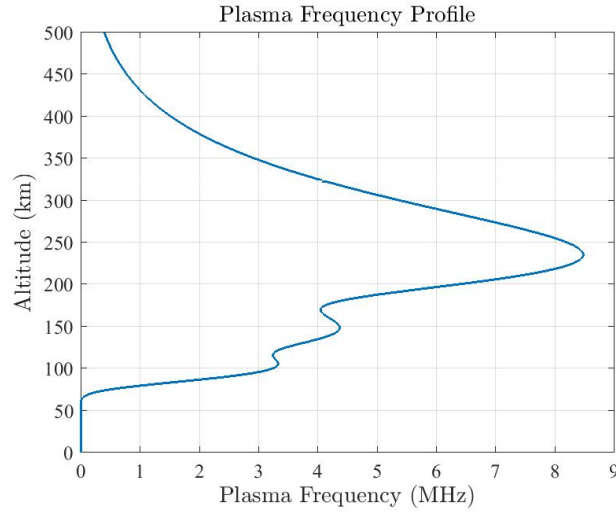


Figure 122. Plasma frequency at 10:23 PST estimated from the ionograms at Point Arguello, CA, Boulder, CO, and Austin, TX.

Figures 123 and 124 show the O- and X-Mode 1-Hop. The rays travel west to east so are approximately transverse to the Earth's magnetic field. The magnetic field bends the O-Mode to the north and the X-Mode to the south. Figures 125 and 126 report the polarization along these paths. The O-Mode path starts with LCP and ends with RCP while passing through vertical polarization. The X-Mode path starts with RCP and ends with LCP while passing through horizontal polarization. This polarization switching and the ground reflection determine that the 2-Hop ray paths reported in Table 16 are the OO- and XX-Modes discussed in Example 8.

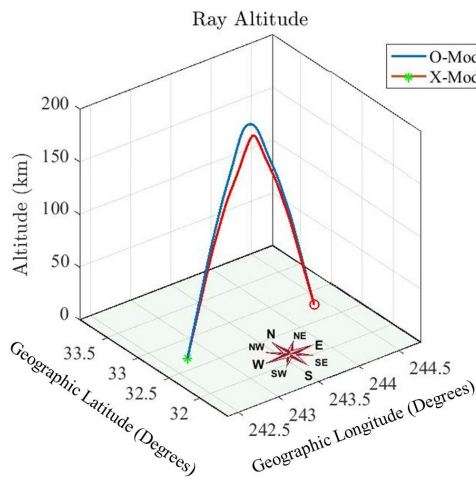


Figure 123. 1-Hops at 10:23 PST.

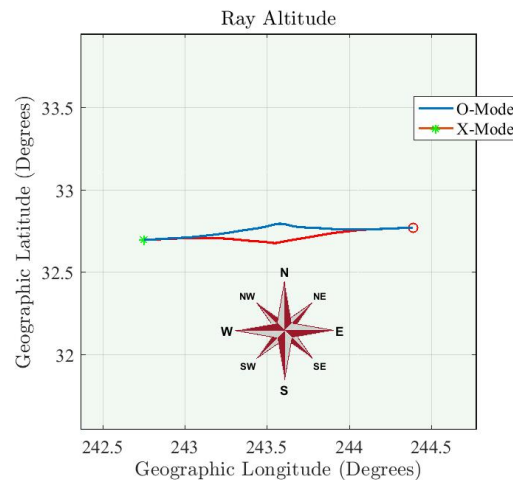


Figure 124. 1-Hops at 10:23 PST (top view).

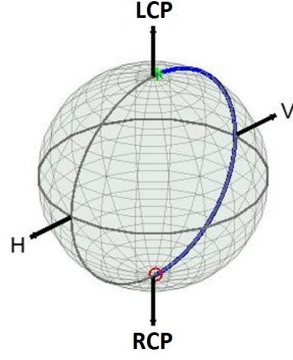


Figure 125. Polarization along the 1-Hop O-Mode ray path at 10:23 PST.

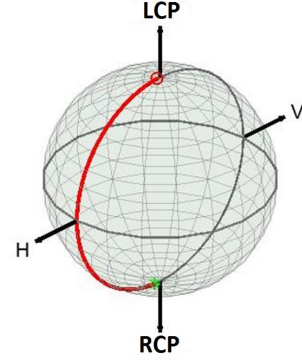


Figure 126. Polarization along the 1-Hop X-Mode ray path at 10:23 PST.

Rather than present the scattering function, this section extracts the fading and the Doppler shifts from the 1-Hop O- and X-Modes in the delay-spread function. Figure 127 shows an estimate of the delay-spread function. The average of this function across the PN sequence is the channel estimate of Figure 120. The closely spaced O- and X-Mode channels show slow modulations. The noise floor rises toward the end of the sounding.

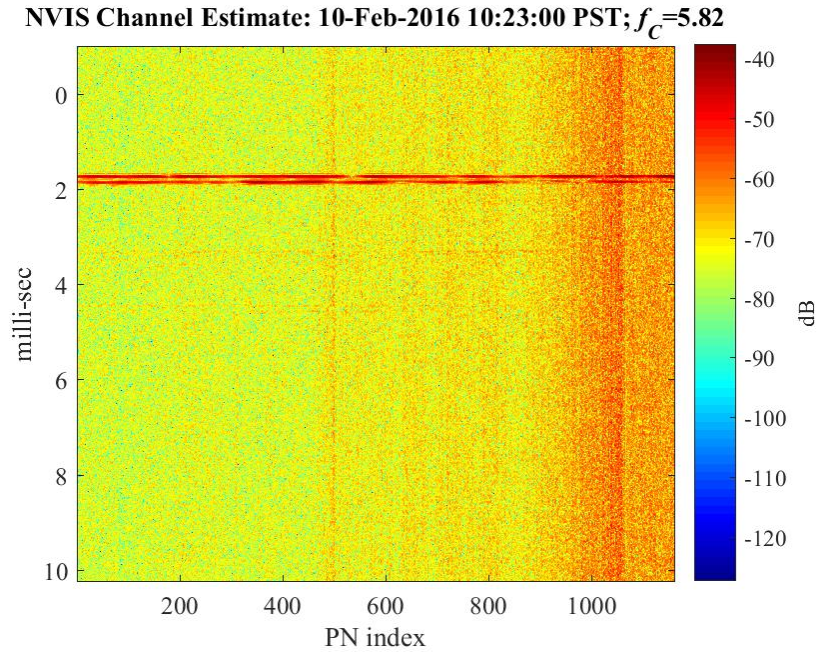


Figure 127. Delay-spread estimate at 10:23 PST.

Figure 128 reports the amplitude  $|h_O|$  and phase  $\angle h_O$  of the 1-Hop O-Mode channel. The upper panel shows that the amplitude is relatively stationary over the first 40 seconds. Rayleigh fading is estimated to be  $f_{N,O} \approx 0.5$  Hz measured around the median line. The lower panel shows the phase and a quadratic fit where the linear term estimates the Doppler shift. The deep fades at 9, 25, 50 seconds cause the jumps in the phase-unwrapping. The quadratic fit provides a more robust estimate of the Doppler shift in the presence of these phase discontinuities rather than averaging the instantaneous frequency. Figure 129



reports the same computations for the 1-Hop X-Mode channel. The upper panel shows multiple fading regions with the noisy burst near 40 seconds causing the perturbation in the phase.

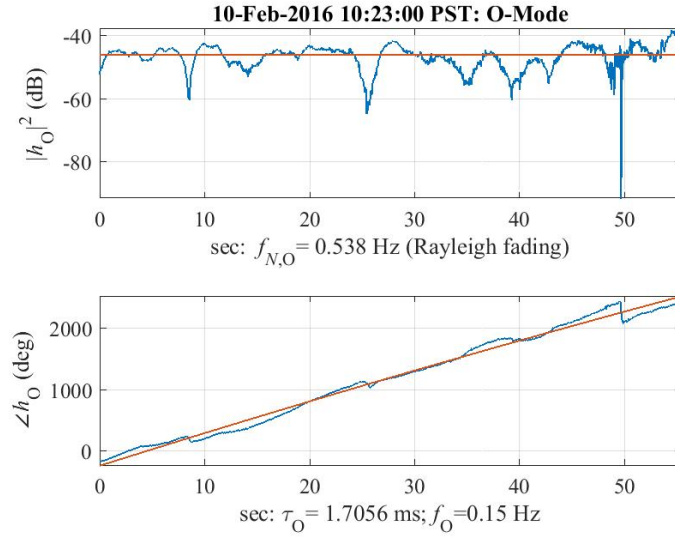


Figure 128. 1-Hop O-Mode amplitude and phase at 10:23 PST.

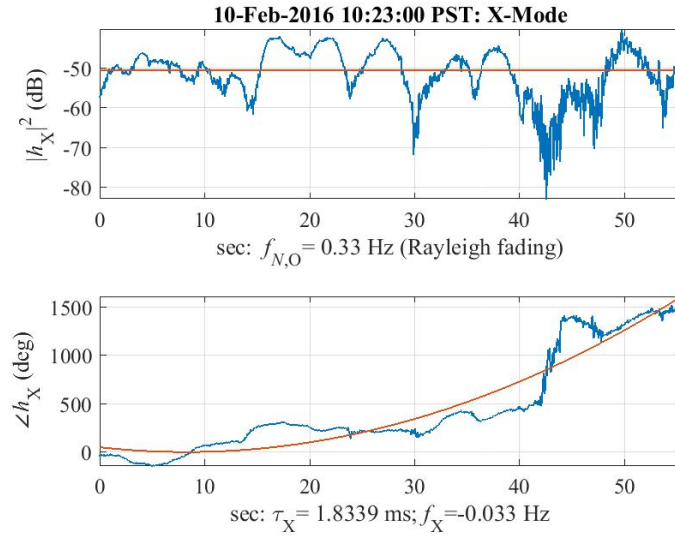


Figure 129. 1-Hop X-Mode amplitude and phase at 10:23 PST.

The best approach to fading identification is based on the physics of the problem. Although Rician fading has been presented plausible fading model on the ray paths [17, Section 7.7.6], fading identification is compounded by the presence of multiple fading processes. Figure 128 shows the O-Mode fading is relatively stationary compared to the X-Mode fading in Figure 129. Therefore, fading identification is restricted to the O-Mode. The increasing background noise limits the fading analysis window to the first 48 seconds. Figure 130 shows one “goodness-of-fit” ranking estimated over this window. These standard “goodness-of-fit” tests are very sensitive to outliers, correlation, and the number of samples. No distribution delivers a significance level over 60%. Figure 131 compares the “fit” of selected distributions to the sample histogram of the O-Mode fading. All distributions provide a reasonable fit. The physical basis for the Rician fading makes it a natural candidate for the fading process.

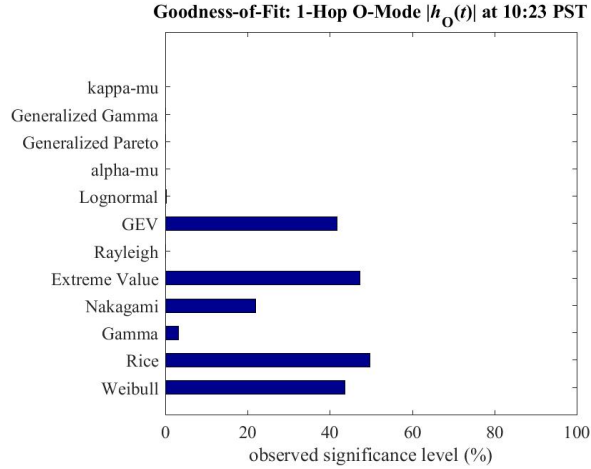


Figure 130. “Goodness-of-fit” for the 1-Hop O-Mode amplitude at 10:23 PST.

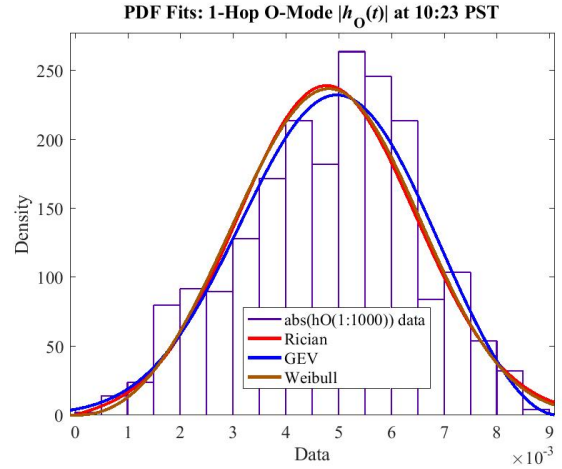


Figure 131. Fitting probability density functions to the 1-Hop O-Mode amplitude at 10:23 PST.

Table 17 encapsulates this channel in a form suitable for channel emulator. The model employs only the 1-Hop O- and X-Modes. The total path loss is scaled to the 1-Hop O-Mode and encompasses both the transmit and receive antenna, including the latter’s orientation and velocity on the mobile.

Table 17. Wideband HF-NVIS channel model; 5.82 MHz; 10 February 2016 10:23 PST.

10:23 PST	Path delay	Total path loss	Doppler shift	Fade rate	Rician $K$ factor
1-Hop O-Mode	1.71 ms	0 dB	0.15 Hz	0.54 Hz	5.2 dB
1-Hop X-Mode	1.83 ms	−3.7 dB	−0.03 Hz	0.33 Hz	3.6 dB

*Remarks:* The 3-D ray tracing estimates the O- and X-Mode hops arrive at the vehicle with elevation angles approximately  $73^\circ$  and  $72^\circ$ , respectively. The maximum Doppler shift is estimated to be 0.7 Hz. These angles put an upper bound on the Doppler shift induced by vehicular motion of approximately 0.2 Hz (see Appendix B.1 for the calculation). Although the Doppler shifts extracted from the fading processes are within this bound, the difference in signs between O- and X-Mode shifts is **not** understood.

## 7.4 HF-NVIS CHANNEL AT 13:00 PST

Figure 132 tracks the mobile approximately 100 km northeast of the transmitter as it exits the Banner Grade in the Cuyamaca Mountains north of Julian, CA. The vehicle is pointed at  $291^\circ$  and traveling 40 to 60 mph. Figure 133 is the topographic view showing that the deep canyon containing the Banner Grade and the terrain of the Cuyamaca Mountains.

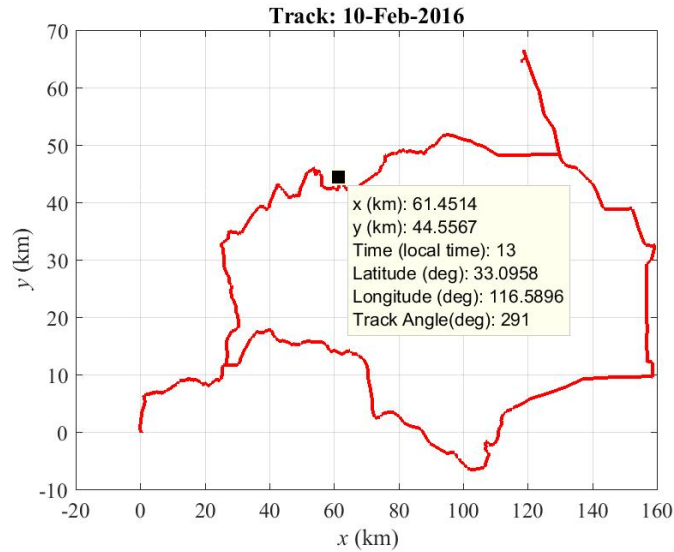


Figure 132. Receiver location on the track at 13:00 PST.

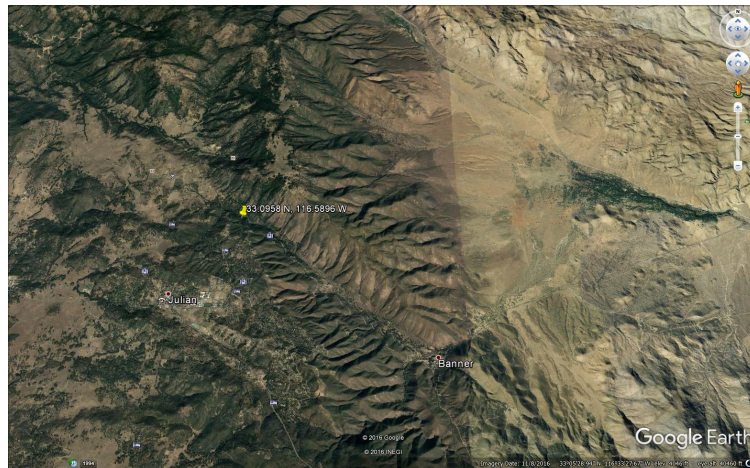


Figure 133. Receiver location at 13:00 PST marked by the yellow "thumbtack."

Figure 134 shows the estimated HF-NVIS channel is essentially the 1-Hop O- and X-Modes. Table 18 compares the hop times between this sounding, the ray paths computed by the 3-D ray-tracing code, and estimates obtained from the ionogram. The ordering of the ray paths is consistent with the O-Modes always arriving before the X-Modes. The 3-D ray tracing has a consistent bias of +0.1 ms on the 1-Hop O-Mode that produces a +0.15 ms bias in the 2-Hop O-Mode and a +0.3 ms bias on the 3-Hop O-Mode. This bias is larger for the X-Mode with a +0.32 ms bias for the 1-Hop X-Mode that runs into a +0.65 ms bias in the 2-Hop X-Mode.

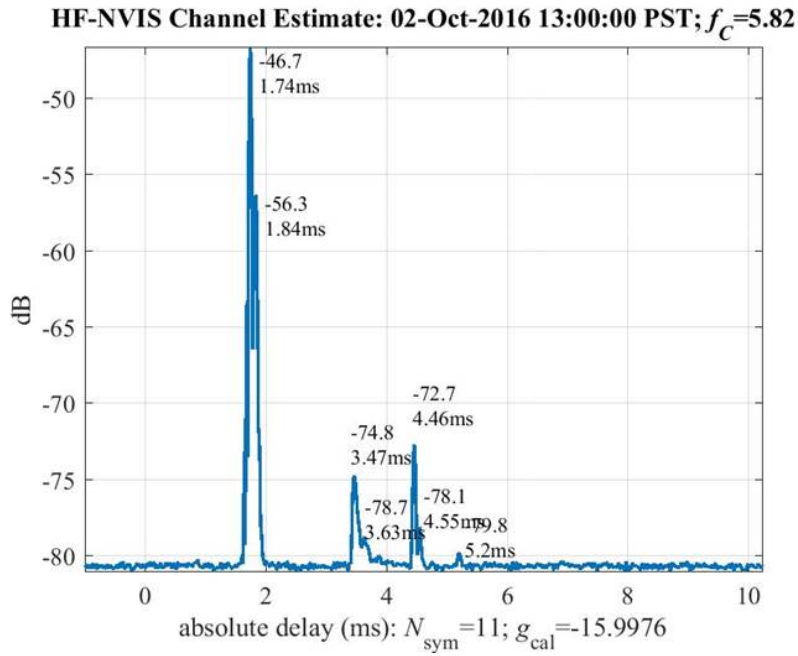


Figure 134. Channel estimate from the loop antenna at 13:00 PST.

Table 18. Comparing O- and X-Mode hop times between the sounding, simulation, and the nearest ionogram (Point Arguello, CA) at 13:00 PST.

13:00 PST	Measured	Simulation	Ionogram
1-Hop O-Mode	1.74 ms	1.83 ms	1.73 ms
1-Hop X-Mode	1.84 ms	2.16 ms	1.87 ms
2-Hop O-Mode	3.47 ms	3.63 ms	3.47 ms
2-Hop X-Mode	3.63 ms	4.28 ms	3.67 ms
2.5-Hop O-Mode (?)	4.33 ms	—	—
2.5-Hop X-Mode (?)	4.43 ms	—	—
3 Hop O-Mode	5.13 ms	5.43 ms	—

The ray-tracing code uses the hybrid ionogram obtained by spatially averaging the ionograms at Point Arguello, CA, Boulder, CO, and Austin, TX. Figure 135 shows the plasma frequency obtained from this hybrid ionogram. Figure 136 is the nearest ionogram measured at Point Arguello, CA. Comparison of the lower edge of the plasma frequencies shows the hybrid is slightly higher than the measured ionogram. The resulting bias shows the limitations of any ray-tracing code—the ray paths are only as accurate as the estimated plasma frequency or, equivalently, the electron density.

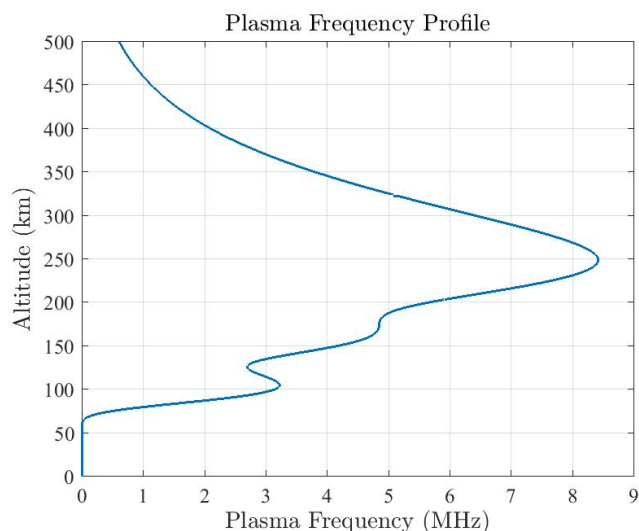


Figure 135. Hybrid plasma frequency at 13:00 PST.

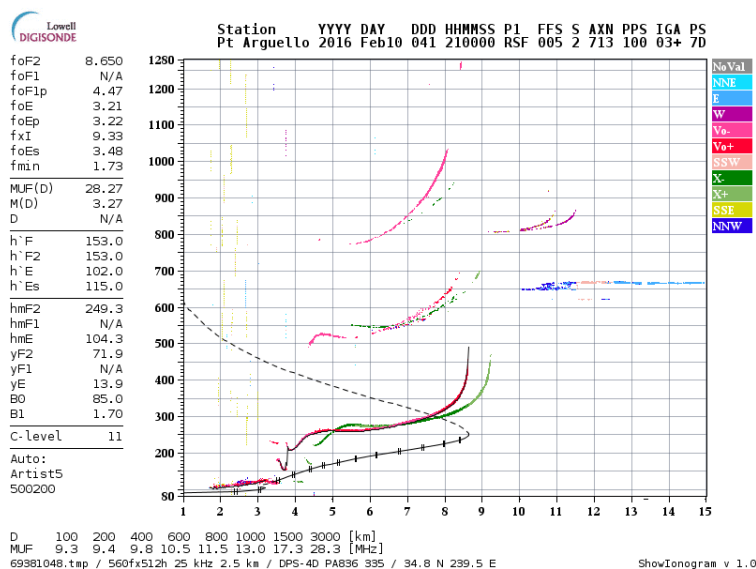


Figure 136. Ionogram at Point Arguello, CA at 13:00 PST. Open source ionograms courtesy of the Global Ionospheric Radio Observatory at the University of Massachusetts, Lowell [64].

Figure 137 shows an estimate of the delay-spread function  $h(t, \tau)$  where “ $t$ ” is determined by the timing of the PN sequences. The average of this function across the PN sequence is the channel estimate of Figure 134. The closely spaced O- and X-Mode channels show slow modulations over a relatively flat noise floor. The 1-Hop ray paths are the strongest just before 2 ms. The 2-Hop and 3-Hop are negligible.

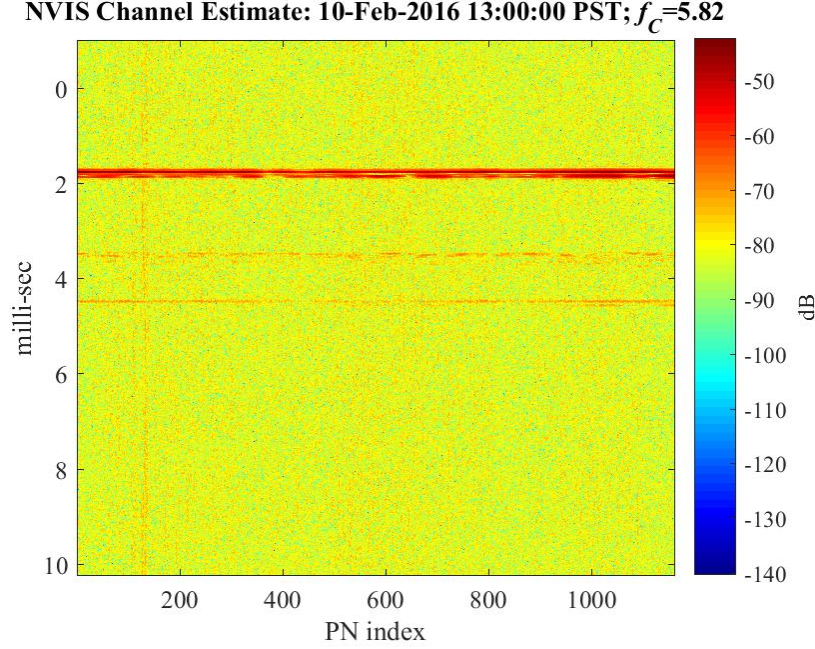


Figure 137. Delay spread estimate at 13:00 PST.

This section extracts the fading and the Doppler shifts from the 1-Hop O- and X-Modes in the delay-spread function rather than the resolution-limited scattering function. The 1-Hop O-Mode fading has amplitude and phase

$$h(t, \tau_O) =: h_O(t) = |h_O(t)| \angle h_O(t).$$

Likewise, the 1-Hop X-Mode fading has amplitude and phase

$$h(t, \tau_X) =: h_X(t) = |h_X(t)| \angle h_X(t).$$

Figure 138 reports 1-Hop O-Mode fading. The upper panel shows that the amplitude is relatively stationary: the envelope varies  $\pm 6$  dB around a mean level of approximately  $-49$  dB. The Rician  $K_O$  factor is the ratio of the specular to the diffuse power [76, page 52]. Under the Rician assumptions, the O-Mode has a strong specular component. The lower panel shows the phase and a quadratic fit

$$\angle h_O(t) \approx \phi_0 + \phi_1 t + \phi_2 t^2$$

where the linear term estimates the Doppler shift.

The Rician  $K_O$  factor is the ratio of the specular to the diffuse power [76, page 52]. Under the Rician assumptions, the O-Mode has a strong specular component. The lower panel shows the phase and a quadratic fit

$$\angle h_O(t) \approx \phi_0 + \phi_1 t + \phi_2 t^2,$$

where the linear term estimates the Doppler shift.



Figure 139 presents the corresponding plots for the X-Mode. The deep fades are reflected in the small Rician  $K_X$  factor. Under the Rician assumptions, the X-Mode is tending toward Rayleigh fading. The deep fades in the envelope cause multiple jumps in the unwrapped phase. Therefore, comparison with other Doppler estimators concludes this section.

The Doppler spread is estimated from the O- and X-Mode phases using Woodward's approach [57]. Figures 140 and 141 show the estimated Doppler spectra of the O- and X-Modes. The Doppler spectra are proportional to the PDF of the instantaneous frequencies obtained from O- and X-Mode phases:

$$\text{O-Mode } f_i(t) = \frac{1}{2\pi} \frac{d\phi_O}{dt}(t); \quad \text{X-Mode } f_i(t) = \frac{1}{2\pi} \frac{d\phi_X}{dt}(t).$$

Both figures compare the histograms of these instantaneous frequencies against the Gaussian and the Stable PDF's. The large tails of instantaneous frequency bias the mean and standard deviation of the Gaussian fit. Nevertheless, the standard deviation of the Gaussian determines the reported Doppler spread  $\Delta f = 2 \times \sigma$  as discussed in Section 4.1.

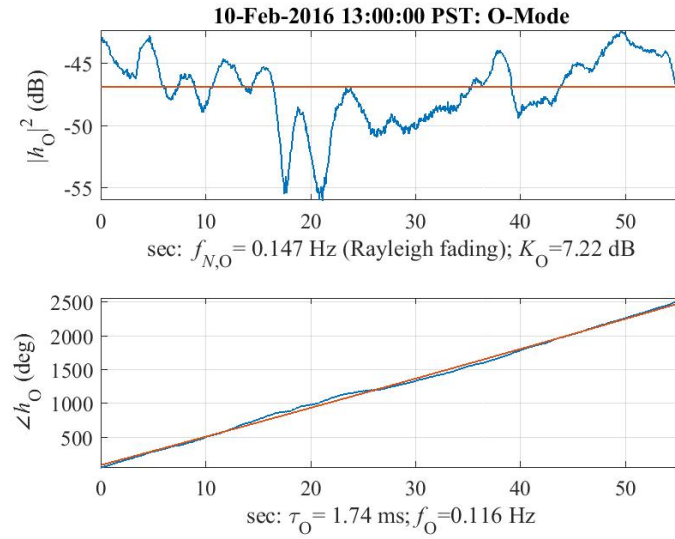


Figure 138. 1-Hop O-Mode amplitude and phase at 13:00 PST.



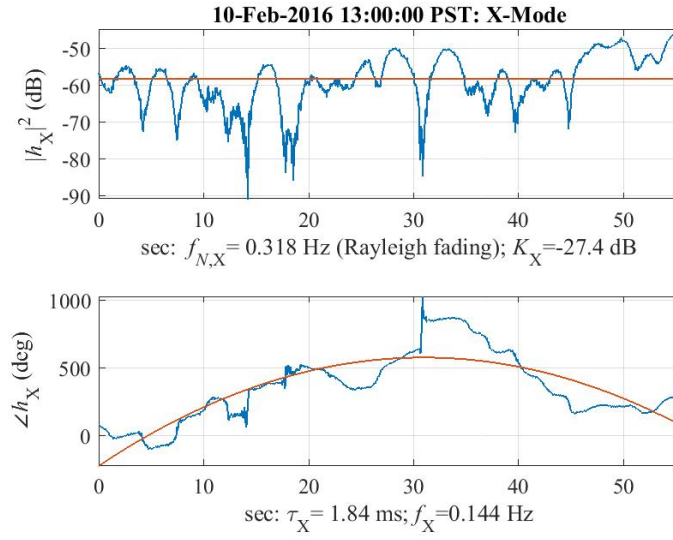


Figure 139. 1-Hop X-Mode amplitude and phase at 13:00 PST.

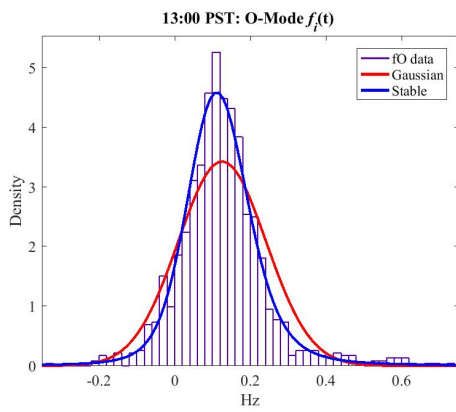


Figure 140. O-Mode Doppler spectrum estimate at 13:00 PST.

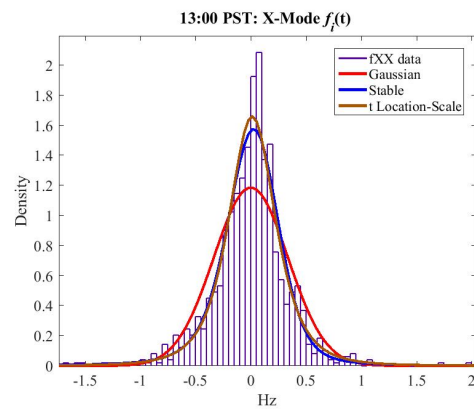


Figure 141. X-Mode Doppler spectrum estimate at 13:00 PST.

Table 19 reports these channel estimates in a form suitable for channel emulator. The model employs only the 1-Hop O- and X-Modes. The total path loss is scaled to the 1-Hop O-Mode and encompasses both the transmit and receive antennas, including the latter's orientation and velocity on the mobile. The positive Doppler shifts are consistent with the receiver traveling toward the transmitter.

Table 19. Wideband HF-NVIS channel model; 5.82 MHz; 10 February 2016 13:00 PST.

<b>13:00 PST</b>	<b>Path delay</b>	<b>Total path loss</b>	<b>Doppler shift</b>	<b>Doppler spread</b>	<b>Fade rate</b>	<b>Rician <i>K</i> factor</b>
1-Hop O-Mode	1.74 ms	0 dB	+0.12 Hz	0.23 Hz	0.15 Hz	7.2 dB
1-Hop X-Mode	1.84 ms	−9.6 dB	+0.14 Hz	0.67 Hz	0.32 Hz	−27.4 dB

## 7.5 HF-NVIS CHANNEL AT 13:41 PST

Figure 142 locates the mobile receiver approximately 71 km northeast of the transmitter and on the plateau heading down to Santa Ysabel, CA. The vehicle is pointed at  $268.3^\circ$  and traveling between 40 to 60 mph. Figure 143 is the topographic view showing the escarpment and the terrain of the Cuyamaca Mountains.

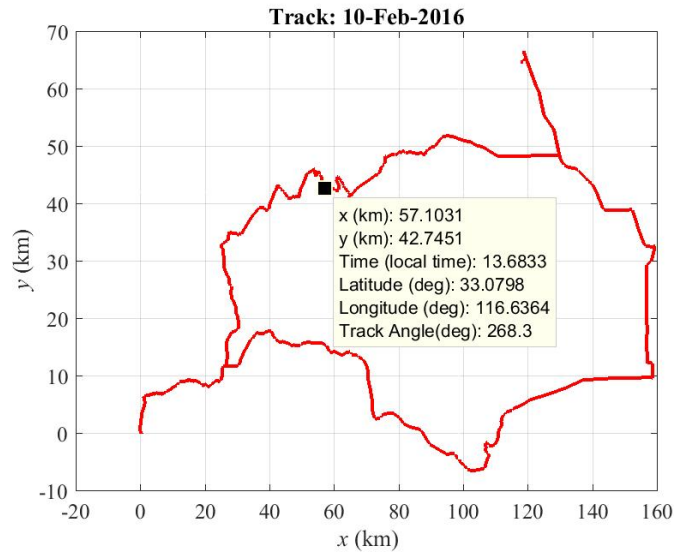


Figure 142. Receiver location on the track at 13:41 PST.

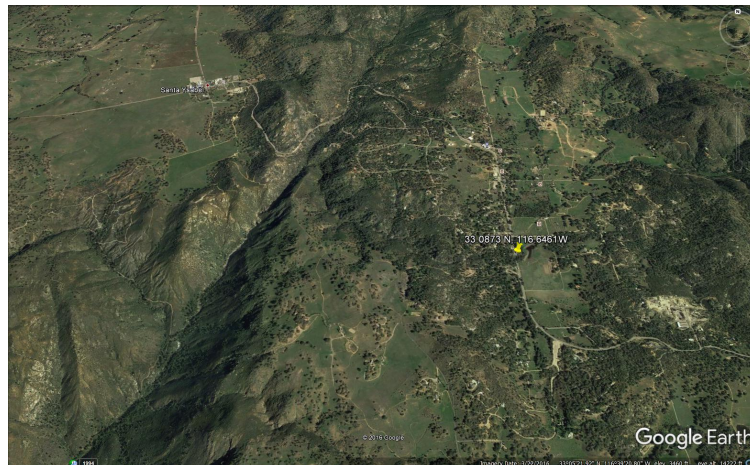


Figure 143. Receiver location marked with yellow “thumbtack” at 13:41 PST.

Figure 144 shows the estimated HF-NVIS channel. The first spike is the ground wave, the large spikes are the 1-Hop O- and X-Modes, followed by a weak 2-Hop O-Mode, and the 2.5 Hop. As a communications channel, this HF-NVIS channel is well-modeled by the 1-Hop O- and X-Modes.

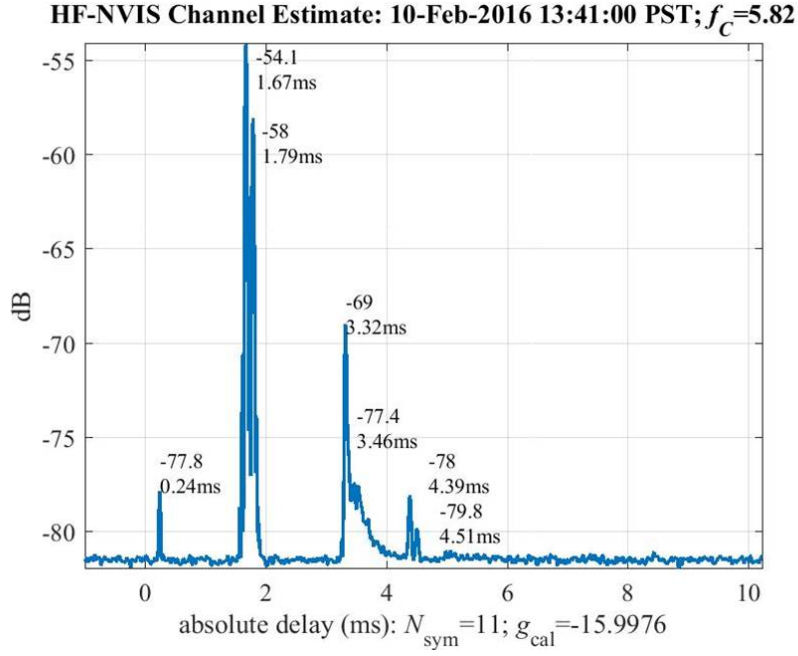


Figure 144. Channel estimate from the loop antenna at 13:41 PST.

There is good agreement between this measured and ideal accuracy of this ground wave delay. The distance between the transmitter and receiver is approximately

$$d_G \approx 71.1241 \text{ [km]}.$$

The ground wave's ideal delay

$$t_G = \frac{d_G}{c_0} \approx 0.2371 \text{ [ms]}$$

aligns with the measured delay. Thus, the system delays seem to be correctly calibrated in Section 5.4.

Table 20 compares the hop times between this sounding, the ray paths computed by the 3-D ray-tracing code, and estimates obtained from the ionogram. The ordering of the ray paths is consistent with the O-Modes always arriving before the X-Modes. The 3-D ray tracing has a bias of +0.06 ms on the 1-Hop O-Mode. This bias produces a +0.11 ms bias in the 2-Hop O-Mode. This bias is larger for the X-Mode. The 1-Hop X-Mode bias is + 0.13 ms that runs into a +0.34 ms bias in the 2-Hop X-Mode.

Table 20. Comparing O- and X-Mode hop times between the sounding, simulation, and the nearest ionogram (Point Arguello, CA) at 13:41 PST.

<b>13:41 PST</b>	<b>Measured</b>	<b>Simulation</b>	<b>Ionogram</b>
1-Hop O-Mode	1.67 ms	1.73 ms	1.63 ms
1-Hop X-Mode	1.79 ms	1.92 ms	1.83 ms
2-Hop O-Mode	3.32 ms	3.43 ms	3.67 ms
2-Hop X-Mode	3.46 ms	3.80 ms	3.53 ms
2.5-Hop O-Mode (?)	4.39 ms	—	—
2.5-Hop X-Mode (?)	4.51 ms	—	—

Comparison with the bias at 13:00 PST shows that these errors are decreasing. Indeed, only a 41-minute difference and a 30-km difference reduces the O-Mode bias from 0.1 ms at 13:00 PST to +0.06 ms at 13:41 PST. As expected, the hybrid ionogram used by the 3-D ray-tracing code has a slightly higher plasma frequency profile than the ionogram measured at Point Arguello, CA. Figure 145 shows the ionogram at 13:45 PST. The black line is the plasma frequency profile. The 3-D ray-tracing code uses the hybrid ionogram obtained by spatially averaging the ionograms at Point Arguello, CA, Boulder, CO, and Austin, TX. Figure 146 shows the plasma frequency profile obtained from this hybrid ionogram. Comparison of the lower edge of the plasma frequencies shows the hybrid plasma frequency profile is slightly higher than the measured ionogram. The resulting bias shows the limitations of any ray-tracing code—the ray paths are only as accurate as the estimated plasma frequency or, equivalently, the electron density.

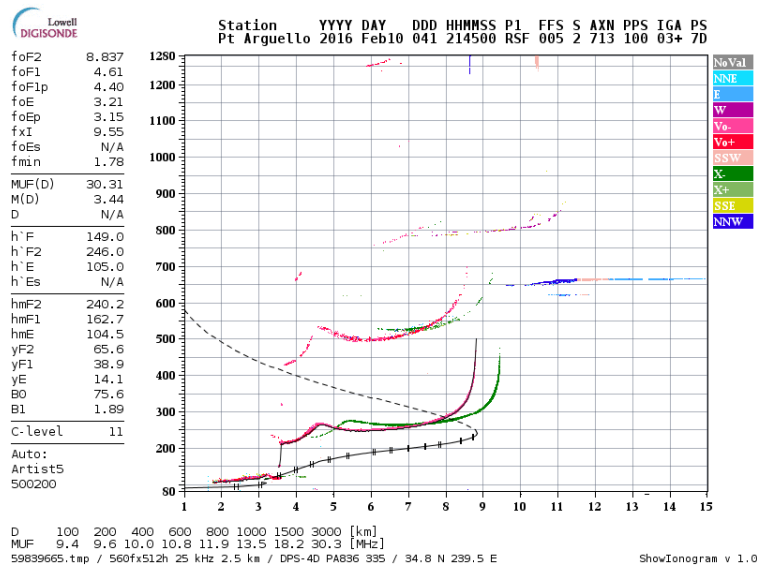


Figure 145. Point Arguello, CA, ionogram at 13:45 PST. Open source ionograms courtesy of the Global Ionospheric Radio Observatory at the University of Massachusetts, Lowell [64].

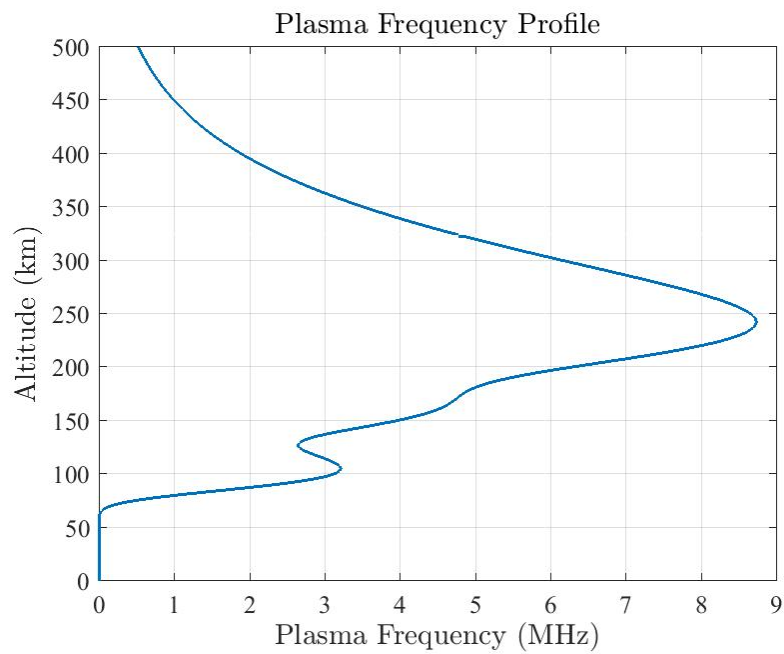


Figure 146. Hybrid plasma frequency estimate at 13:41 PST.

Figure 147 shows the delay-spread function  $h(t, \tau)$  where “ $t$ ” is determined by the timing of the PN sequences. The average of this function across the PN sequence is the channel estimate of Figure 144. The closely spaced O- and X-Mode channels show slow modulations over a relatively flat noise floor. The 1-Hop ray paths are the strongest just before 2 ms. The ground wave, the 2-, and the 2.5-Hop are negligible. Figures 148 and 149 show the respective O- and X-Mode 1-Hop fading at 13:41 PST.

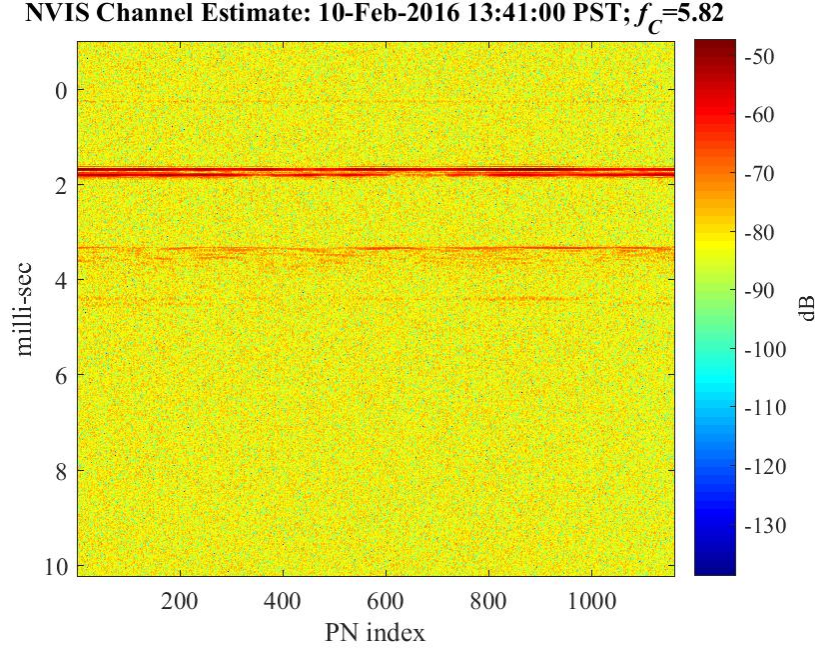


Figure 147. Delay spread estimate at 13:41 PST.

As in the preceding sections, Doppler and fading estimates of these modes are obtained by extracting the amplitude and phase from the delay-spread function. Figure 148 displays the amplitude and phase of the 1-Hop O-Mode channel obtained by scanning the delay-spread function at the O-Mode delay:

$$h_O(t) = |h_O(t)| \angle h_O(t) = h(t, \tau_O).$$

The amplitude in the upper panel shows slow and fast fading. The Rayleigh fading  $f_{N,O} \approx 0.184$  Hz is measured around the median line. This is not the best model for this non-stationary fading. However, the lower panel shows the unwrapped phase and an excellent fit of the quadratic phase model

$$\angle h_O(t) \approx \phi_O(t) := \phi_0 + \phi_1 t + \phi_2 t^2.$$

The linear term estimates the Doppler shift reported on this plot:

$$f_O = \frac{1}{2\pi} \left. \frac{d\phi_O}{dt}(t) \right|_{t=0}.$$

In contrast, Figure 149 shows a deep fade in the amplitude 1-Hop X-Mode channel and an associated phase jump. The deep fade degrades the associated fading statistics. Therefore, estimates of the Doppler spread will omit this deep fade.



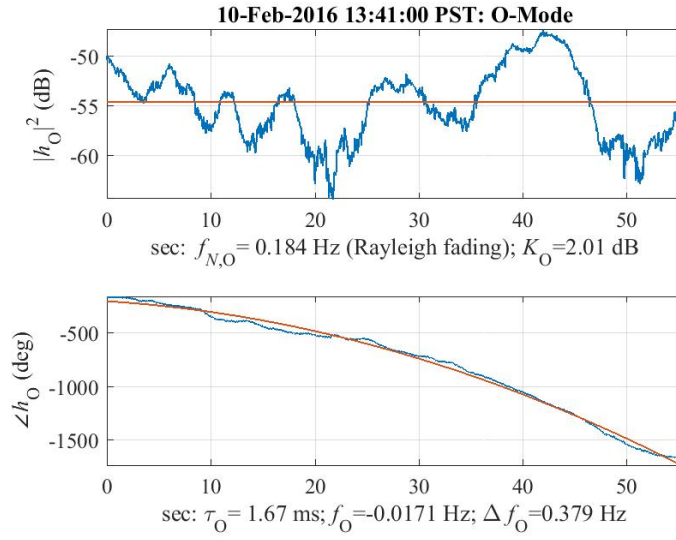


Figure 148. 1-Hop O-Mode amplitude and phase at 13:41 PST.

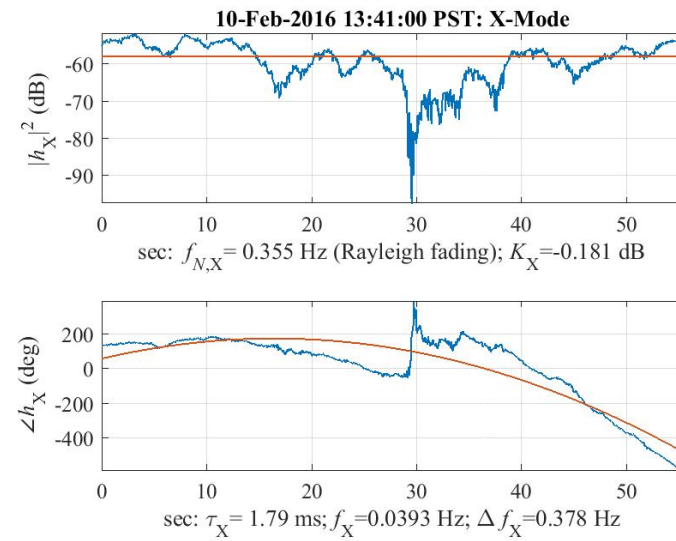


Figure 149. 1-Hop X-Mode amplitude and phase at 13:41 PST.

The last computation of this section estimates the Doppler spread. The Doppler spread is extracted from O- and X-Mode phases using Woodward’s approach [57]. Figures 150 and 151 estimate O- and X-Mode Doppler spectra from the PDF of the instantaneous frequencies:

$$\text{O-Mode } f_i(t) = \frac{1}{2\pi} \frac{d\phi_O}{dt}(t); \quad \text{X-Mode } f_i(t) = \frac{1}{2\pi} \frac{d\phi_X}{dt}(t).$$

Both figures compare the histograms of these instantaneous frequencies against the Gaussian PDF and the  $t$  Location-Stable PDF. The phase jumps in the X-Mode are handled by omitting the instantaneous frequency samples when  $|h_X(t)| < -65$  dB. This omission is marked by the “\*” in Table 21. The large tails of instantaneous frequency bias the estimation of mean and standard deviation to the Gaussian fit. Nevertheless, the standard deviation of the Gaussian determines the reported Doppler spread  $\Delta f = 2 \times \sigma$  as discussed in Section 4.1.

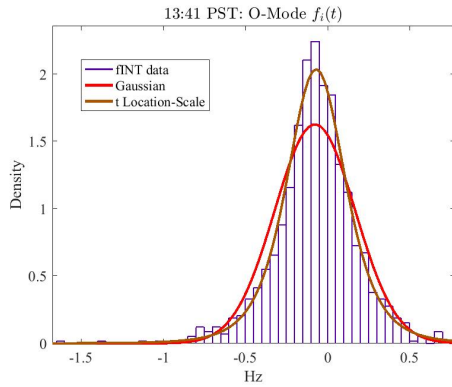


Figure 150. O-Mode Doppler spectrum estimate at 13:41 PST.

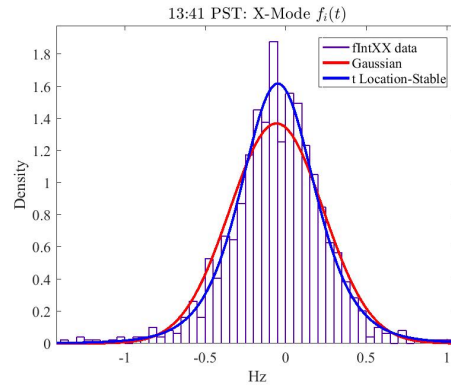


Figure 151. X-Mode Doppler spectrum estimate at 13:41 PST.

Table 21 reports these channel estimates in a form suitable for a channel emulator. The model employs only the 1-Hop O- and X-Modes. The total path loss is scaled to the 1-Hop O-Mode and encompasses both the transmit and receive antennas, including the latter’s orientation and velocity on the mobile. The positive Doppler shifts are consistent with the mobile receiver traveling toward the transmitter.

Table 21. Wideband HF-NVIS channel model; 5.82 MHz; 10 February 2016 13:41 PST.

13:41 PST	Path delay	Total path loss	Doppler shift	Doppler spread	Fade rate	Rician $K$ factor
1-Hop O-Mode	1.67 ms	0 dB	−0.02 Hz	0.38 Hz	0.18 Hz	2 dB
1-Hop X-Mode	1.79 ms	−3.9 dB	−0.07* Hz	0.33 Hz	0.36 Hz	−0.2 dB

## 7.6 MOBILE WIDEBAND HF-NVIS CHANNEL MODEL: NON-TID REGION

The preceding sections extracted HF-NVIS channel models at specific locations. This section extracts over multiple locations to produce representative wideband HF-NVIS models suitable for HF channel simulation and emulation. Referring to Figure 87, the strong O- and X-Modes show that the HF-NVIS channel is well-modeled using the 1-Hop channel of Example 7

$$h(t, \tau) = a_{F,O}(t)\delta(\tau - \tau_{F,O}) + a_{F,X}(t)\delta(\tau - \tau_{F,X}).$$

Figure 152 plots the estimated 1-Hop delays over the entire measurement day. The oscillations between 10:30 to 13:00 PST are likely show the presence of a TID. A relatively stationary non-TID channel exists between 09:30 to 10:30 PST. This section determines a stochastic ensemble parameterizing these HF-NVIS channels in this stationary and non-TID region.

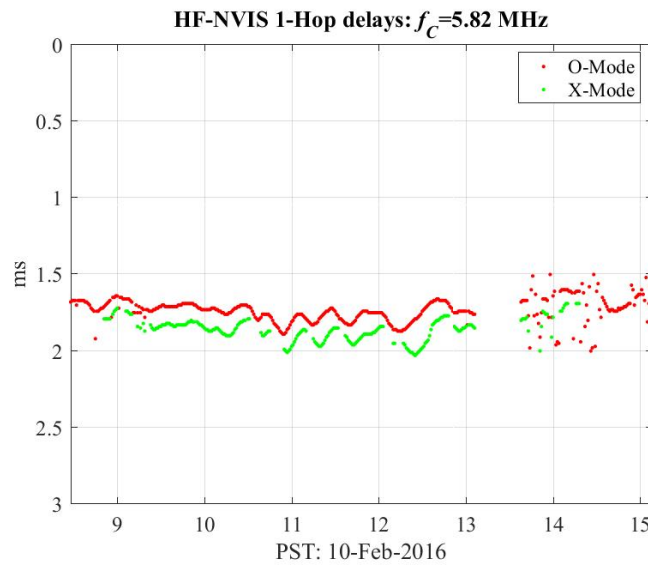


Figure 152. 1-Hop O- and X-Mode delays.

Table 22 summarizes this 1-Hop model. The average channel parameters are listed for comparison to the narrowband HF-NVIS models of Table 7. The following subsections document the probabilistic models used in this model.

Table 22. Mid-Latitude mobile wideband HF-NVIS channel model using only the 1-Hop O- and X-Modes; 5.82 MHz over the non-TID region from 9:30 to 10:30 PST; interference and mode correlation are omitted from this model.

1-Hop: No TID 5.82 MHz	Delay (ms)	Amplitude $H=10\log_{10}( h ^2)$	Rician $K$ factor (9:30 to 10:00 PST)	Doppler shift (Hz)	Doppler spread (Hz)
O-Mode	1.72 ms $\tau_O \sim \text{lognormal}$ $\mu = 0.540$ $\sigma = 0.011$	$H \sim \text{Gaussian}$ $\mu = -44 \text{ dB}$ $\sigma = 2.4 \text{ dB}$	$K_O \sim \text{Gaussian}$ 13 dB 3.4 dB	$f_O \sim \text{Gaussian}$ $\mu = 0 \text{ Hz}$ $\sigma = 0.13 \text{ Hz}$	$\Delta f_O \sim \text{exponential}$ $\mu = 0.44 \text{ Hz}$
X-Mode	1.84 ms $\tau_X = \tau_O + \tau_D$ $\tau_D \sim \text{Weibull}$ $A = 0.131$ $B = 9.25$	$H \sim \text{Gaussian}$ $\mu = -50 \text{ dB}$ $\sigma = 3.4 \text{ dB}$	$K_X \sim \text{Gaussian}$ 12 dB 2.8 dB	$f_X \sim \text{Gaussian}$ $\mu = 0 \text{ Hz}$ $\sigma = 0.12 \text{ Hz}$	$\Delta f_X \sim \text{exponential}$ $\mu = 0.38 \text{ Hz}$

### 7.6.1 Delay

Channel emulators always require the delays. Figure 153 is a histogram of the joint delays  $\tau_O$  and  $\tau_X$  between 9:30 to 10:30 PST. The conditional dependence is approximated by modeling the O-Mode delay  $\tau_O$  as a lognormal random variable based on Figure 154 and the X-Mode delay  $\tau_X$  conditioned on  $\tau_O$  based on Figure 155.

$$\tau_O \sim \text{lognormal}(\mu, \sigma),$$

$$\tau_X = \tau_O + \tau_D; \quad \tau_D \sim \text{Weibull}(A, B)$$

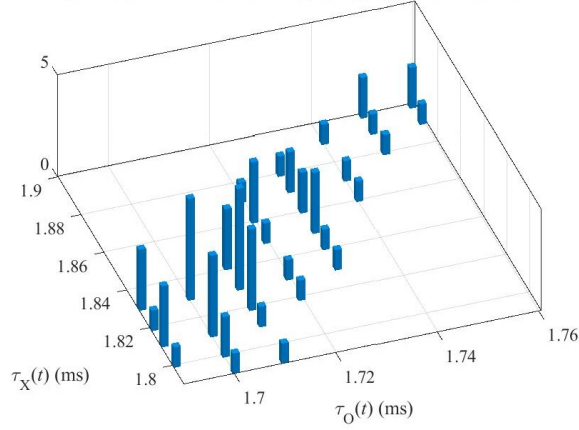


Figure 153. Joint distribution of 1-Hop delays from 09:30 to 10:30 PST.

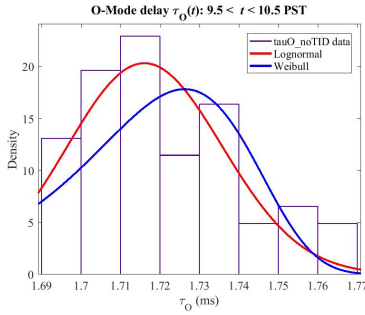


Figure 154. O-Mode delay  $\tau_O$  and fitted distributions.

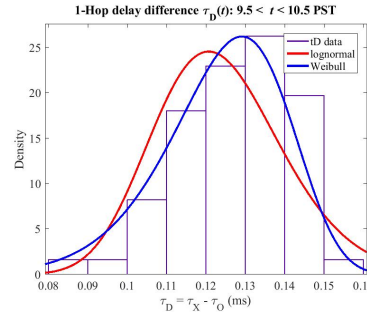


Figure 155. Excess delay  $\tau_D$  and fitted distributions.

### 7.6.2 Fading

Channel emulators associate a mean power level and a fading process with each delay. Rician fading is the assumed model for both the O- and the X-Mode. Rician estimation splits the measured envelope power into specular and the scattered components [76, Section 1.2.2]:

$$E[|h_O(t)|^2] = s_O + 2\sigma_O^2,$$

$$E[|h_X(t)|^2] = s_X + 2\sigma_X^2.$$

Figures 156 and 157 plot the measured envelope power and the scattered powers, assuming Rician fading.

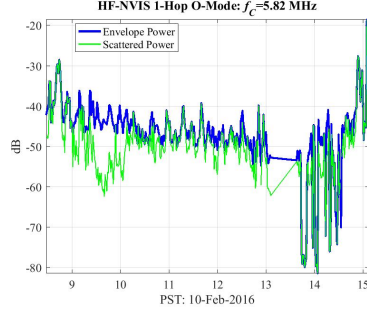


Figure 156. O-Mode envelope and scattered power.

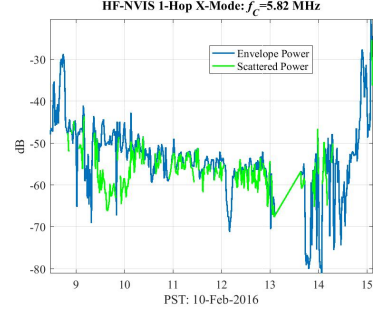


Figure 157. X-Mode envelope and scattered power.

The 10-dB gap between envelopes and their scattered powers argue that Rician fading is a credible model of both modes between 09:30 and 10:30 PST. However, the scattered power closes up to the envelope power starting around 10:00 PST. Therefore, the table reports the envelope power—a nearly direct measurement—over the entire interval but reports the Rician  $K$  factors

$$K_O = 10 \times \log_{10} \left( \frac{s_O^2}{2\sigma_O^2} \right) \quad \text{and} \quad K_X = 10 \times \log_{10} \left( \frac{s_X^2}{2\sigma_X^2} \right)$$

only over a portion of the non-TID region where the  $K$  factors are approximately 12 dB. Small  $K$  factors call into question the Rician assumption. Therefore, modeling a non-stationary  $K$  factor over the entire experiment is one approach to assess this Rician fading assumption [48], [78].

### 7.6.3 Doppler

Channel emulators typically specify a Doppler shift and a Doppler spread. Figures 158 and 159 displays estimates of the Doppler shift and spread for the O- and X-Modes in the no-TID region. The large spike at 9.9 PST is likely caused by interference by the radio tower near Desert View Point described in Section 6.3. The small values of the Doppler shift agree with the narrowband model of Table 7 and the values predicted by the 3-D ray-tracing code. Likewise, the mean values of the exponential distribution fitting the Doppler spreads align with Table 7.

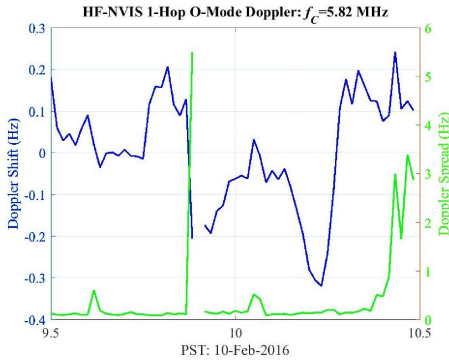


Figure 158. O-Mode Doppler.

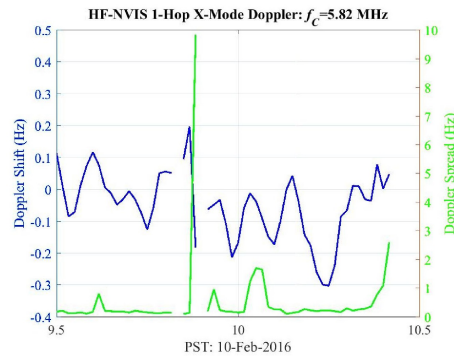


Figure 159. X-Mode Doppler.

### 7.6.4 Mode Correlation

Channel emulators typically allow correlation between taps. Correlated taps challenge radio design because the ray paths will experience deep fades at the same time. Figure 160 is an estimate of the cross correlation between the two modes. If  $h_O(t, \tau)$  and  $h_X(t, \tau)$  are the delay-spread functions, the cross correlation

$$\rho(t, \tau) := \frac{R_{OX}(t, \tau)}{\sqrt{R_{OO}(t, 0)}\sqrt{R_{XX}(t, 0)}}$$

is the normalized cross covariance of the centered random process:

$$R_{OX}(t, \tau) := E \left[ \left( h_O(t, \tau + \tau') - \mu_O(t) \right) \overline{\left( h_X(t, \tau') - \mu_X(t) \right)} \right],$$

where  $\mu_O(t) := E[h_O(t, \tau)]$  and  $\mu_X(t) := E[h_X(t, \tau)]$ . Both the expectation and associated estimators assume jointly stationary random processes. The plot shows that the correlation between the estimated channels is likely caused by the interference reported in Section 6.3. In the interference-free regions, the O- and X-Modes show low correlation—on this day, at this frequency, and along this route. Therefore, mode correlation is omitted from Table 22.

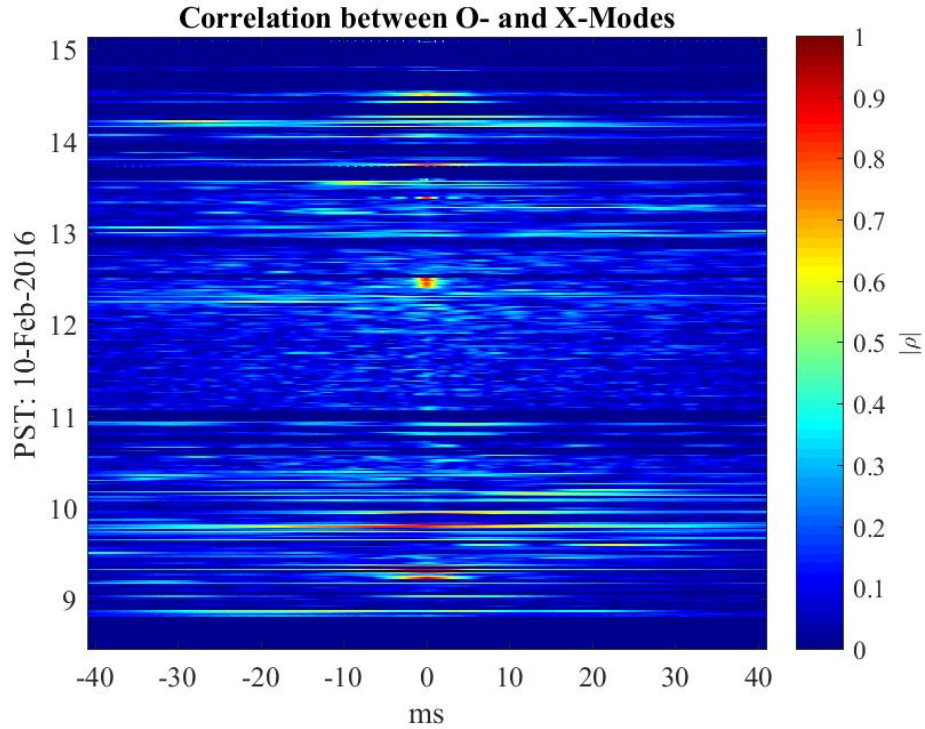


Figure 160. Estimated cross correlation between the O- and X-Modes.

## 8. EXTENDING THE WIDEBAND HF-NVIS CHANNEL ESTIMATES

Comparison between the measured channel and the 3-D ray-tracing code verified that credible ray paths could be simulated assuming only the the hybrid ionogram and the dry ground reflections. Consequently, wideband channel estimates should be possible at other frequencies, other times of day, other seasons, and other locations—assuming that the real-world plasma frequency and ground reflections are well-modeled by the hybrid ionogram and the simulated ground reflections. The following examples use the 3-D ray-tracing code to explore some of these channels and implications for HF system design.

### 8.1 O- AND X-MODE ARRIVAL TIMES

These measured wideband HF-NVIS channels always show the O-Mode arriving before the X-Mode. Therefore, a single-antenna wideband HF receiver could separate these taps to mitigate the Faraday fading that plagues the narrowband HF radios, provided the delay difference is resolvable in the bandwidth. Therefore, the 3-D ray-tracing code simulates these delays as a function of frequency. The ionogram at 09:41 PST is selected to sweep the simulated frequencies because of the excellent agreement with the measured delays at 5.82 MHz. Table 23 lists the measured delays at 5.82 MHz and the simulated delays at 5.82, 4, and 3 MHz. Table 23 predicts that the O- and X-Modes cannot be separated in delay at some frequencies. At 5.82 MHz, the measured O-Modes arrived before the X-Modes. This ordering holds at 4 MHz, but at 3 MHz, the ordering reverses—the X-Modes arrive before the O-Modes. Consequently, wideband HF signal processing seeking to mitigate Faraday fading by resolving these modes using delay only will fail.

Table 23. Measured and simulated hop times as a function of frequency using the ionogram at 09:41 PST.

09:41 PST	Measured 5.82 MHz	Simulation 5.82 MHz	Simulation 4 MHz	Simulation 3 MHz
1-Hop O-Mode	1.71 ms	1.71 ms	1.36 ms	0.82 ms
1-Hop X-Mode	1.83 ms	1.85 ms	1.71 ms	0.75 ms
2-Hop O-Mode	3.37 ms	3.34 ms	2.70 ms	1.66 ms
2-Hop X-Mode	3.64 ms	3.65 ms	3.28 ms	1.43 ms

These simulations highlight the payoff of equipping the receiver with dual-polarization antennas: Faraday fading will be mitigated regardless of mode crossing—provided that O- and X-Modes carry different polarizations. For this reason, the analysis of the channel soundings displayed the evolution of the polarization along each mode. Indeed, the 3-D ray-tracing code shows that the O-Modes start with LCP and arrive as RCP. Likewise, the X-Modes start with RCP and arrive as LCP. This same polarization behavior was observed for the simulations in Table 23. Therefore, polarization propagation and its effect on delays and fading must always be part of HF link analysis.



## 8.2 OVER THE WATER

This section simulates an HF-NVIS channel operating over the water. This example supports assessments of stealthy HF communications and makes explicit the shortfalls of using the standard HF channel modeling versus the coherent modeling delivered by the 3-D ray-tracing code. Figure 161 shows the link between the transmitter on Point Loma and a receiver located on San Clemente Island. Table 24 compares the hop times extracted from the nearest ionogram of Figure 162 and the simulated rays of Figure 163.



Figure 161. Over-the-water link between Point Loma and San Clemente Island.

Table 24. Comparing simulated ray path delays to the delays estimated from the Point Arguello, CA ionogram at 15 December 2015 at 10:00 PST.

Ray paths at 5.82 MHz	Simulation delays	Ionogram delays
1-Hop O-Mode	1.77 ms	1.73 ms
1-Hop X-Mode	1.98 ms	1.80 ms
2-Hop O-Mode	3.47 ms	3.47 ms
2-Hop X-Mode	3.90 ms	3.63 ms
3-Hop O-Mode	5.18 ms	—
3-Hop X-Mode	5.82 ms	—

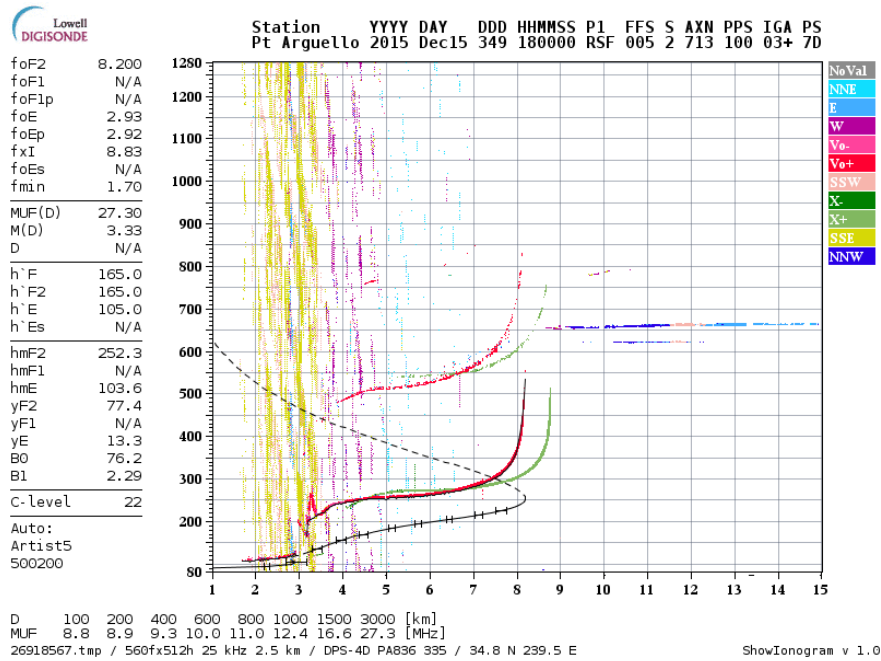


Figure 162. Point Arguello, CA ionogram at 15 December 2015 at 10:00 PST. Open source ionograms courtesy of the Global Ionospheric Radio Observatory at the University of Massachusetts, Lowell [64].

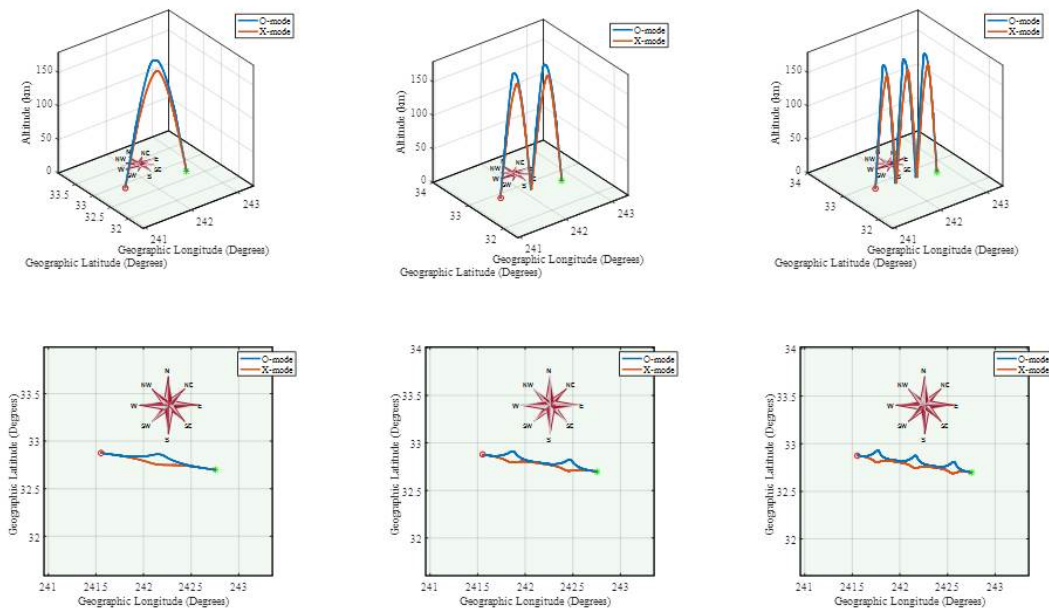


Figure 163. 1-, 2-, and 3-Hop between Point Loma and San Clemente Island, CA; 15 December 2015 at 10:00 PST.

The transmitter broadcasts from a horizontal dipole while the receiver employs a vertical loop made from copper. Table 25 details the simulated antenna parameters. These antennas coherently couple into the O- and X-Mode ray paths.

Table 25. Simulated transmitter and receiver antennas.

TX: horizontal dipole		RX: vertical loop	
Orientation	12°	Orientation	45°
Length	25.2984 m	Loop Radius	0.5 m
Height	12.192 m	Wire Radius	0.00762 m

Figure 164 reports on the over-the-water channel simulation. The polarization switches on both modes. The O-Mode delays are  $\tau_O$ ,  $\tau_{OO}$ , and  $\tau_{OOO}$ . Likewise for the X-Mode delays. As a communications channel, the 1-Hop ray paths show that the coherent processing on the 1-Hop O- and X-Modes will boost receiver diversity.

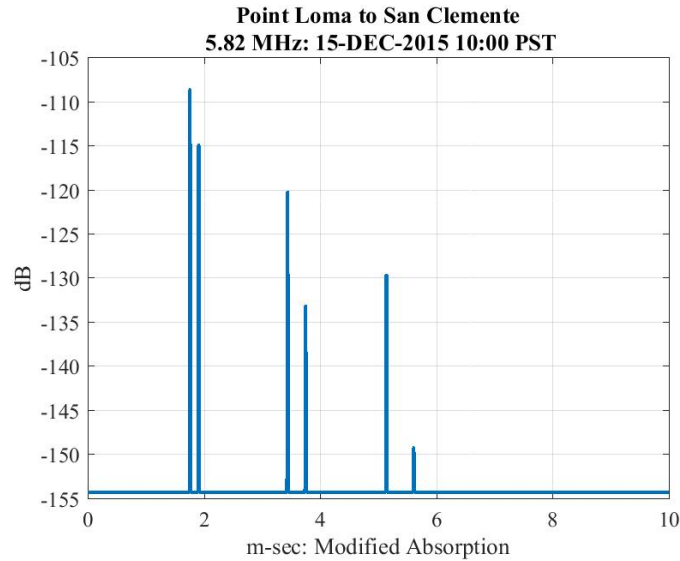


Figure 164. “Channel” between between Point Loma and San Clemente Island; 15 December 2015 at 10:00 PST.

Table 26 shows this channel is governed by the absorption. The reflection off the sea water is negligible and the spreading loss only picks up 4 to 5 dB per hop. However, absorption doubles in dB for each hop. Therefore, low absorption promises a multi-tap channel; high absorption reduces this HF-NVIS channel to 1-Hop O- and X-Modes. The absorption also affects how this HF-NVIS link is detected by a more distant receiver. Low absorption permits greater propagation of the 1-Hop O-Mode power—assuming this particular frequency and propagation conditions—compromising the “stealthiness” of the HF-NVIS link. Therefore, this 3-D ray-tracing code coupled with the semi-empirical absorption models can bound the throughput versus probability-of-detection for such HF-NVIS over-the-water links. The table shows that absorption is the limiting factor in successive hops. Indeed, absorption scales by the number of hops in dB. Therefore, absorption modeling is significant only when absorption is small—high absorption shuts down multiple hops. Using this reduced absorption model, this simulation shows stealthy HF-NVIS is still viable, but interference from the 2-Hop O-Mode requires consideration.

Table 26. Simulated propagation losses between between Point Loma and San Clemente Island; 15 December 2015 at 10:00 PST.

5.82 MHz	Delay	Total loss	Spreading	Mode shedding	Absorption	Reflection
1-Hop O-Mode	1.77 ms	108.6 dB	99.6 dB	3.1 dB	5.9 dB	N/A
1-Hop X-Mode	1.92 ms	114.9 dB	99.1 dB	3.1 dB	12.7 dB	N/A
2-Hop O-Mode	3.45 ms	120.2 dB	105.4 dB	3.2 dB	11.5 dB	0.10
2-Hop X-Mode	3.76 ms	133.1 dB	104.8 dB	3.3 dB	24.9 dB	0.10
3-Hop O-Mode	5.15 ms	129.6 dB	108.9 dB	3.3 dB	17.1 dB	0.21
3-Hop X-Mode	5.62 ms	149.2 dB	108.3 dB	3.5 dB	37.3 dB	0.21

### 8.3 NETWORKING FREQUENCIES

Frequency selection is a basic task of any HF link or HF network. The 3-D ray-tracing code can estimate link quality at frequencies without having to sound the channel—assuming a moderate absorption model. For this example, the antennas are located according to the 09:41 PST scenario and sized as in Table 27. The ray-tracing code uses the hybrid ionogram obtained by spatially averaging the ionograms at Point Arguello, CA, Boulder, CO, and Austin, TX. The end-to-end simulated received power is scaled to the simulated power at 5.82 MHz. Figure 165 shows this relative received power as a function of frequency. Software tools such as Voice of America Coverage Analysis Program (VOACAP) can also compute the total channel loss including propagation and antenna patterns, but this 3-D ray-tracing code is unique by including both mode and polarization effects.

Table 27. Antennas on the 09:41 PST link.

TX: horizontal dipole		RX: vertical loop	
Orientation	12°	Orientation	45°
Length	25.2984 m	Loop Radius	0.5 m
Height	12.192 m	Wire Radius	0.00762 m
Latitude	32° 41' 54.97" N	Latitude	32° 41' 21.84" N
Longitude	117° 14' 52.96" W	Longitude	116° 18' 27.36" W

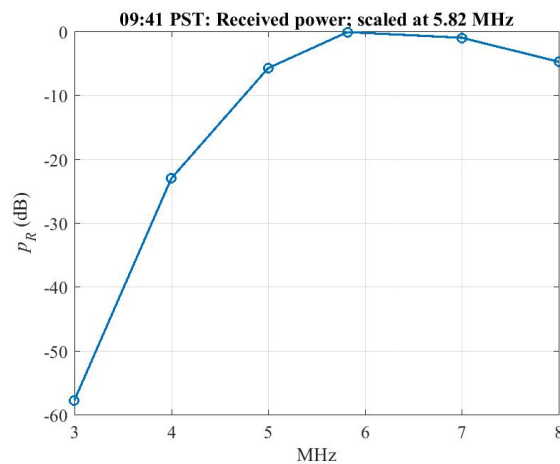


Figure 165. Relative received power over the 09:41 PST link.

## 8.4 SUMMARY

The report started with Sklar's observation that radio design starts from channel characteristics and system requirements. The measurements and analysis show that these mid-latitude daytime HF-NVIS channels are characterized by strong 1-Hop O- and X-Modes arriving within 0.2 ms of one another with opposite polarization. These extended simulations generalize this channel characterization. Section 8.1 demonstrates that these modes arrive in mixed order. Section 8.2 points out that the 2-Hop modes deliver additional diversity when operating over the water. Section 8.3 shows that frequency selection is crucial to link quality. These channels point to a radio design that exploits both the O- and X-Modes rather than suffer from Faraday fading. A single-antenna wideband system requires both modes to be separated in time. Dual-polarization systems drop the time separation, provided the modes are separated in polarization. More robust designs require more breadth in the HF-NVIS channels.

## 9. DEVELOPING THE HF-NVIS PORTFOLIO

This report analyzes mobile wideband HF-NVIS channel soundings at 5.82 MHz collected on 10 February 2016 on a west-to-east route. Two other mobile wideband HF-NVIS experiments expand upon this effort:

- A mid-latitude north-south mobile route on 1 Sept 2016
- A mid-latitude shore-to-ship test during August 2016

In the west-to-east experiments, the Earth's magnetic field exerts maximal effect on the O- and X-Modes. The north-to-south experiment provides a comparison when the Earth's magnetic field effect is minimized: the arrival times of the O- and X-Modes should be reduced, the Faraday fading effect should be more pronounced, and these two experiments bound the delay between these modes. However, one-day experiments only capture part of the ionosphere's daily cycle. The week-long shore-to-ship experiments provide a multi-day evolution of the ionosphere and employ dual-polarization antennas to assess Faraday fading and the possible SIMO gains. However, these three experiments are limited to the mid-latitudes, a handful of frequencies, and at a limited number of days in a particular season. Recommendations for expanding this HF-NVIS portfolio and modeling capability conclude this report.

**Antenna:** Comparison of the whip to the loop showed that the upward pointing pattern of the loop reduced the RF noise level by 20 dB or more (Section 6). This loop was simply placed on the van as shown in Figure 61. There were no modifications to reduce horizontal sidelobes or get a tighter main beam. Both modifications will reduce the RF noise or, equivalently, boost the SNR. Increased SNR has significant implication for the mobile receiver's wideband HF-NVIS link budget (Section 2.3). Therefore, antenna pattern design boosting vertical signal strength and reducing horizontal RF noise for a mobile platform is an excellent HF-NVIS engineering task.

**Fading:** Both the O- and X-Modes exhibited non-stationary envelope fading consistent with "fast" and "slow" fading over the 58-second soundings. Neither fading process is readily available from ionograms sampled at 15-minute increments. The fading analysis simply fit the envelopes with the Rician distribution although other distributions were tested. Extracting a physics-based model of the "rough-surface" scattering from the ionograms is an excellent HF-NVIS topic. Another approach could use the clutter spectrum coupled with the ray-tracing code to establish fading on the ray paths [35]. Likewise, the deep fades in both the O- and X-Modes are puzzling given that the phase is so smooth. One conjecture is that ground effects may cause some fading as the mobile travels through mountainous terrains.

**Doppler:** The Doppler shifts in both the O- and X-Modes are well-modeled using the quadratic phase over the 58-second soundings (Sections 7.1, 7.2). Automatically extracting a physics-based model of this Doppler shift from the ionograms is an excellent enhancement of the 3-D ray-tracing code [43]. Likewise, adapting the Doppler spread computations of Pickering [62] to the O- and X-Mode ray paths is excellent enhancement of the 3-D ray-tracing code.

**Correlation:** Although the O- and the X-Modes showed low cross correlation, this observation is specific to this particular day, this frequency, and the route in the west-to-east direction. Therefore, a physics-based explanation is sought to explain this correlation. The north-to-south channel soundings will assess the role the Earth's magnetic field has in separating the modes on this west-to-east direction.

**Noise:** A positive result of these experiments shows that the HF-NVIS link with a loop antenna reduces noise by 20 dB in comparison with the standard whip. Therefore, a noise analysis comparing all three experiments incorporating the antenna patterns (Section 5.1), the theoretical noise levels (Section 2.3), and the measured noise levels (Section 6.2) will deliver wideband HF-NVIS noise models for the mid-latitudes.

**Interference:** These measurements verified Bark's [5] observation that interference plagues the HF link (Section 6.3). Indeed, both the delay spread and the cross correlation showed strong interference sources along the rural route and a wide noise swath driving through El Centro, CA. Currently, interference models for the mobile wideband HF-NVIS channel do not exist. Therefore, an interference analysis comparing this experiment and the north-south experiment will deliver wideband HF-NVIS interference models for this mobile link.

**Polarization:** The evolution of the polarization along each mode was predicted in 1934 by Booker [9]. One advance of the 3-D ray-tracing code is the tracking the polarization along the ray paths and the interaction with the ground bounces. Understanding the polarization state at the receiver is critical if SIMO gains are to be realized by polarization diversity. The dual-polarization sounding will quantify the SIMO gains for this polarization diversity. More generally, the 3-D ray-tracing code also supports the propagation of the Poynting vector along each mode. Better HF direction finding and vector sensing is enabled by separating these Poynting vectors.

**Absorption:** Although the 3-D ray-tracing code models absorption using the Hamiltonian, the parameters of the Hamiltonian are estimated from the time-varying ionosphere. The excellent review paper by Pederick and Carvera [59] makes explicit the shortfalls in many of the absorption models. Incorporating their semi-empirical model is a current task to upgrade the 3-D ray-tracing code.

**Reciprocity:** Non-reciprocity implies that the full-duplex channel emulators for HF radios must use different channel models for each link. Comparing measured and simulated non-reciprocity effects is an excellent task supporting HF networking.

Finally, efforts to acquire wideband HF-NVIS high-latitude measurements are underway. Figure 4 and the high-latitude long-haul measurements (Section 4.5) show that this ionosphere is challenging both in its static structures (e.g., polar walls) and the substantial time-varying magnetic fields. Maslin's observation [46, Section 8.2.3] that predictions can only be as good as the model shows that multiple high-latitude soundings are required to encompass these channels.



## References

1. Abbasi, N. M. 2012. "An Experimental Investigation into Feasibility of MIMO Techniques within the HF Band." Doctoral thesis. University of Leicester, Leicester, UK.
2. Antoniou, S., L. Christofi, P. R. Green, and G. F. Gott. 2006. "High Rate Data Transmission in the Mid-latitude NVIS HF Channel." *IEEE Proceedings – Communications* 153(2) (pp. 272–278).
3. Appleton, E. V. 1932. "Wireless Studies of the Ionosphere." *Institution of Electrical Engineers - Proceedings of the Wireless Section of the Institution* 7(21) (pp. 251–265).
4. Austin, B. A. and W. C. Liu. 2002. "Assessment of Vehicle-Mounted Antennas for NVIS Applications." *IEE Proceedings - Microwaves, Antennas and Propagation* 149(3) (pp. 147–152).
5. Bark, G. 1999. "Performance Comparison of Spread-spectrum Methods on an Interference-limited HF Channel." *IEEE Proceedings – Communications* 146(1) (pp. 23–28).
6. Balanis, C. A. 1989. *Advanced Engineering Electromagnetics*. John Wiley & Sons, New York, NY.
7. Belknap, D. J., R. D. Haggarty, and B. D. Perry. 1970. "Adaptive Signal Processing for Ionospheric Distortion Correction," Document EDS-TR-70-30. United States Air Force, L. G. Hanscom Field, Bedford, MA.
8. Bello, P. A. 1963. "Characterization of Randomly Time-variant Linear Channels," *IEEE Transactions on Communications Systems* 11(4):360–393.
9. Booker, H. G. 1934. "Some General Properties of the Formulae of the Magneto-Ionic Theory." *Proceedings of the Royal Society of London A: Mathematical, Physical and Engineering Sciences*, 147(861) (pp. 352–382). London, England.
10. Brine, N. L., C. C. Lim, A. D. Massie, and W. Marwood. 2006. "Capacity Estimation for the HF-MIMO Channel," *Proceedings of the Sixth Symposium on Radiolocation and Direction Finding*, Southwest Research institute, San Antonio, TX.
11. Budden, K. G. 1961. *Radio Waves in the Ionosphere*, Cambridge University Press, Cambridge, UK.
12. Crohn, I. and E. Bonek. 1992. "Modeling of Intersymbol-interference in a Rayleigh Fast Fading Channel with Typical Delay Power Profiles," *IEEE Transactions on Vehicular Technology* 41(4):438–446.
13. Daly, M., J. Meloling, J. Rockway, T. Xie, W. Nielsen, P. McGinnis, and A. Monges. 2015. "A Compact Six-port HF Vector Sensor." *Proceedings Antennas Applications Symposium* (pp. 142–163). September 21–23, Monticello, IL.

14. Daly, M., J. Allen, T. Wojtaszek, and M. Ontiveros. 2017. "Mitigation of Spectral Nulls in a Wideband HF Signal," 2017 IEEE AP-S Symposium on Antennas and Propagation and USNC-URSI Radio Science Meeting. 13 July 2017, San Diego, CA.
15. Daniels, R. C., S. W. Peters, and R. W. Heath, Jr. 2013. "HF MIMO NVIS Measurements with Co-located Dipoles for Future Tactical Communications." *Proceedings of MILCOM 2013 - 2013 IEEE Military Communications Conference* (pp. 1250–1255). November 18–20, San Diego, CA.
16. Daniels, R. C., and S. W. Peters. 2013. "A New MIMO HF Data Link: Designing for High Data Rates and Backwards Compatibility." *Proceedings of MILCOM 2013 - 2013 IEEE Military Communications Conference* (pp. 1250–1255). November 18–20, San Diego, CA.
17. Davies, K. 1990. *Ionospheric Radio*. Peter Peregrinus Ltd., London, United Kingdom.
18. Deng, Zh. L., D. B. Zhang, and J. M. Huang. 2010. "Current Research Vehicle Surface Affection on Antenna Polarization." *Proceedings of the 2010 6th International Conference on Wireless Communications Networking and Mobile Computing (WiCOM)*. September 23–25, Chengdu, China.
19. Department of the Army. 2009. "Tactical Radio Operations." Field Manual No. 6-02.53. Field Manual Headquarters, Department of the Army, Washington, DC.
20. Department of the Army. 1987. "Tactical Single-Channel Radio Communications Techniques." Field Manual No. 24-18. Field Manual Headquarters, Department of the Army, Washington, DC.
21. Erhel, Y., D. Lemur, M. Oger, and J. Le Masson. 2016. "Antenna Selection in a SIMO Architecture for HF Radio Links," *Radio Science* 51(3):223–230.
22. Feeny, S. M., S. Salous, E. M. Warrington, S. D. Gunashekar, N. Abbasi, L. Bertel, D. Lemur, and M. Oger. 2009. "Compact Antenna Arrays for HF HIMO Applications." *Proceedings of the 11th International Conference on Ionospheric Radio Systems and Techniques* (pp. 1–5). April 28–30. Edinburgh, Scotland.
23. Feinblum, D. A. and R. J. Horan. 1973. "Hilion – A Model of the High-latitude Ionospheric F2 Layer and Statistics of Regular Ionospheric Effects at Ft. Churchill, 1968," Bell Laboratories on behalf of Western Electric for the U.S. Army SAFEGUARD System Command.
24. Fitz, M. P. 2014. "Advanced High-frequency Wideband Communications." Quarterly Progress Report — July 2014 CRU-52-140807. Trellisware Technologies Inc.
25. Furman, W. N. and J. W. Nieto. 2012. "Latest on-air Testing of U.S. MIL-STD-188-110C Appendix D Wideband HF Waveforms." *Proceedings of the 12th IET International Conference on Ionospheric Radio Systems and Techniques (IRIST 2012)* (pp 1–5). May 15–17, York, United Kingdom.
26. Foust, F. 2016. "Ionospheric Absorption," *IHY Workshop on Advancing VLF through the Global AWESOME Network*, Stanford University, Stanford, CA.

27. Gillies, R. G. 2006. Modeling of Transionospheric HF Radio Wave Propagation for the ISIS II and ePOP Satellites. Doctoral thesis. Department of Physics and Engineering Physics, University of Saskatchewan, Saskatoon, SK.
28. Guanella, G. 1944. "New Method of Impedance Matching in Radio-Frequency Circuits," *The Brown Boveri Review* 327–329.
29. Gunashekar, S. D., E. M. Warrington, H. J. Strangeways, Y. Erhel, S. Salous, S. M. Feeney, N. M. Abbasi, L. Bertel, D. Lemur, F. Marie, and M. Oger. 2009. "Utilization of Antenna Arrays in HF Systems," *Annals of Geophysics* 52(3/4):323–338.
30. Gunashekar, S. D., E. M. Warrington, S. M. Feeney, S. Salous, N. M. Abbasi, L. Bertel, D. Lemur, and M. Oger. 2009. "Investigations into the Feasibility of Multiple Input Multiple Output Techniques within the HF Band: Preliminary Results," *Radio Science* 44(1).
31. Hi-Q-Military Antennas. Available online at <http://hiqantennas.com>. Accessed August 29, 2017.
32. Hoehner, P. 1992. "A Statistical Discrete-time Model for the WSSUS Multipath Channel," *IEEE Transactions on Vehicular Technology* 44(4):461–468.
33. Ignatenko, M., S. Sanghai, G. Lasser, B. Allen, M. Notaros, R. Smith, and D. S. Filipovic. 2016. "Low-Profile HF Antennas for Vehicles on the Move." Antenna Research Group (ARG) Department of Electrical, Computer, and Energy Engineering University of Colorado, Boulder, CO.
34. International Telecommunication Union. 2000. "Testing of HF Modems with Bandwidths of up to about 12 kHz Using Ionosphere Channel Simulators," Recommendation ITU-R F.1487 (05/2000). International Telecommunication Union, Geneva, Switzerland.
35. Jandieri, G. V. and A. Ishimaru. 2013. "Some Peculiarities of the Spatial Power Spectrum of Scattered Electromagnetic Waves in Randomly Inhomogeneous Magnetized Plasma with Electron Density and External Magnetic Field Fluctuations," *Progress In Electromagnetics Research B* (50):77–95.
36. Jones, R. M. and J. J. Stephenson. 1975. "A Versatile Three-Dimensional Ray Tracing Computer program for Radio Waves in the Ionosphere." OT Report 75-76. U.S. Department of Commerce, Washington, DC.
37. Jull, G. W. 1967. "Short-term and Averaged Characteristics of Nonreciprocal HF Ionospheric Paths," *IEEE Transactions on Antennas and Propagation* 15(2):268–277.
38. Kailath, T. 1962. "Measurements on Time-variant Communications Channels," *IEEE Transactions on Information Theory* 8(5):229–236.
39. Katal, N.. 1990. *A Generic Set of HF Antennas for Use with Spherical Mode Expansions*. Master's thesis. Naval Postgraduate School, Monterey, CA.
40. Kim, J. C. and E. I. Muehldorf. 1995. *Naval Shipboard Communications Systems*. Prentice Hall, Englewood Cliffs, NJ.

41. Kose, C. 2012. "High Frequency Ultra-Wideband Communications." Quarterly Progress Report CU-52-120903 to Office of Naval Research. Trellisware Technologies, Inc. San Diego, CA.
42. Larson, H. 1982. *Introduction to Probability Theory and Statistical Interference*, 3rd ed. John Wiley & Sons, New York, NY.
43. Lynn, K. J. W. 2009. "A Technique for Calculating Ionospheric Doppler Shifts from Standard Ionograms Suitable for Scientific, HF Communication, and other OTH Radar Applications," *Radio Science* 44(6):1–11.
44. Malachias, N. 1994. *Doppler Shift and Spread Study for Ionospherically Propagated Signals*. Master's thesis. Naval Postgraduate School, Monterey, CA.
45. Martinsen, W. 2009. "Giselle: A Mutually Orthogonal Triple Twin-loop Ground-symmetrical Broadband Receiving Antenna for the HF Band (U)," DSTO-TR-2331 (July). Command, Control, Communications and Intelligence Division, Defence Science and Technology Organisation, Canberra, AU.
46. Maslin, N. 1987. *HF Communications: A Systems Approach*. Plenum Press, New York, NY.
47. McNamara, L. F. 1991. *The Ionosphere: Communications, Surveillance, and Direction Finding*. Krieger Publishing Company, Malabar, FL.
48. Messier, G., and J. A. Hartwell. 2009. "An Empirical Model for Non-stationary Ricean Fading," *IEEE Transactions on Vehicular Technology* 58(1):14–20.
49. Moynz, J. 2011. "Improved High Frequency Communications," Navy SBIR 2012.1 – Topic N121-097. ONR Code 30, Arlington, VA.
50. Mott, H. 1986. *Polarization in Antennas and Radar*. John Wiley & Sons, New York, NY.
51. Ndao, P. M., D. Lemur, Y. Erhel, and C. Brousseau. 2009. "Capacity Estimation of MIMO Ionospheric Channels." *Proceedings of the Institution of Engineering and Technology 11th International Conference on Ionospheric Radio Systems and Techniques*. April 28–30, Edinburgh, UK.
52. Ndao, P. M., Y. Erhel, D. Lemur, and J. Le Masson. 2011. "Design of a High-frequency (3–30 MHz) Multiple-input Multiple-output System Resorting to Polarisation Diversity," *IET Microwaves, Antennas, & Propagation* 5(11):1310–1318.
53. Ndao P. M., Y. Erhel, D. Lemur, M. Oger, and J. Le Masson. 2013. "Development and Test of a Trans-horizon Communication System Based on a MIMO Architecture," *EURASIP Journal on Wireless Communications and Networking* 2013:167:1–13.
54. Nissen, C. A., and Phillip, A. B. 1994. "Measured Channel Parameters for the Disturbed Wide-bandwidth HF Channel," *Radio Science* 38(2):6-1–6-7.
55. Norman, R. J., J. A. Bennet, P. L. Dyson, J. Le Marshall, and K. Zhang. 2013. "A Ray-tracing Technique for Determining Ray Tubes in Anisotropic Media," *IEEE Transactions on Antennas and Propagation* 61(5):2664–2675.

56. North, R. C. and J. R. Zeidler. 1994. "Multichannel Adaptive Equalization for Improved Performance in LOS Digital Radio." *Proceedings of the IEEE Military Communications Conference*. October 2–5, Fort Monmouth, NJ.
57. Papoulis, A. 1984. *Probability, Random Variables, and Stochastic Processes*, 2nd ed. McGraw-Hill, New York, NY.
58. Papas, C. H. 1988. *Theory of Electromagnetic Wave Propagation*. Dover Publications, Mineola, NY.
59. Pederick, L. H. and M. A. Cervera. 2013. "Semiempirical Model for ionospheric Absorption Based on the NRLMSISE-00 Atmospheric Model," *Radio Science* 49(2):81–93.
60. Perry, B. D. 1983. "A New Wideband HF Technique for MHz-bandwidth Spread-spectrum Radio Communications," *IEEE Communications Magazine* 21(6):28–36.
61. Perrine, C., Y. Erhel, D. Lemur, L. Bertel, and A. Bourdillon. 2004. "A Way to Increase the Bit Rate in Ionospheric Radio Links," *Annals of Geophysics, Supplement to* 47(2/3):1145–1160.
62. Pickering, L. 1975. "The Calculation of Ionospheric Doppler Spread on HF Communication Channels," *IEEE Transactions on Communications* 23(5):526–537.
63. Proakis, J. G. and M. Salehi. 1994. *Communications Systems Engineering*. Prentice Hall, Upper Saddle River, NJ.
64. Reinisch, B. W. and I. A. Galkin. 2011. "Global Ionospheric Radio Observatory (GIRO)," *Earth, Planes, Space* 63(4): 377–381.
65. Salous, S. and E. D. R. Shearman. 1986. "Wideband Measurements of Coherence over an HF Skywave Link and Implication for Spread-spectrum Communication," *Radio Science* 21(3):463–472.
66. Scheible, M. P., J. D. Fite, K. M. Cuomo, J. L. Werth, G. W. Meurer, and C. R. Franzini. 2014. "High Data Rate, Reliable Wideband HF Communications Demonstration," The MITRE Corporation and Worcester Polytechnic Institute.
67. Schwartz, D. F. and J. C. Allen. 2004. Wide-Band Impedance Matching:  $H_\infty$  Performance Bounds, *IEEE Transactions on Circuits and Systems—II: Express Briefs*, 51(7):364–368.
68. Sen, H. K. and A. A. Wyller. 1960. "On the Generalization of the Appleton-Hartree Magnetoionic Formulas," *Journal of Geophysical Research* 65(12):3931–3950.
69. Settini, A., A. Ippolito, C. Cesaroni, C. Scotto. 2014. "Scientific Review on the Ionospheric Absorption and Research Prospects of a Complex Eikonal Model for One-layer Ionosphere," *International Journal of Geophysics* 2014, Article ID 657434.
70. Shkarofsky, I. P. and S. B. Nickerson. 1982. "Computer Modeling of Multipath Propagation: Review of Ray-tracing Techniques," *Radio Science* 17(5):1133–1158.

71. Shih, T. and N. Behdad. 2016. "Bandwidth Enhancement of Platform-mounted HF Antennas Using the Characteristic Mode Theory," *IEEE Transactions on Antennas and Propagation* 64(7):2648–2659.
72. Sklar, B. 1993. "Defining, Designing, and Evaluating Digital Communications Systems," *IEEE Communications Magazine* 31(11):91–101.
73. Stocker, A. J., E. M. Warrington, and D. R. Siddle. 2013. "Observations of Doppler and Delay Spreads on HF Signals Received Over Polar Cap and Through Paths at Various Stages of the Solar Cycle," *Radio Science* 48(5):638–645.
74. Strangeways, H. 2006a. Determination of the Capacity of Ionospheric HF MIMO Systems Employing Linear or Planar Arrays or Co-Located Antennas, *COST 296 Workshop*.
75. Strangeways, H. 2006b. "Investigation of Signal Correlation for Spaced and Co-located Antennas on Multipath HF Links and Implications for the Design of SIMO and MIMO Systems." *Proceedings of the First European Conference on Antennas and Propagation* (pp. 1–6). November 6–10, Nice, France.
76. Stüber, G. L. 2001. *Principals of Mobile Communication*, 2<sup>nd</sup> ed. Kluwer Academic Publishers, Norwell, MA.
77. Sumić, D. and R. Vlačić 2009. "An Assessment of HF-NVIS Radio System Reliability." *Proceedings of the 4th International Conference on Ports and Waterways POWA 2009*. September 10–11, Zagreb, Croatia.
78. Tepedelenlioğlu, C., A. Abdi, and G. B. Giannakis. 2003. "The Ricean K Factor: Estimation and Performance Analysis," *IEEE Transactions on Wireless Communication* 2(4):799–809.
79. Urie, M., G. Thatte, R. McCourt, P. Martin, X. Li, C. Köse, M. Fitz, and S. Enserink. 2015. "A Critique of HF-NVIS Channel Models." *Proceedings of the IEEE Military Communications Conference*. October 26–28, Tampa, FL.
80. Västberg, A., and B. Lundborg. 1997. "Superposition of Signals in Ionospheric Multipath Channels," *Radio Science* 32(5):2083–2090.
81. Wagner, L. S., J. A. Goldstein, W. D. Meyers, and P. A. Bello. 1989. "The HF Skywave Channel: Measured Scattering Functions for Midlatitude and Auroral Channels and Estimates for Short-term Wideband HF Rake Modem Performance." *Proceedings of Military Communications Conference 198* (pp. 48.2.1–48.2.10). October 15–18, Boston, MA.
82. Wagner, L. S. and J. A. Goldstein. 1995. "Channel Spread Parameters for the High-latitude, Near-vertical-incidence-skywave HF Channel: Correlation with Geomagnetic Activity." NRL Report NRL/FR/5550-95-9772, Naval Research laboratory, Washington, DC.
83. Whiteside, H. and R. King. 1964. "The Loop Antennas as a Probe," *IEEE Transactions on Antennas and Propagation* 12(3):291–297.
84. Witvliet, B. A. 2015. *Near Vertical Incidence Skywave: Interaction of Antenna and Propagation Mechanism*. Doctoral thesis. University of Twente, Enschede, Netherlands.

85. Witvliet, B. A. and R. M. Alsina-Pagès. 2017. "Radio Communications via Near Vertical Incidence Skywave Propagation: An Overview," *Telecommunication Systems Online Publication*.
86. Xu, S., H. Zhang, H. Yang, and H. Wang. 2004. "New Considerations for High Frequency Communications." *The 2004 Joint Conference of the 10th Asia-Pacific Conference on Communications and 5th International Symposium on Multi-Dimensional Mobile Communications* (pp. 444–447). August 29–September 1, Beijing, China.
87. Yacoub, M. D. 1993. *Foundations of Mobile Radio Engineering*. CRC Press, Boca Raton, FL.
88. Yau, K. S. B. 2008. *The Fading of Signals Propagating in the Ionosphere for the Wide Bandwidth High-frequency Radio Systems*. Doctoral thesis. School of Electrical and Electrical Engineering, University of Adelaide, AU.
89. Yeh, K. C. and C. H. Lui. 1972. *Theory of Ionospheric Waves*. Academic Press, New York, NY.
90. Yesil, A., M. Aydoğdu, and A. G. Elias. 2008. "Reflection and Transmission in the Ionosphere Considering Collisions in a First Approximation," *Progress in Electromagnetics Letters* 1:93–99.
91. Zhang, H., H. Yang, R. Luo, S. Xu. 2005. "Design Considerations of a New HF Modem and performance Analysis." *2005 IEEE International Symposium on Microwave, Antenna, Propagation and EMC Technologies for Wireless Communications Proceedings* 1:760–763.



## A. CALIBRATION OF THE CHANNEL SOUNDING SYSTEM

### A.1 CALIBRATION FACTOR FOR RECEIVED POWER

This calibration relates the levels of the digitized waveform on the receive software-defined radios (SDRs) to the actual incident power at the receive antenna feed. Two waveforms are used for calibration: a pure tone and the channel sounding waveform. The pure tone calibration produces an adjustment factor to go from digitized samples to incident power. The channel sounding waveform calibration produces an adjustment factor to go from a correlation function peak to incident power. Because the transmit and receive gain may vary with center frequency, the calibration was performed at different frequencies over 2 to 12 MHz.

A block diagram of the calibration setup is shown in Figure A-1. The transmitting radio is a National Instruments® USRP with an LFTX daughterboard. Power amplifiers that would normally go after the transmitting radio are bypassed and 33 dB of attenuation is instead added. The attenuated waveforms go into the receive chain. The first receive chain blocks are a transient power disrupter and a power limiter. Then, unlike the over-the-air channel sounding, the signal does not encounter a 180° hybrid coupler because the signal only enters the receive chain from one port instead of a two-port receive loop. The hybrid coupler was measured to attenuate each port by about 0.1 dB over the entire 2 to 12 MHz band. Then, in this calibration, the signal resumes the same path as with the over-the-air measurements through a bandpass filter, a low-noise amplifier (LNA) rated to 43 dB gain, and finally into an RFSpace® SDR. This receive SDR has internal attenuation that can be set at either 0, 10, 20, or 30 dB. The rated receive SDR maximum input power after internal attenuation is 13 dBm. For all calibration measurements, the SDR had 30 dB of internal attenuation to prevent exceeding the SDR's maximum input power. This 30-dB internal attenuation is taken into account when computing adjustments to dBm, so all adjustments to dBm assume no attenuation inside the receive SDR.

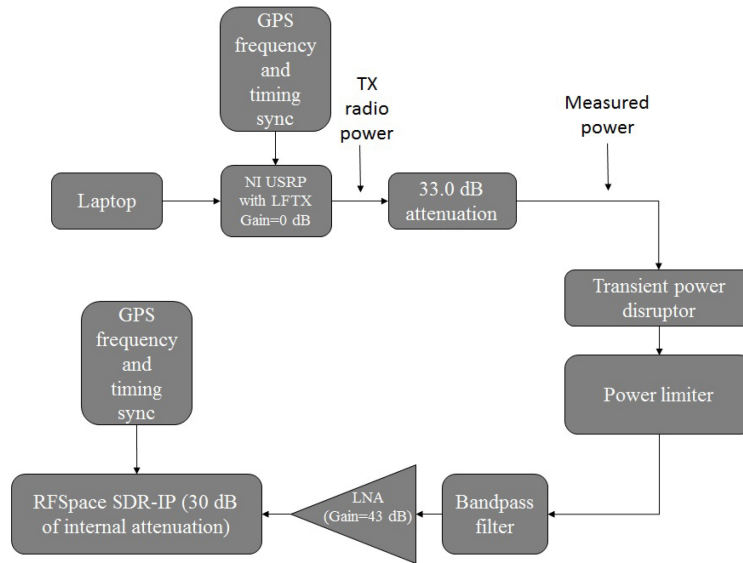


Figure A-1. Block diagram of the calibration using the NI USRP transmit radio (with external power amplifiers bypassed), external attenuators, and the receive chain and receive SDR (RFSPACE® SDR-IP).

Measurements of the transmitted power were made on a Keysight Fieldfox® Spectrum Analyzer at the point in Figure A-1 denoted by “Measured power.” The transmit radio power varies based on the bandwidth of the signal, so the powers of both a pure tone and the 25-kHz channel sounding waveform

were measured. The measurement bandwidths while measuring pure tones and the sounding waveform were 10 kHz and 50 kHz, respectively. These bandwidths were chosen so all of the signal frequency content was sure to be included in the power measurement without adding excessive internal noise in the power meter. Table A-1 gives the power from pure tones. The adjustment factors used to go from “digital power”  $10 \log_{10} (E [|s_{R,D}[n]|^2])$  to power incident on the receive chain in dBm are used as follows:

$$\text{Raw power at receive chain (dBm)} = 10 \log_{10} (E [|s_{R,D}[n]|^2]) + \text{Radio } n \text{ adjustment (dB)},$$

where  $s_{R,D}[n]$  is the digitized signal at the receive SDR and  $E[\cdot]$  is the expectation operator.

Table A-1. Pure tone power measurements and adjustment factors for each radio to go from “digital power” to incident power at the receive chain. Not included in the adjustment factors is the loss through a hybrid coupler, which was measured to be approximately 0.1 dB over the entire HF band.

Freq. (MHz)	Measured pwr. (dBm)	Radio 1: $10 \log_{10} (E [ s_{R,D}[n] ^2])$	Radio 2: $10 \log_{10} (E [ s_{R,D}[n] ^2])$	Radio 1 adjustment to dBm (dB)	Radio 2 adjustment to dBm (dB)
2.000	-29.03	-12.72	-21.55	-46.31	-37.48
2.387	-29.03	-11.35	-20.45	-47.68	-38.58
5.161	-29.14	-7.44	-17.04	-51.70	-42.10
5.820	-29.16	-7.21	-16.78	-51.95	-42.38
12.000	-29.86	-6.15	-15.56	-53.71	-44.30

A similar procedure determines calibration factors to go from the peaks in the correlation of the received signal with the channel sounding waveform and the actual incident power of the channel sounding waveform at the receiver. The channel sounding waveform is a BPSK-modulated pseudo-noise code (PN code 10) sequence with an autocorrelation that is nearly a delta function. The autocorrelation is not a perfect delta function due to the root-raised-cosine filtering of the transmitted waveform. The channel sounding waveform was chosen so that the separate propagation paths between the transmitter and receiver are denoted by distinct peaks after the received signal is correlated with the transmitted waveform. To compute the loss through the channel, the incident power of the signal at the receiver from these propagation paths must be calculated. Consequently, if the transmit power delivered to the antenna and the transmit and receive antenna realized gains (Institute of Electrical and Electronics Engineers [IEEE] Standard 145-1993) are known, the attenuation of each peak or propagation path is computable.

The channel sounding waveform begins each second on the second with 22 PN 10 sequences sent at a rate of 25,000 symbols per second. Because the PN 10 sequence is 1023 bits long, the channel sounding waveform has a duration of 0.9002 seconds. The remainder of each second is followed by silence. Because the correlation to determine channel power only is concerned with the times the waveform is received and not the silent periods, the calibration power measurements do not include a silent period and rather continuously repeat the PN 10 sequence.

Channel correlation is calculated using the procedure outlined in Section 5.3. Because in this calibration there is a 6-ft cable connecting the transmit SDR to the external attenuators and receive chain, the correlation should be a single peak with a delay of zero because the propagation time is much faster than the sampling rate. An example correlation peak from Radio 1 for a 2-MHz center frequency is shown in Figure A-2 and is calculated by  $20 \log_{10} (|R_{RC}(\tau)|)$ , where  $R_{RC}(\tau)$  is the correlation of the received signal with the transmitted signal. All correlations have this similar shape with peaks given in Table A-2.

The adjustment factors are used to go from correlation peak  $20 \log_{10} (|R_{RC}(\tau)|)$  to power incident on the receive chain in dBm as follows:

$$\text{Sounding waveform power at receive chain (dBm)} = 20 \log_{10} (|R_{RC}(\tau)|) + \text{Radio } n \text{ adjustment (dB)}$$

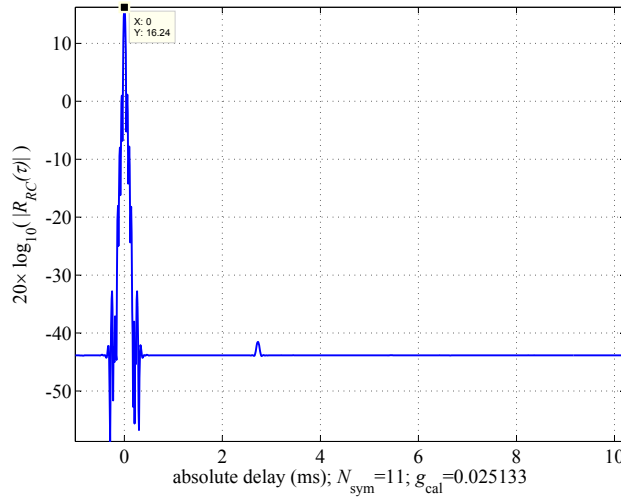


Figure A-2. Channel correlation from calibration setup with a center frequency of 2 MHz.

Table A-2. Channel correlation peak values and adjustment factors for each radio to compute incident power at the receive chain of the channel sounding waveform. Correlations are scaled by a normalization factor of 0.025133. Not included in the adjustment factors is the loss through a hybrid coupler, which was measured to be approximately 0.1 dB over the entire HF band.

Freq. (MHz)	Measured pwr. (dBm)	Radio 1: $20\log_{10}( R_{RC}(\tau) )$	Radio 2: $20\log_{10}( R_{RC}(\tau) )$	Radio 1 adjustment to dBm (dB)	Radio 2 adjustment to dBm (dB)
2.000	-38.04	16.24	8.78	-84.28	-76.82
2.387	-38.07	17.62	9.84	-85.69	-77.91
5.161	-38.27	21.62	13.34	-89.89	-81.61
5.820	-38.25	21.87	13.94	-90.12	-82.19
12.000	-38.91	22.98	15.13	-91.89	-84.04

The digitized power from a tone was on average 7.9 dB less at Radio 2 than at Radio 1. The digitized correlation peak was on average 9.3 dB less at Radio 2 than at Radio 1. Secondary peaks appear in the channel correlations when processing the Radio 2 calibration data but not the Radio 1 calibration data. These peaks occurred at a time delay greater than 2 ms, but the only correlation peak should be at 0 ms delay. These secondary peaks suggest the signal at Radio 2 may have exceeded the radio's dynamic range, as will be explained in Section A.2. However, the over-voltage indicator on Radio 2 was negative during the calibration. To be conservative, the received power at Radio 2 may be accurate only to within 2 dB.

The receive chain as configured in Figure A-1 represents the receive chain for channel soundings after February 2016. For the channel sounding done in February 2016, the receive chains did not include power limiters or bandpass filters. However, the calibration was remeasured after removing the power limiters and bandpass filter in Figure A-1 and the correlation peaks differed by less than 0.1 dB at each frequency.

## A.2 EFFECT OF RECEIVE SDR INTERNAL ATTENUATION

The receive SDR's internal attenuation can be adjusted by 10-dB increments between 0 dB and 30 dB. As expected, increasing the internal attenuation 10 dB scales the digitized signal by about 10 dB. Therefore, the attenuation level must be taken into account when computing the channel. The next set of figures show the correlation peaks for different levels of SDR internal attenuation. Figure A-3 shows the

correlation when no internal attenuation is added to the radio. The additional spikes in the correlation are caused by the received signal exceeding the dynamic range of the SDR's digitizer. The peak value should not be taken as reliable due to this error in quantization.

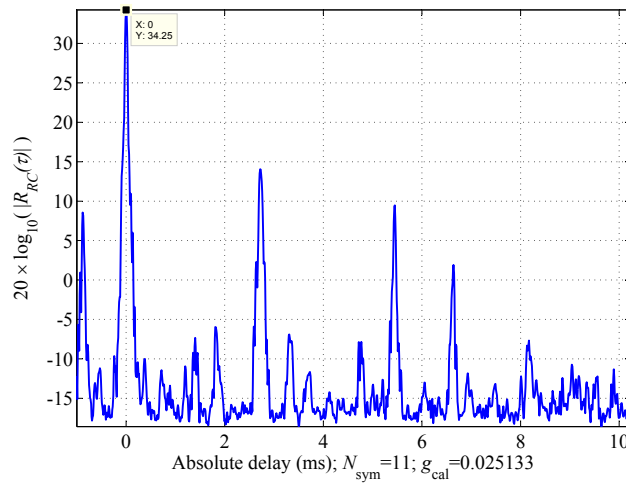


Figure A-3. Channel correlation with no internal attenuation. The additional spikes are due to the received signal constantly exceeding the dynamic range of the SDR's digitizer.

Figures A-4, A-5, and A-6 show the channel correlations when the receive SDR has 10, 20 and 30 dB of internal attenuation, respectively. The level of the maximum correlation decreases 10 dB with less than 0.1 dB of error each time the attenuation is increased 10 dB. The absolute level of these correlation peaks should not be compared directly to Section A.1 because different attenuation was used between transmit and receive chains when each of these measurements was taken.

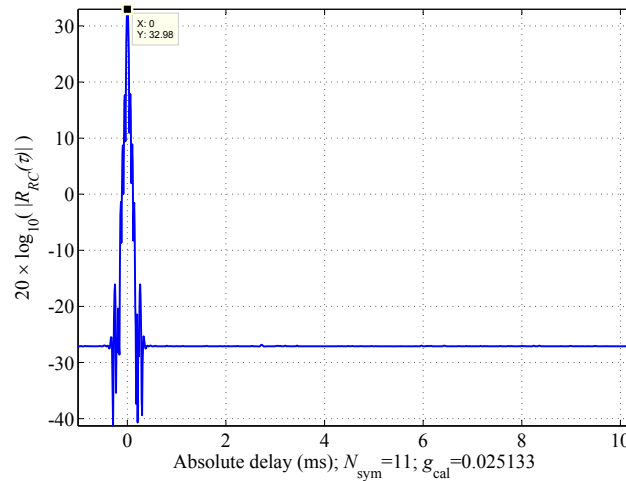


Figure A-4. Channel correlation with 10-dB internal attenuation.

A MATLAB<sup>®</sup> function called “GetInternalAttenuation.m” extracts the radio’s internal attenuator setting in the metadata of a .wav file recorded in SpectraVue<sup>®</sup>. The setting is encoded in the .wav file using the Resource Interchange File Format (RIFF). The RIFF subchunk containing the attenuation is labeled “auxi” and the attenuation is a 32-bit integer after sixteen 16-bit integers and five 32-bit integers in this subchunk. This is documented on page 64 of the SpectraVue<sup>®</sup> manual, available at <http://www.moetronix.com/files/spectravue.pdf>.

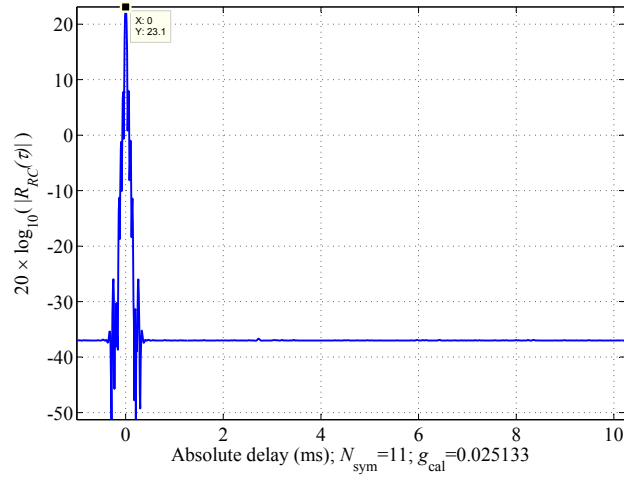


Figure A-5. Channel correlation with 20-dB internal attenuation.

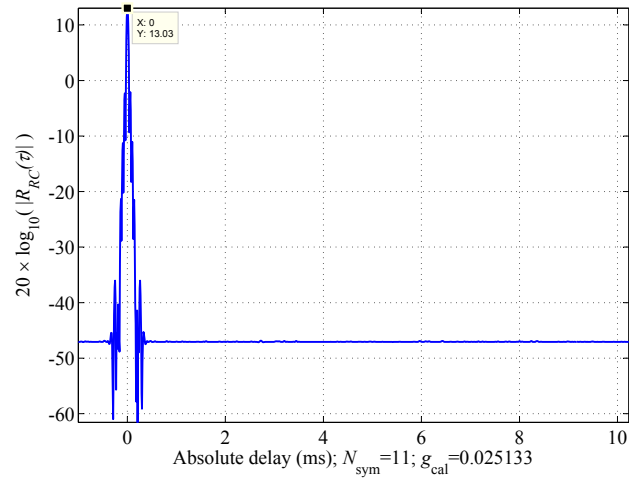


Figure A-6. Channel correlation with 30-dB internal attenuation.

## B. DOPPLER SHIFT MEASUREMENTS

This section undertakes Doppler shift estimation without vehicle motion. The implicit assumption in this approach is that after subtracting the Doppler shift due to vehicle motion, what is left is the Doppler shift produced by the ionosphere. In this context, the natural “test of this approach” requires comparison against other Doppler measurements, albeit limited. This section begins with an estimate of the Doppler shift due to vehicle motion, then presents measured Doppler shifts when subtracting the shift due to vehicle motion, and finally fits these Doppler shifts to statistical distributions.

### B.1 DOPPLER SHIFT DUE TO PLATFORM MOBILITY

The transmitter and receiver platforms are ground-based vehicles. The vehicles’ motions relative to the direction of propagation induces a Doppler shift of the transmitted signal. Because the path taken for NVIS communication is not the direct path between the two vehicles, the Doppler shift is not simply a function of the relative velocities of the two vehicles but rather is dominated by the angle of departure and arrival of the transmitted signal.

Assume two ground vehicles travel with velocities  $v_1$  and  $v_2$  in random directions, as shown in Figure B-1. The transmitted wave refracts off of the ionosphere in more of a curved path due to the gradient in refraction index of the ionosphere as a function of elevation. For simplicity, assume a perfect reflection off of a single layer ionosphere at some virtual height with an angle of reflection  $\theta_R$ .

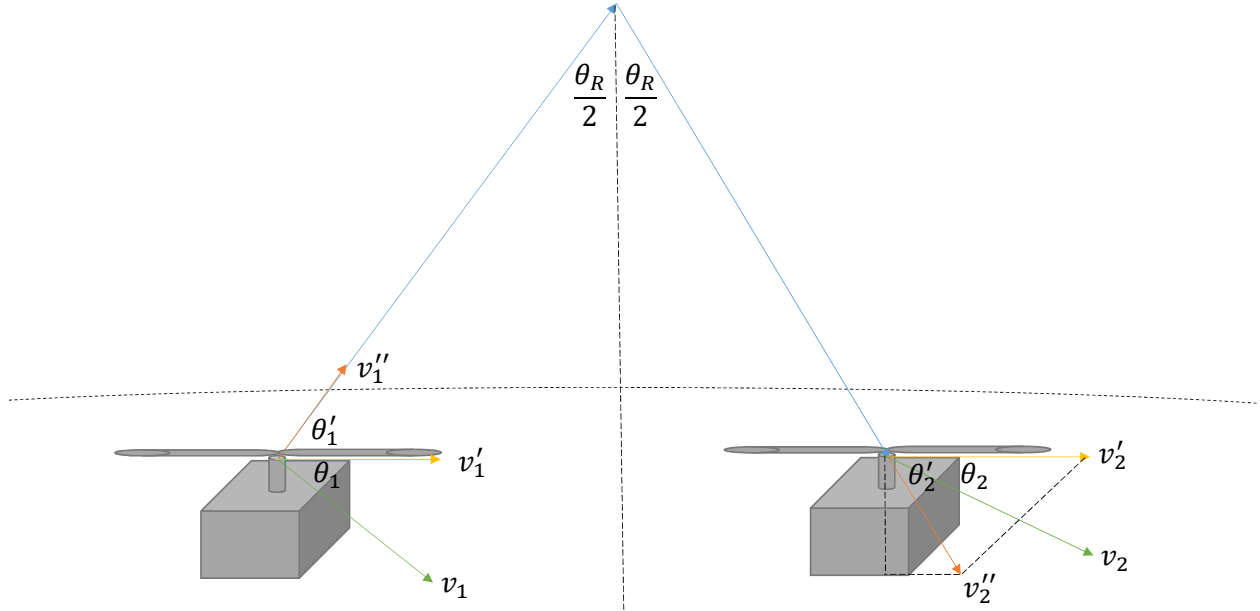


Figure B-1. The direction of propagation of an HF-NVIS signal between two mobile ground vehicles using NVIS antennas with velocities  $v_1$  and  $v_2$ .

The angle made between the ground velocity of the vehicle  $v_i$  and a ground velocity that follows the propagation direction  $v'_i$  is given by the following equation:

$$v'_i = v_i \cos(\theta_i),$$

where  $i$  is either 1 or 2 corresponding to the transmitter and receiver in Figure B-1. The angle between the ground direction velocity vector following propagation and the actual propagation velocity vector  $v''_i$  is

given by:

$$v_i'' = v_i' \cos(\theta_i') = v_i' \sin\left(\frac{\theta_R}{2}\right).$$

The Doppler shift caused by the velocities in the direction of propagation of the transmitter and receiver is given by:

$$f_D = \frac{f_0}{c} v_1'' - \frac{f_0}{c} v_2'' = \frac{v_1'' - v_2''}{\lambda_0},$$

where  $c$  is the speed of light,  $f_0$  is the signal center frequency, and  $\lambda_0$  is the wavelength. Substituting to express the Doppler shift as a function of velocities and ground directions and the ionosphere reflection angle gives:

$$f_D = \frac{v_1 \cos(\theta_1) - v_2 \cos(\theta_2)}{\lambda_0} \sin\left(\frac{\theta_R}{2}\right). \quad (\text{B-1})$$

Simulation and measurement of angles of reflection for NVIS propagation is found in [84]. In that reference, simulations showed that launch elevation angles from  $65^\circ$  to  $90^\circ$  were sufficient for a coverage area with a radius of 150 km. Measurements of the received angle of incidence for transmitters 9 to 165 km away sending a waveform at 7 MHz yielded a distribution of incidence angles between  $70^\circ$  and  $90^\circ$ . Assume the angle of incidence is uniformly distributed from  $65^\circ$  to  $90^\circ$ , which means  $\theta_R$  is uniformly distributed between  $0^\circ$  and  $50^\circ$ .

To compute typical values for Doppler shift, assume that the ground angles  $\theta_1$  and  $\theta_2$  are uniformly-distributed random variables from 0 to  $2\pi$ . Assume the velocity is less than 70 mph or about 32 m/s. The wavelength  $\lambda_0$  for frequencies 2 to 30 MHz ranges from 150 m to 10 m.

Doppler shifts are generated from one hundred thousand Monte Carlo simulations using the previously stated parameters at center frequencies from 2 to 12 MHz. The Doppler shifts are all distributed symmetrically around 0 Hz. The root mean squared Doppler shift for each frequency is shown in Figure B-2.

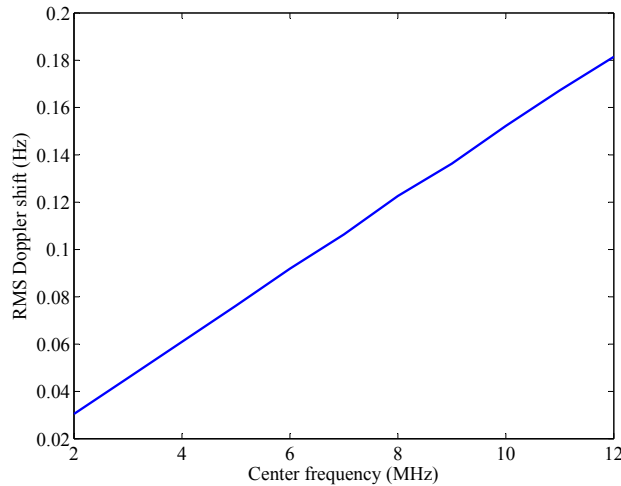


Figure B-2. The root mean squared Doppler shift as a function of frequency.

Two histograms of Doppler shifts at center frequencies of 2 and 12 MHz, respectively, are shown in Figures B-3 and B-4. These frequencies are seen as the lowest and highest feasible NVIS propagation frequencies. The Doppler shift is likely to be the highest at 12 MHz, but even at this frequency, the shift is



not likely to be more than 0.5 Hz. This Doppler shift will be compared with the level of Doppler spread induced by the ionosphere itself caused by the rising and falling of its layers.

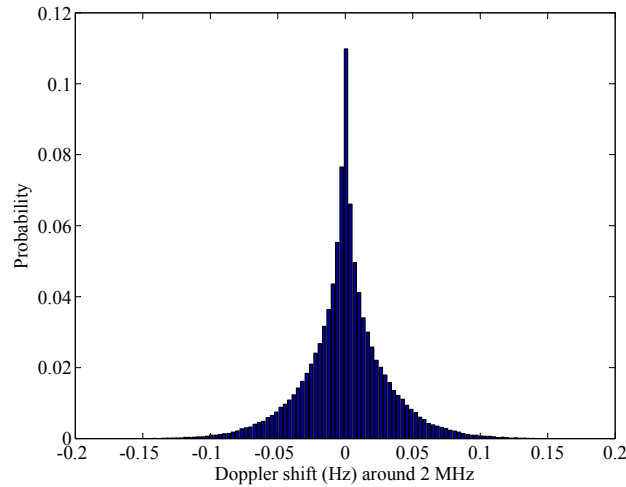


Figure B-3. A histogram of the predicted Doppler shifts when transmitting at 2 MHz.

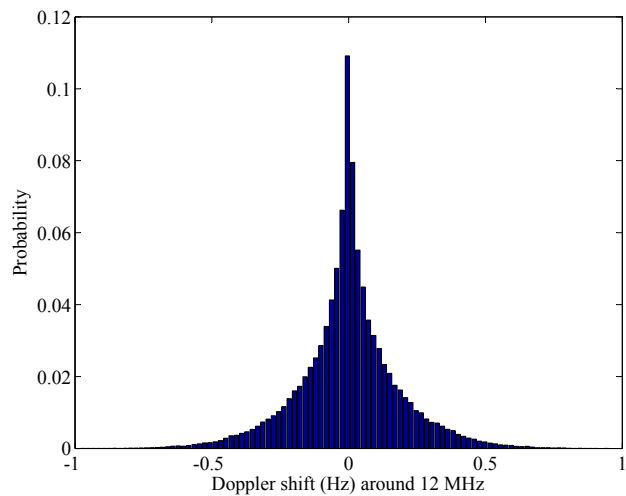


Figure B-4. A histogram of the predicted Doppler shifts when transmitting at 12 MHz.

## B.2 DOPPLER SHIFT FROM MEASURED CHANNEL SOUNDING DATA

The use of frequency-locked transmit and receive radios for channel sounding allows a direct calculation of Doppler shifts. Doppler shifts are calculated from the change in the phase of a peak of the delay-spread function over time. The delay-spread function is calculated by correlating the transmitted waveform with the received signal [8], and the peaks of the absolute value of this correlation correspond to propagation paths.

The distribution of Doppler shifts is the Doppler spread. This section is concerned with the Doppler spread of the first hops of the O- and X-Modes. From the power delay profile plotted over the entire sounding in Figure 87, the first hop delays can be seen by inspection to lie between 1.5 ms and 2.1 ms.

The process of finding correlation peaks is automated according to the following rules. The maximum absolute value of the correlation function is considered a peak. Any additional peaks must be located at a

delay where the absolute value of the correlation that is larger than the two neighboring samples and must be greater than 15 dB down from the global peak. The 15 dB figure comes from the fact that the sidelobes of the autocorrelation of the sounding waveform are about 16 dB down. Also, if there are more than four peaks that meet these criteria, the maximum peak value is likely near the noise floor. In this case, it is difficult to determine secondary peaks, so only maximum peak is recorded.

The phase in radians of the correlation at any peak is taken for just under a minute, out of convenience because the receiver recordings are made into new files each minute. The least-squares fit to the slope of the phase over time divided by  $2\pi$  is the estimate of the Doppler shift.

The Doppler shifts corresponding to all correlation peaks are plotted in Figure B-5. Of the 656 calculated Doppler shifts, there are three points that exist outside  $-0.5$  to  $0.5$  Hz at  $-1.7$  Hz,  $-2.5$  Hz (not shown) and  $-3.0$  Hz (not shown). The Doppler shifts caused by vehicle motion are calculated using Equation B-1. The calculated Doppler caused by vehicle motion is nearly the same for the O- and X-Modes over the same minute, because the difference in delay only slightly changes the angle of reflection off of a virtual height.

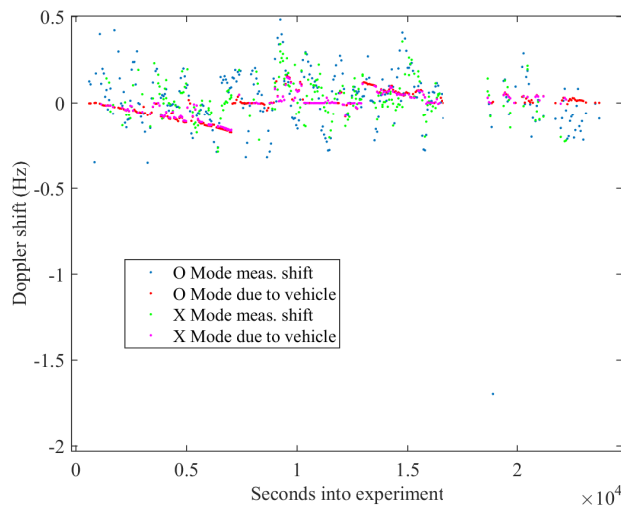


Figure B-5. Doppler shifts of all correlation peaks throughout the El Centro, CA channel sounding run. Doppler shifts of the first hop O-Mode are blue dots, the part of the Doppler shift attributable to vehicle motion for the O-Mode paths are red dots, Doppler shifts of the first hop X-Mode are green dots, and the part of the Doppler shift attributable to vehicle motion for the X-Mode paths are magenta dots

To determine the Doppler shift induced by the ionosphere, the Doppler shift caused by vehicle motion is subtracted from the total calculated Doppler shift. The residual Doppler shifts for the O- and X-Modes are collected into histograms shown in Figure B-6. Both modes present mean Doppler shifts of 0.02 Hz in a univariate distribution of approximately the same variance. The O-Mode variance around approximately 0 Hz is slightly greater. This greater variance is probably because when there is one peak very close to the noise floor, it is assigned to the O-Mode, and some assigned peaks very close to the noise floor might be noise themselves.

### B.3 FITTING A DISTRIBUTION TO THE MEASURED DOPPLER SPREAD

Like ray path delays and attenuation, Doppler shifts for the O- and X-Modes used in a channel emulator are based on a probability distribution. Figure B-6 compares the histograms of the two Doppler shifts. The O-Mode Doppler shifts tend to be slightly lower than the X-Mode Doppler shifts and both are

slightly asymmetric.

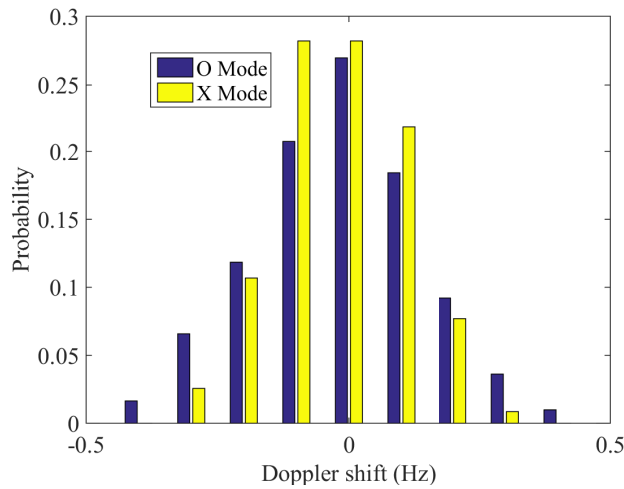


Figure B-6. A histogram of measured Doppler shifts of the first hop O- and X-Modes with Doppler caused by receive vehicle motion subtracted off.

Figures B-7 and B-8 assess the “goodness-of-fit” between the Gaussian distribution and the “*t* Location-Scale” distribution on the O- and X-mode Doppler shifts. Table B-1 compares the mean ( $\mu \approx$  average Doppler shift), standard deviation ( $2\sigma \approx$  Doppler spread), and the log-likelihood [42]. The higher the log likelihood function, the better the distribution fits the measured samples. The asymmetries in the measured data tend to bias the Gaussian estimate more than the “*t* Location-Scale” distribution. These estimates agree with the near-zero Doppler shifts estimated from the ionogram in Section 4.3, and Doppler shift in the selected stops in Section 7 that include the vehicle speed. If the vehicle speed only shifts the Doppler, the associated Doppler spread is unchanged. The Doppler spreads in Table B-1, estimated across the entire experiment, are comparable to the Doppler spreads reported in Table 22 estimated only over the non-TID times. The upshot is that these mobile HF-NVIS mid-latitude rays show near-zero Doppler during the daytime hours—the high angle and relatively low mobile speed do not shift the Doppler induced by the ionosphere.

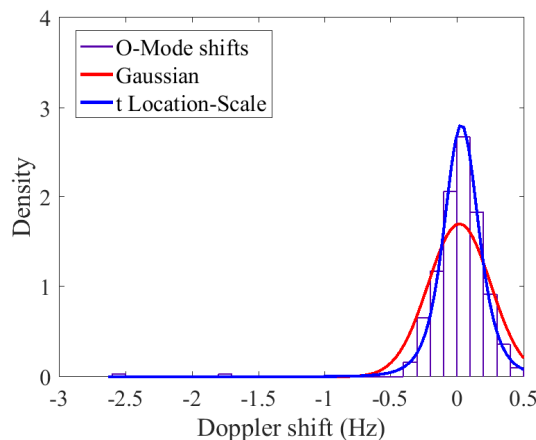


Figure B-7. Histogram of measured O-Mode Doppler shifts with best fit Gaussian and *t* Location-Scale distributions.

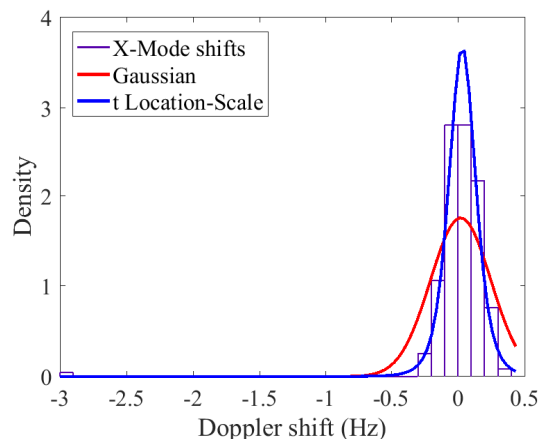


Figure B-8. Histogram of measured X-Mode Doppler shifts with best fit Gaussian and *t* Location-Scale distributions.

Table B-1. Modeling the Doppler shift induced by the ionosphere without vehicle speed.

Ray path	$\mu$	$\sigma$	Distribution	Likelihood
O-Mode	0.0187 Hz	0.234 Hz	Gaussian	10
X-Mode	0.0208 Hz	0.227 Hz	Gaussian	16
O-Mode	0.0335 Hz	0.183 Hz	$t$ Location-Scale	107
X-Mode	0.0331 Hz	0.133 Hz	$t$ Location-Scale	151

## C. DOPPLER SHIFTS AND THE TIME-VARYING TRANSFER FUNCTION

This section reviews the simple 1-Hop model for delay and Doppler shifts in the HF-NVIS channel. The model explains some features observed in the spectrograms of the measured channel soundings. The canonical HF-NVIS channel model consisting of only one strong O- and X-Mode has delay-spread function

$$h(t, \tau) = h_O e^{+j2\pi f_O t} \delta(\tau - \tau_O) + h_X e^{+j2\pi f_X t} \delta(\tau - \tau_X).$$

Bello's time-varying transfer function links the model to the spectrogram. The time-varying transfer function is Fourier transform in delay of the delay-spread function  $h(t, \tau)$  [8]:

$$T(t, f) = \int_{-\infty}^{\infty} e^{-j2\pi f \tau} h(t, \tau) d\tau.$$

Assume the transmitted signal  $s_T \in L^1(\mathbb{R}) \cap L^2(\mathbb{R})$  has the spectral representation

$$s_T(t) = \int_{-\infty}^{\infty} e^{+j2\pi f t} \hat{s}_T(f) df.$$

The time-varying channel acts on the transmitted signal as

$$h *_{\tau} s_T(t) = \int_{-\infty}^{\infty} h(t, t - \tau) s_T(\tau) d\tau = \int_{-\infty}^{\infty} e^{+j2\pi f t} T(t, f) \hat{s}_T(f) df$$

and captures the O- and X-Modes as follows:

$$T(t, f) = h_O e^{+j2\pi f_O t} e^{-j2\pi f \tau_O} + h_X e^{+j2\pi f_X t} e^{-j2\pi f \tau_X}.$$

if the spectrum of the transmitted signal is relatively flat, one estimate of the received signal's spectrogram is  $|T(t, f) \hat{s}_T(f)|^2$ . This spectrogram reveals the constructive and destructive interference of the O- and X-Modes as

$$|H(t, f)| = |h_O| \left| 1 + \rho e^{+j\phi(t, f)} \right|$$

where  $\rho = h_X/h_O$  and the phase is

$$\phi(t, f) := 2\pi(f_X - f_O)t - 2\pi f(\tau_X - \tau_O).$$

The canonical example of the O- and X-Mode interaction assumes both modes have equal power.

**Example 13 (Equal Modes)** Assume  $h_O = h_X = 1$ . In the O-Mode, assume zero Doppler shift  $f_O = 0$  Hz and time delay  $\tau_O = 2.16$  ms. In the X-Mode, assume  $f_O = 0.22$ -Hz Doppler shift and time delay  $\tau_X = 2.34$  ms. Figure C-1 plots  $H(t, f)$  over a 40-kHz band for a 3-second increment. For fixed time, spectrogram sliced in frequency will have minima spaced at multiples of

$$\Delta f_N = \frac{1}{|\tau_X - \tau_O|}.$$

For fixed frequency, spectrogram sliced in time will minima spaced at multiples of

$$\Delta t_N = \frac{1}{|f_X - f_O|}.$$

The minima are lines parallel to

$$t = -f \frac{\tau_X - \tau_O}{f_X - f_O}.$$

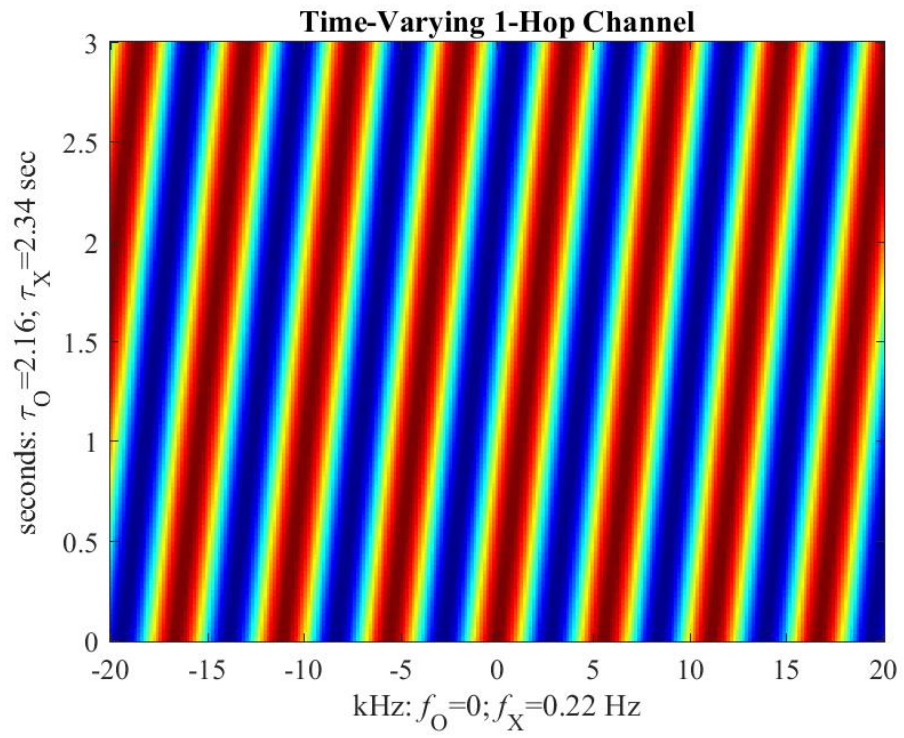


Figure C-1. Time-varying filter.

## D. 3-D IONOSPHERIC RAY TRACING USING *DRION*

*DrIon* is a three-dimensional ionospheric ray-tracing program used to analyze the channel performance for HF communications. This program is being developed in MATLAB<sup>®</sup> based on the Jones-Stephenson formulation of Hamilton's ray-tracing equations [36]. Electromagnetic waves propagating through the ionosphere will split into two possible waves. These are called the ordinary (O-Mode) and extraordinary (X-Mode) waves. *DrIon* computes both of these magneto-ionic waves for single and multiple hops between the transmitter and receiver. Hamilton's ray-tracing equations written in spherical polar coordinates are given by

$$\begin{aligned}\frac{dr}{dP'} &= -\frac{1}{c} \frac{\partial H / \partial k_r}{\partial H / \partial \omega} \\ \frac{d\theta}{dP'} &= -\frac{1}{rc} \frac{\partial H / \partial k_\theta}{\partial H / \partial \omega} \\ \frac{d\phi}{dP'} &= -\frac{1}{rc \sin \theta} \frac{\partial H / \partial k_\phi}{\partial H / \partial \omega} \\ \frac{dk_r}{dP'} &= \frac{1}{c} \frac{\partial H / \partial r}{\partial H / \partial \omega} + k_\theta \frac{d\theta}{dP'} + k_\phi \sin \theta \frac{d\phi}{dP'} \\ \frac{dk_\theta}{dP'} &= \frac{1}{r} \left( \frac{1}{c} \frac{\partial H / \partial \theta}{\partial H / \partial \omega} - k_\theta \frac{dr}{dP'} + k_\phi r \cos \theta \frac{d\phi}{dP'} \right) \\ \frac{dk_\phi}{dP'} &= \frac{1}{r \sin \theta} \left( \frac{1}{c} \frac{\partial H / \partial \phi}{\partial H / \partial \omega} - k_\phi \sin \theta \frac{dr}{dP'} - k_\theta r \cos \theta \frac{d\theta}{dP'} \right),\end{aligned}$$

where  $P' = ct$  is the group path length and  $H$  is the user-selected Hamiltonian. These ray-tracing equations are solved simultaneously using an ordinary differential equation (ODE) solver. The solution of these equations gives the spherical polar coordinates of each point along the ray path  $(r, \theta, \phi)$  and the propagation vector in the wave normal direction  $(k_r, k_\theta, k_\phi)$ . Other ray path quantities are found once the ray path is computed.

The infinitesimal Doppler shift resulting from a time-varying electron density profile is

$$\frac{d(f_D)}{dP'} = -\frac{1}{2\pi c} \frac{\partial H / \partial t}{\partial H / \partial \omega}. \quad (\text{D-1})$$

The total Doppler shift is computed by integrating along the ray path.

The phase path length is the phase shift along the ray path divided by the free space wavenumber. The phase path length is computed by integrating [36, Eq. 16]:

$$\frac{dP}{dP'} = -\frac{1}{\omega} \frac{k_r \frac{\partial H}{\partial k_r} + k_\theta \frac{\partial H}{\partial k_\theta} + k_\phi \frac{\partial H}{\partial k_\phi}}{\partial H / \partial \omega}$$

along the ray path. The phase path length quantity is critical to determine the wave polarization and the polarization fading at the receiver.

Power absorbed in the ionosphere along an infinitesimal segment of the ray path is [36, Eq. 17]:

$$\frac{dA}{dP'} = -\frac{10}{\ln(10)} k_0 \frac{\Im(k_0^2 n^2)}{k^2} \frac{dP}{dP'}.$$

The total amount of power (in dB) lost due electron collisions with neutral particles is the integral along the ray path.



The geometrical path length is computed by integrating [36, Eq. 18]

$$\frac{ds}{dP'} = \frac{1}{c} \frac{\sqrt{\left(\frac{\partial H}{\partial k_r}\right)^2 + \left(\frac{\partial H}{\partial k_\theta}\right)^2 + \left(\frac{\partial H}{\partial k_\phi}\right)^2}}{|\partial H / \partial \omega|}$$

along the ray path.

Both polarization

$$\rho = j \frac{Y_T^2 \pm \sqrt{Y_T^4 + 4Y_L^2 (U - X)^2}}{2Y_L (U - X)}$$

and longitudinal polarization

$$\rho_L = j \frac{Y_T}{(U - X)} (1 - n^2)$$

of the O- and X-Modes are computed along the ray path [11]. These polarization compute the magnitudes of the field components along the ray path, the wave polarization along the ray path, and finally, the correct voltage induced on the receive antenna.

**Hamiltonian:** *DrIon* includes several options for the Hamiltonian. The simplest Hamiltonian is

$$H = \Re \left\{ \frac{1}{2} \left( \frac{k^2}{k_0^2} - n^2 \right) \right\} ,$$

where  $k^2$  is the square of the propagation vector calculated from the solution of the ray-tracing equations and  $n^2$  is the square of the refractive index of the ionosphere. This Hamiltonian can be used with either the Appleton-Hartree formula [11] or the Sen-Wyller formula [68] for the index of refraction and works well for most situations. However, the ray-tracing solution breaks down when the ray path goes through a spitze. A spitze occurs when a ray path never becomes horizontal, but has a cusp at the height where  $X = 1$  [11]. In this case, a Hamiltonian based on the Booker Quartic formula is required. The solution of the Booker Quartic equation is the Appleton-Hartree formula for the index of refraction. The Hamiltonian based on the Booker Quartic,

$$H = \Re \left\{ \left[ (U - X) U^2 - Y^2 U \right] c^4 k^4 + X \left( \vec{k} \cdot \vec{Y} \right)^2 c^4 k^2 + \right. \\ \left. \left[ -2U (U - X)^2 + Y^2 (2U - X) \right] c^2 k^2 \omega^2 - X \left( \vec{k} \cdot \vec{Y} \right)^2 c^2 \omega^2 + \right. \\ \left. \left[ (U - X)^2 - Y^2 \right] (U - X) \omega^4 \right\}$$

is valid in all ray-tracing cases, including ray paths near a spitze. A similar Hamiltonian included in *DrIon* uses a quartic equation whose solution is the Sen-Wyller mono-energetic index of refraction.

**Improvements:** The Hamiltonian encoded in *DrIon* supports substantial improvements. First, improvements and validation of the absorption calculation needs to be performed. The absorption is difficult to compute since it depends on accurate knowledge of the electron density, neutral particle density, and electron temperature. These quantities are used to compute the electron collision frequency. The literature has many conflicting definitions of the electron collision frequency. These differences in definition need to be reconciled and validated with propagation measurements. Second, improved ionospheric models need to be added. This includes the automated assimilation of ionosonde data. There also needs to include a method to fit the ionosonde electron density profile to an analytical model that can

be effectively used by the ODE solver to find the ray paths. In addition to ionosonde data, ways to include traveling ionospheric disturbances and scintillation need to be determined. Finally, with the inclusion of the types of non-stratified ionospheric phenomena, the ray-homing algorithm needs to be improved. It is necessary to generalize this algorithm so that accurate ray paths between fixed transmitter and receiver locations can be determined in a fast and robust manner.

REPORT DOCUMENTATION PAGE				Form Approved OMB No. 0704-01-0188	
<p>The public reporting burden for this collection of information is estimated to average 1 hour per response, including the time for reviewing instructions, searching existing data sources, gathering and maintaining the data needed, and completing and reviewing the collection of information. Send comments regarding this burden estimate or any other aspect of this collection of information, including suggestions for reducing the burden to Department of Defense, Washington Headquarters Services Directorate for Information Operations and Reports (0704-0188), 1215 Jefferson Davis Highway, Suite 1204, Arlington VA 22202-4302. Respondents should be aware that notwithstanding any other provision of law, no person shall be subject to any penalty for failing to comply with a collection of information if it does not display a currently valid OMB control number.</p> <p><b>PLEASE DO NOT RETURN YOUR FORM TO THE ABOVE ADDRESS.</b></p>					
1. REPORT DATE (DD-MM-YYYY) July 2017		2. REPORT TYPE Final		3. DATES COVERED (From - To)	
4. TITLE AND SUBTITLE  Mid-Latitude Mobile Wideband HF-NVIS Channel Analysis: Part 1				5a. CONTRACT NUMBER	
				5b. GRANT NUMBER	
				5c. PROGRAM ELEMENT NUMBER	
				5d. PROJECT NUMBER	
6. AUTHORS Jeffery Allen                      Demi Truong Michael Daly                      Naval Research Enterprise John Meloling                      Internship Program Nazia Mozaffar Marcos Ontiveros Fred Verd SSC Pacific				5e. TASK NUMBER	
				5f. WORK UNIT NUMBER	
7. PERFORMING ORGANIZATION NAME(S) AND ADDRESS(ES) SSC Pacific 53560 Hull Street San Diego, CA 92152-5001				8. PERFORMING ORGANIZATION REPORT NUMBER TR 3075	
9. SPONSORING/MONITORING AGENCY NAME(S) AND ADDRESS(ES) Office of Naval Research 875 N. Randolph Street, Suite 1425 Arlington, VA 22203-1995				10. SPONSOR/MONITOR'S ACRONYM(S) ONR	
				11. SPONSOR/MONITOR'S REPORT NUMBER(S)	
12. DISTRIBUTION/AVAILABILITY STATEMENT Approved for public release.					
13. SUPPLEMENTARY NOTES This is work of the United States Government and therefore is not copyrighted. This work may be copied and disseminated without restriction.					
14. ABSTRACT High-frequency (HF) links (2 to 30 MHz) are an alternative to the cost and tactical fragility of commercial satellite communications (SATCOM) for beyond line-of-sight (LOS) links. However, standard HF systems operating over a 3-kHz bandwidth do not provide sufficient throughput for network applications. Simply increasing bandwidth does increase throughput—provided the radios are properly designed for the time-varying wideband HF channel. The Wideband HF Channel is governed by the inonospheric variations caused by latitude, the night and day cycle, the direction and length of the haul, the seasons, and ionosphere disturbances. This report is the first of a series seeking a better understanding of each of these channel variations to aid in the design of wideband HF systems and the proper comparisons of different HF radios and waveforms. This report uses wideband mid-latitude HF channel soundings and 3-D ray-tracing simulations to develop a statistical model of a particular nearly vertical incidence skywave (NVIS) channel. The immediate application of this particular channel is for small-unit ground-mobile forces with vehicle-mounted antennas. Near-term extensions support mid-latitude short-haul (200 to 1500 km) and long-haul ship-to-ship and ship-to-shore wideband HF channels. Long-term payoffs for the warfighter will be a better HF radio design, leading to increase data rates, more stable networks, reduced power requirements, and improved low probability of detection (LPD).					
15. SUBJECT TERMS high frequency (HF) nearly vertical incidence skywave (HF-NVIS); low probability of detection (LPD); communication design; ionosphere; O-Mode; X-Mode					
16. SECURITY CLASSIFICATION OF:			17. LIMITATION OF ABSTRACT	18. NUMBER OF PAGES	19a. NAME OF RESPONSIBLE PERSON
a. REPORT	b. ABSTRACT	c. THIS PAGE			Michael Daly
U	U	U	U	153	19B. TELEPHONE NUMBER (Include area code) (619) 553-2366

## INITIAL DISTRIBUTION

84300	Library	(1)
85300	Archive/Stock	(1)
52250	Jeffery Allen	(1)
52250	Michael Daly	(1)
52250	John Meloling	(1)
52250	Nazia Mozaffar	(1)
52250	Fred Verd	(1)
52270	Marcos Ontiveros	(1)

Defense Technical Information Center Fort Belvoir, VA 22060–6218	(1)
---	-----

Approved for public release.



SSC Pacific  
San Diego, CA 92152-5001